SUMY STATE
UNIVERSITY

p-ISSN 2312-2498
e-ISSN 2414-9381

http://jes.sumdu.edu.ua
jes@sumdu.edu.ua

JOURNAL OF ENGINEERING SCIENCES

ЖУРНАЛ ІНЖЕНЕРНИХ НАУК

ЖУРНАЛ ИНЖЕНЕРНЫХ НАУК

Volume 6
Issue 1 (2019)

The Ministry of Education and Science of Ukraine

Міністерство освіти і науки України

Министерство образования и науки Украины

JOURNAL OF ENGINEERING SCIENCES

ЖУРНАЛ ІНЖЕНЕРНИХ НАУК

ЖУРНАЛ ИНЖЕНЕРНЫХ НАУК

Scientific Journal

Науковий журнал

Научный журнал

Volume 6, Issue 1 (2019)

Том 6, № 1 (2019)

Founded in 1994

Заснований у 1994 році

Основан в 1994 году

Sumy State University

Сумський державний університет

Сумский государственный университет

The “Journal of Engineering Sciences” is an open access scientific journal that covers urgent issues of the up-to-date high-tech production, development of new engineering trends and future technologies. General topics of the journal concerns manufacturing, mechanical and chemical engineering. The publication language is English. The editorial board represented by scientists from different International research institutions allows covering the journal’s topics and qualitatively evaluate all the submitted papers. The system of double blinded reviewing process provides a high-quality presentation of papers. The editorial police including the submitting, reviewing, acceptance, and publication of the materials are completely transparent.

p-ISSN 2312-2498
e-ISSN 2414-9381

Recommended for publication
by the Academic Council of Sumy State University,
(minutes No. 11 of 15.04.2019)

The Journal is the scientific professional edition of Ukraine (Category “B”) in the field of Engineering Sciences ordered by the Ministry of Education and Science of Ukraine, November 7, 2018, No. 1218.

Crossref

DOAJ DIRECTORY OF OPEN ACCESS JOURNALS

INDEX COPERNICUS INTERNATIONAL

The information support of the “Journal of Engineering Sciences” is provided by the partners:

– Faculty of Manufacturing Technologies, Technical University of Kosice (Slovakia): http://www.fvt.tuke.sk;
– Faculty of Mechanical Engineering and Management, Poznan University of Technology (Poland): https://www.put.poznan.pl;
– Faculty of Mechanical Engineering, University of West Bohemia (Czech Republic): http://www.fst.zcu.cz;
– International Association for Technological Development and Innovations (Ukraine): http://dsmie.sumdu.edu.ua.

Editorial Board: Apt. LA 207, 2 Rymskogo-Korsakova St., 40007 Sumy, Ukraine
Contact Phones: +38 (0542) 331024; +38 (099) 3845740
E-mail: jes@sumdu.edu.ua
Web-site: http://jes.sumdu.edu.ua

State registration certificate of the print mass-media No. 20499-10299 ПР.

JOURNAL OF ENGINEERING SCIENCES
ЖУРНАЛ ІНЖЕНЕРНИХ НАУК
ЖУРНАЛ ИНЖЕНЕРНЫХ НАУК
Web site: http://jes.sumdu.edu.ua
Volume 6, Issue 1 (2019)

CrossRef
https://search.crossref.org

Directory of Open Access Journals (DOAJ)
https://doaj.org

Index Copernicus International Journals Master List
https://journals.indexcopernicus.com

Google Scholar
https://scholar.google.com

International Institute of Organized Research
http://www.i2or.com

Scientific Indexing Services (SIS)
http://www.sindexs.org

Academic Resource Index (Research Bible)
http://researchbib.com

Directory of Research Journals Indexing (DRJI)
http://www.drji.org

World Cat
http://www.worldcat.org

Eurasian Scientific Journal Indexing (ESJI)
http://esjindex.org

China National Knowledge Infrastructure (CNKI)
http://www.cnki.net

Journal Impact Factor
http://jifactor.org

Impact Factor Services for International Journals (IFSIJ)
http://ifsij.com

Journal Factor
http://www.journalfactor.org

Open Academic Journals Index (OAJI)
http://oaji.net

Academic Keys
http://academickeys.com

International Society for Research Activity (ISRA)
Journal Impact Factor (JIF):
http://www.israjif.org
Advanced Science Index (ASI):
http://journal-index.org
International Scientific Indexing (ISI):
http://isindexing.com

Global Digital Publishing Platform
https://issuu.com

Vernadsky National Library of Ukraine
http://www.nbuv.gov.ua

Electronic Sumy State University Institutional Repository
http://essuir.sumdu.edu.ua

EDITORIAL BOARD

EDITOR-IN-CHIEF

Dmytro KRYVORUCHKO, D.Sc., Professor, Sumy State University, Sumy, Ukraine.

MANAGING EDITOR

Ivan PAVLENKO, Ph.D., Associate Professor, Sumy State University, Sumy, Ukraine.

BOARD OF CO-EDITORS

Manufacturing Engineering

Eddy BAJIC, Ph.D., Professor, University of Lorraine, Nancy, France;
Milan EDL, Ph.D., Associate Professor, University of West Bohemia, Pilsen, Czech Republic.

Mechanical Engineering

Jan PITEL, Ph.D., Professor, Technical University of Kosice, Presov, Slovakia;
Praveen AGARWAL, Ph.D., Professor, Anand International College of Engineering, Jaipur, India.

Chemical Engineering

Roman PETRUS, D.Sc., Professor, Rzeszow University of Technology, Rzeszow, Poland;
Vsevolod SKLABINSKYI, D.Sc., Professor, Sumy State University, Sumy, Ukraine.

ADVISORY EDITORIAL BOARD

Volodymyr ATAMANYUK., D.Sc., Professor, Lviv Polytechnic National University, Lviv, Ukraine;
Olaf CISAK, Ph.D., Associate Professor, Poznan University of Technology, Poznan, Poland;
Kostiantyn DYADYURA, D.Sc., Professor, Sumy State University, Sumy, Ukraine;
Oleksandr GUSAK, Ph.D., Associate Professor, Sumy State University, Sumy, Ukraine;
Michal HATALA, Ph.D., Associate Professor, Technical University of Kosice, Presov, Slovakia;
Fuat KARA, Ph.D., Assistant Professor, Duzce University, Istanbul, Turkey;
Serhii KLIMENKO, D.Sc., Professor, Bakul Institute for Superhard Materials, National Academy of Sciences of Ukraine, Kyiv, Ukraine;
Czeslaw KUNDERA, D.Sc., Professor, Kielce University of Technology, Kielce, Poland;
Ivan KURIC, Ph.D., Professor, University of Zilina, Slovakia;
Milovan LAZAREVIC, Ph.D., Associate Professor, University of Novi Sad, Novi Sad, Serbia;
Stanislaw LEGUTKO, D.Sc., Professor, Poznan University of Technology, Poznan, Poland;
Oleksandr LIAPOSHCHENKO, D.Sc., Associate Professor, Sumy State University, Sumy, Ukraine;
Volodymyr MARTSYNKOVSKYY, D.Sc., Professor, Sumy State University, Sumy, Ukraine;
Yirii MATSEVITYI, D.Sc., Professor, Podgornyi Institute for Mechanical Engineering Problems, National Academy of Sciences of Ukraine, Kharkiv, Ukraine;
Yurii PETRAKOV, D.Sc., Professor, National Technical University of Ukraine "Kyiv Polytechnic Institute", Kyiv, Ukraine;
Leonid PLYATSUK, D.Sc., Professor, Sumy State University, Sumy, Ukraine;
Frantisek POCHYLY, Ph.D., Professor, Brno Technical University, Brno, Czech Republic;
Yimin RONG, D.Sc., Professor, South University of Science and Technology, Shenzhen, China;
Vitalii SIMONOVSKIY, D.Sc., Professor, Sumy State University, Sumy, Ukraine;
Michael STORCHAK, D.Sc., Professor, Institute for Machine Tools of Stuttgart University, Stuttgart, Germany;
Fabio TEIXEIRA, D.Sc., Professor, Federal University of Rio Grande do Sul, Porto Alegre, Brazil;
Justyna TROJANOWSKA, Ph.D., Assistant Professor, Poznan University of Technology, Poznan, Poland;
Michal VARCHOLA, Ph.D., Professor, Slovak University of Technology in Bratislava, Bratislava, Slovakia;
Jozef ZAJAC, D.Sc., Professor, Technical University of Kosice, Presov, Slovakia;
Viliam ZALOGA, D.Sc., Professor, Sumy State University, Sumy, Ukraine.

TECHNICAL SECRETARY

Kristina BERLADIR, Ph.D., Assistant Professor, Sumy State University, Sumy, Ukraine.

TOPICS
OF THE “JOURNAL OF ENGINEERING SCIENCE”

1. Manufacturing Engineering:
- (A) Machines and Tools;
- (B) Technical Regulations and Metrological Support;
- (C) Materials Science.

2. Mechanical Engineering:
- (D) Dynamics and Strength of Machines;
- (E) Computational Mechanics.

3. Chemical Engineering:
- (F) Processes in Machines and Devices;
- (G) Energy Efficient Technologies;
- (H) Environmental Protection.

JOURNAL OF ENGINEERING SCIENCES
ЖУРНАЛ ІНЖЕНЕРНИХ НАУК
ЖУРНАЛ ИНЖЕНЕРНЫХ НАУК
Web site: http://jes.sumdu.edu.ua
Volume 6, Issue 1 (2019)

CONTENTS

MANUFACTURING ENGINEERING

MECHANICAL ENGINEERING

CHEMICAL ENGINEERING

Processes in Machines and Devices ○ ○ ○ ○ ○ ● ○ ○ **F**

Energy Efficient Technologies ○ ○ ○ ○ ○ ○ ● ○ **G**

Environmental Protection ○ ○ ○ ○ ○ ○ ○ ● **H**

MANUFACTURING 2019

- Machine design and maintenance
- Manufacturing process planning
- Manufacturing techniques
- Metrology and measurement systems
- Materials engineering
- Management and production engineering
- Solutions for Industry 4.0

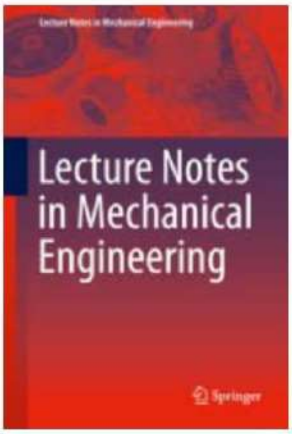

Lecture Notes in Mechanical Engineering

Springer

MANUFACTURING 2017
Indexed in WoS & Scopus

Important Dates:

31.10.2018	Full-paper submission deadline
20.12.2018	Acceptance notification
18.01.2019	Submission of revised papers
01.02.2019	Final version submission and registration
01.02.2019	Payment deadline
19–22.05.2019	**MANUFACTURING 2019 conference**

Contact:

MANUFACTURING team

+48 61 665 27 98
✉ manufacturing@put.poznan.pl
www.manufacturing.put.poznan.pl
fb.com/manufacturing2019

JOURNAL OF ENGINEERING SCIENCES
ЖУРНАЛ ІНЖЕНЕРНИХ НАУК
ЖУРНАЛ ИНЖЕНЕРНЫХ НАУК
Web site: http://jes.sumdu.edu.ua
DOI: 10.21272/jes.2019.6(1).b1 Volume 6, Issue 1 (2019)

UDC 519.86:330.356.7

Analysis of the Methodology of Constructing a Production Function Using Quality Criteria

Skrynkovskyy R. M.[1], Yuzevych V. M.[2], Kataev A. V.[3], Pawlowski G.[4*], Protsiuk T. B.[5]

[1] Lviv University of Business and Law, 99 Kulparkivska St., 79021 Lviv, Ukraine;
[2] Karpenko Physico-Mechanical Institute of the NAS of Ukraine, 5 Naukova St., 79060 Lviv, Ukraine;
[3] Kharkiv Institute of Trade and Economics of Kyiv National University of Trade and Economics,
8 Otakara Yarosha St., 61045 Kharkiv, Ukraine;
[4] Zaklad Handlowo-Uslugowy BHP”, 17 Kostrzynska St., 69-113 Gorzyca, Poland;
[5] Academy of Financial Monitoring, 24 Biloruska St., 04050 Kyiv, Ukraine

Article info:
Paper received: July 20, 2018
The final version of the paper received: December 16, 2018
Paper accepted online: December 20, 2018

[*]Corresponding Author’s Address:
gpawlowski@op.pl

Abstract. In the article to forecast the trends of development of the state's industry (for example, Ukraine), a method for evaluating the parameters included in the classical Cobb-Douglas formula is developed. On the basis of the computational experiment it was established that if the values of the production function Y are close to the numerical values and the deviation between them does not exceed 3.7 %, then for approximation of Y in the industry for small time periods, it makes no sense to complicate the set of its parameters and coefficients. For forecasting the values of Y_i ($Y_i \in Y$) we have evaluated the parameters that are included in the classical Cobb-Douglas formula. To improve the methodology for estimating the coefficients included in the Cobb-Douglas type formula, new variants of the multiplicative and additive quality criteria and for the Ukrainian industry are proposed, based on the analytical data for 2010–2017, the evaluation of the relevant criteria was carried out.

Keywords: production function, Cobb-Douglas function, quality criteria, industry, industrial products.

1 1 Introduction

Over the past decades, a special feature of the practice of analyzing manufacturing processes has been the active use of special methods of statistics modelling. An important role in this context belongs to production functions.

At the present stage of research [1, 2]:

1) the essence of the production function is that it enables to formulate concrete alternatives (variants) of the combination of factors of production to ensure a certain amount of production, that is, the possibility of one factor of production to replace others;

2) the production function is not only the prospect of one of the analytical methods for forecasting the development of the state’s economy, but also an applied instrument used to assess and compare the effectiveness of national economies;

3) the macroeconomic production function has a wide range of applications , since its dynamic analysis allows to solve such key important tasks:

– study the dynamics of the efficiency of production factors (labor productivity, return on investments);

– identify factors of production growth;

– determine the contribution of each production factor to the overall increase in production.

For Ukraine in the conditions of European integration [3], where one of the pressing issues is today to identify the reserves of the growth of the national economy, the use of information about local rates of change in the production function can give impetus to the improvement of existing mechanisms for management and activation of internal factors of development.

2 Literature Review

In theoretical and applied analysis, the most widely used are the following 4 types of production functions:

1) linear [2, 4];
2) Cobb–Douglas function [2, 5–7];
3) function CES (with postmobile elastics) [2];
4) Leontief function [4].

Their advantages are small number of coefficients (parameters) [2], which greatly facilitates the statistical evaluation, as well as indicators of economic growth (efficiency, intensification), calculated on their basis, have a convenient analytical form.

Among the most famous functions is the classic production function of Cobb-Douglas, which has the form [5–7]:

$$Y = AL^{\alpha}K^{\beta}, \qquad (1)$$

where A – technological coefficient (or coefficient characterizing production efficiency); L – work resources; K – volume of fixed investments; α, β – coefficients of elasticity for labor and investments, respectively.

Partial elasticity factor of the product on the funds:

$$E_K = \frac{\partial Y}{\partial K}\frac{K}{Y} = A\beta L^{\alpha}K^{\beta-1}\frac{K}{AL^{\alpha}K^{\beta}} = \beta. \qquad (2)$$

Elasticity of the product by labor:

$$E_L = \frac{\partial Y}{\partial L}\frac{L}{Y} = A\alpha L^{\alpha-1}K^{\beta}\frac{L}{AL^{\alpha}K^{\beta}} = \alpha. \qquad (3)$$

These coefficients of elasticity reflect the percentage of output growth while increasing resource costs by 1 %.

These coefficients of elasticity reflect the percentage of output growth while increasing resource costs by α, β are constant and independent of the factor K, L.

In practice, the use of production functions, verification the sum of the coefficients α and β on one equality is very important, since it determines the type of economic growth [2]:

1) $\alpha + \beta > 1$ (production function with increasing return on a scale) corresponds to intensive economic growth, and in the case of $\alpha > \beta$ there is an intensive economic growth of labor; at $\alpha < \beta$ intensive economic growth of funds;

2) $\alpha + \beta < 1$ (production function with decreasing returns to scale) means that output is growing slower than the growth of the factors K and L, that is, there is no economic growth (or other important factors remain outside consideration);

3) $\alpha + \beta = 1$ there is an extensive type of economic growth (a production function with constant returns on a scale).

Based on research results [8–11] and taking into account the information in the paper [12], one has to agree with the author's opinion [2], that among the important factors not taken into account in the production function of type (1), it is worth noting the elements of scientific and technological progress, in particular, the place and role of information technology. The impact of scientific and technological progress is manifested in the growth or aggregate efficiency of resources, or the effectiveness of an individual resource.

At the same time, the special importance of modern information technologies for economic growth is presented in the work of American economists S. D. Oliner and D. E Sichel [11], who carried out the evaluation of the parameters of the production function, in which the indicators of information technology were included as independent factors of production. The authors [11] built a model that assessed the impact on the economic growth of the following three factors:

1) investments in the software;
2) investments in communications;
3) other costs.

Here the labor quality index was included as labor costs. Quality was taken into account by means of indicators of changes in levels of education, qualifications and structure (by level of education and sex) employed – [12].

In the context of the analysis of various important factors of development, one should note the important feature of the apparatus of production functions, the use of which makes it possible to compare the trends of economic development of different countries [6, 13–15].

An analysis of the methodology for constructing a production function using quality criteria, which is the purpose of this article, can be considered as one of the steps for the active use of the production function in practice. At the same time, it will enable to activate promising directions of research of the Ukrainian economy.

The achievement of the above goal led to the following tasks:

1) to introduce the mathematical tools of the methodology of refining the production function using an expanded set of constant coefficients.

2) to propose the main elements of the methodology for building a production function, using quality criteria in practice.

3 Results and Discussion

3.1 The mathematical tools of the methodology for refining the production function using an expanded set of coefficients

In the paper [6] we propose a method for constructing a function Y with variable elasticity coefficients in the form:

$$Y(L,K,A,\alpha,\beta) = A \cdot L^{f(L,K,\varepsilon)} \cdot K^{g(L,K,\beta)}, \qquad (4)$$

$$f(L,K,\alpha) = \sum_{i=0}^{M}\sum_{m=0}^{N} a_{im}\varphi_i(L)\varphi_m(K), \qquad (5)$$

$$f(L,K,\beta) = \sum_{i=0}^{M}\sum_{m=0}^{N} b_{im}\varphi_i(L)\varphi_m(K), \qquad (6)$$

where a_{im}, b_{im} – constant coefficients; $\varphi_i(L)$, $\varphi_m(K)$ – transcendental functions.

Ukraine is characterized by an unstable development of the economy. Output data for Ukrainian industry is given in Table 1. These data are generated by analogy in accordance with the data given in the papers [5, 6].

To data Table 1, we will apply the valuation technique and take into account the inflation index (Table 2).

Considering the relative index (Table 2), the obtained (calculated) refined data for the parameters *Y*, *L*, *K* and are shown in the Table 3.

Table 1 – Output (general) data on Ukrainian industry [16]

Year	Employed population *L* in industry, thousand people	Volume of sold industrial products (goods, services) *Y*, million UAH	Investments *K* in industry, million UAH
2010	3 462	1 043 111	55 384
2011	3 353	1 305 308	78 726
2012	3 237	1 367 926	91 598
2013	3 170	1 322 408	97 574
2014	2 898	1 428 839	86 242
2015	2 574	1 776 604	87 656
2016	2 495	2 158 030	117 754
2017	2 441	2 625 863	143 300

Table 2 – Inflation indicators in Ukraine [16]

Year	Inflation index, %	The value of the inflation index *Inf* relative to 2010 year
2010	109.1	1.000
2011	104.6	1.046
2012	99.8	1.044
2013	100.5	1.049
2014	124.9	1.310
2015	143.3	1.878
2016	112.4	2.111
2017	113.7	2.400

Table 3 – Data on Ukrainian industry considering the inflation index, million UAH

Year	Volume of sold industrial products (goods, services) *Y*	Investments *K*
2010	1 043 112	55 384
2011	1 248 000	75 263
2012	1 310 200	87 738
2013	1 260 600	93 016
2014	1 090 400	65 813
2015	946 000	46 683
2016	1 022 500	55 792
2017	1 094 100	59 708

For data Table 3 received a production function of a classical type in the form:

$$Y_0 = 0.298 L^{0.75} K^{0.25}. \tag{7}$$

For function (7) according to Table 3, square deviation is established $\sigma_0 = 0.108$.

Using the approach of constructing the function of Y with variable coefficients, similar to that in [6], Y_1 was given a more complex form

$$Y_1 = A_1 L^{\alpha_1+\alpha_2 L+\alpha_3 K} K^{\beta_1+\beta_2 L+\beta_3 K}, \tag{8}$$

for which the mean-square deviation $\sigma_1 = 0.093$, that is less comparing with σ_0 by 14 % ($\Delta\sigma/\sigma_i \sim 0.14$). Here A_1, α_1, α_2, α_3, β_1, β_2, β_3 – are constant coefficients for a given dataset.

To find the refined value σ_1, the classical econometric and mathematical method of exponential smoothing is used to clarify the errors of the results of econometric studies for the Ukrainian industry which do not exceed $\Delta_1 = 8$ %.

In the paper [6], the deviations of the σ_i, Δ_i for agricultural products in Ukraine do not exceed 37 % ($\Delta\sigma/\sigma_i \sim 0{,}37$).

The ratio (8) shows 7 coefficients A_1, α_1, α_2, α_3, β_1, β_2 and β_3, which can be considered conditionally constant for a given set of data, in particular for industry. If we choose data for a period of 7 years, then we will determine the coefficients of this type with a high accuracy that does not exceed the accuracy of the relevant statistics Δ_1. Relevant constraints will be derived from the principles of statistics and metrology for a particular category of research, in particular for the parameters *Y*, *L*, *K*, which characterize the Ukrainian industry.

Since the analysis of the effectiveness of using the production function with variable coefficients in the tasks of the study of manufacturing problems, there is a need in the first approximation to test the advanced method of constructing production functions [6].

We draw attention to a plurality of data in the Table 3. Data from Table 3 for Y_i (2010, 2014, 2016, 2017) are similar and their errors (deviations from the mean value) do not exceed $\Delta_2 = 3.7$ %, that is, significantly less error systems of the type Δ_1 ($\Delta_2 < \Delta_1$). In this case, the task of determining the coefficients A_1, α_1, α_2, α_3, β_1, β_2 and β_3 will be mathematically incorrect and as a result, as established on the basis of a computational experiment, these coefficients will be estimated with a large error of $\Delta_3 \sim 20$–35 %.

On the basis of the data analysis Table 3 observe the unstable development of Ukrainian industry. Therefore, there is no point in forecasting trends in the development of industry in Ukraine to apply the ratio (8). Here it is expedient to use the ratio of type (7) for certain small intervals of time, for example, for 2010–2012 and 2012–2015. For these small periods of time, it is advisable to estimate the rate of change in the coefficients type A, α, β, and information about them to use to predict trends in the volume of sales of industrial products (goods, services) Y.

3.2 Elements of the methodology of constructing a production function using quality criteria

Like in the works [17, 18] we use the product to evaluate the quality of products (industry) $k_P = \{k_1 \cdot k_2 \cdot k_3\}$, where k_1 – coefficient of commercial gain, k_2 – coefficient of product competitiveness level – [19], k_3 – coefficient of product reliability.

Similarly to [17, 18] and taking into account the information given in the Table 3 and [20–23], the multiplicative qualimetric quality criterion will be presented as:

$$Z_1 = \prod_{i=1}^{6} k_i \Rightarrow \max, \tag{9}$$

where k_4 – coefficient of the level of quality (reliability) of the parameters of the type of production function Y_i; k_5 – coefficient of quality (reliability) of type parameters L, α_1, α_2, α_3; k_6 – coefficient of quality (reliability) of type parameters K, β_1, β_2, β_3.

Let's mention the quality criterion of Z_2 in the additive form in the same way as in scientific work [17]:

$$Z_2 = \sum_{i=1}^{6} a_i k_i, \tag{10}$$

where a_j (j = 1, 2, …, 6) – weight coefficients.

In the first approximation we choose $a_j = 1/6$, a $k_j = 1/\Delta_i$. In the first approximation, as an example, let it be $k_1 = k_2 = k_3 = 1/\Delta_1 \approx 12.5$.

According to the Table 3, it is evaluated: $k_4 = 2.83$, $k_5 = 2.90$, and $k_6 = 5.13$.

As a result, $Z_1 = 214\,402$, $Z_2 = 17.11$. (11)

If the errors of the parameters corresponding to the methodology for assessing the quality criteria of the corresponding methodology can be reduced, then the integral parameters of type Z_1 and Z_2 will be increased.

4 Conclusions

According to the results of the research, a method for evaluating the parameters included in the classical Cobb-Douglas formula is developed. On the basis of the computational experiment it was established that if the values of the production function Y are close to the numerical values and the deviation between them does not exceed 3.7 %, then for approximation of Y in the industry for the period 2010–2017, it makes no sense to complicate its appearance. To predict Y_i values, we evaluate the parameters that are included in the classical Cobb-Douglas type formula. To improve the methodology for estimating the coefficients included in the Cobb-Douglas type formula, new variants of the multiplicative and additive quality criteria and for the Ukrainian industry are proposed, based on the analytical data for 2010–2017, the evaluation of the relevant criteria was carried out. The above example has an analytical orientation and illustrates the possibility of using a Cobb-Douglas formula for analyzing the coefficients of a given model with sufficient reliability. Research focused on controlling the development of industry in Ukraine by means of quality criteria.

References

1. Zahorodnii, A. H., & Vozniuk, H. L. (2005). *Financial and Economic Dictionary*. Lviv: Lvivska Politekhnika [in Ukrainian].
2. Shumska, S. S. (2007). Production Function in Economic Analysis: Theory and Practice of Use. *Ekonomika Prohnozuvannia*, Vol. 2, pp. 138–153 [in Ukrainian].
3. Heiets, V. M., & Ostashko, T.O. (2016). *Implementation of the Association Agreement between Ukraine and the EU: Economic Challenges and New Opportunities*. Kyiv, National Academy of Sciences of Ukraine [in Ukrainian].
4. Fandel, G. (1991). Limitational Production Functions. *Theory of Production and Cost*, pp. 111–146, doi: 10.1007/978-3-642-76812-5_4.
5. Cobb, C. W., & Douglas, P. H. (1928). A Theory of Production. *The American Economic Review*, Vol. 18, No. 1, pp. 139–165.
6. Lytvyn, O. M., & Artiukh, M. V. (2018). Testing the method of constructing production functions with variable coefficients (PFVCE). *Mathematical and computer modelling, Series: Technical Sciences*, Vol. 17, pp. 117–123 [in Ukrainian].
7. Lytvyn, O. M., & Artiukh, M. V. (2012). The Production Function with Variable Elasticity Coefficients, Based on the Experimental Data of Cobb-Douglas. *Bulletin of the National Technical University "KhPI", Series: Mathematical Modeling in Engineering and Technologies*, Vol. 27, pp. 124–129.
8. Hicks, J. R. (1937). Mr. Keynes and the "Classics"; A Suggested Interpretation. *Econometrica*, Vol. 5(2), pp. 147, doi: 10.2307/1907242.
9. Solow, R. M. (1956). A Contribution to the Theory of Economic Growth. *The Quarterly Journal of Economics*, Vol. 70(1), pp. 6, doi: 10.2307/1884513.
10. Harrod, R. F. (1939). An Essay in Dynamic Theory. *The Economic Journal*, Vol. 49(193), pp. 14, doi: 10.2307/2225181.
11. Oliner, S. D., & Sichel, D. E. (2000). The Resurgence of growth in the Late 1990s: Is Information technology the Story? *The Jornal of Economic Perspectives*, Vol. 14(4), pp. 3–22, doi: 10.1257/jep.14.4.3.
12. Skrynkovskyy, R. M. (2018). Diagnosing the Maturity Level of IT Processes at the Enterprise. *Business Inform*, Vol. 4(483), pp. 377–383.
13. Lukashin, Yu., & Rahlina, L. (2004). Production Functions in the Analysis of the World Economy. *Mirovaya Ekonomika i Mejdunarodnyie Otnosheniya*, Vol. 1, pp. 17–27 [in Russian].
14. Mankiw, N. G., Romer, D., & Weil, D. (1990). *A Contribution to the Empirics of Economic Growth*. Cambridge, NBER Working Papers Series, doi: 10.3386/w3541.
15. Hall, R., & Jones, C. (1999). *Why Do Some Countries Produce So Much More Output per Worker than Others?* Cambridge, NBER Working Papers Series, doi: 10.3386/w6564.
16. State Statistics Servise of Ukraine (2018). *Statistical Information*. Retrieved from: http://www.ukrstat.gov.ua.

17. Yuzevych, L., Skrynkovskyy, R., & Koman, B. (2017). Development of information support of quality management of underground pipelines. *EUREKA: Physics and Engineering*, Vol. 4, pp. 49–60, doi: 10.21303/2461-4262.2017.00392.
18. Panchenko, S., Lavrukhin, O., & Shapatina, O. (2017). Creating a qualimetric criterion for the generalized level of vehicle. *Eastern-European Journal of Enterprise Technologies*, Vol. 1(3 (85)), pp. 39–45, doi: 10.15587/1729-4061.2017.92203.
19. Skrynkovskyy, R. M. (2015). Diagnostics of the Enterprise Production Competitiveness. *The Problems of Economy*, Vol. 4, pp. 240–246 [in Ukrainian].
20. Amosha, O. I., Bulieiev, I. P., Zemliankin, A. I., et al. (2017). *Industry of Ukraine – 2016: The State and Prospects of Development*. National Academy of Sciences of Ukraine, Kyiv [in Ukrainian].
21. Parkhomenko, M. N. (2010). International Experience of Providing of Quality of Products. *Forum Prava*, Vol. 3, pp. 344–350 [in Ukrainian].
22. Pawlowski, G. (2017). Development of the system of management diagnostics of the enterprise: Doctoral dissertation. Retrieved from: http://irbis-nbuv.gov.ua/ASUA/1257760.
23. Yuzevych, V., Klyuvak, O., & Skrynkovskyy, R. (2016). Diagnostics of the system of interaction between the government and business in terms of public e-procurement. *Economic Annals-XXI*, Vol. 160(7–8), pp. 39–44, doi: 10.21003/ea.v160-08.

Аналіз методології побудови виробничої функції з використанням критеріїв якості

Скриньковський Р. М.[1], Юзевич В. М.[2], Катаєв А. В.[3], Павловські Г.[4], Процюк Т. Б.[5]

[1] Львівський університет бізнесу та права, вул. Кульпарківська, 99, м. Львів, 79021, Україна;
[2] Фізико-механічний інститут ім. Г. В. Карпенка НАН України, вул. Наукова, 5, м. Львів, 79060, Україна;
[3] Харківський торговельно-економічний інститут Київського національного торговельно-економічного університету, пров. Отакара Яроша, 8, м. Харків, 61045, Україна;
[4] Компанія “Zaklad Handlowo-Uslugowy BHP”, вул. Костшинська, 17, м. Гужиця, 69-113, Польща;
[5] Академія фінансового моніторингу, вул. Білоруська, 24, м. Київ, 04050, Україна

Анотація. У статті на прикладі України розроблено методику оцінювання параметрів класичної формули типу Кобба–Дугласа для прогнозування тенденцій розвитку промисловості держави. На основі обчислювального експерименту встановлено, що для значень виробничої функції Y, близьких за числовими значеннями і відхиленнями до 3,7 %, апроксимування Y у сфері промисловості для невеликих часових періодів є неможливим з огляду на ускладнення множини її параметрів та коефіцієнтів. Для прогнозування значень Y_i ($Y_i \in Y$) проведено оцінювання параметрів, що входять до класичної формули типу Кобба–Дугласа. Для удосконалення методики оцінювання коефіцієнтів, що входять до цієї формули, запропоновано нові варіанти мультиплікативного та адитивного критеріїв якості. Виходячи із аналітичних даних за 2010–2017 рр., проведено оцінювання відповідних критеріїв для промисловості України.

Ключові слова: виробнича функція, функція Кобба–Дугласа, критерії якості, промисловість, промислова продукція.

MANAGEMENT
OF MANUFACTURING SYSTEMS

MMS 2019 - 4th EAI International Conference on Management of Manufacturing Systems

EAI

Call for Papers

Indexing

Proceedings will be submitted for inclusion in leading indexing services: Ei Compendex, ISI Web of Science, Scopus, CrossRef, Google Scholar, DBLP, and more.

Publication

Springer Wireless Networks Journal (WINET) (IF 1.981)

EAI Endorsed Transactions on Industrial Networks and Intelligent Systems

Learn more

October 8–10, 2019 Krynica Zdroj, Poland http://manusystems.org

The conference aims at creating synergies of “practice and research” increasing the potential and commercial viability of research and development in the field of innovative technologies in ICT, Industry 4.0, logistics and traffic system.

Topics: Industry 4.0; Case Studies in Logistics; Case Studies with RFID Applications; Economic Impacts in Logistics; ICT Support for Industry 4.0; Industrial and Smart Logistics; Intelligent Manufacturing Systems and Applications; Enterprise Information Systems; Manufacturing Cell Concepts in Manufacturing Systems; RFID in Manufacturing, RFID Technologies in Material Handling System; Supply Chain Approaches, Tools and Methods for Management Systems; Workplaces, Modern trends in Manufacturing Management, Clusters in SME; Complexity of Supply Chain Management; Decision-making processes; Innovation and Knowledge Management; Lean Management and Manufacturing; Modelling and Simulation of Manufacturing Companies; New Trends in Entrepreneurship; New Trends in Crisis Management; Production Management Approaches; Process Management; Production Planning and Scheduling; Quality Control and Management TPM; Sequencing solutions for Lean Manufacturing; SMART Technologies; Transportations; Smart City, Information and Communication Networks and Innovative Services; Information and Communication Security/e-Forensics; Policy of Innovative Communication Services; Traffic Management and Intelligent Infrastructure (road, freight, public transport); Safe and Secure Intelligent Transport Systems; Traffic Modelling and Simulation; Sensors, Detectors, and Actuators; Research and Development of Information and Communication Assistive Technology.

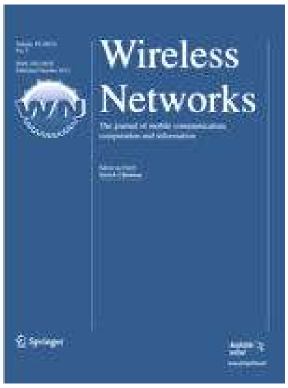

JOURNAL OF ENGINEERING SCIENCES
ЖУРНАЛ ІНЖЕНЕРНИХ НАУК
ЖУРНАЛ ИНЖЕНЕРНЫХ НАУК

Web site: http://jes.sumdu.edu.ua

DOI: 10.21272/jes.2019.6(1).c1 Volume 6, Issue 1 (2019)

UDC 621.74

Experiment of Polylactic Acid as a Material for Candle Molding on Origami-Shaped Crash Box Patterns

Kusyairi I.[1*], Himawan H. M.[1], Choiron M. A.[2], Irawan Y. S.[2]

[1] Politeknik Kota Malang, 3 Jalan Raya Tlogowaru, 65141 Malang, Indonesia;
[2] Universitas Brawijaya, Jalan Veteran, 65145 Malang, Indonesia

Article info:

Paper received:	October 15, 2018
The final version of the paper received:	December 3, 2018
Paper accepted online:	December 7, 2018

[*]Corresponding Author's Address:
kusyairi1408@gmail.com

Abstract. This paper study experiment by utilizing Polylactic Acid (PLA) which was printed with 3D Printing technology by taking the form of origami-shaped crash box pattern designed for MPV cars. The first step is to design crash box origami patterns with CAD software, and continue with the mold wax design. Then print the model in the Cura software. Then print the mold with approximately 56 hours 31 minutes and spend a 16.38 m long PLA filament weighing 128 g. Then pour wax, as for the wax used is carnauba wax with the temperature of pouring into the mold approximately 110 °C, let it chilled for 11 minutes then the mold is released from the wax. The final step is inspection. The result of this experiment is that the PLA-based mold is capable of printing the origami-shaped crash box pattern well, shown by clear printing of sharp indentations both inside and outside. Percentage of nonconformity with design area A of 0.52 %, area B of 0.43 %, area C of 0 %, area D of 10.8 %, area of E1–4 of 0 % and area E5 of 3.2 % are obtained. A comparison of the overall size of the design with the experiment was 0.29 mm. PLA tends to show consistency of experimental results. This is shown in the consistency of experimental results 1 to 3 in areas A, B, C and E. But there are inconsistencies in the experimental results in area D which represents the thickness dimension. This is influenced by changes in mold patterns which are affected by temperature pour wax into the mold and trigger the change of mold due to heat received continuously.

Keywords: carnauba wax, mold, PLA, sharp indentation, crash box pattern.

1 Introduction

Investment casting is a metal casting process with results having high precision. This method is used to produce several diverse and complex industrial components (Huang and Lin, 2015). This consists of several processes, namely: making wax patterns, coating ceramic porridge, and pouring (Liu et. at, 2015). In the process of making mold wax, in some industries using iron so that the resulting pattern can be precise. However, wax molds made of iron requires a high cost for some circles. The researchers conducted experiments to solve this issue, using silicone rubber-based wax molds (Kuo and Shi, 2012). The advantages of rubber-based silicon molds producing precised assembly and 2.19 % shrinkage dimensions. As it develops, the silicone rubber mold is given by the taguchi method, producing optimal temperature in the tax process is the injection temperature of 82 °C, injection time of 2 seconds, injection pressure of 0.06 MPa and mold temperature of 60 °C (Kuo and Tsai, 2015). Other study produced an optimal temperature of 5 °C mold temperature, 85 °C for wax temperature, at 5.05 MPa (Rahmati et. al., 2007). The research also developed for aluminum-filled of epoxy resin mold. The main benefits of this technique include low production costs, a simple manufacturing process, and a short time of total process (Kuo et. al., 2017). At present the three-dimensional (3D) printer moves are fast, not least in engineering. Some researchers conducted research using 3D printers combined with changing the material phase for making wax molds (Wang and Millogo, 2012).

In this paper, mold wax is made using 3D printing and filament made from Polylactic Acid (PLA) which includes aliphatic polyester biodegradable thermoplastic material. To test the ability to print complex and thin objects, a candle pattern in the form of a crash box origami pattern is used.

2 Research Methodology

2.1 CAD modelling

The pattern used in this paper is the origami-shaped crash box pattern (Ma and You, 2013) which has been modified to be applied to the MPV (Multi-Purpose Vehicle) Car which circulates in Indonesia (Kusyairi, 2017). This experiment prints half of the origami pattern crash box, as seen in Figure 1. The cross section is rectangular in shape and has a thickness of 3 mm in all parts. This will be a challenge when pouring wax into the mold, which has sharp angles and curves.

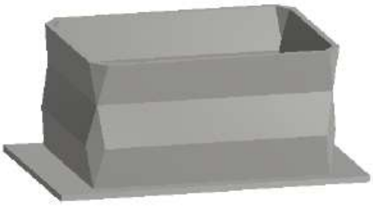

Figure 1 – Origami-shaped crash box pattern

The mold wax design in this paper is as shown in Figure 2. In Figure 2.a, it is divided into 2 parts, the inside and the outer parts of the mold. In the inner mold, the outline consists of two parts, but the actual part is the most complicated part, because in the 3D printing process it is divided into 5 parts. This is so that the mold is easily removed and does not have to damage the wax. The outer mold generally consists of 1 part, but in the 3D Printing process is divided into 2 parts, where between the inner and outer mold is connected to the nut so that there is no shift when pouring wax into the mold.

a b c

Figure 2. Origami-shaped crash box pattern mold:
a – inner part; b – outer part; c – mold hilistically

2.2 3D printing process

After designing the pattern of the object to be printed and the mold wax design, the next step is to print the mold with 3D Printing which is operated with cura software. The material used is PLA and its properties can be seen in Table 1. Setting the cura software by entering temperature data of 240 ^{o}C, diameter of 1.75 mm at a speed of 30 mm/s. The time required for the mold making process is 56 hours 31 minutes and consumes a 16.38 m PLA filament weighing 128 g. The results of the 3D Printing process can be seen in Figure 3, with a not-so-smooth surface.

Table 1 – Material properties of PLA (Farbman, McCoy, 2016)

Properties	Parameters
Melting Point	175 °C
Density	1.23–1.25 g/cm^3
Elongation at Break	3.8 %
Glass Transition	60–65 °C
Tensile Strength	57.8 MPa
Flexural Strength	55.3 MPa
Tensile Modulus	3.3 GPa
Flexural Modulus	2.3 GPa

Figure 3 – 3D Printing result

2.3 Wax pouring

In this experiment, carnauba wax material is used. This material was obtained from palm trees that grow in Brazil with the Latin name Copernicia pruniferacerifera. The content of these waxes are fatty esters (80–85 %), free alcohols (10–15 %), acids (3–6 %) and hydrocarbons (1–3 %) (Sandhu and Sharma, 2012). Carnauba wax is widely used in the investment casting process because it has high dimensional accuracy. The carnauba wax property material is shown in Table 2. After the mold has been printed, the next step is to coat the mold with a non-sticky liquid, which functions to make the wax easily separated from the mold. The next step is heating the wax to a temperature of 85–120 °C. After a while, the wax is poured into the mold and is chilled for 11 minutes. Next, separating the mold one by one from wax.

Table 2 – Material properties for a carnauba wax (Rani, 2013)

Density	Melting point	Flash Point	Volumetric shrinkage
970 kg/m^3	82–86 °C	300 °C	5.45

2.4 Inspection

After the wax has been printed 3 times, the next step is measuring the experimental results. The measured area is as shown in Figure 4. It consists of five areas to be measured, in area A represents the long dimension, area B represents the width dimension, area C represents the high dimension, area D represents the thick dimension, and area E represents the angular dimension. After the measurement process, the next step is to calculate the percentage dimension mismatch $PDD = (\Delta y/x)\cdot 100$ %, where x – design dimensions; Δy – the differences of design and result dimensions.

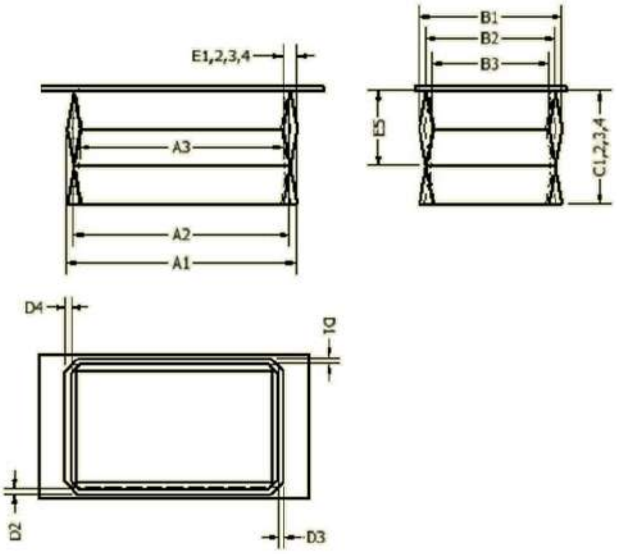

Figure 4 – Measurement area:
A1 – length of distance between the outer corner; A2 – length of distance between the middle angles; A3 – length of distance between inner angles; B1 – width The distance between the outer corner; B2 – width distance between the middle angles; B3 – width distance between inner angles; C1–4 – height of objects; D1–4 – thicknesses; E1–4 – angular width; E5 – high angle

3 Results

Experiment results can be seen in Figure 5. It looks like the pattern has been successfully printed; this is evidenced by the formation of wax in accordance with the design. The inside of the experiment results can follow the outer grooves so well that the inner sharp angles are able to form, this can be seen in Figure 5.a. On the outside, the shape matches the design and the curve of the angular pattern is able to form, this can be seen in Figure 5.b and 5.c. The roughness of the wax surface tends to follow from the surface structure of the mold. In this experiment, the molds made from PLA from the 3D process have a non-smooth surface. This affects the results of the smooth surface of the wax.

a b c

Figure 5 – Experimental results: top (a), front (b) and side (c) views

In Table 3, there is a comparison of the size and percentage of non-conformity with the experiment. In area A which represents the long dimension, the percentage of non-conformity with the design is 0.52 %, in area B is 0.43 %, in area C is 0%, in area D is 10.8 %, in the area of E1–4 – 0 % and in the E5 area the height of the angle is 3.2 %.

Data Table 3 shows that PLA can be used as a wax-making mold. This is evidenced by the comparison of the overall size of the design with the experiment of 0.29 mm, as shown in Figure 6. Mold wax made from PLA has an average difference with experiments in the length dimension 0.6 mm, width of 0.17 mm, height of 0.05 mm and thickness of 0.65 mm. This means that PLA can be used for parts that have a tolerance below 1 mm.

Table 3 Results of the size experiment and presentation of non-conformity design

Area	Design size	Test 1		Test 2		Test 3		Average size, mm	Average difference, mm	Average percentage, mm
		Size, mm	Percentage (%)	Size, mm	Percentage, %	Size, mm	Percentage, %			
A1	121.5	119.5	1.6	119.5	1.6	119.5	1.6	119.5	2.0	1.6
A2	114.5	112.7	1.6	112.7	1.6	112.7	1.6	112.7	1.8	1.6
A3	107.0	106.0	0.9	106.0	0.9	106.0	0.9	106.0	1.0	0.9
B1	75.5	75.0	0.7	75.0	0.7	75.0	0.7	75.0	0.5	0.7
B2	68.5	69.0	-0.7	69.0	0.7	69.0	-0.7	69.0	-0.5	-0.2
B3	61.4	62.0	1.0	62.0	1.0	62.0	1.0	62.0	-0.6	1.0
C1	60.0	60.0	0.0	60.0	0.0	60.0	0.0	60.0	0.0	0.0
C2	60.0	60.0	0.0	60.0	0.0	60.0	0.0	60.0	0.0	0.0
C3	60.0	60.0	0.0	60.0	0.0	60.0	0.0	60.0	0.0	0.0
C4	60.0	60.0	0.0	60.0	0.0	60.0	0.0	60.0	0.0	0.0
D1	3.0	3.0	0.0	3.0	0.0	3.0	0.0	3.0	0.0	0.0
D2	3.0	3.4	13.3	3.2	6.7	3.0	0.0	3.2	–0.2	6.7
D3	3.0	3.4	13.3	3.8	26.7	3.4	13.3	3.5	–0.5	17.8
D4	3.0	3.6	20.0	3.9	30.0	3.2	6.7	3.6	–0.6	18.9
E1	10.0	10.0	0.0	10.0	0.0	10.0	0.0	10.0	0.0	0.0
E2	10.0	10.0	0.0	10.0	0.0	10.0	0.0	10.0	0.0	0.0
E3	10.0	10.0	0.0	10.0	0.0	10.0	0.0	10.0	0.0	0.0
E4	10.0	10.0	0.0	10.0	0.0	10.0	0.0	10.0	0.0	0.0
E5	40.0	38.7	3.2	38.7	3.2	38.7	3.2	38.7	1.3	3.2

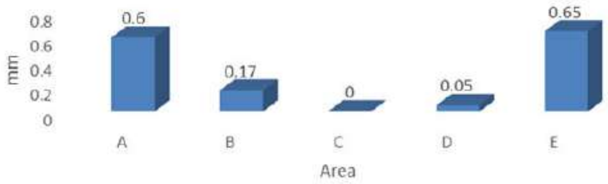

Figure 6 – Average difference between the design and experiments

Table 3 shows the consistency of experimental results 1 to 3. It can be seen that the results of the area A1 of the overall wax pattern consistently produce a measurement of 119.5 mm. Likewise for A2 and A3 areas produce consistent sizes. In area B, there is also a consistent measurement between the first experiment and the third. In area C, which represents a high dimension, it is consistent with all experimental results and also in accordance with the size of the design. PLA-based molds are also able to form angles consistently, this can be seen in the E1–4 areas which still show the same size in each experiment, and more than that the resulting dimensions are the same as the design size. This can be seen further in Figure 7, which shows the constitution of experimental results.

But this is different from area D which represents the thickness dimension; there are inconsistencies size of experimental result 1, 2 and 3. This is due to the PLA pattern that has shaped mold wax has changed. The first change occurs when the mold is finished with 3D Printing, the second change occurs when the mold is poured into wax which reaches a temperature of approximately 110 °C. This makes PLA experience a sideways change in shape, where the inner and outer molds are narrowed and widened. This can be seen when experiments 1, 2, and 3 results vary. Form changes can be reduced by enlarging the thick dimensions of the mold.

PLA is able to form a wax pattern that has the complexity of objects with the same results in each process, but this is only to produce in small quantities. If used continuously with quantity equated with molds made of metal, PLA-based mold will change shape and will produce products that are not precise anymore. Continuous heat when pouring wax into molds made from PLA will cause the mold to change shape continuously, this is what will cause inconsistency.

4 Conclusions

PLA-based molds are able to print origami pattern crash box well, this can be seen by the clear printing of sharp indentations both inside and outside. But the surface does not have a smooth surface, this is because following the results of the surface roughness of 3D Printing products. It is necessary to examine more effective ways to smooth the surface of the results of 3D Printing.

Percentage of nonconformity with design area A at 0.52 %, area B at 0.43 %, area C at 0 %, area D at 10.8 %, area E1–4 at 0 % and area E5 – at 3.2 %.

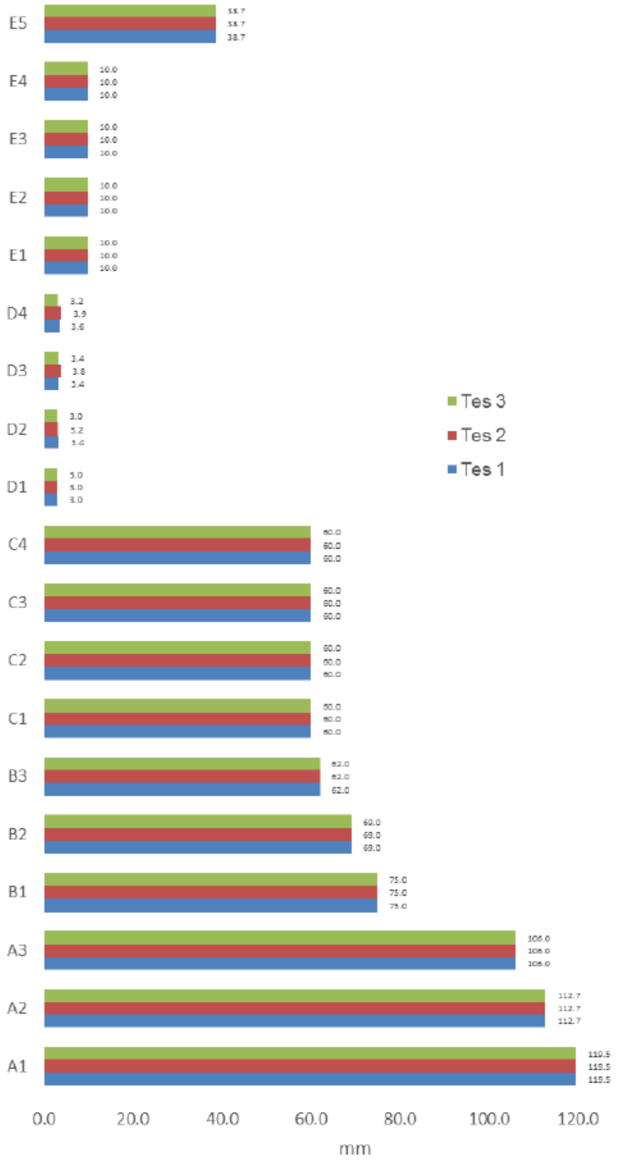

Figure 7 – Consistency of the experimental results

PLA can be used as a mold composition used for wax making. This is evidenced by the comparison of the overall size of the design with the experiment of 0.29 mm.

PLA tends to show consistency of experimental results. It is shown in areas A, B, C and E that there is consistency of experimental results 1 to 3, but in contrast to area D which represents the thickness dimension, there is an inconsistency in the experimental results. This is due to the pattern of PLA that has been shaped as mold wax has changed. The first change occurs when the mold is finished with 3D Printing, the second change occurs when the mold is poured into wax which reaches a temperature of approximately 110 °C. This makes PLA experience a sideways change in shape, where between the inside mold and the outer mold is narrowing and widening. This can be seen when experimentations 1, 2 and 3 result vary. Form changes can be reduced by enlarging the thick dimensions of the mold.

5 Acknowledgements

The researchers would like to express a deep gratitude to the Ministry of Research, Technology and Higher Education, the Directorate General of Strengthening Research and Development, and the Directorate of Research and Community Service that has financed the entire research, Announcement 0045/E3/LL/2018, January 16, 2018.

References

1. Farbman, D, & McCoy, C. (2016). Materials Testing of 3D Printed ABS and PLA Samples to Guide Mechanical Design. *ASME International Manufacturing Science and Engineering Conference*, Vol. 2, V002T01A015, doi: 10.1115/MSEC2016-8668.
2. Huang, P.-H., & Lin, C.-J. (2015). Computer-aided modeling and experimental verification of optimal gating system design for investment casting of precision rotor. *International Journal of Advanced Manufacturing Technology*, Vol. 79(5–8), pp. 997–1006, doi: 10.1007/s00170-015-6897-5.
3. Kuo, C.-C., Chen, W.-H., & Xu, W.-C. (2017). A cost-effective approach for rapid manufacturing wax injection molds with complex geometrical shapes of cooling channels. *International Journal of Advanced Manufacturing Technology*, Vol. 91(5–8), pp. 1689–1695, doi: 10.1007/s00170-016-9886-4.
4. Kuo, C.-C., & Shi, Z.-S. (2012). Fabrication of a high precision silicon rubber mold for replicating wax patterns of cylinder heads. *Indian Journal of Engineering and Materials Sciences*, Vol. 19, pp. 157–162.
5. Kuo, C.-C., & Tsai, R.-L. (2015). Fabrication and Application of Low-pressure Wax Injection Rapid Toolings. *Polymers and Polymer Composites*, Vol. 23(9), pp. 647–652.
6. Kusyairi, I. (2017). The Influence Of Origami And Rectangular Crash Box Variations On MPV Bumper With Offset Frontal Test Examination Toward Deformability. *Journal of Energy, Mechanical, Material and Manufacturing Engineering*, Vol 2, No. 2, pp. 1–8.
7. Liu, C., et al. (2015). Influence of complex structure on the shrinkage of part in investment casting process. *International Journal of Advanced Manufacturing Technology*, Vol. 77(5–8), pp. 1191–1203, doi: 10.1007/s00170-014-6523-y.
8. Ma, J., & You, Z. (2013). Energy Absorption of Thin-Walled Square Tubes With a Prefolded Origami Pattern – Part I: Geometry and Numerical Simulation. ASME Journal of Applied Mechacics, Vol. 81(1), art. no. 011003-011003-11, doi: 10.1115/1.4024405.
9. Rahmati, S., Akbari, J., & Barati, E. (2007). Dimensional accuracy analysis of wax patterns created by RTV silicone rubber molding using the Taguchi approach. *Rapid Prototyping Journal*, Vol. 13(2), pp. 115–122, doi: 10.1108/13552540710736803.
10. Rani, D. (2013). Recycling of Pattern Wax In The Investment Casting Process Using Microwave Dewaxing. *IOSR Journal of Engineering*, Vol. 3, pp. 5–10, doi: 10.9790/3021-03520510.
11. Sandhu, C. S., & Sharma, A. (2012). Investigation Of Optimize Wax Pattern In The Investment Casting By Using The Different Form Of Waxes. *IOSR Journal of Mechanical and Civil Engineering*, Vol. 3(4), pp. 1–6, doi: 10.9790/1684-0340106.
12. Wang, S., & Millogo, J. (2012). Rapid prototype mold for wax patterns with the help of phase change materials. *International Journal of Advanced Manufacturing Technology*, Vol. 62(1–4), pp. 35–41, doi: 10.1007/s00170-011-3784-6.

Дослідження полілактиду як матеріалу для свічкового лиття в руйнівних шаблонах у формі орігамі

Кусяірі І.[1], Хімаван Х. М.[1], Хоірон М. А.[2], Іраван Й. С.[2]

[1] Державний політехнічний інститут м. Маланґ , вул. Джалан Сукарно Хатта, 9, 65141, м. Маланґ, Індонезія;
[2] Університет Бравіджайа, вул. Джалана, 65145, м. Маланг, Індонезія

Анотація. Стаття присвячена експериментальним дослідженняи полілактиду, надрукованого за технологією тривимірного друку руйнівного шаблону формі орігамі, призначеного для автомобільної промисловості. Перший етап досліджень присвячений моделюванню шаблона з подальшим проектуванням форми для свічкового лиття із застосуванням відповідного програмного забезпечення. Другий етап стосується лиття приблизно 56 год. і 31 хв. з витратами волокон полілактиду довжиною 16,38 м вагою 128 г. Після виливання карнаубського воску з температурою розливання у прес-форми 110 °С, матеріал охолоджується впродовж 11 хв., після чого форма виділяється. На останньому кроці відбувається перевірка. У результаті експерименту встановлено, що форма з полілактиду здатна відбивати добре виражений рисунок руйнівного шаблону. Підтверджене чітке відбиття різких відступів як внутрішніх, так і зовнішніх. Відсоткова невідповідність форми у зоні А складає 0,52 %, В – 0.43 %, С – 0 %, D – 10.8 %, E1–4 – 0% і E5 – 3.2 %. Порівняльний аналіз підтвердив загальне відхилення форми від експериментальних даних 0,29 мм. Таким чином, продемонстрована послідовність експериментальних досліджень полілактиду в зонах А, В, С і Е. Проте є невідповідність експериментальних даних у зоні D, що відповідає за товщину, у результаті зміни форми шаблона під впливом температури розливання воску.

Ключові слова: карнаубський віск, форма, полілактид, різкий відступ, руйнівний шаблон.

JOURNAL OF ENGINEERING SCIENCES
ЖУРНАЛ ІНЖЕНЕРНИХ НАУК
ЖУРНАЛ ИНЖЕНЕРНЫХ НАУК

Web site: http://jes.sumdu.edu.ua

DOI: 10.21272/jes.2019.6(1).c2 Volume 6, Issue 1 (2019)

UDC 620.18

Influences of Aluminium / E-Glass Volume Fraction on Flexural and Impact Behaviour of GLARE Hybrid Composites

Santhosh M. S.*, Sasikumar R.

Selvam College of Technology, NH 7 Salem Road, Namakkal, 637003 Tamilnadu, India

Article info:
Paper received: October 23, 2018
The final version of the paper received: December 12, 2018
Paper accepted online: December 16, 2018

***Corresponding Author's Address:**
mozhuguan.santhosh@gmail.com

Abstract. Composites with different configuration of fiber (E-Glass) and metal (Aluminium) laminates were fabricated and tested for grasping optimum hybrid structure. GLARE (Glass laminate aluminium reinforced epoxy) is a unique composite recently being used by wide engineering domains like defense body and vehicle armors, aerospace, marine and structural applications. The GLARE hybrid composites are manufactured by adding very thin layer of aluminium sheets (surface treated) on the surface of unidirectional E-Glass fiber fabrics in presence of epoxy polymer. Firstly three hybrid GLARE laminates were fabricated with different volume fractions. Consequently, impact and flexural behaviors are measured by izod, charpy impact and flexural tests for all volume configurations. Impact resistance of such hybrid laminate is intensively great. The results depicts that the linear metal volume fraction (MVF) increment on fiber metal laminates greatly increases impact energy absorption capacity of composites and little difference in flexural modulus. Finally the fractured surfaces were analyzed by optical microscope.

Keywords: GLARE composite, impact energy, flexural test, epoxy polymer, aluminium sheet, E-Glass fiber.

1 Introduction

The authentic approach and supplementary evolution of GLARE / Fiber metal laminates (FML's) are commenced in 1980–90's to use in the high fatigue areas of civil modern aircrafts (Airbus A380 upper fuselage) and defense armors [1]. The exclusive nature of polymer composites such as low crack propagation rate and higher tolerance on damage pushes the researchers to utilize it among various engineering applications. PMC's are well known for its enhanced mechanical properties and tailorability [2]. Glass fibers are one of the emerging and versatile materials available in practically incalculable quantity and supply. Silica is a major chemical constituent of glass fiber. It exhibits appropriate property like transparency, electrical and chemical resistivity, inertness and stability [3–5]. Castrodeza [6] used compliance technique to calculate crack resistance of Bidirectional compact tension GLARE composite specimens and reported that elastic compliance technique provides highly accurate and predictable results on flexural and crack propagation behavior of the GLARE composites (Table 1).

In [8] Gopalakrishnan Ramya Devi fabricated fiber metal sandwich (Hand layup process) structure made up of aluminium sheet AA1050, woven E-Glass Fabric reinforced with epoxy polymer and analyzed various drilling parameters and reported that influence of stacking sequence on impact parameters of fiber metal configuration.

Santiago reported that higher volume fraction of metal layers results in good impact resistance [9]. Gonzalez studied tensile behavior of low ductile aluminium reinforced FML's and reported that an increase in the metal composition may results in higher strain to failure [10]. Aghamohammad et al., studied surface morphologies of various fractured fiber metal laminates by using profilometry, SEM and optical microscopy, they reported that FPL-Etching and anodizing treatments remarkably improves the flexural properties of FML's [11].

This proposed work focuses on fabrication of hybrid GLARE composites with different fiber metal laminate (FML) volume fraction; flexural and impact study of hybrid configurations under varying load conditions; fractured surface morphological analysis with different magnification ratios by using Olympus metallurgical microscope; identification of optimum hybrid structure for proposed applications.

2 Research Methodology

2.1 Material

The epoxy LY 556 polymer base matrix (density 0.9 g/cm^3, viscosity $1.25 \cdot 10^4$ cP) was used to fabricate hybrid laminates supplied by Covai Seenu and Company, Coimbatore, Tamilnadu-India. W152 LR hardener (density 1.2 g/cm^3, viscosity $1.30 \cdot 10^4$ cP) used as resin acceleration catalyst. The resin hardener mixed in the proportion of 65/35. AA 2024 (thickness per layer 0.1 mm) laminated E-Glass fiber with areal density of 200 g/m^2 supplied by Hindustan composite solutions, Mumbai-India, is utilized as reinforcement. Properties of reinforcements are shown in Table 1.

Table 1 – Properties of reinforcement, MPa

Parameter	Value
Maximum strength	35
Young modulus	$2.45 \cdot 10^5$
Fracture toughness	229
Yield Stress	365

2.2 Laminates preparation

The volume fraction of a resin-fiber mixture is calculated by the following relationship:

$$V_f = \frac{W_f / \rho_f}{\frac{W_m}{\rho_m} + \frac{W_{f1}}{\rho_{f1}} + \frac{W_{f2}}{\rho_{f2}}}, \quad (1)$$

where $W_{f1,2}$, W_m – weight of fibers 1, 2 and matrix; $\rho_{f1,2}$, ρ_m – density of fibers 1, 2 and matrix.

The reinforcement and matrix volume fraction of all the three hybrid laminates were depicted in Table 2.

Table 2 – FML volume fraction, %

Specimen	Reinforcement (Al + E-Glass)	Matrix (Epoxy)
GLARE 1	70	30
GLARE 2	65	35
GLARE 3	60	40

Similarly micro surface of the specimens before testing is exposed in Figure 1 a, b in the magnification ratio of 100 X and 200 X respectively.

In the proposed study GLARE hybrid composites with different volume fraction configurations were fabricated by Vacuum Assisted Resin Transfer Molding Process, which is well known for its quality of finishing and non-pores strong products. Three hybrid laminates (250×250 mm plate) as shown in Table 2 were fabricated and samples were prepared as per ASTM standard by water jet machining process. The surface and edge smoothened samples of Impact (izod and charpy) and Flexural tests are shown in Figure 1.

2.3 Characterization

The impact tests were carried out by the AIT-300N impact pendulum which has strike velocity of 5.6 m/sec, pendulum diameter 1600 mm, hammer weight 18.7 kg. ASTM D256 and ASTM D6110 standards were followed for izod and charpy tests respectively. The three point bending tests were done for specimens made as per ASTM 790 standard (80×13×3 mm) using Instron 4486 (short head speed 4 mm/min). The test results are reported for various hybrid GLARE laminates.

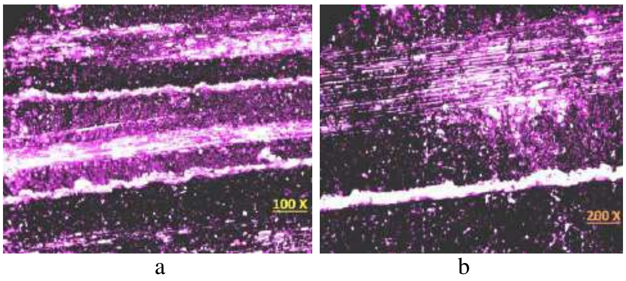

Figure 1 – Optical microscope images of specimens before test for the magnification ratio 100 X (a) and 200 X (b)

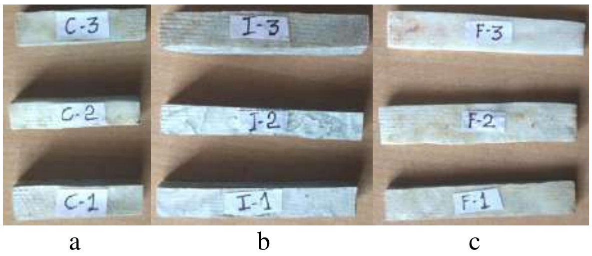

Figure 2 – Charpy (a), Izod (b) and flexural (c) impact test specimens

3 Results and Discussion

3.1 Impact tests

Charpy and izod impact test results of hybrid GLARE laminates were shown in Figure 3. The 70 % fiber metal laminate reinforced composites shows better impact resistance than other two composites.

Comparison of energy absorption rate of fiber metal laminates shows that the higher FML volume results in better energy absorption. The above results clearly depicts among 60, 65, and 70 % of fiber volume fractions 60 and 70 % FML shows good resistance against impact energy where as 35% epoxy matrix GLARE laminate has moderate impact resistance. Specimen 3 (70 % FML reinforced) absorbs 15 % higher impact load than other two configurations due to its great inter facial bonding between metal laminates and matrix. Results show that higher the volume fraction possesses better mechanical properties.

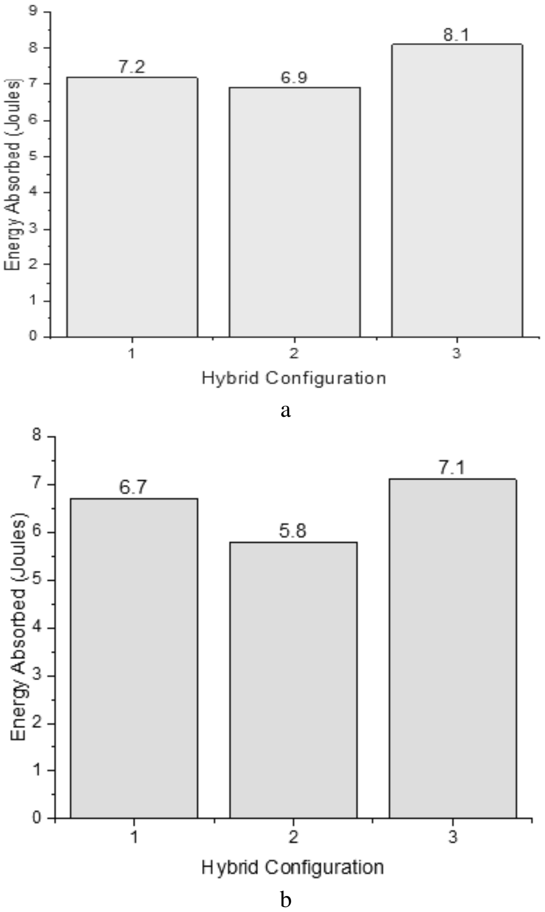

a

b

Figure 3 – Izod (a) and Charpy (b) impact test results

3.2 Flexural test

Figures 4 and 5 provides the stress-strain and force displacement relationship curves 60, 65, and 70 % of fiber metal reinforced laminates. Among these three hybrid laminates 65 % FML reinforced samples shows 20 % higher flexural modulus than other two configuration. It clearly indicates that moderate FML reinforcement improves the flexural property significantly.

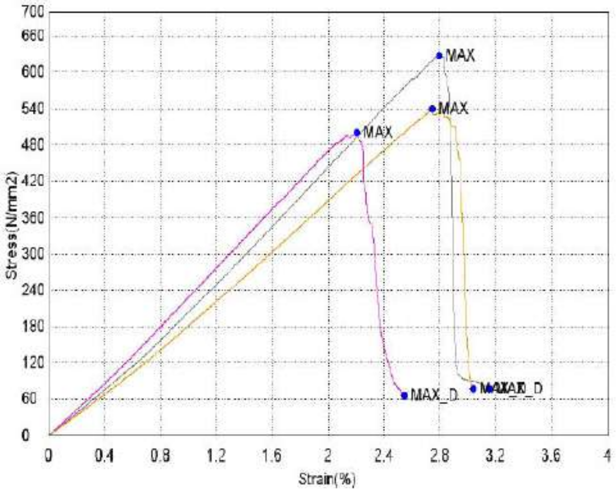

Figure 4 – Stress-strain curve

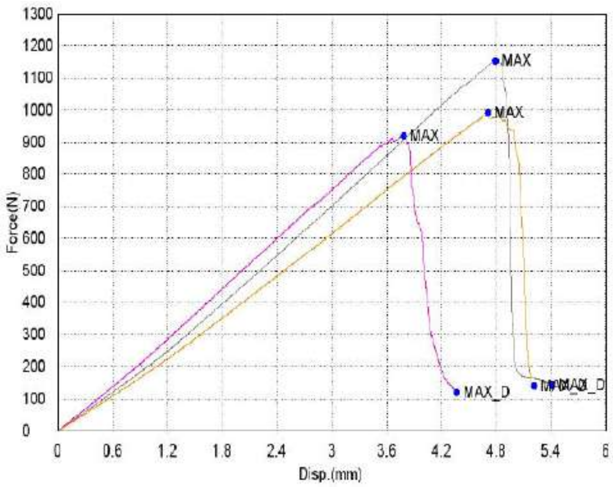

Figure 5 – Force-displacement curve

3.3 Optical microscope analysis

The characteristics of the flexural and impact tested composite surfaces of the proposed work are studied with optical microscope (Olympus Metallurgical Microscope). Cross sectional specimens of fractured surface were prepared for analysis. The observed microscope images containing matrix material, Aluminium and E-Glass laminates are shown in Figure 6.

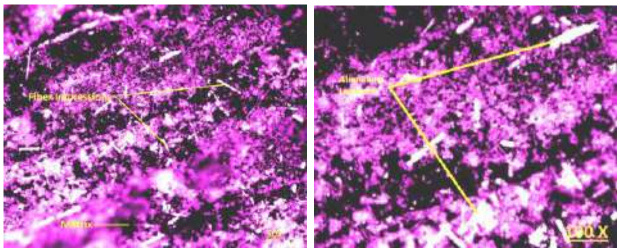

a

b

Figure 6 – Cross-sectional optical microscope images of fractured surface for matrix (a) and Aluminium / E-Glass laminates (b)

The results portrays that the deformation or breaking of fiber laminates are restricted by the aluminium reinforcement. Contemporaneously aluminium laminates shows uneven fracture. These phenomena spectacles the moderate weight percentage inclusion of FML considerably enhances the mechanical properties of GLARE.

4 Conclusions

Epoxy matrix aluminium laminated glass fiber reinforced (GLARE) composites fabricated by vacuum assisted resin transfer molding with different volume fractions and its impact, flexural behavior and fracture surface analysis were done. The test results shows that higher fiber metal laminate volume possesses excellent impact resisting property, dynamic mechanical property and very minor crack propagation, whereas moderate FML volume possess good flexural property than higher volume of

FML. Both the static and dynamic mechanical testing reveals that inclusion of metal layers into the fibers provides higher resistance to catastrophic failure. The proposed outcome of this research is suitable for high strength aerospace applications, armors of the defense industry and high impact ballistic profiles.

5 Acknowledgements

Authors appreciate the management of Selvam College of Technology for the deliberate support to carry out this research at Selvam Composite Material Research Laboratory (SCMRL), Namakkal, Tamilnadu, India.

References

1. Van, R., Sinke, J., de Vries, T., & van der Zwaag, S. (2004). Property optimization in fiber metal laminates. *Applied Composite Materials*, Vol. 11(2), pp. 63–76.
2. Wang, R. M., Zheng, S. R., & Zheng, Y. G. (2011). *Polymer Matrix Composites and Technology*. Elsevier.
3. Wallenberger, F. T., Watson, J. C., & Li, H. (2001) *Glass Fibers*. Materials Park, ASM International.
4. Vlot, A., Kroon, E., & Rocca, G. L. (1997). Impact response of fiber metal laminates. *Key Engineering Materials*, Vol. 141, pp. 235–276.
5. Cortes, P., & Cantwell, W. (2006). The fracture properties of a fiber-metal laminate based on magnesium alloy. *Composites: Part B*, Vol. 37, pp. 163–170.
6. Castrodeza, E., Soldan, L., & Bastian, F. (2006). Crack resistance curves of GLARE laminates by elastic compliance. *Congresso Brasileiro de Engenharia e Ciencia dos Materials*.
7. Karatas, M. A., & Gokkaya, H. (2018). A review on machinability of carbon fiber reinforced polymer (CFRP) and glass fiber reinforced polymer (GFRP) composite materials. *Defence Technology*, doi: 10.1016/j.dt.2018.02.001.
8. Devi, G. R., & Palanikumar, K. (2018). Analysis on drilling of woven glass fibre reinforced aluminium sandwich laminates. *Journal of Materials Research and Technology*, doi: 10.1016/j.jmrt.2018.06.021.
9. Santiago, R. C., Cantwell, W. J., Jones, N., & Alves, M. (2018). The modelling of impact loading on thermoplastic fibre-metal laminates. *Composite Structures*, Vol. 189, pp. 228–238.
10. Gonzalez-Canche, N. G., Flores-Johnson, & E. A., Carrillo, J. G. (2017). Mechanical characterization of fiber metal laminate based on aramid fiber reinforced polypropylene. *Composite Structures*, Vol. 172, pp. 259–266.
11. Aghamohammad, H., Abbandanak, N. H., Eslami-Farsani, R., & Siadati, S. M. H. (2018). Effects of various aluminum surface treatments on the basalt fiber metal laminates interlaminar adhesion. *International Journal of Adhesion and Adhesives*, doi: 10.1016/j.ijadhadh.2018.03.005.
12. Santhosh, M. S., Sasikumar, R., Natrayan, L., Kumar, M. S., Elango, V., & Vanmathi, M. (2018). Investigation of mechanical and electrical properties of Kevlar / E-glass and Basalt / E-glass reinforced hybrid composites. *International Journal of Mechanical and Production Engineering Research and Development*, Vol. 8(3), pp. 591–598.
13. Hassan, M. K., Abdellah, M. Y., Azabi, S. K., &Marzouk, W. W. (2015). Fracture Toughness of a Novel GLARE Composite Material. *International Journal of Engineering and Technology*, Vol. 15(6), pp. 36–41.
14. Golshahr, A., Natarajan, E., Santhosh, M. S., Sasikumar, R., Ramesh, S., &Durairaj, R. (2018). Multiwall Carbon Nanotube Reinforced Silicone for Aerospace Applications. *International Journal of Mechanical and Production Engineering Research and Development*, Vol. 8(4), pp. 743–752.
15. Crupi, V., Kara, E., Epasto, G., Guglielmino, E., & Aykul, H. (2014). Prediction model for the impact response of glass fiber reinforced aluminium foam sandwiches. *International Journal of Impact Engineering*, doi: 10.1016/j.ijimpeng.2014.11.012.
16. Kumar, S., Shivashankar, G. S., Dhotey, K., & Singh, J. (2017). Experimental study wear rate of glass fiber reinforced epoxy polymer composites filled with aluminium powder. *Materials Today*, Vol. 4, pp. 10764–10768.
17. Mariam, M., Afendi, M., Majid, M. S. A., Ridzuan, M. J. M., & Gibson, A. G. (2017). Tensile and fatigue properties of single lap joints of aluminium alloy/glass fiber reinforced composites fabricated with different joining methods. *Composite Structures*, doi: 10.1016/j.compstruct.2018.06.003.
18. Sarkar, P., Modak, N., & Sahoo, P. (2018). Mechanical and Tribological Characteristics of Aluminium Powder filled Glass Epoxy Composites. *Materials Today*, Vol. 5, pp. 5496–5505.
19. Trzepiecinski, T., Kubit, A., et al. (2018). Strength properties of aluminium/glass-fiber reinforced laminate with additional epoxy adhesive film interlayer. *International Journal of Adhesion and Adhesives*, doi: 10.1016/j.ijadhadh.2018.05.016.
20. Rajkumar, G. R., Krishna, M., et al. (2014). Investigation of tensile and bending behaviour of aluminium based hybrid fiber metal laminates. *Proceedia Material Science*, Vol. 5, pp. 60–68.

Вплив об’ємної концентрації алюмосилікатних фолокон на гнучкість гібридних алюмополімерних композитів

Сантош М. С., Сашікумар Р.

Технологічний коледж Сільвам, 7 Салем шлях, 637003, Намакхал, м. Тамілнаду, Індія

Анотація. Композити з різною структурою алюмосилікатних волокон були виготовлені і випробувані для отримання оптимальної гібридної структури. Алюмополімерний композит є унікальним матеріалом, який останнім часом має широку сферу використання в інженерії, оборонному комплексі, транспортних засобах, аерокосмічній і морській галузях. Гібридні композити GLARE виробляються із додаванням надтонкого поверхнево обробленого шару алюмінію на поверхні однонаправлених тканин E-Glass із включеннями епоксидного полімеру. Спочатку було виготовлено декілька матеріалів GLARE з різним фракційним складом. У результаті досліджувалась поведінка матеріалу при згинанні для виявлення усіх параметрів гнучкості. Виявлено надвеликий коефіцієнт ударного опору такого гібридного матеріалу. Результати показали, що збільшення концентрації металу значно збільшує здатність поглинання енергії на композит, а також підтвердили незначну зміну модуля пружності першого роду. Наостанок, зруйновані поверхні були досліджені із застосуванням оптичного мікроскопу.

Ключові слова: алюмополімерний композит, енергія впливу, тест на гнучкість, епоксидний полімер, алюмінієвий лист, алюмосилікатне волокно.

JOURNAL OF ENGINEERING SCIENCES
ЖУРНАЛ ІНЖЕНЕРНИХ НАУК
ЖУРНАЛ ИНЖЕНЕРНЫХ НАУК
Web site: http://jes.sumdu.edu.ua
DOI: 10.21272/jes.2019.6(1).c3 Volume 6, Issue 1 (2019)

UDC 620.178:621.793

Increased Wear Coatings due Intrastructural Self-Correction

Babak V. P., Bilchuk Ye. Yu.*, Shchepetov V. V.

Institute of Engineering Thermophysics of National Academy of Sciences of Ukraine,
2a Zhelyabova St., 03057 Kyiv, Ukraine

Article info:
Paper received: August 29, 2018
The final version of the paper received: December 13, 2018
Paper accepted online: December 17, 2018

***Corresponding Author's Address:**
admin@ittf.kiev.ua

Abstract. A mechanism for blocking and subsequent annihilation of endogenous microcracks due to their intrastructural self-correction has been proposed. It has been established that during tribomechanical processes of friction interaction under conditions of additive influence of temperature fluctuations and specific loads in the contact zone, all possible factors take place simultaneously, from the point of view of physicochemical anomalous transformations in the solid phase, as a result of which thermal destruction of carbides and the formation of structurally free α-graphite. The test results prove that the anti-friction surface layer, which contains graphite, is formed in the run-in regime. The composition and the equilibrium roughness of the surface layer are reproduced and maintained throughout the normal range of wear, and also form an integral system of dynamically stable wear-resistant structures.

Keywords: detonation spraying, wear resistance, surface layer, structural adaptability, doping.

1 Introduction

Among the technological problems that are associated with the surface strength of metallic materials under friction, damageability, as opposed to the regeneration process, is of particular importance. There are many types of damage, and the results are often the idem. The process can be represented as the result of nucleation and subsequent growth of cracks, the onset of which is preceded by plastic deformation. The study of the processes of nucleation and development of destruction, as well as the inhibition and regeneration of cracks in materials, is an actual task.

Papers [1, 2] present the results of studying the laws of the effect of all-round pressure and temperature on the kinetics of the process of healing the pores and cracks of grain boundaries in polycrystalline materials. In [3, 4], data on the transformation of defects such as flat microcracks in the material of parts under the influence of a high-energy pulsed electromagnetic field were obtained. The processes that occur in the material during the processing of metal samples with short pulses of high-density electric current are also researched. In [5, 6], the results of processing a pulsed magnetic field of samples with a crack on their resistance to fracture are presented. It is noted that the action of a pulsed magnetic field causes stress relaxation due to plastic flow at the crack tip. Note that the tip of the crack is often blunted. In [7, 8], studies of the structure and properties of metals, the deformation of which occurs at high constantly operating hydrostatic pressures, are analyzed. In this case, as established, the greater the compressive stresses, the more plastic deformation the material can undergo without destruction.

Describing the overall state of research, both in our country and in the world, it can be noted that the existing technologies are ineffective, their implementation presents certain difficulties in operating conditions, especially in non-stationary conditions, and does not have a simple and reliable solution for real production.

In the surface layers, under friction loading, microcracks and pores are formed, the kinetic development of which determines the durability resource of moving couple. However, in turn, the creation of conditions for their inhibition and regeneration may be one of the promising ways to improve the wear resistance and durability of parts.

The aim of the work is to study ways to improve wear resistance due to intrastructural self-correction of endogenous microcracks with carbon nanotubes.

2 Research Methodology

Detonation spraying of nanoscale composite coatings was formed with Nb-V-Si nanopowders [9]. Nanopowders were obtained by the method of mechanochemical synthesis with the subsequent addition, according to the developed technology, of carbon frame structures in the form of nanotubes. The maximum length of the nanotubes was about a hundred micrometers. The deformation energy of nanotubes is inversely proportional to the square of the radius; therefore, nanotubes with a diameter of tens of micrometers were used.

The wear resistance of the researched coatings was evaluated by the friction of model samples according to the end contact scheme with a distributed load and in the absence of lubricant. The tests were carried out in continuous slide mode with a load of 10.0 MPa. The thickness of the coatings after final processing was 0.20–0.30 mm with roughness Ra = 0.63–0.32. At the same time, coatings of the same composition, but not containing carbon nanotubes, as well as the traditionally used coatings of tungsten-containing powders of the type VC15 and doped on the basis of nickel, were tested using the same method.

A metallographic research of samples of coatings was done taking into account the specifics of the tasks being solved, by appropriate methods of complex physicochemical analysis.

3 Results

The main factors that determine the development of mechanochemical processes of friction and which determine the degree and gradients of elastoplastic deformation, temperature effects, structural phase transformations, and, ultimately, the main type of wear, are the speed of relative movement, load, temperature, environment. At the same time, there is a stable correlation of tribology parameters with plastic deformation processes [10].

The test results of the researched coatings (Fig. 1) by the dependences of the wear intensity on the sliding speed at a constant load of 10 MPa.

As can be seen, nanoscale coatings of the Nb-V-Si system with carbon framework structures (nanotubes) have the smallest breaking-in duration, wear rate and friction coefficient (Fig. 1, curves 1 and 1'). Moreover, it should be noted that changes in friction coefficients are consistent with the profile of the wear intensity curve, and its stability over time with a monotonous increase in the sliding speed indicates a high performance of the coating material, for which the main is mechanochemical wear.

The results of micro X-ray spectroscopic and X-ray phase physicochemical studies of nanoscale Nb-V-Si coatings with carbon nanotubes made it possible to classify them as a thin-differentiated phase mixture with an average grain size of 35-60 nm and an almost homogeneous distribution over the section.

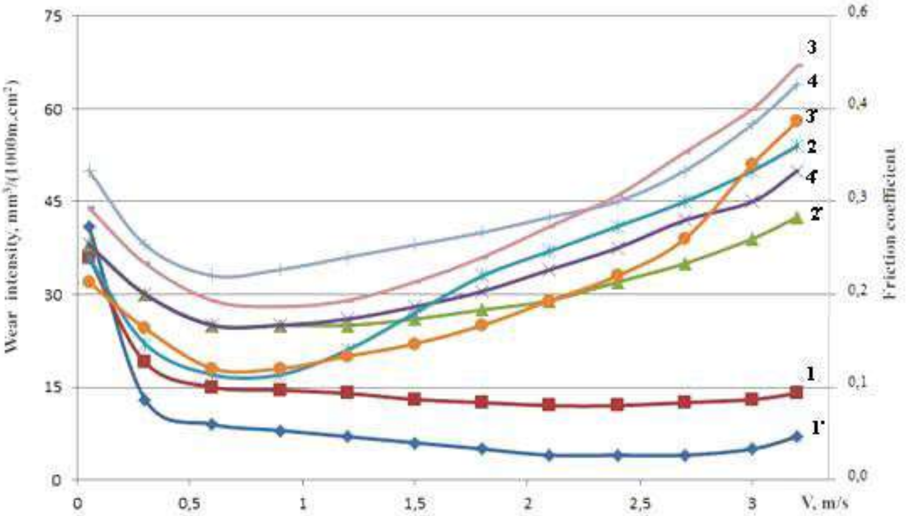

Figure 1 – The dependence of wear intensity (1–4) and friction coefficients (1'–4') on the sliding speed of coatings:
1, 1' – Nb-V-Si nanoscale system containing carbon nanotubes; 2, 2' – type VK15 (WC-Co);
3, 3' – nanoscale composition of Nb-V-Si; 4, 4'- based on nickel (Ni-Cr-Al-B)

However, fragments of imprints obtained in absorbed electrons and X-rays, which correspond to individual bunches with local heterogeneity, were also recorded. Their ultrafine structure differs from granular and is close to thin-lamellar formations. In our opinion, they are due both to nanoscale and to the fact that, during X-ray studies, the main contribution to the interference function is made by metal atoms, since the atomic scattering factor for them is much larger than for metalloids. In addition, their content is more.

To determine the properties of nanoscale composite coatings and their interaction under operating conditions, regularities of interaction of the components included in their composition were established.

It is established that a conglomerate of ultradispersed coating components are, first of all, chemical compounds and mechanical mixtures of different composition, size and shape.

The presence of the matrix phase in the form of solid solutions of Nb with V and Si, as well as ternary solid solutions with inclusions of chemical compounds of the VSi type has been established. It should be noted that the presence of V and Si contributes to an increase in the recrystallization temperature of Nb. Different sizes, but with the same distribution over the cross section, were determined, strengthening the phases of niobium and vanadium silicide's (Nb_5Si_3, $NbSi_2$, V_5Si_3, VSi_2, etc.) and niobium and vanadium intermetalic metal. The presence of niobium, vanadium, silicon carbides (NbC, VC, V_2C, SiC) and carbide compounds of the type $Me'_mMe''_mC$ (Si_2V_2C, Si_2Nb_2C) distributed throughout the coating volume was also established.

In thin-dispersed surface compositions, the main role of substructural components becomes. They have both an extraordinary chemical activity, which is due to a nanoscale level, and a significant ability to exchange energy and matter with the environment, and are in very non-equilibrium conditions. Therefore, the formation of surface structures can be considered as self-organization processes, as a result of which dynamically stable solid-phase wear-resistant structures are formed.

The principal feature of the introduction of carbon frame formations (nanotubes) into the composition of nanoscale coatings is due to the evolution of their carbon atoms under activation conditions. In the process of forming a homogeneous powder mixture under conditions of mechanochemical synthesis, the carbon atoms of the end layers of the nanotubes are activated and, as a result of selective thermal diffusion interaction, form stable chemical compounds. In addition, as a result of detonation gas spraying under conditions of structural thermal activation, carbon atoms initiate bonds with the metal atoms of the surface layer, providing the formation of secondary structures.

The process of structural activation is determined by the kinetics of nucleation and movement of the imperfections of the crystal structure in the deformation zone, which, in turn, is related to the energy state of the atoms, which depends on thermal activation due to their small size, activated carbon atoms, leaving the framework structure of nanotubes, easily diffuse and their cooperative clusters migrate to the places of formation of microcracks with excess surface energy. The atomic bonds formed due to the chemical and van der Waals attraction forces contribute to the creation of interatomic bonds and as a result of blocking the development of cracks and their subsequent annihilation. Thus, carbon nanotubes are actively involved in surface carbonization and providing the formation of an anti-friction film chemically bonded to the surface of the nanoscale layer. They are also a source of active carbon capable of long-term migration and chemical interaction during the healing of defects in the crystal structure. That is, to reduce their concentration, especially in the near-surface layers, where both dislocation clusters and microcracks are concentrated.

Figure 2a illustrates typical micrographs of friction surfaces. A micrograph of the working surface of the sample of the Nb-V-Si coating, which does not have carbon nanostructures and for which the development of the initial phase of irreversible processes of deformation and damage is typical.

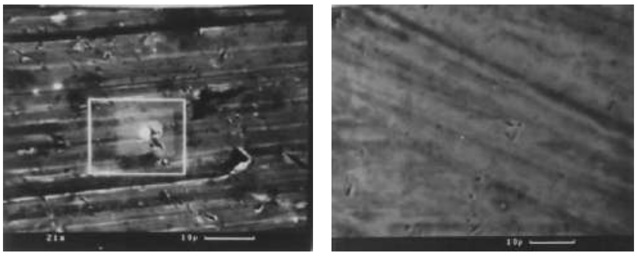

a b

Figure 2 – Friction surfaces:
a – coatings Nb-V-Si; b – Nb-V-Si coating with carbon nanotubes (2.7 m/s, 10.0 MPa)

The surface of the Nb-V-Si coating with carbon nanotubes (Figure 2b), there are no signs of macroscopic damage. The friction surface is covered with a continuous film of mostly dark color, has no defects, cracks, signs of chipping, which confirms its high plasticity and adhesive strength.

X-ray spectral microanalysis of the friction surface determined the presence of a film of α-graphite on the nanocoating with carbon nanotubes. This, according to the authors, is explained by the structural-energy factor. In more detail, the energy partially accumulated by the friction surface is concentrated, as is known, in the thinnest layer (about hundreds of nanometers) and its density in the element of the activated coating volume is close to the critical amount of energy that a material can absorb before destruction.

The high density of stored energy under the conditions of tribomechanical contact interaction processes, with the additive influence of temperature fluctuations and specific pressures, causes the simultaneous initiation of virtually all possible physicochemical anomalous transformations in the solid phase in the friction zone. Also, as a result of the thermal decomposition of carbides, structurally free α-graphite is released, on the basis of which an anti-friction surface film is formed.

4 Discussion

The test results show that a protective surface thin-film layer with graphite is formed already during the running-in process. The composition of the surface layer and the equilibrium roughness are reproduced throughout the entire range of normal operation and remain practically constant, which provides the stability of the indications of friction coefficients. At the same time, the metal atoms after the partial destruction of surface carbides form silicide and, for the most part, oxide phases. Oxide phases, as shown by submicrostructural studies, fill the surface microscopic microroughnesses, microcracks and are fixed in the micropins of the contacting surfaces. Their antiwear and antifriction effects, according to the authors, persist for a long time and correspond to the entire period of normal operation of the coupling surfaces and are not associated only with the running-in period.

Obtaining an energy level corresponding to a change in the specific work of destruction, as shown by calculations, from 10 kJ/mm^3 to 85 000 kJ/mm^3, causes the completion of the burn-in process and determines the parameters of friction. The friction parameters, in turn, are characterized by minimizing the wear rate, correlation with friction coefficients, stable roughness and the formation of optimal structures, as well as the properties of the surface layers that cause the flow of normal wear.

Figure 3 illustrates the friction surfaces of the coating with carbon nanotubes corresponding to the mechanochemical wear mode with the display of the kinetics of the local microcrack self-correction process.

Under the conditions of steady mechanochemical wear, using electron microscopic studies using the dark field method, it was possible to establish that the inner surface zone is a carbide-oxide conglomerate of nanoscale particles chemically bound to the base material. The outer surface object consists of a thin graphite layer with nanoscale inclusions that cannot be fully identified. However, in our opinion, they even in nanovolumes have a complex phase composition and consist of a mixture of Nb_2O_5 (NbO), V_2O_5, SiO_2.

In accordance with modern views, destruction is not an instantaneous act, but is a process that develops over time. From the standpoint of kinetics, the moment of formation of a crack of critical size, capable of spreading spontaneously without receiving external energy (according to the Griffith mechanism), is preceded by the gradual accumulation of foci of destruction in the form of endogenous microcracks.

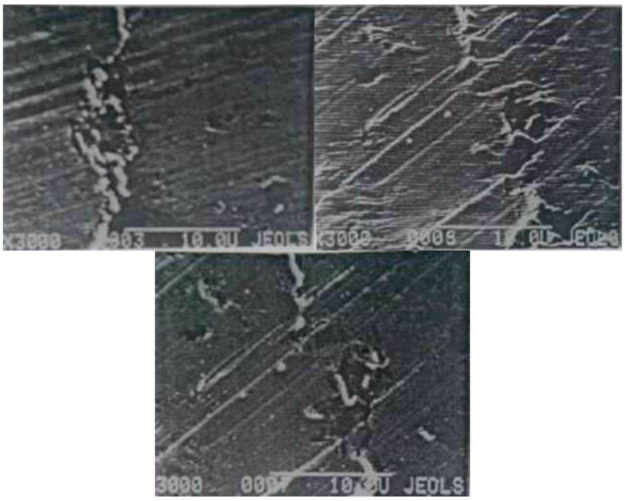

Figure 3 – Friction surfaces of Nb-V-Cu coating with carbon nanotubes, illustrating the kinetics of the process of self-correction of a transverse microcrack (2.5 m/s, 10.0 MPa)

The initiation of the phenomenon of intrastructural self-correction of endogenous microcracks in the near-surface layers of coatings is initiated, firstly, with activated carbon atoms, and secondly, with the self-consistency of two complementary processes. On the one hand, the working temperature reaches about 0.2–0.3 Tm, on the other hand, the action of compressive stress fields covering the volume of microcracks, at which both the diffusion mobility of carbon atoms and the tubular diffusion of vacancies along the cores of dislocations are activated.

Studies of the surface layers carried out by fine analysis methods revealed microcrack foci occurring under friction loading and found that their average sizes, which were identified, are from 0.8 to 2.0 μm at a concentration of about 10^{16}–10^{18} m^{-3} (in volume by two or three orders less). The thickness of the surface layer with a high concentration of microcracks correlates with the porosity of the coating material.

Thus, the use of carbon frame structures in the composition of nanoscale coatings is a promising direction of surface engineering, providing a significant increase in wear resistance and durability of products.

This publication continues the cycle of systematic research on the creation of promising nanomaterial's to reduce friction coefficients and increase the wear resistance of tribocontacts.

5 Conclusions

The validity of the used methodologies and algorithms for conducting experimental studies was defined to improve the wear resistance of detonation nanoscale composite coatings due to intrastructural self-correction of endogenous microcracks by carbon frame structures in the form of nanotubes.

It is noted that activated carbon atoms not only form surface carbides, but due to their size they easily diffuse and are able to migrate to the places of formation of microcracks, which have excess surface energy. Due to chemical and van der Waals attraction, these carbon atoms block the development of microcracks and their subsequent annihilation.

It has been established that a high density of energy stored in the surface layer under conditions of tribomechanical interaction, with the additive influence of thermodynamic factors and specific pressures, causes the appearance of almost all possible physicochemical anomalous transformations in the solid phase in the frictional contact zone. In this case, as a result of the thermal destruction of carbides, structurally free α-graphite is formed.

The obtained results illustrated that the antifriction surface thin-film layer containing graphite is formed during the running-in process, and its composition and equilibrium roughness is reproduced and maintained, forming an integral system of dynamically stable secondary structures. In the entire range of normal wear and tear, a distinctive feature of these secondary structures is that they represent an active environmental, in each microvolume of which energy is accumulated and released.

It has been established that for the formation of processes of intrastructural self-correction of endogenous microcracks in the near-surface layers, not only activated carbon atoms are needed, but also the influence of the operating temperature and the effect of compressive stress fields that cover the volume of microcracks.

The test results prove that partial healing of endogenous microcracks accumulating in the surface layers during friction due to their intrastructural self-correction using carbon frame structures in the form of nanotubes more than doubles the durability of coatings.

6 Acknowledgements

The authors thank the academician of NAS of Ukraine Yury F. Snezhkin and corresponding member of NAS of Ukraine Natalia M. Fialko for their support and participation in the discussion of this article.

References

1. Petrov, A. I., & Razuvaeva, M. V. (2005). Initial Stage of Void and Crack Healing in Polycrystalline Metals under Uniform Compression. *Physics of The Solid State*, Vol. 47(5), pp. 907–912, doi: 10.1134/1.1924854.
2. Dienwiebel, M., Verhoeven, G. S., Pradeep, N., Frenken, J. W. M., Heimberg, J. A., & Zandbergen, H. W. (2004). Superlubricity of graphite. *Physical Review Letters,* Vol. 92, pp. 448–451, doi: 10.1103/PhysRevLett.92.126101.
3. Kukudzhanov, K. V., & Levitin, A. L. (2015). About the treatment of high energy pulsed electromagnetic field on the microcracks in elastoplastic conductive material. *Problems of Strength and Plasticity*, No. 77, pp. 217–226.
4. Song, H., Wang, Z.-J., & Gao, T.-J. (2007). Effect of high density electropulsing treatment on formability of TC4 titanium alloy sheet. *Transactions of Nonferrous Metals Society of China*, No. 17, pp. 87–92, doi: 10.1016/S1003-6326(07)60053-3.
5. Stepanov, G. V., Kharchenko, V. V., Kotlyarenko, A. A., & Babutskii, A. I. (2013). Effect of Pulsed Magnetic Field Treatment on the Fracture Resistance of a Cracked Specimen. *Strength of Materials*, Vol. 45(2), pp. 154–162.
6. Gallo, F., Satapathy, S., & Ravi-Chandar, K. (2011). Melting and crack growth in electrical conductors subjected to short-duration current pulses. *International Journal of Fracture,* Vol. 167(2), pp. 183–193, doi: 10.1007/s10704-010-9543-0.
7. Kotrechko, S. A., & Meshkov, Yu. A. (2008). *Ultimate Strength. Crystals, Metals, Constructions: Monograph.* Naukova Dumka, Kyiv, Ukraine.
8. Shapoval, A. A., Mos'pan, D. V., & Dragbetskii, V. V. (2016). Production of periodic bars by vibrational drawing. *Steel in Translation*, Vol. 46(7), pp. 474–478, doi: 10.3103/S096709121607007X.
9. Babak, V. P., Shchepetov, V. V., Mirnenko, V. I., & Yakovleva, M. S. (2016). *High-temperature wear-resistant nanomaterial.* Patent, No. 11394, Ukraine, IPC (2006): B22F 7/00, C22C 27/02 (2006.01), C23C 4/126 (2016.01), C23C 4/067 (2016.01), Institute of Technical Thermophysics of the National Academy of Sciences of Ukraine, No. a201601802, stated in 25.02.2016, published in 27.03.2017, bulletin No. 6/2017.
10. Veprek, S., Veprek-Heijman, M. G. J., Karvankova, P., & Prochazka, J. (2005). Different approaches to super hard coatings and nanocomposites. *Thin Solid Films*, Vol. 476, pp. 1–29, doi: 10.1016/j.tsf.2004.10.053.

Підвищення зносостійкості покриттів за рахунок внутрішньоструктурного самокорегування

Бабак В. П., Більчук Є. Ю., Щепетов В. В.

Інститут технічної теплофізики НАН України, вул. Желябова, 2а, 03057, м. Київ, Україна

Анотація. Запропоновано механізм блокування та подальшої анігіляції ендогенних мікротріщин за рахунок їх внутрішньоструктурної самокорекції. Встановлено, що під час трибомеханічних процесів фрикційної взаємодії в умовах адитивного впливу температурних флуктуацій і питомих навантажень у контактній зоні відбувається одночасна дія всіх можливих впливів з точки зору фізико-хімічних аномальних перетворень у твердій фазі, результатом яких є термічний розклад карбідів і утворення структурно вільного α- графіту. Результати, отримані під час випробувань, дозволяють припустити, що антифрикційний поверхневий шар, що містить графіт, утворюється у режимі прироблення, а його склад, як і рівноважна шорсткість, відтворюються і підтримуються, утворюючи цілісну систему динамічно стійких зносостійких структур у всьому діапазоні нормального зношення.

Ключові слова: детонаційне напилення, зносостійкість, поверхневий шар, структурна пристосованість, легування.

JOURNAL OF ENGINEERING SCIENCES
ЖУРНАЛ ІНЖЕНЕРНИХ НАУК
ЖУРНАЛ ИНЖЕНЕРНЫХ НАУК
Web site: http://jes.sumdu.edu.ua
DOI: 10.21272/jes.2019.6(1).c4 Volume 6, Issue 1 (2019)

UDC 621.791.927.5

Study of a Welding Pool Harmonic Oscillations Influence on the Welded Metal Hardness and Weld Bead Width

Lebedev V. A., Solomiichuk T. G., Novykov S. V.*

E. O. Paton Electric Welding Institute of the National Academy of Sciences of Ukraine,
11 Kazymyra Malevycha St., 03150 Kyiv, Ukraine

Article info:
Paper received: December 20, 2018
The final version of the paper received: February 8, 2019
Paper accepted online: February 13, 2019

***Corresponding Author's Address:**
novykov76@ukr.net

Abstract. The comparison results of the hardness measuring of welded metal and the heat-affected zone of the eight welded beads from low-carbon steel obtained by surfacing CO_2/MAG with welding bath oscillation influence at values of amplitude equaled 0.5 mm (frequency values were 2.5, 3.0, 4.0, and 4.5 Hz) and 4.0 mm (frequency values were 3.7, 3.8, 3.9, and 4.0 Hz) are presented. A technological mode was the same for all specimens. The special influence of amplitude on the hardness value is noted. The structural metal components of the beads with a maximum hardness value are presented. An analytical calculation of the beads width depending on the value amplitude equaled 6 mm and oscillation frequency (values equal 2.5, 3.0, 4.0, and 4.5 Hz) of the weld pool is presented. A comparative analysis of the calculated and experimental values of the beads width is given. The influence of the oscillation frequency on the width value is noted.

Keywords: surfacing, oscillations, amplitude, frequency, acicular ferrite, hardness.

1 Introduction

One of the ways to increase the technological strength of welded structures is to control for the crystallization of the weld pool. A control tool is a welding torch or a melt of a weld pool on which a periodic influence in the form of vibrations or vibrations is superimposed. Crystallization of the weld pool metal in such conditions contributes to the formation of a fine-grained structure of the weld metal and directional crystal growth it is reasons to obtaining high mechanical properties [1–3].

The method of imposing oscillations (vibrations) can be mechanical, i. e. when the weld pool [1–6, 8–10] or the welding tool [2, 7] oscillates during the process of welding or surfacing; the use of modulated welding current (pulsed current) [11]; periodic influence of an external magnetic field [12], which in a certain way influences the melt of the weld pool, the welding arc [13] or the laser beam [14].

However, the simplest and cheapest way to control the structure of the crystallizing metal of the weld pool, which does not require expensive and complex equipment, is the mechanical method of superimposing external oscillations.

2 Literature Review

Nowadays, welding technologies with different types of mechanical periodic influences on the crystallization of a weld pool melt exist and have being investigated. So, the use of transverse mechanical vibrations of the weld pool makes it possible to increase the hardness of the weld metal by 2.5 % at a frequency of 60 Hz and by 7.3 % at a frequency of 376 Hz [4] on stainless steel specimens.

The apply of longitudinal oscillations of the weld pool with a frequency of 400 Hz and an amplitude of 40 µm provides the formation of a weld when welding medium-carbon steel with significantly improved mechanical properties: the yield strength is increased by 21 %, the ultimate tensile strength is 26 %, and breaking strength – by 39 % compared with specimens were obtained without the influence of oscillations [5].

In the case of multi-pass manual welding of plane stainless steel specimens, the use of vibrations at constant amplitude and frequency made it possible to obtain welds with a resistance to crack propagation greater by 25 % and tensile strength greater by 8.8 % compared to specimens welded without oscillation [6]. Combining the transverse oscillations of the welding torch and the pulsed mode of welding, it is possible to carry out multi-pass automatic welding without the use of a backing plate of the seam already at a frequency of 2.5 Hz. Herewith, the depth is higher than at a frequency of 5 Hz [7].

The apply of vibrations of the weld pool in welding of aluminum alloy AA7075 has significantly improved the resistance to hot cracking. So, with a frequency of 2050 Hz reported to the weld pool, it was possible to reduce the sensitivity to hot cracking to 20 %, while in the without of vibrations this value reached 82 %. However, the apply of vibrations frequency of the order of 100 Hz does not only not makes reduce the sensitivity of hot cracking, but increases it to 87 % [8].

The authors of work [9] executed welding of specimens from mild steel with a vibrator immersed in the weld pool and which transmitted vibrations from the ERM motor to the weld pool with a maximum frequency of 300 Hz and an amplitude of 0.5 mm. specimens welded at this frequency had an increased micro hardness due to the favorable orientation of the crystals and their refinement. At the same time, yield strength increased by 27 %, and ultimate tensile strength – by 23 % compared with samples welded without the influence of vibration.

A key feature of manual welding technology of the low carbon and stainless steels specimens with vibrations applying described in [10] is the use of vibrating engravers, where the welder’s hand with a welding torch is placed. The vibration frequency in the experiments was 600 Hz, 800 Hz, and 1 kHz, and the amplitudes were 0.235, 0.324, and 0.425 mm, respectively. It was noted that due to dendrites refinement, it was possible to maximally (at 1 kHz) increase the impact strength of welded specimens by 25 %.

From the above examples it follows that the use of periodic mechanical action during the welding process forms crystals during the period of crystallization by refinement and accelerates their growth, it most favorably takes influence the mechanical properties such as hardness, yield strength, impact strength and especially tensile strength (an increase of 39 % [5]) and sensitivity to hot cracking (decrease to 20 % [8]).

The aim of this work is to study the effluence of the amplitude - frequency characteristics of the weld pool low - frequency mechanical oscillations on the weld metal hardness and the weld beads width. A key feature of the research is the type of transverse oscillations. They are reciprocating motion along a circle arc, as shown in Figure 1. The deviation angle from the vertical position does not exceed 20°.

3 Research Methodology

3.1 Experiments

Experiments are semiautomatic CO_2\MAG surfacing. As electrode is a steel wire enveloped into the copper of type ER70S-6 (C: 0.06-0.15 %; Si: 0.80–1.15 %; Mn: 1.40–1.85 %; P: 0.025 %; S: 0.035 %) with a diameter of 1.2 mm is fed by a welding semiautomatic feed device (SFD) through the welding torch into arc burning zone.

The surfacing current is controlled by the electrode wire feed speed. The wire feed speed is carried out both smoothly and discreetly through the corresponding toggle switches on the control panel. The surfacing current value was determined by an ammeter located on the front of the power source. The power source is a rectifier for manual and automatic welding, providing a maximum current of up to 400 A.

A welding torch mechanical rectilinear motion is carried out through a movable frame with a smooth control tumbler of motion speed.

A specimen is fixed on a welding frame oscillating along a circle arc in the direction perpendicular to the surfacing direction. The welding frame oscillations are generated by a stepper motor. The amplitude and frequency of oscillations are set directly through the stepper motor control panel Figure 2. The maximum frequency at which the stepper motor is a stable mode work is 4.5 Hz. The amplitude of the surfacing bead stable formation is does not exceed 6–7 mm. The welding frame was set in oscillatory motion state after 5–7 seconds from the moment ignition of welding arc.

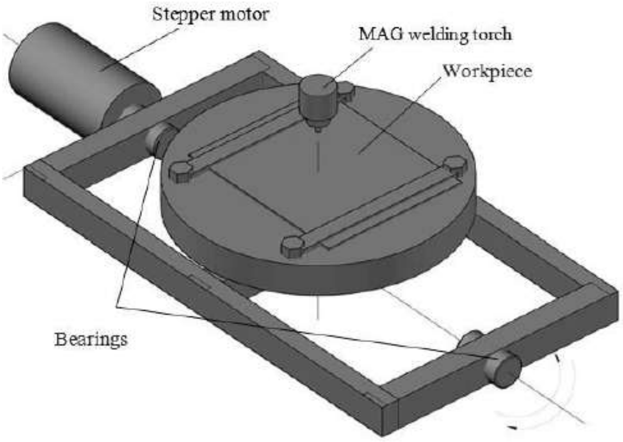

Figure 1 – The welding frame scheme of transverse vibrations of the weld pool

Figure 2 – The appearance of the control panel stepper motor

Nine plates with size 180×40 mm of low-carbon steel thickness 8 mm were used as specimens for surfacing. Before surfacing, each specimen was cleared of protective coating, rust and oils by means of mechanical grinding.

As gas used in the experiments was technical CO_2 – 99.5 %. Technological modes of surfacing were: $I = 215$ A, $U = 26$ V; $V = 36$ m/h; gas flow rate in a range of 9–12 l/min; amplitude-frequency responses of the welding frame oscillations are presented in Table 1.

Table 1 – The values of amplitude-frequency characteristics at which specimens were obtained

Specimen no.	Frequency, Hz	Amplitude, mm
1	Without oscillations	
2	2.5	0.5
3	3.0	
4	4.0	
5	4.5	
6	3.7	4.0
7	3.8	
8	3.9	
9	4.0	

3.2 Hardness measurement

For hardness measure all specimens were cut transversely and then all weld bead cross sections were polished to purity level of 14. Then there were etched about chemically in a 4 % alcoholic solution of nitric acid for 10 seconds.

The study of the welded metal structure and heat-affected zone (HAZ) metal structure, as well as photographing the structures obtained were carried out on a microscope "NEOPHOT-32" and using the "OLYMPUS" digital camera.

Vickers hardness at a load of 100 g (microhardness) was measured in the center of casted crystallites. The values of the welded beads hardness are presented in Table 2.

3.3 The calculation of welded bead width by the amplitude-frequency response

It is known, in surfacing it is necessary to achieve the minimum penetration depth of the base metal and to obtain a weld bead with a maximum width and minimum gain. However, to increase the width, it is necessary to increase the input of heat into the base metal, that also increases the depth of penetration [16, 17]. Using transverse oscillations, it is possible to reduce the penetration depth and significantly increase the weld bead width without arc current and voltage increase.

When surfacing a workpiece that performs harmonic oscillations by a given law, the width of the weld bead H is described by the equation of harmonic oscillator forced oscillations:

$$\frac{d^2x}{dt^2} + 2\gamma\frac{dx}{dt} + \omega_0^2 x = \frac{F_0}{m}\cos 2\pi\nu t, \tag{1}$$

Where x – current coordinate of the weld pool melt mass center, m; $2\gamma = \beta/(\rho_{p\text{м}} h^2)$ – coefficient of viscous friction; $\omega_0 = (g/l)^{1/2}$ – eigenfrequency of free oscillations of melt; β – viscosity coefficient of melt metal, Pa·s; m – mass of the welding frame on which the specimen is fixed, kg; h – distance from the melt mass center to the interfacial border, m; ρ_{ls} – density of liquid steel, g/cm^3; g – acceleration of gravity, m/s^2; l – distance from the axis of oscillation to the melt mass center, m; F_0 – driving force amplitude, N; ν – the external oscillation frequency that is given, Hz.

A solution of equation (1) will have the form [18]:

$$x(t) = \frac{F_0}{m\sqrt{\left(\omega_0^2 - \nu^2\right)^2 + 4\gamma^2\nu^2}}\cos(2\pi\nu t + \theta), \tag{2}$$

where $\theta = arctg[2\gamma\nu/(\omega_0^2 - \nu^2)]$ – shear angle between driving force $F_0\cos\omega t$ and $x(t)$ coordinate. The driving force F_0 is related to the torque on the shaft of the stepping motor M_0, N·m by the expression: $F_0 = M_0/l$. The moment magnitude M_0 is determined by the oscillation amplitude and the welding frame mass of the frame with the workpiece fixed on it by the expression: $M_0 = Amg$, where A is oscillations amplitude.

The weld pool melt within of the heat saturation period t has the sphere shape of a volume V, one can approximately determine the distance from the melt mass center to the interfacial border h as the sphere radius:

$$h = \sqrt[3]{\frac{3V}{4\pi}} = \sqrt[3]{\frac{3m}{4\pi\rho_{ls}}}. \tag{3}$$

The metal mass of the weld pool m [kg] without taking into account the losses for spraying and evaporation taking into account (2), can be determined by the expression [19, 20]:

$$\begin{aligned} m &= \alpha_m I_a t + \rho_{ls}F_m L = \alpha_m I_a \frac{q}{2\pi\lambda(T_m - T_i)V_{sf}} + \frac{\rho_{ls}Lq}{eV_{sf}c\varphi T_m} = \\ &= \alpha_m I_a \frac{\eta I_a U_a}{2\pi\lambda(T_m - T_i)V_{sf}} + \frac{\rho_{ls}}{2}\frac{\eta^2 I_a{}^2 U_a{}^2}{\pi\lambda(T_m - T_i)V_{sf}ec\varphi T_m} = \\ &= \frac{\eta I_a{}^2 U_a}{2\pi\lambda(T_m - T_i)V_{sf}}\left(\alpha_m + \frac{\rho_{ls}\eta U_a}{ec\varphi T_m}\right), \end{aligned} \tag{4}$$

where $\alpha_m I_a t$ - the mass of weld pool metal because of the electrode melting. Where $\alpha_m = 15–25$ g/(A·h), when surfacing /welding in CO_2 – the melting coefficient; $\rho_{ls}F_m L$ – mass of weld pool metal because of the base metal melting; F_m – melting cross-sectional area of the base metal, m^3; L – weld pool length, m; $c\varphi$ – volumetric heat capacity, J/(m^3·K); $q = \eta I_a U_a$ – effective power of welding arc, W; η – efficiency of arc heating; I_a – arc current, A; U_a – arc voltage, V; λ – coefficient of thermal conductivity, W/(m·K); T_m – metal melting temperature, K; T_i – initial metal temperature, K; V_{sf} – surfacing speed, m/s.

4 Results

4.1 The influence of amplitude-frequency response on the value of hardness

As a result, the Vickers hardness values of welded beads are presented in Table 2.

The study of the welded metal beads microstructure of all nine specimens showed the classical orientation of the crystallites - the crystals grow perpendicular to the section plane of the metal bath and the base metal. Besides, in all specimens the crystallites become larger, as the distance from the fusion zone increases [15].

In all surfacing variants the structure is same approximately and consists of various modifications ferrite (polygonal, polyhedral, acicular) and perlite (Figure 3).

Polygonal ferrite is observed in the form thin lengthen extractions along of casted crystallites boundaries. Polyhedral ferrite is clusters in the equiaxial ferritic grains form. Acicular ferrite is observed in the bodies of casted crystallites in the form of basket weaving plates. Perlite is observed in the form of dispersed extractions along the ferritic grains boundaries.

Table 2 – The Vickers hardness values of welded beads

Specimen number	Vickers hardness, kgf/mm^2				
	elded metal	Large grain region	Small grain region	Partial melt region	Base metal
1	201–210	233–283	240–242	205–207	179–189
2	201–206	296–297	240–243	193–213	185–187
3	202–213	294–297	280–283	218–256	176–188
4	201–206	203–264	198–199	189–190	180–187
5	199–212	206–254	223–225	165–169	172–186
6	187–199	198–209	170–176	169–182	169–176
7	228–236	228	213	199–213	189–191
8	218–230	213–216	188–213	187–193	181–199
9	242–245	206–236	191–215	156–264	160–181

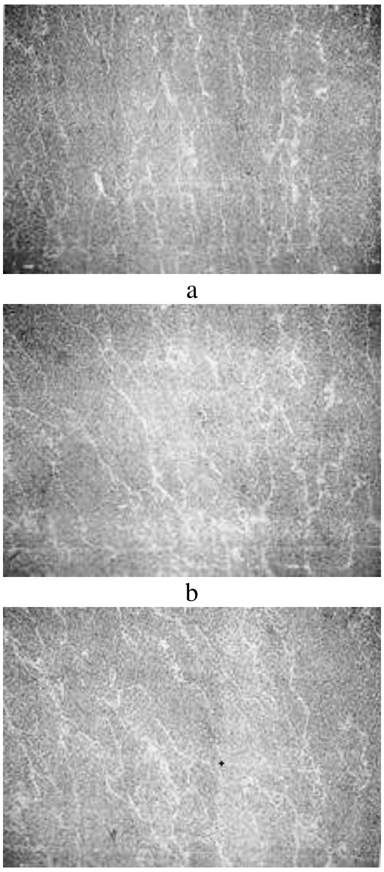

a

b

c

Figure 3 – Characteristic types of specimens microstructures ×200: a – cross section center of welded bead; b – fusion line; c – root part

According to the Table 2 data, specimens 9 has the maximum hardness value is caused by a rather large proportion of acicular ferrite in the crystallites structure compared to other specimens. The specimen 6 has the smallest hardness value of both the weld metal and HAZ, that is due to a significant proportion of polygonal ferrite, despite the content of acicular ferrite in the crystallite. The highest hardness HAZ value is in specimens 2 and 3 in areas of large grain, that is a consequence of the presence of a structure consisting from mixture of upper and lower bainite.

4.2 The influence of amplitude-frequency response on the value of width

For five different the oscillation frequency values v, the calculation was carried out with the technological mode parameters: $I_a = 100$ A; $U_a = 20$ V; $\eta = 0.8$; $V_{sf} = 0.003$ m/s; and with an amplitude of 6 mm, black steel thermophysical properties: $\alpha_m = 15–25$ g/(A·h); $\rho_{ls} = 7.02$ g/cm^3; $c\varphi = 4.8$ J/(cm^3·K); $T_m = 1\,810$ K (for Fe); $T_i = 293$ K; $\lambda \approx 50$ W/(m·K); $\beta = (5.0–8.5)\cdot 10^{-3}$ Pa·s; $l = 150$ mm.

For the welding frame and workpiece with total weight $m = 5$ kg that is experiencing oscillations with amplitude equals up to 6 mm, it is necessary to choose an engine with a torque will be not less $M_0 = 6\cdot 5\cdot 9.81 = 0.3$ (N·m).

Considering the friction in the bearings, the value $M_0 = 0.5$ N·m is assumed for calculation.

Also, five welded specimens were obtained at adjusted frequencies, amplitude and technological mode. The results of calculating the welded beads widths and their real width values are given in Table 3. The welded beads appearance is shown in Figure 4.

Table 3 – The calculated and measured width values of the weld beads

Specimen number	Frequency, Hz	Calculated weld bead width, mm	Measured weld bead width, mm
1	4.5	13.0	14
2	4.0	12.0	13
3	3.0	10.4	12
4	2.5	10.0	12
5	without oscillations	–	8

Figure 4 – Weld beads for the different frequencies: 1 – 4.5 Hz; 2 – 4.0 Hz; 3 – 3.0 Hz, and 4 – 2.5 Hz; 5 – without oscillations

5 Conclusions

These studies demonstrate a tendency to increase the weld bead metal hardness and HAZ with increasing frequency and especially the amplitude of external oscillations. Consequently, if at amplitude value of 0.5 mm and an oscillations frequency of 4.5 Hz, the hardness of a welded bead metal did not almost change in comparison with a welded bead metal of bead obtained without weld pool oscillations, then at an amplitude of 4 mm, the hardness increased 1.16 times. The reason for this effect is to increase the degree of fine-grained metal confirmed by the results of the work [3], obtained under conditions close to that experiments. In addition, this effect is due to a significant increase in the proportion of acicular ferrite in the weld bead metal compared to the amount of polyhedral and polygonal ferrite, which confirms the hypothesis outlined in the work [21] according to it by means of a weld pool mechanical oscillations can change not only the grain size, but also to form useful structural components of the welded metal without introducing additional alloying.

This analytical calculation allows us to estimate the weld bead width with an accuracy of 7–20 %. Moreover, the lower the frequency, the higher a magnitude of the error. This is probably due to a features of a welding arc burning, a degree of burning stability of which somewhat decreases at a lower frequency due to re-ignition after a short circuit. This feature requires further study and is not taken into account in this calculation. Also, these studies have shown that the frequency is not only a factor in controlling the metal microstructure of the weld bead, but also controlling its width, which is confirmed by the results of the work [22].

References

1. Kuo, C.-W., Yang, S.-M., Chen, J.-H., Lai, G.-H., Chen, Y.-C., Chang, Y.-T., & Wu, W. (2008). Preferred Orientation of Inconel 690 after Vibration Arc Oscillation Welding. *Materials Transactions*, Vol. 49(3), pp. 688–690, doi: 10.2320/matertrans.mep2007305.
2. Jose, M. J., Kumar, S. S., & Sharma, A. (2016). Vibration assisted welding processes and their influence on quality of welds. *Science and Technology of Welding & Joining*, Vol. 21(4), doi: 10.1179/1362171815y.0000000088.
3. Selvi, A. A. (2014). *Effect of linear direction oscillation on grain refinement*. Ohio State University.
4. Hsieh, C.-C., Wang, P.-S., Wang, J.-S., & Wu, W. (2014). Evolution of microstructure and residual stress under various vibration modes in 304 stainless steel welds. *The Scientific World Journal*, Vol. 2014, pp. 1–9, doi: 10.1155/2014/895790.
5. Tewari, S. P. (2009). Influence of Longitudinal Oscillation on Tensile Properties of Medium Carbon Steel Welds of Different Thickness. *Thammasat International Journal of Science and Technology*, Vol. 14(4), pp. 17–27.
6. Gill, J. S., Kalyan, R. T. (2018). Effect of Weld Pool Vibration on Fatigue Strength and Tensile Strength of Stainless Steel Butt Welded Joints by GTAW Process. *Proceedings of the World Congress on Engineering*, Vol. 2.
7. Yamane, S., Yoshida, T., Nakajima, T., Yamamoto, H., & Oshima, K. (2009). In process control of weld pool using weaving control in switch back welding. *Quarterly Journal of the Japan Welding Society*, Vol. 27(2), pp. 32s–36s, doi: 10.2207/qjjws.27.32s.
8. Balasubramanian, K. (2011). Studies on the effect of vibration on hot cracking and grain size in AA7075 aluminum alloy welding. *International Journal of Engineering Science and Technology*, Vol. 3(1), pp. 681–686.
9. Singh, P. K., Patel, D., & Prasad, S. B. (2016). Development of vibratory welding technique and tensile properties investigation of shielded metal arc welded joints. *Indian Journal of Science and Technology*, Vol. 9(35), pp. 1–6, doi: 10.17485/ijst/2016/v9i35/92846.
10. Kalpana, J., Srinivasa, R. P., & Govinda, R. P. (2016). Effect of frequency on impact strength of dissimilar weldments produced with vibration. *International Journal of Chemical Science*, Vol. 14(3), pp. 1797–1804, doi: 10.13140/RG.2.2.17394.91840.

11. Subravel, V., Padmanaban, G., & Balasubramanian, V. (2017). Optimizing the magnetic arc oscillation process parameters to attain maximum tensile strength using RSM. *Journal of Manufacturing Engineering*, Vol. 12(1), pp. 49–54.
12. Razmyshlyaev, A. D., Ahieieva, M. V., & Lavrova, E. V. (2018). TMF Influence on Weld Structure at the Welding of 12Cr18N9T. *Materials Science Forum*, Vol. 927, pp. 1–5, doi: 10.4028/www.scientific.net/msf.927.1.
13. Sundaresan, S., & Ram, G. D. J. (1999). Use of magnetic arc oscillation for grain refinement of gas tungsten arc welds in α-β titanium alloys. *Science and Technology of Welding and Joining*, Vol. 4(3), pp. 151–160, doi: 10.1179/136217199101537699.
14. Schmitt, F., Mehlmann, B., Gedicke, J., Olowinsky, A., Gillner, A., & Poprawe, R. (2010). Laser beam micro welding with high brilliant fiber lasers. *Journal of Laser Micro/Nanoengineering*, Vol. 5(3), pp. 197–203, doi: 10.2961/jlmn.2010.03.0003.
15. Rabin, V. F., & Denisenko, A.V. (1978). *Metal science of low- and medium-alloyed steels welding*. Naukova Dumka, Kyiv.
16. Mondal, A., Kumar Saha, M., Hazra, R., & Das, S. (2016). Influence of heat input on weld bead geometry using duplex stainless steel wire electrode on low alloy steel specimens. *Cogent Engineering*, Vol. 3(1), pp. 14, doi: 10.1080/23311916.2016.1143598.
17. Gautam, U., & Abbas, M. (2013). Analysis of weld bead geometry in saw and modeling using CCD. *International Journal of Mechanical Engineering and Robotics Research*, Vol. 2(3), pp. 168–181.
18. Trubetskov, D. I., & Rozhnev, A. G. (2001). *Linear oscillations and waves*. Fizmatlit, Moscow.
19. Volchenko, V. N., Yampolsky, V. M., Vinokurov, V. A., etc. (1988). *Theory of welding processes*. Vyschaya Schkola, Moscow.
20. Rykalin, N. N. (1951). *Calculations of thermal processes in welding*. Mashgiz, Moscow.
21. Lebedev, V. A., Yarovitsyn, O. V., & Novykov, S.V. (2016). Methods of acicular ferrite forming in the weld bead metal (Brief analysis). *Reporter of the Priazovskyi State Technical University. Section: Technical Sciences*, Vol. 32(1), pp. 113–117.
22. Xu, W., Lin, S., Yang, C., & Fan, C. (2015). Weld bead formation in oscillating arc narrow gap vertical-up GMAW process. *Transactions of the China Welding Institution*, Vol. 36(4), pp. 56–60.

Вивчення впливу гармонічних коливань зварювальної ванни на твердість зварювального металу і ширину зварного шва

Лебедєв В. А., Соломійчук Т. Г., Новиков С. В.

Інститут електрозварювання ім. Є. О. Патона НАН України, вул. К. Малевича, 11, 03150, м. Київ, Україна

Анотація. У роботі наведено результати порівняння твердості зварюваного металу і зони теплового впливу восьми зварних швів з низьковуглецевої сталі, отриманої наплавленням CO_2/MAG за впливу коливань на зварювальну ванну при значеннях амплітуд 0,5 мм (для частот 2,5, 3,0, 4,0 і 4,5 Гц) та 4.0 мм (для частот 3,7, 3,8, 3,9 і 4.0 Гц). При цьому технологічний режим був однаковим для всіх зразків. У результаті відзначено особливий вплив амплітуди на значення твердості. Також наведені структурні металеві компоненти швів з максимальним значенням твердості. Запропоновано методику аналітичного розрахунку ширини шва в залежності від амплітуди (дорівнює 6 мм) і частоти коливань (значення 2,5, 3,0, 4,0 і 4.5 Гц) зварювальної ванни. Наведено порівняльний аналіз розрахункових та експериментальних значень ширини шва. Відзначено вплив частоти коливань зварювальної ванни на ширину зварного шва.

Ключові слова: наплавлення, коливання, амплітуда, частота, голчастий ферит, твердість.

interpartner.odessa.ua

Grabchenko’s International Conference on Advanced Manufacturing Processes

(InterPartner-2019)

September 10-13, 2019 | Odessa, Ukraine

The primary goal of the conference is to promote research and developmental activities, to intensify scientific information interchange between researchers, developers, engineers, students, and practitioners working in and around the world. The conference is an ideal platform for people to share views and experiences in Engineering related areas.

Conference Proceedings will be submitted to the database SCOPUS and other indexing services. Paper submission is supported by EasyChair Conference Management System.

Conference Topics

- ✓ Manufacturing Engineering
- ✓ Mechanical Engineering
- ✓ Materials Science
- ✓ Quality Assurance

Important Dates:

June 15, 2019 - Paper submission
July 20, 2019 - Acceptance notification
August 1, 2019 - Camera-ready version
August 15, 2019 - Registration

InterPartner-2019 is under the patronage of
Prof. Anatolii Grabchenko,
Honorary Conference Chair

Organizers:

- Odessa National Polytechnic University
- National Technical University “Kharkiv Polytechnic Institute”
- Sumy State University
- Lviv Polytechnic National University
- Donbass State Engineering Academy
- V. Bakul Institute for Superhard Materials of the National Academy of Sciences of Ukraine

Contacts:
Prof. Volodymyr Tonkonogyi,
Conference Chair
E-mail: vmt47@ukr.net

JOURNAL OF ENGINEERING SCIENCES
ЖУРНАЛ ІНЖЕНЕРНИХ НАУК
ЖУРНАЛ ИНЖЕНЕРНЫХ НАУК
Web site: http://jes.sumdu.edu.ua
DOI: 10.21272/jes.2019.6(1).d1
Volume 6, Issue 1 (2019)

UDC 681.5

Improved Response Performance of Two-Phase Hybrid Stepping Motor Control Using PID Tuned Outer and Inner Loop Compensators

Onyeka E. B.[1*], Chidiebere M.[2], Nkiruka A. P.[2]

[1] Department of Electronic Engineering, University of Nigeria, Nsukka, Nigeria;
[2] Department of Electrical and Electronic Engineering, C. O. Ojukwu University, P.M.B.02 Uli, Nigeria

Article info:
Paper received: October 10, 2018
The final version of the paper received: December 8, 2018
Paper accepted online: December 11, 2018

[*]**Corresponding Author's Address:**
bonaventure.ekengwu@unn.edu.ng

Abstract. This paper has presented improved response performance of two-phase hybrid stepping motor control using proportional integral and derivative (PID) tuned outer and inner loop compensators. It is desired to improve the response performance tracking of a two-phase hybrid stepper motor to achieved overshoot less than 5 %, settling time less than 0.16 s, and rise time less then 0.02 with 2 % criterion. To achieve the objective of the study, a dynamic model of a two-phase hybrid stepper motor was obtained in the form of a transfer function. A robust PID tuning technique was adopted using the single input single output (SISO) Graphic User Interface (GUI) of the design task of the Control and Estimation Tool Manager (CETM) of MATLAB software in designing the compensators. A single compensator was designed and added to control loop of a two-phase hybrid stepping motor to improve the response performance. Simulation was performed in MATLAB and an overshoot of 8 % with the single loop compensator. However, the overshoot of the system requires further improvement. A new control loop was proposed using two-compensator loop structure. The outer loop and inner loop compensators were designed and added to the two-phase hybrid stepper motor control. Simulation was performed in MATLAB and the result obtained showed that with the two-compensator loop structure, the overshoot was greatly reduced to 2.6 % with rise time of 12 ms and settling time 11 ms. This indicates that the response tracking performance of the system has been improved by the combined outer and inner loop compensators.

Keywords: compensator, control loop, graphic user interface, proportional integral and derivative, PID tuning.

1 Introduction

Stepper motors are a kind of electromagnetic mechanical devices that can transform discrete electric impulses, typically of square wave pulses, into linear or angular displacement [1]. They are special type of synchronous motors designed to rotate through fixed angle called a step for each electrical pulse received from control unit [2]. They are usually employed in control and measurement applications because of the advantage of easy open loop control and no error accumulation which they offer [1, 3]. Stepping motors are perfect choice for applications with small power (less than 100 W) while maintaining fast and efficient positioning control such as in robotics, machine tools, servos, aerospace applications, printers, and scanners [1, 4].

There are various advantages offer by stepper motors such as small inertia, great output torque, and high frequency response [1]. These characteristics have made the use of stepping motors to be wide in the industry currently, especially in control applications and measurement [1, 5]. Apart from the benefits mentioned above, such advantages like compatibility with digital system and no feedback sensor requirement for position and speed sensing [2, 6] have made their use worthwhile in control systems engineering. However, some drawbacks of stepping motor are its relatively long settling time and overshoot for a given step response [1]. There are different types of stepping motors. One of them is the hybrid stepping motor.

A stepping motor that contains the permanent magnet rotor and many teeth both on the rotor and stator poles is called the hybrid stepping motor. Two- phase hybrid stepper motor is stepper motor that contains the permanent magnet rotor and many teeth both on the rotor and the stator poles [1]. These devices are most commonly employed in the industry as ensures that the power electronic circuits are relatively simple because of higher efficiencies over the variable reluctance permanent magnet stepping motors.

In this paper, the objective is to develop PID tuned two-compensator control loop structure that will improve the performance response of a two-phase hybrid stepper motor. The system is expected to meet the following performance criteria. Overshoot is less than 5 %, settling time – 0.16 s, and rise time – 0.02 with 2 % criterion.

2 Literature Review

Attiya et al [1] designed a fuzzy-proportional integral and derivative (PID) controller for variable speed control of two-phase stepping motor in robotic grinding. It aimed to improve the speed control performance of two-phase hybrid stepping motor. Six motor speed input conditions were considered for simulations. Simulations were conducted in MATLAB. Salis et al [12] studied learning position controls for hybrid step motors, from current fed to full order models. Experimental study of both adaptive and repetitive learning position control presented in literature for voltage-fed hybrid step motors was carried out. Liu and Li [13] designed a stepper motor position control system based on digital signal processor (DSP). An incremental PID control algorithm was designed. Experimental and simulation comparison of open-loop control and closed-loop with PID effect was conducted. With the PID closed-loop control, the results indicated that effective improvement of the precision and dynamic performance of the stepper motor can be realized. An emotional controller for position control of hybrid stepper motor derives called Brain Emotional Learning Based Intelligent Controller (BELBIC) was proposed by Khalilian et al [14]. It adopted direct torque control technique. Simulations were conducted to ascertain the effectiveness of the controller and the results obtained indicated fast response, no overshoot and zero steady-state error. A bang-bang control strategy was proposed in [9] for two-phase hybrid stepper motor. Current tracking was performed and the current was continuously maintained within sustained limit in phase and desired speed obtained. However, the control technique has fast switching limitation. Two-phase hybrid stepper motor control using Fuzzy-PID is presented by Zhang and Wang [6]. A comparison of the Fuzzy-PID with conventional PID indicated that the former yielded better performance than the later.

Impressively, stepper motors have multiple “toothed” electromagnets arranged around a central gear-shaped piece of iron [1]. Figures 1 and 2 show the general stepping motor main parts and a cross-section of two-phase hybrid motor.

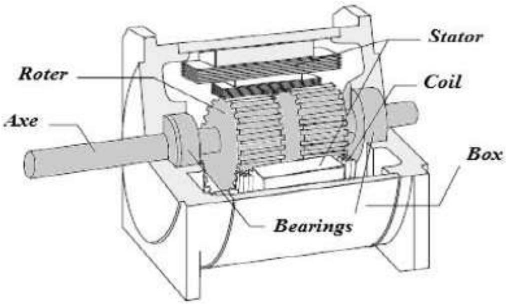

Figure 1 – General stepping motor with its main parts[1, 7]

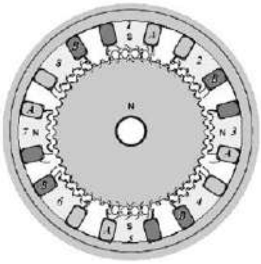

Figure 2 – Cross-section of two-phase hybrid stepping motor [1, 8]

3 Research Methodology

3.1 Mathematical modelling

3.1.1 General equations

Only A typical model of a two-phase hybrid stepping motor consists of the shaft mechanical dynamics together with the electrical dynamics of the stator coils [1, 9]. The electrical response is faster than the mechanical response [1, 9, 10] which makes it possible to consider the mathematical dynamics only [9].the model consists of electrical and mechanical equations [9]. The electrical dynamics are given by [9]:

$$\frac{dI_a}{dt} = \frac{1}{L}\left(V_a - RI_a + K_m \omega \sin N\theta\right); \tag{1}$$

$$\frac{dI_b}{dt} = \frac{1}{L}\left(V_b - RI_b + K_m \omega \cos N\theta\right). \tag{2}$$

Mechanical equations are [9]:

$$dI_a/dt = (K_m I_a \cos N\theta - K_m I_a \sin N\theta - \\ - B\omega - T_L - K_m \sin 4N\theta); \tag{3}$$

$$\frac{d\theta}{dt} = \omega \tag{4}$$

where I_a and I_b are the currents in phases A and B respectively, A; V_a and V_b are the voltages in phases A and B respectively, V; ω is the rotor speed, rad/s; θ is rotor position, rad; R is the resistance of the phase winding Ω; L is the self-inductance constant, H; B is the viscous friction constant (N·m·s/rad); J is the rotor inertia, kg·m^2; T_L is the load torque, N·m.

3.1.2 Transfer function model

Figure 3 shows the model of a two-phase hybrid stepping motor [1]. The open loop transfer function of *G*(*s*) of two-phase hybrid stepping motor is given by [1, 6, 11].

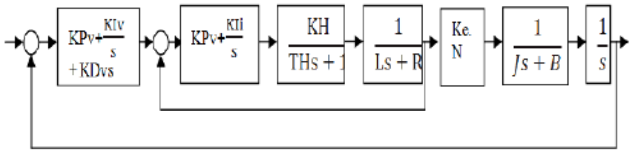

Figure 3 – Model of two-phase hybrid stepping motor [1]

The values of the parameters of selected stepping motor for MATLAB simulation are presented in Table 1.

Table 1 –Simulation parameters [8]

Parameter	Value	Unit
L	4.0	mH
R	1.2	Ω
J	260	$kg{\cdot}m^2$
B	0	N·m·s/rad
β	1	–
K_{Dv}	100	–
K_e	0.2	N·m/A
N	180	–
K_{iv}	0	–
K_H	15	–
K_{Ii}	500	–
K_{pi}	5	–
K_{pv}	500	–

The open-loop transfer function of two-phase hybrid stepping motor considered in this paper given by [6]:

$$G(s) = \frac{2700000(s+5)(s+100)}{s^4+19799s^3+650000s^2+7500s}. \tag{5}$$

3.1.3 State space model

The transfer function of a two-phase hybrid stepping motor presented in equation (5) is transformed into a state space model as follows:

$$\frac{Y(s)}{U(s)} = \frac{2.7\cdot 10^6(s+5)(s+100)}{s^4+19799s^3+6.5\cdot 10^5 s^2+7500s}; \tag{6}$$

$$\frac{X(s)}{U(s)}\cdot\frac{Y(s)}{X(s)} = \frac{2.7\cdot 10^6(s+5)(s+100)}{s^4+19799s^3+6.5\cdot 10^5 s^2+7500s}; \tag{7}$$

$$\frac{X(s)}{U(s)} = \frac{2.7\cdot 10^6}{s^4+19799s^3+6.5\cdot 10^5 s^2+7500s}; \tag{8}$$

$$X(s)\cdot[s^4+19799s^3+6.5\cdot 10^5 s^2+7500s] = 2.7\cdot 10^6 U(s). \tag{9}$$

Assuming zero initial conditions:

$$\begin{gathered} s^4X(s)+19799s^3X(s)+6.5\cdot 10^5 s^2X(s) \\ +7500sX(s) = 2.7\cdot 10^6 U(s). \end{gathered} \tag{10}$$

The expression in s-domain is converted into time domain as follows:

$$x = x_1; \tag{11}$$

$$\frac{dx_1}{dt} = x_2; \tag{12}$$

$$\frac{dx_2}{dt} = x_3; \tag{13}$$

$$\frac{dx_3}{dt} = x_4; \tag{14}$$

$$\dot{x}_4 = -7500x_2 - 6.5\cdot 1^5 x_3 - 19799x_4 + 2.7\cdot 10^6 u(t). \tag{15}$$

Transforming equations (11)–(15) into state space form gives:

$$\begin{bmatrix} \dot{x}_1 \\ \dot{x}_2 \\ \dot{x}_3 \\ \dot{x}_4 \end{bmatrix} = \begin{bmatrix} 0 & 1 & 0 & 0 \\ 0 & 0 & 1 & 0 \\ 0 & 0 & 0 & 1 \\ 0 & -7500 & -6.5\cdot 10^5 & -19799 \end{bmatrix} \begin{bmatrix} x_1 \\ x_2 \\ x_3 \\ x_4 \end{bmatrix} + \begin{bmatrix} 0 \\ 0 \\ 0 \\ 2.7\cdot 10^6 \end{bmatrix} u(t); \tag{16}$$

$$\frac{Y(s)}{X(s)} = s^2+105s+500; \tag{17}$$

$$Y(s) = (s^2+105s+500)X(s). \tag{18}$$

Solving equation (18) and transforming it into state space form gives:

$$y = [500 \quad 105 \quad 1 \quad 0]\cdot[x_1 \quad x_2 \quad x_3 \quad x_4]^T. \tag{19}$$

Equations (16) and (19) match the general, linear state space form:

$$\dot{x} = Ax + Bu; \tag{20}$$

$$y = Cx + Du, \tag{21}$$

where $D = 0$ for simulation in this paper.

3.2 System Configuration and Compensator Design

3.2.1 System configuration

Two closed-loop structures of the two-phase hybrid stepper motor control system were considered in this paper as shown in Figures 4 and 5. The structures conform to single-input single-out feedback loop of the MATLAB control tool. The loop has two compensators, two summing points, and a unit feedback gain.

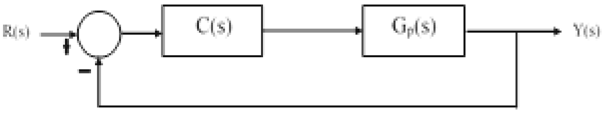

Figure 4 – Initial system configuration

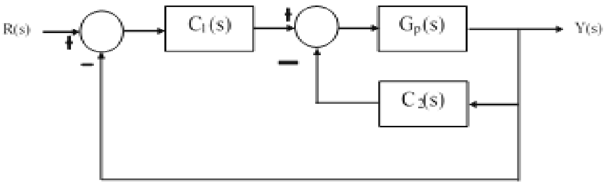

Figure 5 – Final system configuration

3.2.2 Compensator design

In this paper, three compensators were designed using proportional integrating and derivative (PID) tuning method. Automatic (balanced performance and robustness) design mode was adopted. This was achieved using the SISO graphic user interface (GUI) design task of the Control and Estimation Tool Manager (CETM) of MATLAB software. The first compensator, $C(s)$ was designed and added to the control loop and simulation performed as shown in Figure 4. In a bid to further improve the response performance of the plant, two-compensator control technique was developed, with outer loop compensator, $C_1(s)$ and inner loop compensator, $C_2(s)$ as shown in Figure 5. Tables 2–4 show parameters of the developed compensators.

Table 2 – Parameters of compensator, $C(s)$

Type	Location	Damping	Frequency
Real Pole	–175.40	1	175.4
Integrator	0.0	–1	0.0
Real Zero	-83.3	1	83.3

Table 3 – Parameters of compensator, $C_1(s)$

Type	Location	Damping	Frequency
Real Pole	–2.38	1	2.38
Integrator	0.00	–1	0.00
Real Zero	–1.18	1	1.18

Table 4 – Parameters of compensator, $C_2(s)$

Type	Location	Damping	Frequency
Real Pole	–1.00	1	1.00
Real Pole	–5.88	1	5.88
Real Zero	–1.00	1	1.00
Real Zero	–1.00	1	1.00

The gain of the compensator is equal to 0.6, 944.1 and 3.0 for data presented in Tables 2, 3, 4 correspondently.

Hence, the mathematical expressions of the compensators are given by equations (22)–(24). The closed loop control structure for the simulation in MATLAB environment is shown in Figure 5:

$$C(s) = 0.6 \cdot \frac{1+0.012s}{s(1+0.0057s)}; \tag{22}$$

$$C_1(s) = 944.1\frac{1+0.85s}{s(1+0.42s)}; \tag{23}$$

$$C_2(s) = 3.0\frac{(1+s)(1+s)}{(1+s)(1+0.17s)}. \tag{24}$$

4 Results

This section presents the simulation results obtained in MATLAB. Figure 6 is simulation results for control loop simulation of the plant (uncompensated). With first feedback compensator added to the forward path of the closed-loop, simulation was conducted and result obtained is shown in Figure 7. Figure 8 is the simulation result of the final proposed closed control system for two-phase hybrid stepping motor with two-compensator control algorithm. Figure 9 is the Bode stability plot of the proposed two-compensator closed loop control. The performance comparison of the system for various simulation cases considered is presented in Table 5.

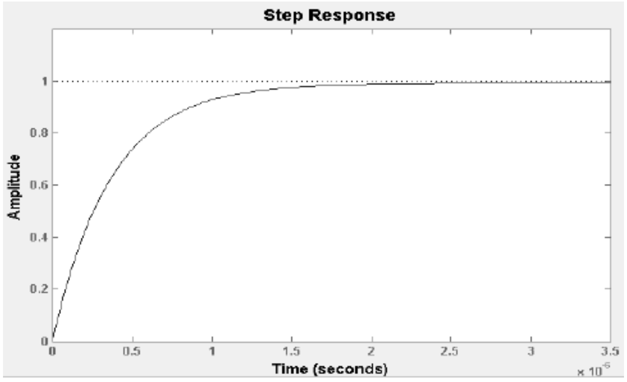

Figure 6 – Step response plot for uncompensated system

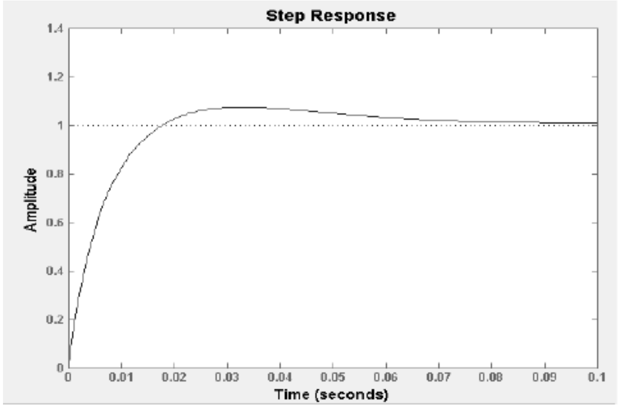

Figure 7 – Closed loop step response with compensator C(s)

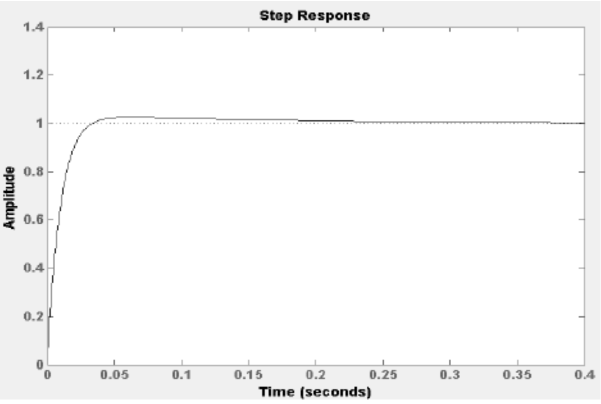

Figure 8 – Closed loop step response with two-compensator

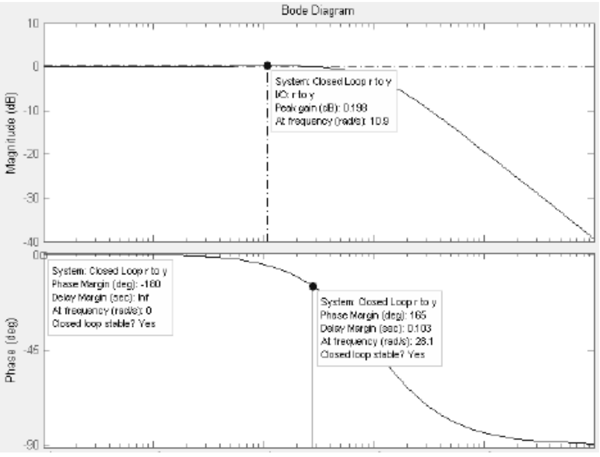

Figure 9 – Bode plot of the final simulation closed-loop system

Table 5 – Characteristics performance comparison

Characteristics	uncompensated	$C(s)$	$C_1(s)$ and $C_2(s)$
Rise time (s)	$8.3 \cdot 10^{-7}$	0.01	0.02
Settling time (s)	$1.6 \cdot 10^{-6}$	0.07	0.11
Overshoot (%)	0.0	8.01	2.56

5 Discussion

The step response performances of the various cases considered are presented in Table 5. It can be seen that the result of the uncompensated two-phase hybrid stepping motor control loop shown in Fig. 6 is quite promising. However, the response performance gives 0 % overshoot and below the setpoint value. This indicates that the system is sluggish and requires that the response being improved to enhance the setpoint tracking performance. With the first compensator $C_1(s)$ added to the forward path of the closed loop control structure, the step response curve (Figure 7) shows that system characteristics performance is enhanced with a better tracking performance. However, the system overshoot is higher than the desired overshoot (less than 5 %). In Figure 8, the step response performance of the system is well improved by the proposed two-compensator control network for two-phase hybrid stepper. A more preferred stable control loop is achieved with better tracking performance than the single loop compensator control system. Figure 9 shows the stability plot of the proposed control loop structure for a two-phase hybrid stepper motor. The plot shows that the system is stable

6 Conclusions

This paper has successfully simulated a two-compensator control loop network for two-phase hybrid stepper motor. Though many control techniques using bang –bang control, conventional PID, Fuzzy-PID, and other form of controllers have been widely implemented in Literature. However, in this paper, a new approach has been proposed which combines two-compensator in a two-phase hybrid steeper motor control loop to improve tracking response performance. The result obtained shows that the developed control system meets the required performance criteria in terms of rise time, settling time, and % overshoot.

References

1. Attiya, A. J., Shneen, S. W., Abbas, B. A., & Wenyu, Y. (2016). Variable Speed Control Using Fuzzy-PID Controller for Two-phase Hybrid Stepping Motor in Robotic Grinding. *Indonesian Journal of Electrical Engineering and Computer Science*, Vol. 3(1), pp. 102–118, doi: 10.11591/ijeecs.v3.i1.pp102-118.
2. Nagrath, I. J., & Gopal, M. (2005). *Control Systems Engineering*. 4th Edition, New Age International Publishers.
3. Zhan, R., Wang, X., Yang, Y., & Qiao, D. (2008). Design of two-phase hybrid stepping motor driver with current closed-loop control based on PIC 18F2331. *Electrical Machines and Systems, ICEM 2008. International Conference on IEEE.*
4. Bellini, A., Concari, C., Franceschini, G., & Toscani, A. (2004). Mixed mode PWM for high performance stepping motors. *Conference of IEEE Industrial Electronics Society, IECON.*
5. Zhaojin, W., Weihai C., Zhiyue, X., & Jianhua, W. (2006*).* Analysis of Two-Phase Stepper Motor Driver Based on FPGA. *IEEE International Conference on Industrial Informatics*.
6. Zhang, S., & Wang, X. (2013). Study of Fuzzy-PID Control in MATLAB for Two-phase Hybrid Stepping Motor. *Proceeding of the 2nd International Conference on Systems Engineering and Modeling (ICSEM-13)*, pp. 1011–1014.
7. Melin, P., & Oscar, C. (2005). Intelligent control of a stepping motor drive using an adaptive neuro–fuzzy inference system. *Information Sciences*, Vol. 170(2), pp. 133–151.
8. Wale, J. D., & Pollock, C. (2001). Hybrid stepping motors and drives. *Power Engineering Journal*, Vol. 15(1), pp. 5–12.
9. Baldha, S., Shukla, J., & Tarpara, K. (2015). Design and Simulation of Two-Phase Hybrid Stepper Motor with Current Tracking. *National Conference on Emerging Trends in Computer, Electrical & Electronics (ETCEE-2015), International Journal of Advance Engineering and Research Development (IJAERD).*
10. Degang, C., & Brad, P. (1993). Adaptive Linearization of Hybrid Step Motors: Stability Analysis. *IEEE Transactions on Automatic Control*, Vol. 38(6), 8pp. 74–887.
11. Xu, W., & Jianhong, Y. (2011). Derivation of Transmission Function Model of Two-phase Hybrid Stepping Motor. *Space Electronic Technology*, Vol. 3, pp. 50–53.

12. Salis, V., Chiappinelli, N., Costabeber, A., Zanchetta, P., Bifaretti, S., Tomei, P., Verelli, C. M. (2018). Learning Position Controls for Hybrid Step Motors: from Current-fed to Full-Order Models. *IEEE Transactions On Industrial Electronics*, Vol. 1, 326543.
13. Liu, G. F., & Li, H. W. (2017). Design of stepper motor position control system based on DSP. *2nd International Conference on Machinery, Electronics and Control Simulation, Advance in Engineering Research*, Vol. 138, pp. 207–211.
14. Khalilian, M., Abedi, A., & Zadeh, A. D., (2012). Position Control of Hybrid Stepper Motor Using Brain Emotional Controller. *Energy Procedia*, pp. 1999–2003, doi: 10.1016/j.egypro.2011.12.1200.

Покращення характеристики керування двофазним гібридним кроковим двигуном із застосуванням PID-налаштованих компенсаторів зовнішнього та внутрішнього контурів

Ониека Е. Б.[1], Чід'єбере М.[2], Нкірука А. П.[2]

[1] Кафедра електроніки, Університет Нігерії, м. Ншукка, Нігерія;
[2] Кафедра електротехніки та електроніки, Університет Ч. О. Оджуку, м. Улі, Нігерія

Анотація. У статті наведено поліпшену характеристику керування двофазним гібридним кроковим двигуном із використанням PID-налаштованих компенсаторів зовнішнього та внутрішнього контурів. Підвищено ефективність відгуку двофазного гібридного крокового двигуна до досягнутого пере регулювання нижче 5 % і часу регулювання 0,16 с. Для досягнення мети дослідження створено динамічну модель двофазного гібридного крокового двигуна за допомогою передаточної функції. Обрано надійну методику PID-налаштування, яка використовує єдиний вхідний сигнал із застосуванням графічного інтерфейсу користувача, а також диспетчера інструментів контролю та оцінки програми MATLAB для проектування компенсаторів. Для підвищення ефективності відгуку один компенсатор спроектовано і вбудовано до керуючого контуру двофазного гібридного крокового двигуна. Числове моделювання виконувалось у програмі MATLAB, а коефіцієнт перерегулювання становив 8 % для одноланкового компенсатора. Однак наявне перерегулювання системи вимагає подальшого її удосконалення. У зв'язку із цим, було запропоновано новий контур керування із використанням структури з двокомпенсаторним контуром. У результаті розроблено компенсатори зовнішнього і внутрішнього контуру, які застосовані при керуванні двофазним гібридним кроковим двигуном. Числове моделювання здійснювалось із застосуванням MATLAB, а отриманий результат показав, що для двокомпенсаторної структури перерегулювання було значно скорочено до 2,6 % з часом регулювання 12 мс. Цей результат свідчить про покращення ефективності системи відстеження відгуками шляхом застосування комбінованих зовнішніх і внутрішніх контурів компенсаторів.

Ключові слова: компенсатор, контур керування, графічний інтерфейс користувача, пропорційні інтеграл і похідна, PID-налаштування.

JOURNAL OF ENGINEERING SCIENCES
ЖУРНАЛ ІНЖЕНЕРНИХ НАУК
ЖУРНАЛ ИНЖЕНЕРНЫХ НАУК
Web site: http://jes.sumdu.edu.ua
DOI: 10.21272/jes.2019.6(1).d2
Volume 6, Issue 1 (2019)

UDC 519.63:539.3

Ritz Variational Method for the Flexural Analysis of Rectangular Kirchhoff Plate on Winkler Foundation

Ike C. C.*

Enugu State University of Science and Technology, P.M.B. 01660, Enugu, Nigeria

Article info:
Paper received: May 19, 2018
The final version of the paper received: December 14, 2018
Paper accepted online: December 18, 2018

***Corresponding Author's Address:**
charles.ike@esut.edu.ng

Abstract. In this study, the Ritz variational method has been applied to solve the bending problem of rectangular Kirchhoff plate resting on Winkler foundation for the case of simply supported edges and transverse distributed load. The problem was presented in variational form using energy principles to obtain the total potential energy functional. Ritz technique was then used to find the generalised displacement parameters which minimized the total potential energy functional; where basis functions were choose to apriori satisfy the boundary conditions. Analytical solutions were obtained which were found to be identical with Navier's series solutions for the general case of arbitrary distributed transverse load, as well as the specific cases of point loads, sinusoidal load, uniform and linearly distributed loads.

Keywords: Ritz variational method, Kirchhoff plate, Winkler foundation, total potential energy functional, generalised displacement parameters, displacement basis functions.

1 Introduction

Problems of the flexure of plates resting on elastic foundations are fundamental in geotechnical and structural engineering and analysis. They are encountered in the analysis and design of foundations such as column footings, combined footings and raft foundations. They are also encountered in problems of structural analysis that are mathematical analogues of the plate on Winkler foundation problem. Many theories exist for the analysis of the flexural behaviour of plates. They include: Lagrange plate theory, Germain theory, Kirchhoff theory, Von Karman theory, Reissner [1, 2] theory, Mindlin [3], Shimpi [4] theory, Reddy [5] theory, and other variants of Refined plate theory and shear deformation plate theories. Kirchhoff plate theory also called the classical thin plate theory is adopted in this paper. The fundamental hypothesis of the Kirchhoff plate theory includes:

1) straight lines normal to the plate's middle surface remain straight after bending deformation;

2) straight lines normal to the plate middle surface before deformation remain normal to the middle surface after bending deformation;

3) the thickness of the plate does not change during flexural deformation.

The Kirchhoff plate theory is a two dimensional approximation of the mathematical theory of elasticity applied to plates to determine the stress and deformation fields in thin plates subject to forces and moments under different restraint conditions. It is an extension of the Euler-Bernoulli beam theory, and assumes that a middle plane surface, neutral during deformation can be used to represent a three dimensional plate in two dimensional form (Mama et al, [6]). The obvious merits of Kirchhoff plate theory include:

1) the problem is reduced to two dimensional one;

2) the uncoupling of bending and stretching behaviours;

3) the linear nature of the governing partial differential equation;

4) stresses can be calculated from the stress-displacement relations;

5) it is commonly applied.

The most significant defect is the neglect of transverse shear deformation and its inability to model cases in which shear deformation plays a significant role. The interaction of soil on the foundation structure is represented by the soil reactive pressure distribution (Caselunghe and Erikson, [7]).

Many models exist for describing the soil interaction on the foundation structure. The elastic foundation models are classified as discrete parameter models, simplified elastic continuum models and elastic continuum models (Rajpurohit et al, [8]; Ghaitani et al, [9]). In discrete parameter models, the elastic foundation is modeled as a set of closely spaced discrete individual springs that may or may not be coupled to one another. In continuum models, the mathematical theory of elasticity is used to find complex analytical expressions that describe the soil reaction. Simple elastic continuum foundation models are models that may be described as simplifications of the theory of elasticity formulation for the soil reaction. Discrete parameter foundation models include: Winkler [10], Pasternak [11], Filonenko-Borodich [12], and Hetenyi [13] foundation models, as well as generalised two- and multi-parameter foundation models.

The simplest representation of soil reactive pressure distribution is provided by the classical Winkler foundation model which replaces the subgrade by a mechanical analogy made up of single bed of closely spaced independent vertical springs, without interaction with one another. In the Winkler foundation idealization, the soil reaction at any point on the foundation (plate) is directly proportional to the deformation of the foundation (plate) at that point. Thus, analytically,

$$p(x, y) = k_s w(x, y), \tag{1}$$

where $p(x, y)$ is the soil reactive pressure distribution at an arbitrary point (x, y) in the plate-soil interface area, $w(x, y)$ is the corresponding vertical deformation and k_s is the constant of proportionality, representing contact pressure per unit deformation – commonly referred to as the Winkler coefficient or coefficient of subgrade reaction or simply the subgrade modulus.

Hence in the Winkler model, k_s is the only foundation parameter characterizing the elastic response of the soil, Winkler's foundation has the basic demerit of resulting in a vertical deformation of only those springs alone that are located under the loaded region. Thus the Winkler model leads to discontinuity of vertical deformation at the edges of the loaded plate. In addition, the Winkler model implies that a point undergoes vertical deformation that is independent of the vertical deformation of other adjoining points; which is not in line with elasticity findings. These shortcomings have led to the development of other discrete parameter foundation models that account for the effect of shear interaction (Pasternak, [11]). However, the simplificity of the Winkler model and its long term familiarity has ensured its usage till today. The Filonenko-Borodich, and Pasternak foundation models are two parameter discrete parameter foundation models where the soil reaction pressure is given generally by (Pasternak, [11]):

$$p(x, y) = k_1 w(x, y) - k_2 \nabla^2 w(x, y), \tag{2}$$

where k_1 and k_2 are two discrete parameters of the model, and ∇^2 is the Laplacian operator with respect to coordinates x, y. In the Kerr [14] model, a shear layer is introduced in the numerator Winkler foundation and the shear layer separates the elastic bed into two beds with two different spring constants, k_1 for the first layer interfacing the plate and k_2 for the second layer making contact with a rigid base.

The governing differential equation of the Kerr [14] foundation is given by

$$\left(1 + \frac{k_2}{k_1}\right) p = \frac{G}{k_1} \nabla^2 p + k_2 w - G \nabla^2 w, \tag{3}$$

where k_1 is the spring constant of the first layer, k_2, the spring constant of the second layer and $w(x, y)$ is the deflection of the first layer, G is the shear modulus of the shear layer which separates the first and second layers in a Kerr foundation.

The research [15] expanded the previous work done by Mama et al [6] by considering new particular types of distributed transverse load namely, bisinusoidal distribution and linear distribution over the entire plate domain and using the Fourier sine transform method. In addition, paper [15] considered and solved numerical problems for simply supported Kirchhoff plates resting on Winkler foundations for different values of the dimensionless Winkler parameter; for cases of uniformly distributed transverse load on the plate domain.

Other researchers who have studied the plate on elastic foundation problem are: Althobaiti and Prikazchikov [16]; Zhong, Zhao and Hu [17]; Li, Zhong and Li [18]; Li, Zhong and Tian [19]; Li et al [20]; Zhang, Shi and Wang [21]; Agarana, Gbadeyan and Ajayi [22]; Are, Idowu and Gbadeyin [23]; Agarana and Gbadeyin [24]; Tahuoneh and Yas [25]; and Ye et al [26].

The research aim is to apply the Ritz variational method to obtain solutions for the flexural problem of simply supported Kirchhoff plate resting on Winkler foundation for cases of transversely distributed loads. The specific objectives include:

1) to obtain the Ritz variational statement of the problem of Kirchhoff plate on Winkler foundation for the case of arbitrary distribution of transverse loads;

2) to solve the variational problem using the energy minimization principle to obtain the general solution for the deflection for any distributed load as well as the corresponding internal force resultants;

3) to obtain solutions for deflections and internal forces for particular types of transverse loads namely:

– point load P_0 applied at a known point (x_0, y_0) on the plate domain;

– bisinusoidal distributed load over the entire plate domain;

– uniformly distributed load over the entire plate domain;

– linearly distributed load over the plate domain.

2 Research Methodology

Kirchhoff plate theory was adopted for the plate while Winkler foundation model was used to describe the soil reaction pressure on the plate. Kirchhoff plate theory is based on the following kinematic assumptions:

1) straight lines normal to the middle surface remain straight after deformation;

2) straight lines normal to the middle surface remain normal to the middle surface after deformation;

3) the thickness of the plate does not change during flexural deformation.

Using the strain energy density for a generalised three dimensional state of stress, the generalized Hooke's stress-strain law for isotropic elastic plates and the fundamental assumption of thin plate theory, the bending strain energy functional U_b for the Kirchhoff plate is obtained by the following formula:

$$U_b = \frac{D}{2}\iint\limits_R \left[(\nabla^2 w)^2 + 2(1-\mu)(w_{xy}^2 - w_{xx}w_{yy})\right]dxdy\ ,(4)$$

where R is the two dimensional domain of the plate on the xy coordinate plane, D is the plate flexural rigidity given by

$$D = \frac{Eh^3}{12(1-\mu^2)}\ ; \tag{5}$$

h is the plate thickness, w_{xx} denotes the second partial derivative of $w(x, y)$ with respect to x, while w_{xy} is the mixed partial derivative of $w(x, y)$ with respect to x and y variables.

The potential energy of the distributed transverse load $p(x, y)$ is given by

$$V = -\iint\limits_R p(x, y)\, w(x, y)dxdy\ . \tag{6}$$

The potential energy functional due to the Winkler foundation is given by:

$$W_s = \frac{1}{2}\iint\limits_R k\left(w(x, y)\right)^2 dxdy\,, \tag{7}$$

where $p_s(x, y)$ is the soil reactive pressure on the plate. The total potential energy functional Π then becomes

$$\Pi = U_b + W_s + V\ ; \tag{8}$$

The problem of flexure under static transverse loads for Kirchhoff plate on Winkler foundation then reduces to one of finding the value of the deflection $w(x, y)$ that minimizes the total potential energy functional expressed as the abovementioned equation; a problem situated in calculus of variations. Thus, for equilibrium of the Kirchhoff plate on Winkler foundation problem

$$\delta\Pi = 0\,, \tag{9}$$

where $\delta\Pi$ denotes the first variation in the total potential energy functional.

Ritz variational method is based on the principle of minimum total potential energy functional for equilibrium. The principle states that the displacement field (function) that corresponds to the minimum total potential energy functional represents a state of equilibrium, provided the displacement function satisfies the given boundary conditions. Thus, the Ritz variational method seeks to obtain the displacement field defined over the plate domain such that the total potential energy functional of the Kirchhoff plate on Winkler foundation carrying known transverse distributed load is minimized. In the Ritz method, the unknown displacement field (function) $w(x, y)$ is sought or defined in terms of a finite or infinite number of basis (shape or coordinate) functions as follows:

$$w(x, y) = \sum_m^{\infty}\sum_n^{\infty} w_{mn}\, X_m(x)Y_n(y)\,, \tag{10}$$

where $X_m(x)$ and $Y_n(y)$ are the basis (coordinate or shape) functions in the x and y coordinate directions respectively, chosen such that they identically satisfy the end condition along the x and y directions respectively; and w_{mn} are the generalised displacement parameters which are sought.

For Kirchhoff plate on Winkler foundation, extremization of the total potential energy functional (8) in terms of the unknown generalised displacement parameters w_{mn}

$$\frac{\partial\Pi}{\partial w_{mn}} = 0 \tag{11}$$

allows obtaining the system of algebraic equations:

$$\sum_{m=1}^{\infty}\sum_{n=1}^{\infty} k_{mn}\, w_{mn} = \sum_{m=1}^{\infty}\sum_{n=1}^{\infty} F_{mn}\ . \tag{12}$$

3 Results

3.1 Arbitrary distributed load *p*(*x*, *y*) over the simply supported Kirchhoff plate

A rectangular Kirchhoff plate of length a and width b resting on Winkler foundation as shown in Figure 1 was considered.

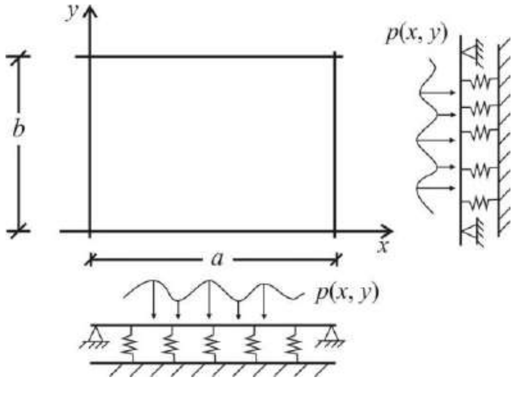

Figure 1 – Kirchhoff plate on Winkler foundation under arbitrary load, $p(x, y)$

The geometric and force boundary conditions at the simply supported edges are: $w(0, y) = w(a, y) = 0$; $\frac{\partial^2 w}{\partial x^2}(x=0, y) = \frac{\partial^2 w}{\partial x^2}(x=a, y) = 0$; $w(x, 0) = w(x, b) = 0$; $\frac{\partial^2 w}{\partial y^2}(x, y=0) = \frac{\partial^2 w}{\partial y^2}(x, y=b) = 0$.

The displacement basis functions that satisfy the boundary conditions are:

$$X_m(x) = \sin\frac{m\pi x}{a} = \sin\alpha_m x\,;\ Y_n(x) = \sin\frac{n\pi y}{b} = \sin\beta_n y\,, \quad (13)$$

where $\alpha_m = \frac{m\pi}{a}$; $\beta_n = \frac{n\pi}{b}$.

For simply supported plates, the Gaussian curvature given by ($w_{xy}^2 - w_{xx}w_{yy}$) contributes nothing to the total potential energy since its integral vanishes and Π simplifies to:

$$\Pi = \frac{D}{2}\iint_R (\nabla^2 w)^2\,dxdy + \frac{1}{2}\iint_R kw^2 - \iint_R pw\,dxdy\,. \quad (14)$$

Let the arbitrary distributed transverse load be represented using Fourier sine series as

$$p(x, y) = \sum_{m=1}^{\infty}\sum_{n=1}^{\infty} p_{mn}\sin\frac{m\pi x}{a}\sin\frac{n\pi y}{b}\,. \quad (15)$$

where p_{mn} are the Fourier coefficients of the distributed load, then

$$\Pi = \frac{D}{2}\sum_m^{\infty}\sum_n^{\infty}\left(\left(\frac{m\pi}{a}\right)^2 + \left(\frac{n\pi}{b}\right)^2\right)^2 w_{mn}^2\, I_1 + + \frac{1}{2}k\sum_m^{\infty}\sum_n^{\infty} w_{mn}^2\, I_1 - p_{mn}\, w_{mn}\, I_1\,, \quad (16)$$

where

$$I_1 = \int_0^a\int_0^b \sin^2\frac{m\pi x}{a}\sin^2\frac{n\pi y}{b}\,dxdy\,. \quad (17)$$

Extremizing Π with respect to the generalised coordinates after simplifying allows obtaining

$$w_{mn} = \frac{p_{mn}/D}{\left(\left(\frac{m\pi}{a}\right)^2 + \left(\frac{n\pi}{b}\right)^2\right)^2 + \left(\frac{k}{D}\right)}\,. \quad (18)$$

Using the dependence

$$p_{mn} = \frac{4}{ab}\int_0^a\int_0^b p(x, y)\sin\frac{m\pi x}{a}\sin\frac{n\pi y}{b}\,dxdy\,, \quad (19)$$

it can be obtained:

$$w(x, y) = \sum_m^{\infty}\sum_n^{\infty}\frac{p_{mn}\sin\frac{m\pi x}{a}\sin\frac{n\pi y}{b}}{D\left[\left(\left(\frac{m\pi}{a}\right)^2 + \left(\frac{n\pi}{b}\right)^2\right)^2 + \frac{k}{D}\right]}\,. \quad (20)$$

In this case, the bending and twisting moments are

$$M_{xx} = \sum_m^{\infty}\sum_n^{\infty}\frac{\left(\left(\frac{m\pi}{a}\right)^2 + \mu\left(\frac{n\pi}{b}\right)^2\right)p_{mn}\sin\frac{m\pi x}{a}\sin\frac{n\pi y}{b}}{\left[\left(\left(\frac{m\pi}{a}\right)^2 + \left(\frac{n\pi}{b}\right)^2\right)^2 + \frac{k}{D}\right]}\,;$$

$$M_{yy} = \sum_m^{\infty}\sum_n^{\infty}\frac{\left(\left(\frac{n\pi}{b}\right)^2 + \mu\left(\frac{m\pi}{a}\right)^2\right)p_{mn}\sin\frac{m\pi x}{a}\sin\frac{n\pi y}{b}}{\left[\left(\left(\frac{m\pi}{a}\right)^2 + \left(\frac{n\pi}{b}\right)^2\right)^2 + \frac{k}{D}\right]}\,; \quad (21)$$

$$M_{xy} = -(1-\mu)\sum_m^{\infty}\sum_n^{\infty}\frac{p_{mn}\left(\frac{m\pi}{a}\frac{n\pi}{b}\right)\cos\frac{m\pi x}{a}\cos\frac{n\pi y}{b}}{\left(\left(\frac{m\pi}{a}\right)^2 + \left(\frac{n\pi}{b}\right)^2\right)^2 + \frac{k}{D}}\,.$$

3.2 Ritz variational solutions for point load P_0 at (x_0, y_0)

For the case of point load P_0 applied at the arbitrary point x_0, y_0, within the plate domain, the Fourier series coefficient p_{mn} is

$$p_{mn} = \frac{4P_0}{ab}\sin\frac{m\pi x_0}{a}\sin\frac{n\pi y_0}{b}\,. \quad (22)$$

Then, the solutions for transverse deflections and bending moments become:

$$w(x, y) = \frac{4P_0}{abD}\sum_m^{\infty}\sum_n^{\infty}\frac{\sin\frac{m\pi x_0}{a}\sin\frac{n\pi y_0}{b}\sin\frac{m\pi x}{a}\sin\frac{n\pi y}{b}}{\left(\left(\frac{m\pi}{a}\right)^2 + \left(\frac{n\pi}{b}\right)^2\right)^2 + \frac{k}{D}}$$

$$M_{xx} = \frac{4P_0}{ab}\sum_m^{\infty}\sum_n^{\infty}\frac{\left(\left(\frac{m\pi}{a}\right)^2 + \mu\left(\frac{n\pi}{b}\right)^2\right)\sin\frac{m\pi x_0}{a}\sin\frac{m\pi x}{a}\sin\frac{n\pi y_0}{b}\sin\frac{n\pi y}{b}}{\left(\left(\frac{m\pi}{a}\right)^2 + \left(\frac{n\pi}{b}\right)^2\right)^2 + \frac{k}{D}} \quad (23)$$

$$M_{yy} = \frac{4P_0}{ab}\sum_m^{\infty}\sum_n^{\infty}\frac{\left(\left(\frac{n\pi}{b}\right)^2 + \mu\left(\frac{m\pi}{a}\right)^2\right)\sin\frac{m\pi x_0}{a}\sin\frac{m\pi x}{a}\sin\frac{n\pi y_0}{b}\sin\frac{n\pi y}{b}}{\left(\left(\frac{m\pi}{a}\right)^2 + \left(\frac{n\pi}{b}\right)^2\right)^2 + \frac{k}{D}}$$

where $m, n = \{1, 3, 5, \ldots\}$.

When the point load is applied at the center of the plate ($x_0 = a/2$, $y_0 = b/2$), the maximum deflection and bending moments would occur at the plate center and are found as:

$$w\left(a/2, b/2\right) = \frac{4P_0}{abD}\sum_m^{\infty}\sum_n^{\infty}\frac{\sin^2\frac{m\pi}{2}\sin^2\frac{n\pi}{2}}{\left(\left(\frac{m\pi}{a}\right)^2 + \left(\frac{n\pi}{b}\right)^2\right)^2 + \frac{k}{D}}$$

$$M_{xx}\left(a/2, b/2\right) = \frac{4P_0}{ab}\sum_m^{\infty}\sum_n^{\infty}\frac{\left(\left(\frac{m\pi}{a}\right)^2 + \mu\left(\frac{n\pi}{b}\right)^2\right)\sin^2\frac{m\pi}{2}\sin^2\frac{n\pi}{2}}{\left(\left(\frac{m\pi}{a}\right)^2 + \left(\frac{n\pi}{b}\right)^2\right)^2 + \frac{k}{D}} \quad (24)$$

$$M_{yy}\left(a/2, b/2\right) = \frac{4P_0}{ab}\sum_m^{\infty}\sum_n^{\infty}\frac{\left(\left(\frac{n\pi}{b}\right)^2 + \mu\left(\frac{m\pi}{a}\right)^2\right)\sin^2\frac{m\pi}{2}\sin^2\frac{n\pi}{2}}{\left(\left(\frac{m\pi}{a}\right)^2 + \left(\frac{n\pi}{b}\right)^2\right)^2 + \frac{k}{D}}$$

For square plates on Winkler foundation where the point load P_0 acts at the center ($a = b$), and the maximum deflection and bending moments occur at the center, and are given by:

$$w\left(\tfrac{a}{2},\tfrac{b}{2}\right) = \frac{4P_0a^2}{D}\sum_m^\infty\sum_n^\infty \frac{\sin^2\frac{m\pi}{2}\sin^2\frac{n\pi}{2}}{\left(\pi^4(m^2+n^2)^2+\frac{ka^4}{D}\right)};$$

$$M_{xx}\left(\tfrac{a}{2},\tfrac{b}{2}\right) = 4P_0\sum_m^\infty\sum_n^\infty \frac{\pi^2(m^2+\mu n^2)\sin^2\frac{m\pi}{2}\sin^2\frac{n\pi}{2}}{\pi^4(m^2+n^2)^2+\frac{ka^4}{D}}. \quad (25)$$

Additionally, $M_{yy}(a/2, b/2) = M_{xx}(a/2, b/2)$.

3.3 Ritz variational solutions for transverse sinusoidal load

In the case of transverse sinusoidal load $p(x,y) = p_0\sin\frac{\pi x}{a}\sin\frac{\pi y}{b}$, the Fourier sine series coefficient for the sinusoidal load $p_{mn} = p_0 \quad m = 1, \quad n = 1$ and $p_{mn} = 0 \quad m \neq 1, \quad n \neq 1$. Then by substitution into the Ritz variational solutions for arbitrary distribution of transverse load, the solutions for sinusoidal loads become:

$$w(x,y) = \frac{p_0\sin\frac{\pi x}{a}\sin\frac{ny}{b}}{D\left[\left(\left(\frac{\pi}{a}\right)^2+\left(\frac{\pi}{b}\right)^2\right)^2+\frac{k}{D}\right]};$$

$$M_{xx} = \frac{\left(\left(\frac{\pi}{a}\right)^2+\mu\left(\frac{\pi}{b}\right)^2\right)p_0\sin\frac{\pi x}{a}\sin\frac{ny}{b}}{\left(\left(\frac{\pi}{a}\right)^2+\left(\frac{\pi}{b}\right)^2\right)^2+\frac{k}{D}}; \quad (26)$$

$$M_{yy} = \frac{\left(\left(\frac{\pi}{b}\right)^2+\mu\left(\frac{\pi}{a}\right)^2\right)p_0\sin\frac{\pi x}{a}\sin\frac{ny}{b}}{\left(\left(\frac{\pi}{a}\right)^2+\left(\frac{\pi}{b}\right)^2\right)^2+\frac{k}{D}}.$$

The maximum values of deflection and bending moments occur at the plate center, and are given by:

$$w\left(\tfrac{a}{2},\tfrac{b}{2}\right) = \frac{p_0\sin^2\left(\tfrac{\pi}{2}\right)}{D\left[\left(\left(\frac{\pi}{a}\right)^2+\left(\frac{\pi}{b}\right)\right)^2+\frac{k}{D}\right]};$$

$$M_{xx}\left(\tfrac{a}{2},\tfrac{b}{2}\right) = \frac{\left(\left(\tfrac{\pi}{a}\right)^2+\mu\left(\tfrac{\pi}{b}\right)^2\right)p_0\sin^2\left(\tfrac{\pi}{2}\right)}{\left(\left(\frac{\pi}{a}\right)^2+\left(\frac{\pi}{b}\right)^2\right)^2+\frac{k}{D}}; \quad (27)$$

$$M_{yy}\left(\tfrac{a}{2},\tfrac{b}{2}\right) = \frac{\left(\left(\tfrac{\pi}{b}\right)^2+\mu\left(\tfrac{\pi}{a}\right)^2\right)p_0\sin^2\left(\tfrac{\pi}{2}\right)}{\left(\left(\frac{\pi}{a}\right)^2+\left(\frac{\pi}{b}\right)^2\right)^2+\frac{k}{D}}.$$

For square plates ($a = b$) it can be obtained:

$$w(x,y) = \frac{p_0a^4}{D}\frac{p_0\sin\frac{\pi x}{a}\sin\frac{\pi y}{a}}{4\pi^4+\frac{ka^4}{D}};$$

$$w_{yy}\left(\tfrac{a}{2},\tfrac{a}{2}\right) = \frac{p_0a^4}{D}\left(\frac{\sin^2\left(\tfrac{\pi}{2}\right)}{4\pi^4+\frac{ka^4}{D}}\right); \quad (28)$$

$$w_{\max} = \left(\frac{1}{4\pi^4+\frac{ka^4}{D}}\right)\frac{p_0a^4}{D}.$$

Similarly, the maximum bending and twisting moments for square plates on Winkler foundation for the case of sinusoidal load are:

$$M_{xx_{\max}} = \left(\frac{\pi^2(1+\mu)}{4\pi^4+\frac{ka^4}{D}}\right)p_0a^2 = M_{yy_{\max}};$$

$$M_{xy_{\max}} = M_{xy}(x=0, y=0) = \frac{-(1-\mu)\pi^2p_0a^2}{\left(4\pi^4+\frac{ka^4}{D}\right)}. \quad (29)$$

3.4 Ritz variational solution for uniformly distributed load $p(x,y) = p_0$ = const

The Fourier sine series coefficients for the uniformly distributed load are:

$$p_{mn} = \frac{16p_0}{mn\pi^2}. \quad (30)$$

Then, the Ritz variational solutions become:

$$w(x,y) = \frac{16p_0}{\pi^2D}\sum_m^\infty\sum_n^\infty\left\{\frac{\sin\frac{m\pi x}{a}\sin\frac{n\pi y}{b}}{mn\left[\pi^4\left(\left(\frac{m}{a}\right)^2+\left(\frac{n}{b}\right)^2\right)^2+\frac{k}{D}\right]}\right\}$$

$$w\left(\tfrac{a}{2},\tfrac{b}{2}\right) = w_{\max} = \frac{16p_0}{\pi^2D}\sum_m^\infty\sum_n^\infty\left\{\frac{\sin\frac{m\pi x}{a}\sin\frac{n\pi y}{b}}{mn\left[\pi^4\left(\left(\frac{m}{a}\right)^2+\left(\frac{n}{b}\right)^2\right)^2+\frac{k}{D}\right]}\right\} \quad (31)$$

The bending moment distributions are:

$$M_{xx}(x,y) = \frac{16p_0}{\pi^2}\sum_m^\infty\sum_n^\infty\left\{\frac{\left(\left(\frac{m\pi}{a}\right)^2+\mu\left(\frac{n\pi}{b}\right)^2\right)\sin\frac{m\pi x}{a}\sin\frac{n\pi y}{b}}{mn\left[\left(\left(\frac{m\pi}{a}\right)^2+\left(\frac{n\pi}{b}\right)^2\right)^2+\frac{k}{D}\right]}\right\}$$

$$M_{yy}(x,y) = \frac{16p_0}{\pi^2}\sum_m^\infty\sum_n^\infty\left\{\frac{\left(\left(\frac{n\pi}{b}\right)^2+\mu\left(\frac{m\pi}{a}\right)^2\right)\sin\frac{m\pi x}{a}\sin\frac{n\pi y}{b}}{mn\left[\left(\left(\frac{m\pi}{a}\right)^2+\left(\frac{n\pi}{b}\right)^2\right)^2+\frac{k}{D}\right]}\right\} \quad (32)$$

The maximum moments occur at the center $(x = a/2, y = b/2)$ and are given by:

$$M_{xx_{\max}} = 16 p_0 a^2 \sum_{m}^{\infty} \sum_{n}^{\infty} \left\{ \frac{\left(m^2 + \mu (nr)^2\right) \sin \frac{m\pi}{2} \sin \frac{n\pi}{2}}{mn\left[\left(m^2 + (nr)^2\right)^2 \pi^4 + \frac{ka^4}{D}\right]} \right\};$$

$$M_{yy_{\max}} = 16 p_0 a^2 \sum_{m}^{\infty} \sum_{n}^{\infty} \left\{ \frac{\left((nr)^2 + \mu m^2\right) \sin \frac{m\pi}{2} \sin \frac{n\pi}{2}}{mn\left[\left(m^2 + (nr)^2\right)^2 \pi^4 + \frac{ka^4}{D}\right]} \right\}. \quad (33)$$

where $r = a/b$.
For square plates ($r = 1$):

$$w_{\max} = \frac{16 p_0 a^4}{D} \sum_{m}^{\infty} \sum_{n}^{\infty} \left\{ \frac{\sin \frac{m\pi}{2} \sin \frac{n\pi}{2}}{mn\left[(m^2 + n^2)^2 \pi^4 + \frac{ka^4}{D}\right]} \right\};$$

$$M_{xx_{\max}} = M_{yy_{\max}} = 16 p_0 a^2 \sum_{m}^{\infty} \sum_{n}^{\infty} \frac{(m^2 + \mu n^2) \sin \frac{m\pi}{2} \sin \frac{n\pi}{2}}{mn\left[(m^2 + n^2)^2 \pi^4 + \frac{ka^4}{D}\right]}. \quad (34)$$

The twisting moments are:

$$M_{xy} = -\frac{(1-\mu) 16 p_0}{ab} \sum_{m}^{\infty} \sum_{n}^{\infty} \frac{\cos \frac{m\pi x}{a} \cos \frac{n\pi y}{b}}{\left[\pi^4 \left(\frac{m^2}{a^2} + \frac{n^2}{b^2}\right)^2 + \frac{k}{D}\right]};$$

$$M_{xy_{\max}} = -\frac{16 p_0 (1-\mu) a^3}{b} \sum_{m}^{\infty} \sum_{n}^{\infty} \frac{1}{\pi^4 (m^2 + n^2 r^2)^2 + \frac{ka^4}{D}}. \quad (35)$$

For square plates:

$$M_{xy_{\max}} = -16 p_0 (1-\mu) a^2 \sum_{m}^{\infty} \sum_{n}^{\infty} \left(\frac{1}{\pi^4 (m^2 + n^2)^2 + \frac{ka^4}{D}} \right). \quad (36)$$

3.5 Ritz variational solutions for linearly distributed load $p(x, y) = p_0 x/a$

The Fourier sine series coefficient for linearly distributed load $p(x, y) = p_0 x/a$ is:

$$p_{mn} = \frac{8 p_0 \cos m\pi}{mn\pi^2}. \quad (37)$$

Then the deflection field (function) becomes:

$$w(x, y) = \frac{8 p_0 a^4}{\pi^2 D} \sum_{m}^{\infty} \sum_{n}^{\infty} \frac{\cos m\pi \sin \frac{m\pi x}{a} \sin \frac{n\pi y}{b}}{mn\left[\pi^4 (m^2 + n^2 r^2)^2 + \frac{ka^4}{D}\right]}. \quad (38)$$

At the plate center:

$$w_{\max} = w\left(a/2, b/2\right) = \frac{8 p_0 a^4}{\pi^2 D} \sum_{m}^{\infty} \sum_{n}^{\infty} \frac{\cos m\pi \sin \frac{m\pi}{2} \sin \frac{n\pi}{2}}{mn\left[\pi^4 (m^2 + n^2 r^2)^2 + \frac{ka^4}{D}\right]}. \quad (39)$$

The bending moments are obtained from the moment-displacement (moment-curvature) relations as:

$$M_{xx} = \frac{8 p_0 a^2}{\pi^2} \sum_{m}^{\infty} \sum_{n}^{\infty} \frac{\pi^2 \left(m^2 + \mu n^2 r^2\right) \cos m\pi \sin \frac{m\pi x}{a} \sin \frac{n\pi y}{b}}{\left[\pi^4 \left(m^2 + (nr)^2\right)^2 + \frac{ka^4}{D}\right] mn};$$

$$M_{yy} = 8 p_0 a^2 \sum_{m}^{\infty} \sum_{n}^{\infty} \frac{(n^2 r^2 + \mu m^2) \cos m\pi \sin \frac{m\pi x}{a} \sin \frac{n\pi y}{b}}{mn\left(\pi^4 (m^2 + n^2 r^2)^2 + \frac{ka^4}{D}\right)}. \quad (40)$$

Bending moments at the plate center, is given by:

$$M_{xx}\left(a/2, b/2\right) = p_0 a^2 \cdot 8 \sum_{m}^{\infty} \sum_{n}^{\infty} \frac{(m^2 + \mu (nr)^2) \cos m\pi \sin \frac{m\pi}{2} \sin \frac{n\pi}{2}}{\left[\pi^4 \left(m^2 + (nr)^2\right)^2 + \frac{ka^4}{D}\right] mn};$$

$$M_{yy_{\max}} = 8 p_0 a^2 \sum_{m}^{\infty} \sum_{n}^{\infty} \frac{(n^2 r^2 + \mu m^2) \cos m\pi \sin \frac{m\pi}{2} \sin \frac{n\pi}{2}}{mn\left(\pi^4 (m^2 + n^2 r^2)^2 + \frac{ka^4}{D}\right)}. \quad (41)$$

For square plates ($r = 1$):

$$w_{\max} = \frac{8 p_0 a^4}{\pi^2 D} \sum_{m}^{\infty} \sum_{n}^{\infty} \frac{\cos m\pi \sin \frac{m\pi}{2} \sin \frac{n\pi}{2}}{mn\left(\pi^4 (m^2 + n^2)^2 + \frac{ka^4}{D}\right)};$$

$$M_{xx_c} = 8 p_0 a^2 \sum_{m}^{\infty} \sum_{n}^{\infty} \frac{(m^2 + \mu n^2) \cos m\pi \sin \frac{m\pi}{2} \sin \frac{n\pi}{2}}{mn\left(\pi^4 (m^2 + n^2)^2 + \frac{ka^4}{D}\right)}; \quad (42)$$

$$M_{yy_c} = 8 p_0 a^2 \sum_{m}^{\infty} \sum_{n}^{\infty} \frac{(n^2 r^2 + \mu m^2) \cos m\pi \sin \frac{m\pi}{2} \sin \frac{n\pi}{2}}{mn\left(\pi^4 (m^2 + n^2)^2 + \frac{ka^4}{D}\right)}.$$

The Ritz variational solutions for the maximum deflection and maximum bending moments which occur at the plate center $(x = a/2, y = b/2)$ for square simply supported Kirchhoff plate resting on Winkler foundation for values

$$K = \left(\frac{ka^4}{D}\right)^{1/4} \quad (43)$$

equal $K = 0$, 1, 3, and 5 have been determined and presented in Table 1 for the case of uniformly distributed transverse load p_0 over the entire plate domain. Similarly, the Ritz variational solutions for the maximum deflection and maximum bending moments for square simply supported Kirchhoff plates resting on Winkler foundations for values of K equal to $K = 0$, 3, 5 and 7; for the case of sinusoidal load distribution over the plate domain have been determined and are shown in Table 2.

Table 1 – Ritz variational solution for deflection and bending moment coefficients for simply supported square Kirchhoff plate on Winkler foundation under transverse uniform load (for Poisson's ratio 0.3)

ka^4/D	K	w_{xx}, $\times 10^{-3} pa^4/D$	M_{xx}, $\times 10^{-2} pa^2$	M_{yy},· $\times 10^{-2} pa^2$	M_{xy}, $\times 10^{-2} pa^2$
0	0	4.062	4.790	4.790	–
1	1	4.053	4.809	4.809	2.943
81	3	3.348	3.910	3.910	2.456
625	5	1.507	1.575	1.575	1.181

Table 2 – Ritz variational solutions for maximum deflection and bending moment coefficients for simply supported square Kirchhoff plate on Winkler foundation under transverse sinusoidal load (for Poisson's ratio 0.3)

ka^4/D	K	w_{xx}, $\times 10^{-3} pa^4/D$	M_{xx}, $\times 10^{-2} pa^2$	M_{yy},· $\times 10^{-2} pa^2$	M_{xy}, $\times 10^{-2} pa^2$
0	0	2.566	3.293	3.293	1.797
1	1	2.560	3.285	3.285	1.792
81	3	2.125	2.726	2.726	1.487
625	5	0.986	1.265	1.265	0.069
2401	7	0.358	0.460	0.460	0.025

4 Discussion

The Ritz variational method has been effectively used in this study to solve the flexural problem of simply supported rectangular Kirchhoff plate resting on a Winkler foundation, when the plate domain is subjected to transversely distributed loads. The problem was presented in variational form using the principle of minimization of the total potential energy functional. The total potential energy functional was obtained using the stress-strain laws, the geometric relations in the strain energy density expression together with the considerations of work done by the externally applied distributed loads, and soil reactive forces. The total energy functional for the problem was obtained as Equation (28). The variational statement of the problem was then expressed as Equation (29). The displacement shape functions that satisfy the simply supported conditions at the plate edges were given as Equations (38) and (39). The Ritz variational solution obtained for any arbitrary distribution of transverse load was given as Equaton (52) where the arbitrary load distribution could be described using Fourier sine series. The bending and twisting moments were found using the moment curvature relations as Equations (57), (58) and (59). From the general solutions obtained for arbitrary load distributions, solutions were obtained for the following specific cases:

1) point load P_0 acting at a point (x_0, y_0) in the plate domain where $0 \le x_0 \le a$, $0 \le y_0 \le b$;

2) sinusoidal load distribution over the entire plate surface;

3) uniform load distribution over the entire plate area;

4) hydrostatic (linear) distribution of load over the entire plate.

Ritz variational solutions obtained for the deflections and bending moments for the case of point load P_0 acting at point (x_0, y_0) on the plate are given as equations (23). Their maximum values for square thin plates on Winkler foundations were obtained as equations (24) and (25).

For the case of transverse sinusoidal load, the deflections and bending moments were obtained as equations (26). Their maximum values for square Kirchhoff plates on Winkler foundations were found at the plate center as equations (27), (28) and (29).

The Ritz variational solution for the case of uniformly distributed transverse load were found for deflection and bending moments as equations (31) and (32). The maximum values for deflection and bending moments for square Kirchhoff plate on Winkler foundation were found as equations (31), (33) and (34).

The Ritz variational solutions for linearly distributed transverse load on the Kirchhoff plate on Winkler foundation were obtained as equations (38) and (40). The deflections and bending moments were obtained at the plate center as equations (39) and (41). For square Kirchhoff plate on Winkler foundation, the solutions for linear loads are Equations (42). Here the maximum values may not occur at the plate center due to the non-symmetrical load distribution with respect to the plate center.

The Ritz variational solutions obtained for square Kirchhoff plate on Winkler foundation for the case of uniform transverse load and simply supported edges shown tabulated in Table 1 for various values of the dimensionless parameter K show that the maximum deflections and bending and twisting moments at the plate center decrease as the elastic stiffness of the Winkler foundation, measured by parameter K increases. It is further observed that the Ritz variational solutions obtained in this study for Kirchhoff plate on Winkler foundation with simply supported edges ($x = 0$, $x = a$, $y = 0$, $y = b$) yielded mathematical closed form solutions which were identical with the solutions obtained using a Navier double Fourier sine series method for the problem.

5 Conclusions

As a result of the presented research, the following conclusions are made.

The Ritz variational method yielded mathematically closed form solutions for the deflection, and bending moments for the rectangular Kirchhoff plate on Winkler foundation with simply supported edges, and under transverse distributed load.

The analytical closed form solutions obtained were exact within the limitations and foundational assumptions of the classical Kirchhoff thin plate theory and the Winkler foundation model used in the problem formulation.

The Ritz variational solutions were exactly identical with the solutions obtained using Navier trigonometric series method for the same problem.

The Ritz variational solutions obtained were exact because exact shape functions were used in the displacement trial function.

The Winkler foundation has the effect of diminishing the maximum deflections and bending moments at the center of the plate for symmetrical loads about the plate center.

The use of displacement functions with orthogonality properties simplified the resulting definite integrations and simplified the process of minimization of the total potential energy functional.

Convergence of the expressions obtained for the displacements were faster than those obtained for the bending moments.

Convergence of the expressions obtained for the case of concentrated load on the plate was very slow due to the singularity property of the point load, and its representation by many terms of the Fourier sine series.

References

1. Reissner, E. (1944). On the theory of bending of elastic plates. *Journal of Mathematics and Physics*, Vol. 23, pp 184–191.
2. Reissner, E. (1945). The effect of shear deformation on the bending of elastic plates. *Journal of Applied Mechanics*, Vol. 12, pp 69–75.
3. Mindlin, R. D. (1951). Influence of rotary inertia on flexural motion of isotropic, elastic plates. *Journal of Applied Mechanics*, Vol 18(1), pp. 31–38.
4. Shimpi, R. P. (2002). Refined plate theory and its variants. *AIAA Journal*, Vol. 40, pp 137–146.
5. Reddy, J. N. (1984). A refined non linear theory of plates with transverse shear deformation. *International Journal of Solids and Structures*, Vol. 20, pp. 881–896.
6. Mama, B. O., Ike, C. C., Onah, H. N., & Nwoji, C. U. (2017) Analysis of rectangular Kirchhoff plate on Winkler foundation using finite Fourier sine transform method. *IOSR Journal of Mathematics*, Vol. 13(1), pp 58–66, doi: 10.9790/5728-1301065866.
7. Caselunghe, A., & Eriksson, J. (2012). *Structural Element Approaches for Soil Structure Interaction*. MSc thesis, Chalmer University of Technology, Goteborg, Sweden.
8. Rajpurohit, V. K., Gore, N. G., & Sayagavi, V. G. (2014). Analysis of structures supported on elastic foundations. *International Journal of Engineering and Technology*, Vol. 4(1), pp. 1–6.
9. Ghaitani, M. M., Esmaieili, H. A., & Kolahchi, R. (2014). Elastic foundation effect on bending behavior of oil pipelines. *International Conference on Civil, Biological and Environmental Engineering*, Istanbul, Turkey, pp. 36–39.
10. Winkler, E. (1867). *Lehre vouder elastizitat und festigkeit*. Dominicus, Prague.
11. Pasternak, P. L. (1954). On a new method of analysis of an elastic foundation by means of two foundation constants. State Publishing House, Moscow [in Russian].
12. Filonenko-Borodich, M. M. (1945). A very simple model of an elastic foundation capable of spreading the load. *Proceeding of the Moscow Electronic Institure*, Moscow, Russia.
13. Hetenyi, M. (1946). *Beams on Elastic Foundation: Theory with Applications in the fields of Civil and Mechanical Engineering*. The University of Michigan Press, Ann Arbor, Michigan.
14. Kerr, A. D (1964). Elastic and visco-elastic foundation models. *Journal of Applied Mechanics*, Vol. 31, pp. 491–498.
15. Ike, C. C. (2017). Flexural analysis of Kirchhoff plates on Winkler foundations using finite Fourier sine integral transform method. *Mathematical Modelling of Engineering Problems*, Vol. 4(4), pp. 145–154, doi: 10.18280/mmep.040402.
16. Althobaiti S, Prikazchikov D.A. (2016). Edge bending waves on an orthotropic elastic plate resting on the Winkler–Fuss foundation. Vol. 69(1), pp. 16–24.
17. Zhong, Y., Zhao, X.–F., & Hu, H. (2014). Vibration of plate on foundation with four edges free by finite cosine integral transform method. *Latin American Journal of Solids and Structures*, Vol. 11(5), pp. 854–863.
18. Li, R., Zhong, Y., & Li, M. L. (2013). Analytic bending solutions of free rectangular thin plates resting on elastic foundations by a new symplectic superposition method. *Proceedings of the Royal Society*, Vol. 46, pp. 468–474.
19. Li, R., Zhong, Y., & Tian, B. (2011). On new symplectic superposition method for exact bending solutions of rectangular cantilever thin plates. *Mechanics Research Communications*, Vol. 38, pp 111–116.
20. Li, R., Zhong, Y., Tian, B., & Lin, Y. M. (2009). On the finite integral transform method for exact bending solutions of fully clamped orthotropic rectangular thin plates. *Applied Mathematics Letters*, Vol. 22(12), pp. 1821–1827.
21. Zhang, H., Shi, O. H., & Wang, Q. S. (2016). Free vibration analysis of the moderately thick laminated composite rectangular plate on two-parameter elastic foundation with elastic boundary conditions. *ASRTU Symposium on Advanced Materials and Processing Technology*, Vol. 2016, pp. 189–192, doi: 10.18502/kms.vi/1.584.
22. Agarana, M. C., Gbadeyan, J. A., & Ajayi, O. O. (2016). Dynamic response of inclined isotropic elastic clamped rectangular Mindlin plate resting on Pasternak foundation under a moving load. *Proceedings of the International Multiconference of Engineers and Computer Scientists, IMECS 2016*, Vol II, pp. 1–6.
23. Are E.B., Idowu A.S, Gbadeyin J.A (2013). Vibrations of damped simply supported orthotropic plate resting on elastic Winkler's foundation subjected to moving loads. Advances in Applied Science Research Vol 4, No 5, pp. 387 – 393.
24. Agarana, M. C., & Gbadeyan, J. A. (2015). Finite difference dynamic analysis of railway bridges supported by Pasternak foundation under uniform partially distributed moving railway vehicle. *International Conference on Systems Engineering and Engineering Management, WCECS 2015*, Vol. II, pp. 1–5.

25. Tahouneh, V., & Yas, M. H. (2012). 3D free vibration analysis of thick functionally graded annular sector plates on Pasternak foundation via 2-D differential quadrature method. *Acta Mechanica*, Vol. 223(9), pp. 1879–1897.
26. Ye, T., Jin, G., Su, Z., & Chen, Y. (2014). A modified Fourier solution for vibration analysis of moderately thick laminated plate with general boundary restraints. *International Journal of Mechanical Sciences*, Vol. 80, pp 29–46.

Застосування варіаційного методу Рітца для дослідження вигину прямокутної пластини на вінклеровій основі

Іке Ч. Ч.

Державний університет науки і технології м. Енугу , П.М.Б. 01660, м. Енугу, Нігерія

Анотація. У роботі застосовано варіаційний метод Рітца до роз'язання задачі вигину прямокутної пластини на вінклеровій основі під дією поперечного навантаження за умов відповідності гіпотезам Кірхгофа для випадку шарнірно закріплених країв. Поставлена задача представлена у варіаційній формі із застосуванням принципу мінімуму функціонала повної потенціальної енергії пластини. Для отримання узагальнених переміщення застосовано метод Рітца для функцій переміщення, що задовольняють кінематичні граничні умови задачі. Шляхом застосування тригонометричного ряду Фур'є отримані аналітичні розв'язки для загального випадку довільно розподіленого навантаження. Додатково розглянуто окремі випадки, зокрема, для прикладення сили у точці, навантаження за синусоїдальним законом розподілу, а також для рівномірного та рівнозмінного навантажень.

Ключові слова: варіаційний метод Рітца, гіпотеза Кірхгофа, вінклерова основа, функціонал повної потенціальної енергії, узагальнені переміщення, базисні функції переміщення.

JOURNAL OF ENGINEERING SCIENCES
ЖУРНАЛ ІНЖЕНЕРНИХ НАУК
ЖУРНАЛ ИНЖЕНЕРНЫХ НАУК
Web site: http://jes.sumdu.edu.ua
DOI: 10.21272/jes.2019.6(1).d3 Volume 6, Issue 1 (2019)

UDC 539.41

Computer-Aided Design of Prophylactic Metal Reinforcement of the Proximal Femur

Savielieva O.[1], Starushkevych T.[2], Matveev, A.[3]

[1] South Ukrainian National Pedagogical University named after K. D. Ushynsky,
26 Staroportofrankivska St., 65020 Odessa, Ukraine;
[2] Odessa National Polytechnic University, 1 Shevchenka Av., 65044 Odessa, Ukraine;
[3] Novokujbyshevsk City Central Hospital, 32 Ostrovskogo St., 446206, Novokujbyshevsk, Russia

Article info:
Paper received: November 25, 2018
The final version of the paper received: January 31, 2019
Paper accepted online: February 5, 2019

***Corresponding Author's Address:**
kupimnebarbie@gmail.com

Abstract. Hip fractures are among the most dangerous fractures, because they are quite common in older people and are difficult to treat. Based on the general opinion, the most effective tactic is surgical treatment, but its results against the background of osteoporosis are not satisfactory. Reducing the likelihood of hip fractures is a complex problem that can only be solved by combining the idea of medical science and mechanical research of a deformable solid. In this paper, the calculation of stresses arising from exposure to the reinforced femur neck of various loads is considered. At the current stage of the study, calculations of the stress–strain state corresponding to the loads at the moment of impact when a person falls on the thigh are carried out. Comparison of the values of withstanding stresses indicates the utility of using the considered implants, which in consequence will reduce the likelihood of a hip fracture. Using reinforcing metal structures in the bone has led to increasing of the highest extremes by about 140%, which confirms the utility of their use. Thus, pre–reinforcement of the femoral neck in elderly people at risk reduces the likelihood of fracture due to the reduction of critical stresses in hazardous areas.

Keywords: numerical simulation, femur neck, mathematical modeling, deflected mode.

1 Introduction

Three-dimensional modeling allows obtaining the necessary information to study the mechanical compatibility of the implant with the bone, which determines the ability of body systems to adapt and function correctly in a new biotechnical system. By analyzing the loads, it is possible to calculate whether the design of the implant, its material and placement in the bone are successful.

The relevance of the topic is to use three–dimensional models of original designs of implants and prostheses in studying the effect of these structures on the strength of the femur.

The aim of the work is to develop various types of implants and to study, with the help of stress simulation, their effect on the resistance of the proximal femur.

The tasks of the work are to develop three-dimensional models of new implants, create three-dimensional models of various "bone – implant" systems, simulate the loads for each system, analyze the results and draw a conclusion on the use of implants.

2 Literature Review

Among all the fractures of the lower extremity, one of the leading places is occupied by fractures of the proximal femur, which lead to hypostatic functional disorders, "sliding" syndrome of state decompensation and high mortality (41–67 %) [1].

Fractures of the proximal femur are pathological fractures, as they are a consequence of the structural failure of the bone in osteoporosis, much less often in tumors accompanied by dystrophic and dysplastic processes in the bones [2, 3].

From 75 % to 90 % of persons with abnormal bone fractures due to osteoporosis are not examined, and are not treated by specific pharmacotherapy after low-energy bone fractures of different localizations [4].

The occurrence of pathological fractures of the proximal femur and femoral neck in older individuals remains an unsolved problem, which is associated with the structural failure of the bone in degenerative–dystrophic skeletal diseases. So far, the treatment of osteoporosis in the elderly has not been developed, which could actually prevent the occurrence of pathological fractures [5]. The weakening of the bone tissue to critical values is an indication for the prophylactic use of fixers in certain parts of the skeleton [6–8]. The method of femoral neck prophylactic reinforcement in endoprosthetics of the contralateral limb reduces the risk of new femoral neck fractures in the elderly. Prevention of contralateral fractures significantly reduces the cost of treating patients. In elderly with fractures, prophylactic reinforcement is shown from the opposite side, which undoubtedly requires a deeper study of the long–term effects [9, 10]. To solve the above problems, the method of metal structures preventive implantation – preventive reinforcement – is successfully used in many countries [11–14].

3 Research Methodology

3.1 The bone creating

The task of holding prophylactic reinforcement is the need to strengthen specifically the femoral neck, while increasing its strength due to reinforcing metal structures. The blood circulation of the proximal, cervical and femoral head is such that when fractures of the cervix take place, a very serious impairment of blood circulation occurs, which ultimately leads to destruction, and, consequently, to aseptic necrosis – death – to the femoral head. This forces the traumatologist - orthopedic surgeon to carry out endoprosthetic replacement of the entire hip joint. For many old people, this becomes a death sentence, since 50 % of these patients die in the first year after the injury. The idea of reinforcing the femoral neck is aimed at preserving it and, most importantly, preserving the life of the patient. The complex geometric structure of the bone requires sufficiently accurate measurements to build a computer model. In order to bring the calculations and construction of implants for the required level of detail, it was decided to build a bone model by extracting a three-dimensional model from a computed tomography image and transforming, using polygonal modeling, into a model that is convenient to work with.

3.2 The implant creating

Four types of the implants have been patented and designed for the reinforcement of biological composite material and prevention of femoral neck fractures in patients who belong to risk groups. Telescopic implants are presented in corkscrew and auger versions (Figure 1). Spoke implants are presented in the version with diverging spokes and in the version with crossed ones (Figure 2). Endoprostheses are presented in the version with a needle and in the version with a plate (Figure 3). Also two simple version of the implants were considered – only the spoke – auger and only the spoke – corkscrew (Figure 4). The objective of these implants is to minimize the likelihood of fracture not only of the cervix, but also of the vertical region of the femur, primarily in elderly patients who suffer from destructive – degenerative diseases of the bone tissue. This task is solved by introducing the implant in the unaffected proximal femur to increase its strength.

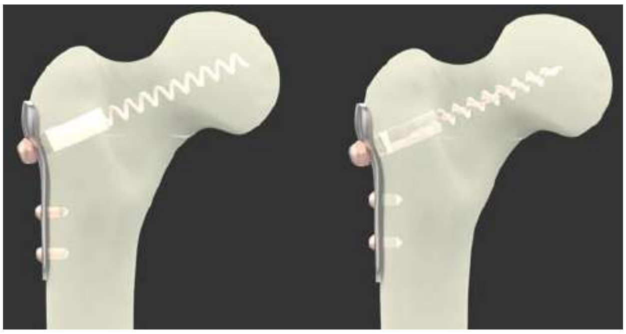

Figure 1 – Image of the bone-implant system with telescopic implants

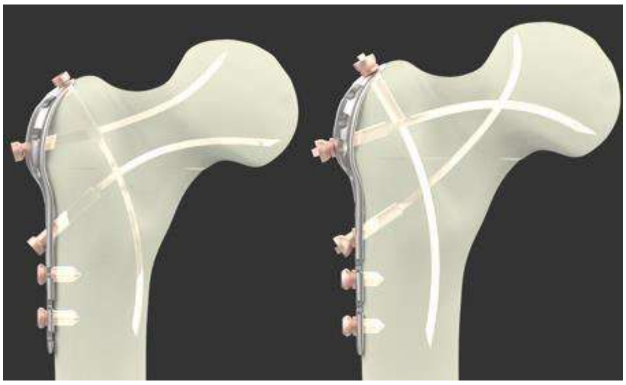

Figure 2 – Image of the bone-implant system with spoke implants

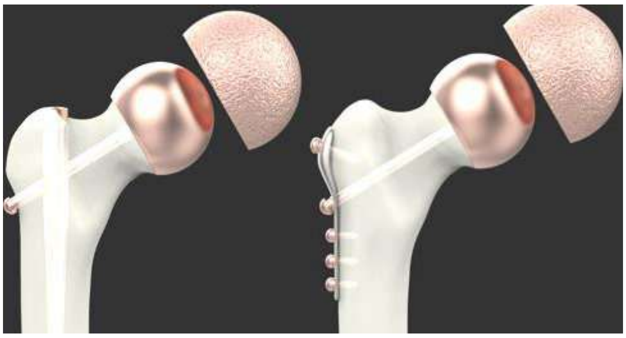

Figure 3 – Image of the bone-implant system with endoprostheses

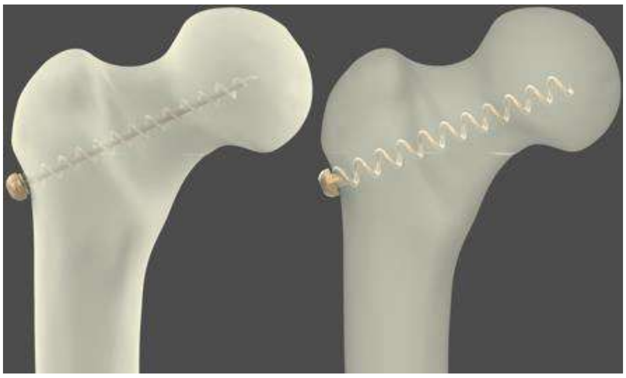

Figure 4 – Image of the system “bone – implant” with a spoke –auger and a spoke – corkscrew

Mathematical modeling of stress conditions. The study of stressed sections of elastic deformation arising under the load of intact and reinforced bone is carried out using the finite element method and by means of mathematical modeling.

For mathematical modeling of stress conditions, the following types of loads were selected (Figure 5): vertical (fixation of the knee joint, application of load vertically to the head of the femur), horizontal (fixation of the knee joint and large trochanter, application of loads horizontally to the head of the femur) and rotational (fixation of the femoral head bones, application of torque to the diaphysis part of the bone).It is these states that most clearly demonstrate the imitation of actions leading to a fracture of the femoral neck.

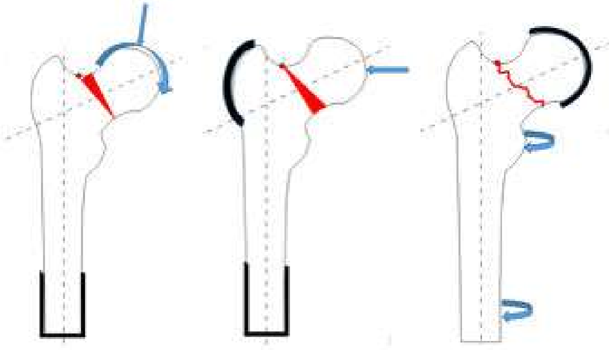

Figure 5 –The purpose of the areas of fixation and application of the load: vertical, horizontal and rotational

As a load application, a force of 700 N was chosen, which is equal to an action of 70 kg.

Physical indicators of materials used in the calculations of stress conditions are presented in Table 1.

Mathematical modeling of stress states was carried out in the Ansys Workbench software package. In each of the studies, according to the above situations of loads, the area of fixation and application of loads is indicated, as the strength of the load, and the simulation of stress states is carried out.

4 Results

The results of mathematical modeling are noted in Table 2.

As can be seen from the table of results, when metal structures are used in prophylactic reinforcement, the maximum load increases, which implies that the reinforced bone can withstand the effects of a fall, saving the patient from a hip fracture. This proves that reinforcement has a positive effect on increasing the strength characteristics of the bone and leads to its preservation from destruction under critical loads. Through the use of reinforcing steel, reduced stress – deformed condition of the bone.

Table 1 – Physical and mathematical indicators of materials

Material	Density, kg/m^3	Young's modulus, GPa	Poisson's ratio	Tensile strength limit, MPa	Compressive strength limit, MPa
Bone	1 750	16.7	0.31	43.44	115.3
Ti-6Al-4V	4 500	120.0	0.32	993.0	1 086.0

Table 2 – Physical and mathematical indicators of materials

Implant type	Vertical, % (MPa)	Horizontal, %, (MPa)	Rotational, % (MPa)
Bone	100.0 (16.5)	100.0 (2.8)	100.0 (0.5)
Telescopic corkscrew	162.4 (26.8)	164.2 (4.6)	196.3 (0.98)
Telescopic auger	153.3 (25.3)	159.2 (4.5)	184.1 (0.92)
Corkscrew	107.9 (17.8)	110.2 (3.1)	140.0 (0.73)
Auger	107.5 (17.7)	128.4 (3.5)	128.0 (0.64)
Cross spokes	120.1 (19.8)	126.7 (3.4)	122.2 (1.61)
Diverging needles	117.6 (19.4)	119.2 (3.3)	124.2 (0.62)
Kernel	129.7 (21.4)	182.1 (5.1)	150.0 (0.8)
Plate	112.1 (18.5)	175.1 (4.9)	148.2 (0.74)

5 Conclusions

With the help of mathematical modeling of stress states, the useful effect of using the original developed reinforcing metal structures was proved.

Consequently, this theoretical study can serve as a justification from the position of the mechanics of a deformable solid body with the method of hip fractures prevention due to preliminary, prophylactic, reinforcement.

In the future, as a result of the repeated positive result of the stresses in the "bone-implant" system calculation, experimental models will be produced, which will undergo bench tests. If, as a result of tests, the usefulness of the application of these metal structures is confirmed, they will be used for preventive reinforcement.

The task of the follow-up study is to prove the practicality of reinforcing the material of the bone tissue of the femoral neck in the elderly at risk. These studies are necessary because this procedure reduces the likelihood of fracture, due to the reduction of critical stresses in hazardous areas by transferring part of the load to the reinforcement element.

References

1. Lazarev, A. (2012). Operative treatment of the proximal femur fractures. *VIII Congress of Traumatologists-Orthopedists of Uzbekistan "Actual Questions of Traumatology and Orthopedics"*, pp. 153–154.
2. Zorya, V. (2016). Treatment and prevention of fractures of the femoral neck in elderly and senile patients. *Organizational and Clinical Issues of Rendering Assistance to Patients in Traumatology and Orthopedics*, pp. 34–36.
3. Matveev, A. (2008). *Operative way of prevention of femoral neck fractures*. Patent No. 2316280, Russian Federation, IPC 7 A61B 17/56, applicant and patent owner: Matveev, A. L., No. 2006114271/14; claimed 26.04.2006; published 10.02.2008, bulletin No. 4.
4. Kotelnikov, G., Bulgakova, S., & Shafieva, I. (2012). Evaluation of the effectiveness of a set of measures for the prevention of fractures - markers of osteoporosis in elderly women. *V Conference with international participation "The problem of Osteoporosis in Traumatology and Orthopedics"*, pp. 72–73.
5. Kochish, A., Ivanov, S., & Sannikova, E. (2013). Comparative analysis of adherence to the diagnosis and treatment of osteoporosis in patients with low-energy fractures. *V Russian Congress on Osteoporosis and Other Metabolic Skeletal Diseases*, pp. 45–50.
6. Povoroznyuk, V. (2005). Osteoporosis – The Problem of the XXI Century. *The Art of Treatment*.
7. Faucett, S., Genuario, J., Tosteson, A., & Koval, K. (2010). Is Prophylactic Fixation a Cost-Effective Method to Prevent a Future Contralateral Fragility Hip Fracture? *Journal of Orthopedic Trauma*, pp. 65–74.
8. Dimitrienko, Yu. (2011). Modelling of Mechanical Properties of Composite of 3D orthogonal woven composites. *Composites Science and Technology*, Vol. 71, pp. 1777–1788.
9. Zacherl, M., Gruber, G., Glehr, M., Ofner, P., Radl, R., Greithbauer, M., Vecsei, V., & Windhager R. (2011). Surgery for pathological proximal femoral fractures, excluding femoral head and neck fractures. Resection vs. Stabilization. *Department of Orthopedic Surgery, Medical University Graz (SICOT), Austria*, pp. 1537–1543.
10. Tonkonogiy, V., Savel'eva, O.,& Bets, A. (2012). Information technology in education, science and production. *Collection of Scientific Works, Bakhava JSC*, Vol. 1(2), pp.182–188.
11. Kanis, J., Burlet, N., & Cooper C. (2008). European guidance for the diagnosis and management of osteoporosis in postmenopausal women. *Osteoporos Int*.
12. Kucher, N., Zemtsov, M., & Zarazovsky, M. (2006). Deformation of layered epoxy composites reinforced with high-strength fibers. *Problems of Strength*, pp. 41–57.
13. Nekhozhin, A. (2013). Bilayer mathematical model of human femur neck for the stress state research after reinforcement with different designs of implants. *Herald of the Samara State Technical University*, Vol. 3(32), pp. 129–135.
14. Savelieva, O., Prokopovich, I., Pavlyshko, A., Matveev, A., & Starushkevych T. (2018). Computer modeling of implant for femur reinforcement. *Proceedings of Odessa Polytechnic University*, Vol. 1(54), pp. 51–61.

Комп'ютерне проектування профілактичного зміцнення армованої шийки проксимальної стегнової кістки

Савельєва О.[1], Старушкевич Т.[2], Матвєєв А.[3]

[1] Південноукраїнський національний педагогічний університет ім. К. Д. Ушинського,
вул. Старопортофранківська, 26, 65020, м. Одеса, Україна;
[2] Одеський національний політехнічний університет, просп. Шевченка, 1, 65044, м. Одеса, Україна;
[3] Новокуйбишевський міський центральний госпіталь, вул. Островського, 32, 446206, м. Новокуйбишевськ, Росія

Анотація. Перелом стегна є одним з найнебезпечніших переломів, оскільки він є достатньо поширеним у літніх людей та важко піддається лікуванню. З огляду на загальноприйняту практику, найбільш ефективним способом лікування є хірургічне втручання, але його результати на тлі остеопорозу не є задовільними. Зменшення імовірності переломів стегна є складним завданням, яке може бути вирішене лише шляхом об'єднання медицини і досліджень механіки деформованого твердого тіла. У цій роботі розглянуто розрахунок напружень, що виникають від впливу армованої шийки стегнової кістки під дією різних навантажень. На сучасному етапі дослідження проводяться розрахунки напружено-деформованого стану, що відповідають навантаженням від удару при падінні людини на стегно. Порівняння значень напружень свідчить про надійність використання розглянутих імплантатів, що у результаті зменшує імовірність перелому стегна. Використання армуючих металевих конструкцій у кістковій тканині призвело до збільшення найбільших допустимих значень приблизно на 140 %, що підтверджує практичну цінність їх застосування. Таким чином, попереднє зміцнення шийки стегнової кістки у людей похилого віку знижує імовірність руйнування унаслідок зменшення граничних напружень у небезпечних зонах.

Ключові слова: комп'ютерне моделювання, шийка стегна, числове моделювання, напружено-деформівний стан.

JOURNAL OF ENGINEERING SCIENCES
ЖУРНАЛ ІНЖЕНЕРНИХ НАУК
ЖУРНАЛ ИНЖЕНЕРНЫХ НАУК
Web site: http://jes.sumdu.edu.ua
DOI: 10.21272/jes.2019.6(1).e1 Volume 6, Issue 1 (2019)

UDC 66.045.122

Numerical Investigation of the Concave-Cut Baffles Effect in Shell-and-Tube Heat Exchanger

Petinrin M. O.*, Dare A. A.

University of Ibadan, Oduduwa Rd, 200284 Ibadan, Oyo State, Nigeria

Article info:

Paper received:	August 5, 2018
The final version of the paper received:	December 24, 2018
Paper accepted online:	December 29, 2018

***Corresponding Author's Address:**
layopet01@yahoo.com

Abstract. In this paper, the performance of shell-and-tube heat exchangers with single-segmental baffle and varying configurations of concave-cut baffles (10, 15 and 20 %) was investigated. The study was carried out for a heat exchanger having either engine oil, water and air as shell-side fluid. For each configuration of the baffles, the results of both the the k-ε and RNG k-ε turbulent models were in very close agreement. The heat exchangers with concave-cut baffles had higher pressure drops and lower performance factors than that of single-segmental baffle at the same range of mass flow rates for all fluid cases. Also, the concave-cut baffle heat exchangers had lower shell-side heat transfer coefficients at the same pressure drop against that of single-segmental baffles. Thus, the use of concave-cut baffles did not exhibit desirable performance in heat exchanger as compared with the segmental baffles.

Keywords: shell-and-tube heat exchanger, pressure drop, weighted performance factor, weighted heat transfer coefficient, concave-cut baffle.

1 Introduction

Heat exchanger is a device which transfers thermal energy between fluids at significantly different temperatures [1]. They are widely used for engineering applications in industries, such as in chemical, petroleum, HVAC, auto and aerospace, electronics, power generation and process industries [2, 3]. The most used and widespread type of heat exchangers found in these industries are the shell-and-tube types. The high level of acceptance of shell-and-tube heat exchanger (STHE) is due to its robustness and versatile materials used in construction, ease of maintenance and very wide range of operating conditions [4–7].

The thermal-hydraulic performance of a heat exchanger has significant effect on energy requirement and efficiency of a system. Thus, an optimally balanced thermal-hydraulic design is required but most often attempting to enhance the heat transfer within a heat exchanger raise its pressure drop, which results in increase power demand of fluid handling equipment within the system [2, 3]. Heat transfer enhancement can be achieved through insertion of baffles on the shell-side of STHE [8]. The baffles increase the flow turbulence by creating tortuous motion of the fluid for better interaction with the tube surface. Hence, the geometrical shapes and forms of baffles affect greatly the overall performance of STHEs [9]. The various baffle designs used in heat exchangers are not limited to segmental, helical, trefoil-hole, disc-and-donought, and rod baffles.

Zhou et al. [10] numerically studied on the improvement of the shell-side heat transfer with trefoil-hole baffles. They observed a longitudinal flow of the fluid and also noticed that the multidirectional jets and secondary flow on the sides of the baffles enhanced the heat transfer rate. Wang et al. [11] performed periodic simulation of shell-side heat transfer of STHE with longitudinal flow using rod baffles as supporting structure. Their results were well correlated with experimental data. The research [12] dials with the thermo-hydraulic performance of a STHE with trefoil-hole baffles with a turbulent flow regime. Their experimental results showed that there was a considerable high heat transfer enhancement with substantially increased pressure drop using the trefoil-hole baffles as compared with STHE without baffle. It was discovered from their numerical results that the very high thermal performance was as a result of the high speed recirculation flow and high level of turbulence intensity created by trefoil-hole baffles. Ozden and Tari [13] used three turbulent models to investigate a heat exchanger with single-segmental baffles considering the baffle spacing to shell diameter ratio for two baffle cuts (25 and 36 %). Their results were in good agreement with the Bell-Delaware method; and the 25 % baffle-cut heat exchanger had better thermal-hydraulic performance.

The conventional single-segmental baffles are commonly used in heat exchangers for their high heat transfer capability. Although, some other baffle designs have been reportedly proved to have lower shell-side pressure drops as compared with the single-segmental baffle but their overall performance are reduced by their heat transfer rate [14, 15]. The baffle cut and spacing of single-segmental baffles have much effect on the heat exchanger performance. The optimum baffle spacing ratio, which is the baffle spacing to shell inside diameter, recommended is between 0.3 and 0.6, while the baffle cut ranges from 15 to 45 % of the baffle diameter [16, 17]. As shown in Figure 1, the baffle cut creates a segment known as baffle window, which allows the passage of shell-side fluid from one shell zone to another within the heat exchanger. However, Bouhairie [18] reported that the optimum and widely used allowance is the 25 %.

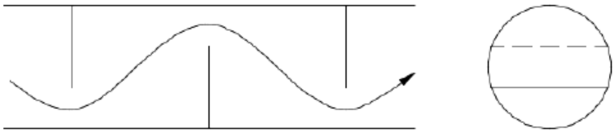

Figure 1 – Schematic representation of flow inside shell-and-tube heat exchanger

Jozaei et al. [19] studied the performance of a heat exchanger with varying baffle spacings (101.6, 203.2, 304.8, 406.4, 508.0 and 609.6 mm) and shell inside diameter of 477.8 mm. It was observed that there was a reduction in the overall heat transfer coefficient and pressure drop as the baffle spacing increased. The optimum ratio of the overall heat transfer coefficient to pressure drop was found between baffle spacing of 203.2 and 304.8 mm, which are ranged between 0.43 and 0.64 of shell inside diameter. Prasanna et al. [20] numerically investigated the effect of 25 and 36 % baffle cuts on the performance of heat exchangers with varying number of baffles from 6 to 12. It was reported that the STHE with 25 % baffle cut had higher heat transfer coefficient and pressure drop than STHE with 36 % baffle cut for the range of shell inlet flow rate of 0.5 to 2 kg/s considered.

Even though quite number of studies have been conducted on the performance of various baffle designs and cuts in heat exchanger, studies are rare in open references on the effects of modifying the shape of baffle window. Thus in this study, a numerical investigation of thermal-hydraulic performance of STHEs with the 25 % cut single-segmental baffle (SS_STHE) and three configurations of concave-cut baffle (CaC_STHE) will be carried out for the same area of baffle window.

2 Research Methodology

2.1 Geometrical model

The profile of the concave-cut baffle was generated by fixing a value for either height, *h* or profile radius, *R* and determining the other from iteration while maintaining the same segment or window area as the 25 % cut single-segmental baffle (Figure 2). In order to get the concave profile on the baffle, the start out height, *h* was kept lower than the segment height, *H* of the single-segmental baffle. Therefore, based on the ratio of *h* to the baffle diameter, the configurations of the concave-cut baffles and other selected parameters for modelling the shell-and-tube heat exchanger are presented in Table 1.

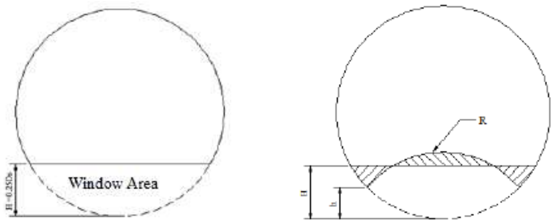

a b

Figure 2 – The configurations of a single-segmental (a) and concave-cut (b) baffles

Table 1 – Geometrical parameters of the shell-and-tube heat exchanger

Parameter		Value
Shell diameter		108.06 mm
Shell duct diameter		30.00 mm
Baffle type	Segmental	25 %
	Concave-cut	10, 15 and 20 %
Baffle spacing		43.26 mm
Baffle number		6
Heat exchanger length		302.58 mm
Tube layout		Triangular (30°)
Tube diameter		15.88 mm
Tube number		19
Tube pitch ratio		1.25

The shell-side working fluids were engine oil, water and air for each run of the heat exchanger while water was kept in the tube. The thermophysical properties of the fluids were as obtained in literature [21, 22].

2.2 The governing equations and numerical methods

Two turbulent models (k-ε and RNG k-ε) were adopted for the simulation of the heat exchanger models. The k-ε model was selected for its robustness and wide application areas [23] while the RNG k-ε model was chosen for its highly swirling characteristics on the shell-side [10]. Thus in tensor form, the governing equations for modelling the fluid flow and heat transfer within the STHEs are the same for the two turbulent models and are given as follow [24, 25].

Continuity equation:

$$\frac{\partial\left(\bar{\rho}u_j\right)}{\partial x_j}=0 \tag{1}$$

Momentum equations:

$$\frac{\partial\left(\bar{\rho}u_j u_i\right)}{\partial x_j}=-\frac{\partial\bar{p}}{\partial x_i}+\frac{\partial}{\partial x_j} \tag{2}$$

$$\left[\left(\mu+\mu_T\right)\left(\left(\frac{\partial u_i}{\partial x_j}+\frac{\partial u_j}{\partial x_i}\right)-\frac{2}{3}\delta_{ij}\frac{\partial u_k}{\partial x_k}\right)-\frac{2}{3}\bar{\rho}k\delta_{ij}\right]$$

Energy equation:

$$\frac{\partial}{\partial x_j}\left(\bar{\rho}c_p T u_j\right)=\frac{\partial}{\partial x_j}\left(\left(\eta+\eta_T\right)\frac{\partial T}{\partial x_j}\right) \tag{3}$$

Turbulent kinetic energy:

$$\frac{\partial\left(\bar{\rho}k u_j\right)}{\partial x_j}= \tag{4}$$

$$\frac{\partial}{\partial x_j}\left[\left(\mu+\frac{\mu_T}{\sigma_k}\right)\frac{\partial k}{\partial x_j}\right]+P_k-\bar{\rho}\varepsilon$$

Turbulent dissipation energy:

$$\frac{\partial\left(\bar{\rho}\varepsilon u_j\right)}{\partial x_j}=\frac{\partial}{\partial x_j}\left[\left(\mu+\frac{\mu_T}{\sigma_\varepsilon}\right)\frac{\partial\varepsilon}{\partial x_j}\right] \tag{5}$$

$$+C_{\varepsilon 1}\frac{\varepsilon}{k}P_k-C_{\varepsilon 2}\rho\frac{\varepsilon^2}{k}$$

where the production term P_k from equations 4 and 5

$$P_k=\frac{\partial u_i}{\partial x_j}\left[\mu_T\left(\left(\frac{\partial u_i}{\partial x_j}+\frac{\partial u_j}{\partial x_i}\right)-\frac{2}{3}\delta_{ij}\frac{\partial u_k}{\partial x_k}\right)-\frac{2}{3}\bar{\rho}k\delta_{ij}\right] \tag{6}$$

The closure constants for the k-ε model are $C_{\varepsilon 1}=1.44$, $C_{\varepsilon 2}=1.92$, $C_\mu=0.09$, $\sigma_k=1.0$ and $\sigma_\varepsilon=1.3$. In the RNG k-ε model the $C_{\varepsilon 1}$ is modified as an auxiliary function, which is expressed as

$$C_{\varepsilon 1}=C^*_{\varepsilon 1}-\frac{\lambda\left(1-\lambda/\lambda_o\right)}{1+\beta\lambda^3} \tag{7}$$

with the following papameter:

$$\lambda=\frac{k}{\varepsilon}\sqrt{2S_{ij}S_{ij}} \tag{8}$$

Other constants are: $C^*_{\varepsilon 1}=1.42$, $C_{\varepsilon 2}=1.68$, $C_\mu=0.0845$, $\sigma_k=0.7194$, $\sigma_\varepsilon=0.7194$, $\lambda_o=4.38$ and $\beta=0.012$ [26].

At the inlets of the tubes and shell, velocity-inlet conditions were set based on the mass flow rates. The tube-side flow rate was 0.3 kg/s while it was ranged from 0.10 to 3.10 kg/s for engine oil and water, and 0.0025 to 0.0325 kg/s for air on shell-side. The tube- and shell-inlets temperatures were set at 303.15 and 373.15 K respectively (Figure 3).

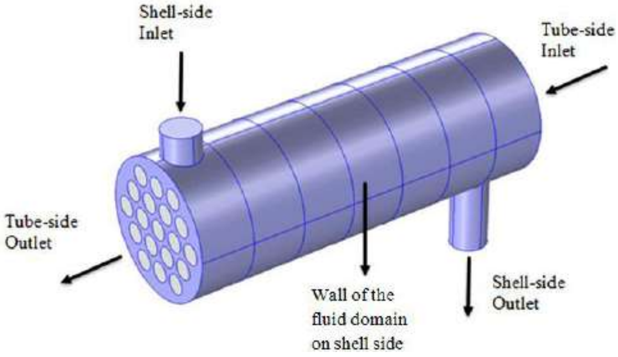

Figure 3 – Boundaries of the computational domain

In order to obtain the relative pressure drops between each inlet and outlet of the shell and tube, zero-gauge pressure was applied at each outlet. Wall functions were specified for walls of the tubes and shell, and baffle surfaces to account for viscous effects. By assuming a well-insulated heat exchanger, zero heat flux was imposed on the shell outer surface.

Each of the computational domains was discretised into unstructured tetrahedral elements and the sets of the governing equations were solved using a finite element based COMSOL Multiphysics CFD code. However, solutions to the RNG k-ε model were obtained by replacing the default constants of the k-ε model with the closure constants and auxiliary function of the RNG k-ε model. To improve on the accuracy and stability of the computation, the streamline-upwind Petrov-Galerkin and Galerkin Least-Square were employed [27–29]. Solutions to dependent variables were obtained using three segregated solvers: One GMRES solver for velocity and pressure, another one for temperature and one MUMPS solver for turbulent kinetic energy and rate of dissipation [30].

2.3 Heat exchanger performance

The thermal-hydraulic performance of the CaC_STHE was measured against the SS_STHE using two criteria. In the first criterion, the performance was calculated by dividing the shell gain factor of the CaC_STHE against that of SS_STHE at the same Reynolds number or mass flow rate. This factor was defined by Mohammadi et al. [31] as the ratio of the shell-side heat transfer coefficient against the shell-side pressure drop. Thus, the shell gain ratio of a value greater than one would indicate a more suitable concave-cut baffle than single-segmental baffle in heat exchanger and if on the contrary, the single-segmental baffle would be better. Using the second criterion, the performance was evaluated by determining the equivalent shell-side heat transfer coefficient of each heat exchanger at the same pressure drop with SS_STHE [8,32]. Thus, the weighted performance of each CaC_STHE against SS_STHE for the same ranges of Reynolds numbers or pressure drops as applied to any of the two criteria was calculated as

$$WP=\frac{1}{N}\sum_{N=1}^{N}\frac{P_{CaC}-P_{SS}}{\left(P_{CaC}+P_{SS}\right)/2} \tag{9}$$

where P is the performance factor or the equivalent shell-side heat transfer coefficient for the first or second criterion, respectively. Also the WP is actually the weighted performance factor (WPF) or weighted shell-side heat transfer coefficient (WSHTC) as it is applicable.

3 Results and Discussion

3.1 Model validation

This numerical model was validated by running a simulation of shell-and-tube heat exchanger with horizontal baffles using the experimental data for segmental baffle heat exchanger in [33]. The comparison between the experimental and numerical results for the average Nusselt number and pressure drop in the shell-side are as presented in Figures 4 and 5. It can be observed that the variations of the numerical results are in good agreement with that of the experiment. The average difference between the experimental and numerical results for Nusselt number and pressure drop are 11 and 26 % respectively. The observed discrepancies may be as a result of the model simplification such as no-leakage flow, and some unavoidable measurement errors.

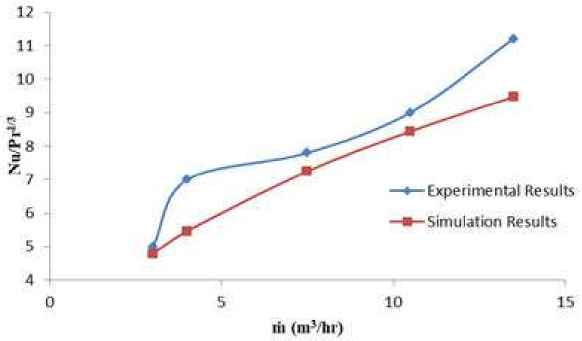

Figure 4 – Comparison of Nusselt number of the experimental and simulation results

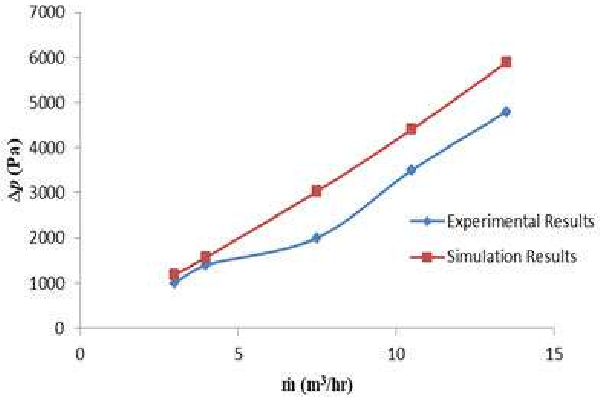

Figure 5 – Comparison of pressure drop of the experimental and simulation results

3.2 Shell-side flow field

The flow path lines of water at 3.10 kg/s on the shell-sides of the heat exchangers are shown in Fig. 6. It can be observed that the shape of the baffles affects the rambling of the fluid from shell-inlet duct to the outlet duct. The flow in CaC_STHE is more concentrated at the centre of the baffle cut than that of SS_STHE, which spreads over the baffle cut. Also, the fluid velocity is reduced within the shell because of the larger flow area than the shell ducts. The combined fluid mixing by cross- and counter-flows in the shell produces a good interaction of the shell-side fluid with tube outer surfaces which enhances the transfer of heat between the working fluids.

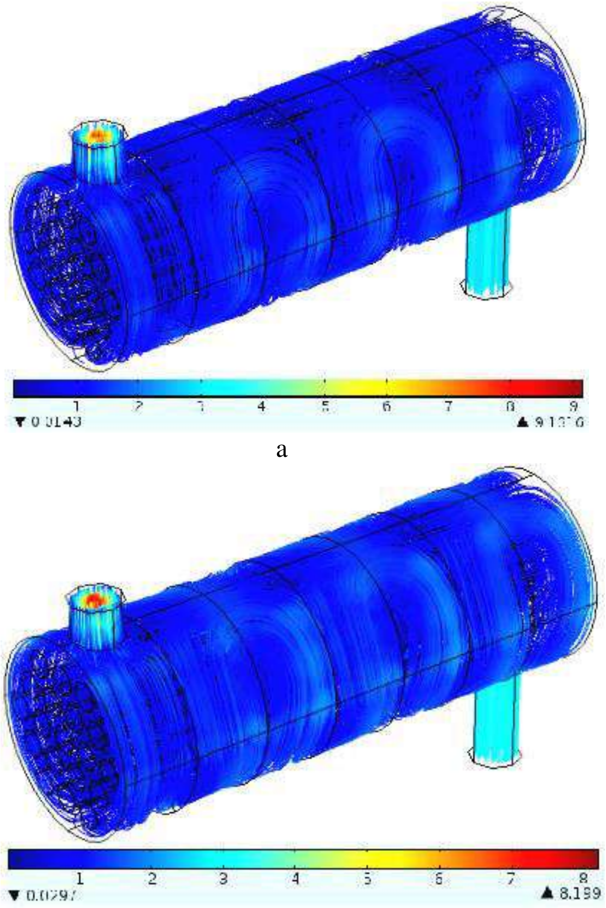

a

b

Figure 6 – Streamline flow of water as shell-side fluid using SS_STHE (a) and CaC_STHE (b)

3.3 Temperature distribution

The shell-side temperature distributions for the heat exchangers are as presented in Fig. 7. It can be seen that the fluid temperature reduces from the fluid entry point to the outlet of the shell. Also, it is observed that greater reduction in fluid temperature occurred across the tube bundles due to larger surface area to conduct heat by the tubes in cross-flow than the tubes in the baffle windows. This observation is synonymous for the two heat exchangers.

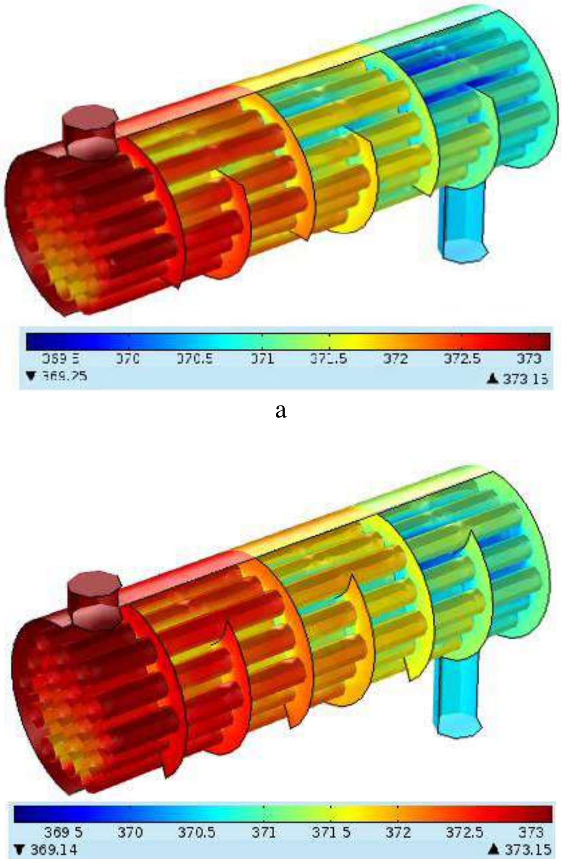

a

b

Figure 7 – Temperature distribution in the shell-side (working fluid: engine oil using SS_STHE (a) and CaC_STHE (b)

3.4 Heat transfer coefficient

The plots of the heat transfer coefficient on the shell-side of the SS_STHE and CaC_STHE against the Reynolds number are as shown in Fig. 8 for engine oil, water and air respectively. It can be observed for each baffle and working fluid that the heat transfer coefficient increases with the Reynolds number, which corresponds to the range of mass flow rates considered for each fluid. Although, the rate of increment in coefficient of heat transfer tends to reduce at higher Reynolds number as indicated for engine oil and water, it increases linearly for air. This can be attributed to the physical nature of each fluid.Amongst other results, the percentage differences in heat transfer coefficients of the SS_STHE with each of the CaC_STHEs are presented in Table 2. From this table, non-zero positive value indicates higher heat transfer coefficient of CaC_STHE while negative value means lower heat transfer coefficient of CaC_STHE.Generally, it is observed that CaC_STHEs had lower heat transfer coefficient. This is partly due to the less interaction of the fluids with the outer tubes since the flow is more concentrated through the centre of the tube bundle. On the contrary, CaC_STHEs with engine oil gave better heat transfer coefficients as depicted from the two turbulent models, and this may also be attributed to fluid's thermodynamic characteristics.

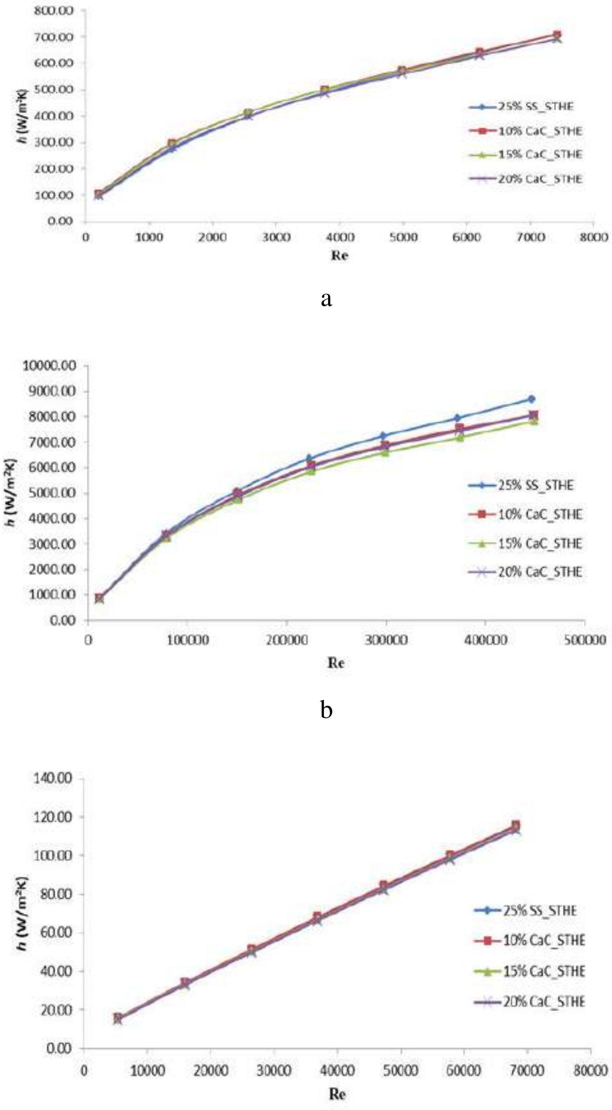

a

b

c

Figure 8 – Shell-side heat transfer coefficient against the Reynolds number for the engine oil (a), water (b) and air (c) as a shell-side working fluid

Table 2 – The comprehensive performance of CaC_STHEs

STHE Model	Fluid	h, % (k-ε)	h, % (RNG k-ε)	Δp, % (k-ε)	Δp, % (RNG k-ε)	WPF (k-ε)	WPF (RNG k-ε)	WSHTC (k-ε)	WSHTC (RNG k-ε)
10 % CaC_STHE	Engine oil	4.40	4.32	–16.91	–16.96	–0.125	–0.127	–0.021	–0.022
15 % CaC_STHE		2.69	2.72	–9.54	–9.59	–0.069	–0.069	–0.010	–0.010
20 % CaC_STHE		0.02	0.03	–8.43	–8.45	–0.084	–0.084	–0.035	–0.034
10 % CaC_STHE	Water	–4.14	–	–15.76	-	–0.199	–	–0.090	–
15 % CaC_STHE		–7.57	–	–7.89	-	–0.154	–	–0.103	–
20 % CaC_STHE		–4.95	–	–9.46	-	–0.144	–	–0.082	–
10 % CaC_STHE	Air	1.30	–	–15.29	-	–0.140	–	–0.056	–
15 % CaC_STHE		–0.75	–	–7.56	-	–0.083	–	–0.042	–
20 % CaC_STHE		–1.56	–	–8.69	-	–0.102	–	–0.056	–

3.5 Pressure drop

The pressure drops of the SS_STHE and CaC_STHEs for varying Reynolds number are presented in Fig. 9 for the three working fluids. The plots showed that the pressure drop increases with increasing Reynolds number (by implication the mass flow rate). However, as the Reynolds number (mass flow rate) increases, the pressure drop continues to rise rapidly due to increasing turbulence. The same trend was reported by Kuppan [14], and also observed by Wang et al. [32] and Zhang et al. [34] from their studies. The percentage differences in pressure drops for the same range of Reynolds numbers with SS_STHE can as well be found in Table 2. The negative values indicate that the CaC_STHEs have higher pressure drops than the SS_STHE for all the shell-fluids. The higher pressure drops demonstrated by CaC_STHEs could be as a result of the more concentrated cross-flow through the centres of the tube bundles and the subsequently reduced bypass flow through the shells.

3.6 Performance factor

The performance factors of the CaC_STHEs in relation to the SS_STHE at varying Reynolds numbers are as shown in Fig. 10 for all the shell-side working fluids. It is observed that the performance factor of none of the CaC_STHEs is up to a value of one for the range of Reynolds numbers considered. The weighted performance factors (WPF) of these heat exchangers relative to SS_STHE in the same range of mass flow rates or Reynolds numbers are also presented in Table 2. The negative values of the weighted performance factors showed that the CaC_STHEs have lower overall performances in comparison with SS_STHE.

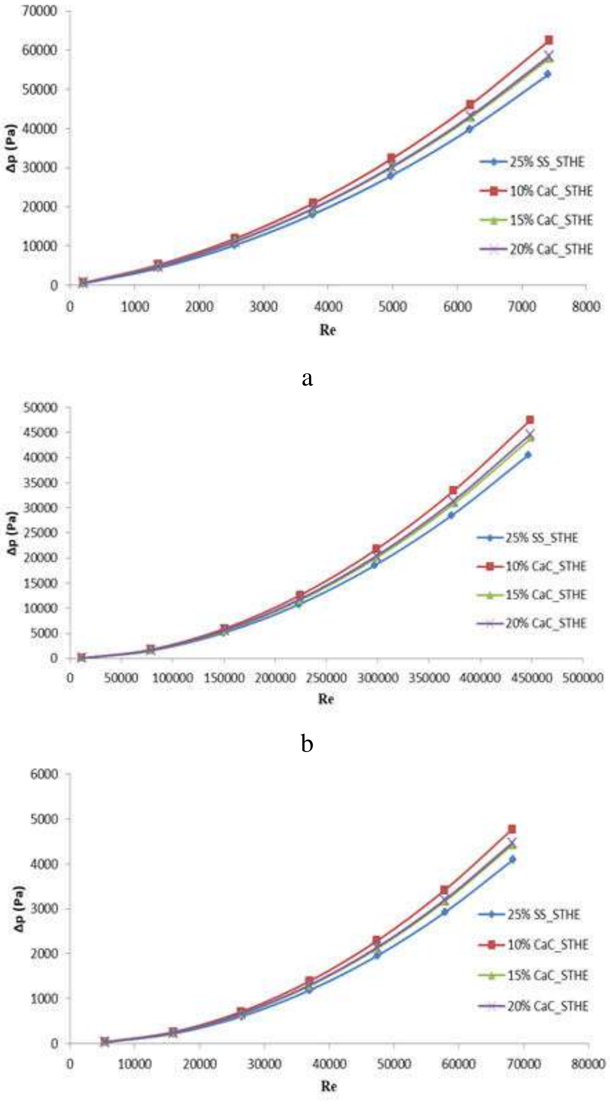

a

b

c

Figure 9 – Pressure drop versus the Reynolds number for the engine oil (a), water (b) and air (c) as a shell-side working fluid

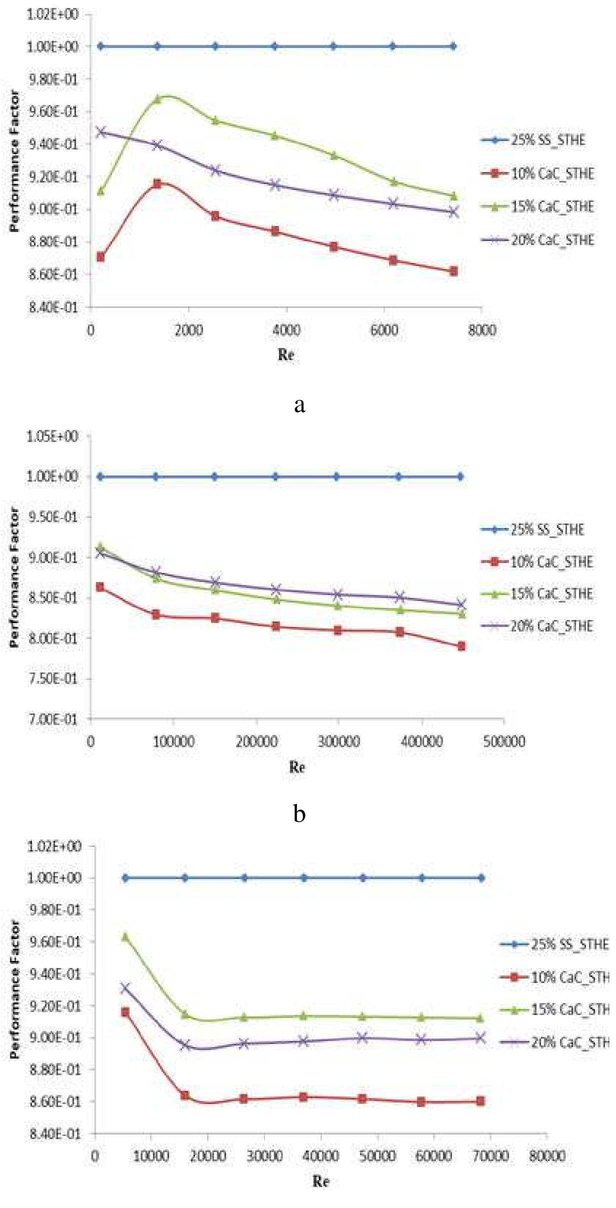

a

b

c

Figure 10 – The performance factor and the Reynolds Number for the engine oil (a), water (b) and air (c) as a shell-side working fluid

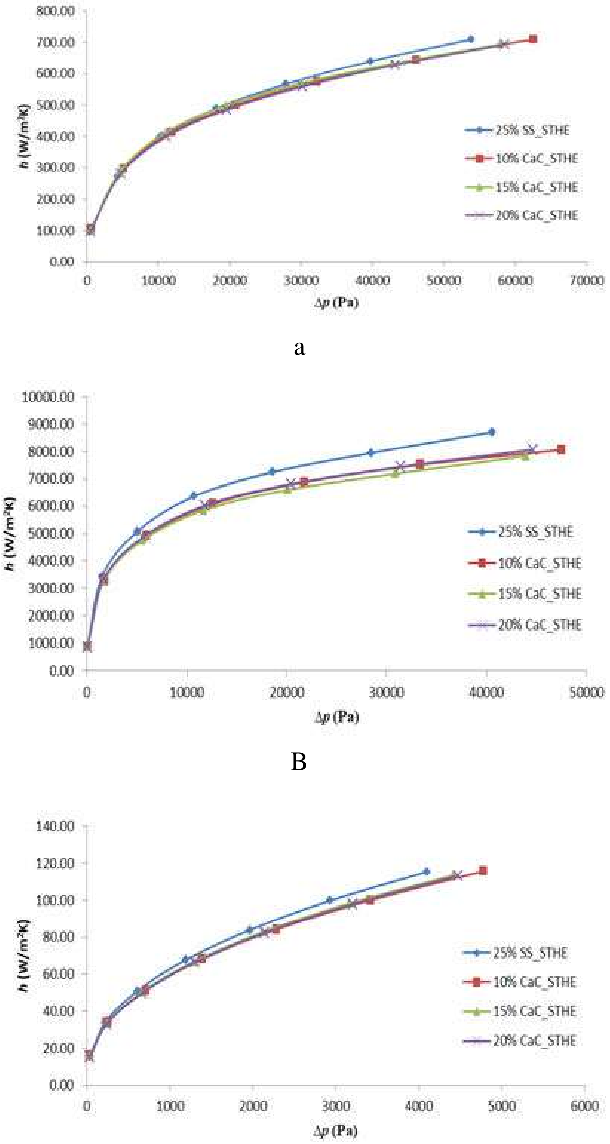

a

B

c

Figure 11 – Heat transfer coefficient and the pressure drop for the engine oil (a), water (b) and air (c) as a shell-side working fluid

3.7 Shell side heat transfer and pressure drop variation

The variations between the shell-side heat transfer coefficient and pressure drop at the same mass flow rate are as indicated in Fig. 11. It is observed that increase in pressure drop is more rapid than that of heat transfer coefficient with increasing mass flow rate, and this confirms the assertions given by Kuppan [14] and Mukherjee [16], and conforms with the observations of Wang et al. [8, 32]. Assessing the heat exchangers at the same pressure drop, the SS_STHE exhibits higher heat transfer coefficient than other heat exchangers for all the working fluids. The weighted shell-side heat transfer coefficients (WSHTC) of the CaC_STHEs against the SS_STHE are as depicted as well with other results in Table 2. The negative values are indications that the SS baffles will be more desirable than the CaC baffles based on this criterion.

4 Conclusion

In the research, the flow and heat transfer characteristics of varying configurations of concave-cut baffles (10, 15 and 20 % CaC_STHEs), and single-segmental baffles (SS_STHE) in shell-and-tube heat exchanger have been numerically investigated. Overall, shell and tube heat exchanger with concave-cut baffles had lower performance as compared with the single-segmental baffle type.

5 Nomenclature

STHE	Shell-and-Tube Heat Exchanger;
u	Velocity component, m/s;
p	Pressure, Pa;
T	Temperature, K;
x	Cartesian coordinate;
c_p	Specific heat capacity at constant pressure, J/(kg·K);
k	turbulence kinetic energy, m^2/s^2;
Re	Reynolds number;
Pr_T	Turbulent Prandtl number;
Δp	Pressure drop, Pa;
h	Heat transfer coefficient, $W/(m^2 \cdot K)$;
Nu	Nusselt number;
P	Performance factor;
WPF	Weighted performance factor;
$WSHTC$	Weighted shell-side heat transfer coefficient;
ρ	Density, kg/m^3;
μ	Dynamic viscosity, Pa·s;
μ_T	Turbulent Eddy viscosity, Pa·s;
η	Thermal conductivity, W/(m·K);
η_T	Turbulent thermal conductivity, W/(m·K);
ε	Dissipation rate, m^2/s^3;
i, j, k	Tensor.

References

1. Dubey, V. V. P., Verma, R. R., Verma, P. S., & Srivastava, A. K. (2014). Steady State Thermal Analysis of Shell and Tube Type Heat Exchanger to Demonstrate the Heat Transfer Capabilities of Various Thermal Materials using Ansys. *Glob. Journals Inc.*, Vol. 14, pp. 1–7.
2. Kapale, U. C., & Chand, S. (2006). Modeling for shell-side pressure drop for liquid flow in shell-and-tube heat exchanger. *Int. J. Heat Mass Transf.*, Vol. 49, pp. 601–610, doi: 10.1016/j.ijheatmasstransfer.2005.08.022.
3. Nasiruddin, M. H. K. (2007). Heat transfer augmentation in a heat exchanger tube using a baffle. *Int. J. Heat Fluid Flow*, Vol. 28, pp. 318–328, doi: 10.1016/j.ijheatfluidflow.2006.03.020.
4. Petinrin, M. O., & Dare, A. A. (2016). Performance of Shell and Tube Heat Exchangers with Varying Tube Layouts. *Br. J. Appl. Sci. Technol.*, Vol. 12, pp. 1–8, doi: 10.9734/BJAST/2016/20021.
5. Wang, Q., Zeng, M., Ma, T., Du, X., & Yang, J. (2014). Recent development and application of several high-efficiency surface heat exchangers for energy conversion and utilization. *Appl. Energy*, doi: 10.1016/j.apenergy.2014.05.004.
6. Zhou, J. F., Wu, S. W., Chen, Y., & Shao, C. L. (2015). Semi-numerical analysis of heat transfer performance of fractal based tube bundle in shell-and-tube heat exchanger. *Int. J. Heat Mass Transf.*, Vol. 84, pp. 282–292, doi: 10.1016/j.ijheatmasstransfer.2015.01.038.
7. Mohammadi, K., & Malayeri, M. R. (2013). Parametric study of gross flow maldistribution in a single-pass shell and tube heat exchanger in turbulent regime. *Int. J. Heat Fluid Flow*, Vol. 44, pp. 14–27, doi: 10.1016/j.ijheatfluidflow.2013.02.010.
8. Wang, Q., Chen, G., Zeng, M., Chen, Q., Peng, B., Zhang, D., & Luo, L. (2010). Shell-side heat transfer enhancement for shell-and-tube heat exchangers by helical baffles. *Chem. Eng. Trans.*, Vol. 21, pp. 217–222, doi: 10.3303/CET1021037.
9. El Maakoul, A., Laknizi, A., Saadeddine, S., El Metoui, M., Zaite, A., Meziane, M., & Ben Abdellah, A. (2016). Numerical comparison of shell-side performance for shel and tube exchangers with trefoil-hole, helical and segmental baffles. *Appl. Therm. Eng.*, doi: 10.1016/j.applthermaleng.2016.08.067.
10. Zhou, G., Xiao, J., Zhu, L., Wang, J., & Tu, S. (2015). A numerical study on the shell-side turbulent heat transfer enhancement of shell-and-tube heat exchanger with trefoil-hole baffles. *Energy Procedia*, Vol. 75, pp. 3174–3179, doi: 10.1016/j.egypro.2015.07.656.
11. Wang, Y., Dong, Q., & Liu, M. (2007). Characteristics of Fluid flow and heat transfer in Shellside of Heat Exchangers with Longitudinal Flow of Shellside Fluid with Different Supporting structures. *Challenges of Power Engineering and Environment, Springer*, pp. 474–475.
12. You, Y., Fan, A., Lai, X., Huang, S., & Liu, W. (2013). Experimental and numerical investigations of shell-side thermo-hydraulic performances for shell-and-tube heat exchanger with trefoil-hole baffles. *Appl. Therm. Eng.*, Vol. 50, pp. 950–956, doi: 10.1016/j.applthermaleng.2012.08.034.
13. Ozden, E., & Tari, I. (2010). Shell side CFD analysis of a small shell-and-tube heat exchanger. *Energy Convers. Manag.*, Vol. 51, pp. 1004–1014, doi: 10.1016/j.enconman.2009.12.003.
14. Kuppan, T. (2013). *Heat Exchanger Design. Taylor and Francis, Boca Raton.*
15. Shah, R. K., & Sekulic, D. P. (2003). *Fundamentals of heat exchanger design. John Wiley and Sons, Hoboken.*
16. Mukherjee, R. (1998). Effectively design shell-and-tube heat exchangers. *Chem. Eng. Prog.*
17. Sinnott, R. K. (2005). *Chemical Engineering Design*. Coulson & Richardson's Chemical Engineering, Elsevier, Butterworth-Heinemann, Oxford.
18. Bouhairie, S. (2012). Selecting Baffles for Shell-and-Tube Heat Exchangers. *Heat Transf.*, pp. 27–33.
19. Jozaei, A. F., Baheri, A., Hafshejani, M. K., & Arad, A. (2012). Optimization of Baffle Spacingon Heat Transfer, Pressure Drop and Estimated Price in a Shell-and-Tube Heat Exchanger. *World Appl. Sci. J.*, Vol. 18, pp. 1727–1736, doi: 10.5829/idosi.wasj.2012.18.12.2484.

20. Prasanna, V., Purushothama, H. R., et al. (2013). A numerical analysis of hydrodynamic and heat transfer effects of shell-and-tube heat exchanger for different baffle space and cut. *Mech. Confab.*, Vol. 2.
21. Bergman, T. L., Lavine, A. S., Incropera, F. P., & Dewitt, D. P. (2011). *Fundamentals of heat and mass transfer*. John Wiley and Sons, New Jersey.
22. Cengel, Y. A., & Ghajar, A. J. (2015). *Heat and mass transfer: fundamentals and applications*. McGraw-Hill, New York.
23. You, Y., Chen, Y., Xie, M., Luo, X., Jiao, L., & Huang, S. (2015). Numerical simulation and performance improvement for a small size shell-and-tube heat exchanger with trefoil-hole baffles. *Appl. Therm. Eng.*, Vol. 89, pp. 220–228, doi: 10.1016/j.applthermaleng.2015.06.012.
24. Tannehill, J. C., Anderson, D. A., & Pletcher, R. H. (1997). *Computational fluid mechanics and heat transfer*. Taylor and Francis, Washington.
25. Wilcox, D. C. (2006). *Turbulence modeling for CFD*. DCW Industries, California.
26. Marzouk, O. A., Huckaby, E. D. (2010). Simulation of a swirling gas-particle flow using different k-epsilon models and particle-parcel relationships. *Eng. Lett.*, Vol. 18.
27. COMSOL (2013). *CFD module user's guide*. COMSOL AB.
28. Fries, T., & Matthies, H. G. (2004). A Review of Petrov-Galerkin Stabilization Approaches and an Extension to Meshfree Methods. *Inst. Sci. Comput. Tech. Univ. Braunschweig*, pp. 1–68.
29. Zienkiewicz, O. C., & Taylor, R. L. (2000). *The Finite Element Method: Fluid Dynamics*. Butterworth and Heinemann, Oxford.
30. Petinrin, M. O., Dare, A. A., & Asaolu, G. O. (2016). Finite Element Stabilization Methods and Solvers for Heat Exchanger Applications: A Review. *Proc. Int. Conf. Mech. Eng. Energy Technol. Manag.*, pp. 977–987.
31. Mohammadi, K., Heidemann, W., & Muller-Steinhagen, H. (2009). Numerical Investigation of the Effect of Baffle Orientation on Heat Transfer and Pressure Drop in a Shell and Tube Heat Exchanger With Leakage Flows. *Heat Transf. Eng.*, Vol. 30, pp. 1123–1135, doi: 10.1080/01457630902972694.
32. Wang, Q., Chen, Q., Chen, G., & Zeng, M. (2009). Numerical investigation on combined multiple shell-pass shell-and-tube heat exchanger with continuous helical baffles. *International Journal of Heat and Mass Transfer*, Vol. 52, pp. 1214–1222, doi: 10.1016/j.ijheatmasstransfer.2008.09.009.
33. Zhang, J., Li, B., Huang, W., Lei, Y., He, Y., & Tao, W. (2009). Experimental performance comparison of shell-side heat transfer for shell-and-tube heat exchangers with middle-overlapped helical baffles and segmental baffles. *Chemical Engineering Science*, Vol. 64, pp. 1643–1653, doi: 10.1016/j.ces.2008.12.018.
34. Zhang, M., Meng, F., & Geng, Z. (2015). CFD simulation on shell-and-tube heat exchangers with small-angle helical baffles. *Front. Chem. Sci. Eng.*, pp. 1–11, doi: 10.1007/s11705-015-1510-x.

Числове дослідження ефекту увігнуто-вирізаних перегородок у теплообміннику

Петінрін М. О., Даре А. А.

Університет м. Ібадан, Обудува роуд, 200284, м. Ібадан, Нігерія

Анотація. У роботі досліджено ефективність теплообмінних апаратів з односегментними перегородками і різними їх конфігураціями увігнуто-вирізаних перегородок (10, 15 і 20 %). Дослідження проводилось для теплообмінника з трьома робочим середовищами: моторне масло, вода, повітря. Для кожної конфігурації перегородок отримані результати, добре узгоджені для двох моделей турбулентності: *k-ε* і RNG *k-ε*. Підтверджено, що теплообмінники з увігнутими перегородками мають більші перепади тиску і нижчі показники ефективності, ніж одиничні сегментні перегородки у тому ж массогабаритному діапазоні. Крім того, теплообмінники з увігнуто-вирізаними перегородки мають нижчі коефіцієнти теплопередачі зі сторони оболонки за однакового перепаду тиску порівняно з коефіцієнтом теплопередачі для односегментних перегородок. Таким чином, використання перегородок з увігнутим вирізом не сприяє бажаному підвищенню ефективності теплообмінника порівняно з сегментними перегородками.

Ключові слова: кожухотрубний теплообмінник, перепад тиску, коефіцієнт продуктивності, коефіцієнт теплопередачі, увігнуто-вирізана перегородка.

JOURNAL OF ENGINEERING SCIENCES
ЖУРНАЛ ІНЖЕНЕРНИХ НАУК
ЖУРНАЛ ИНЖЕНЕРНЫХ НАУК
Web site: http://jes.sumdu.edu.ua
DOI: 10.21272/jes.2019.6(1).e2
Volume 6, Issue 1 (2019)

UDC 621.311:[681.515+658.012]

Comparison between PID and Artificial Neural Networks to Control of Boiler for Steam Power Plant

Salim H., Sultan Kh. F., Jawad R.*

University of Technology, Al-Sinaa St., 10066 Baghdad, Iraq

Article info:

Paper received:	October 12, 2018
The final version of the paper received:	January 2, 2019
Paper accepted online:	January 7, 2019

***Corresponding Author's Address:**
rjawad192@gmail.com

Abstract. This paper presents is to develop and compare neural network and conventional based controllers for a boiler of steam power plant. Designs of two different controllers for pressure and temperature are presented for keeping the boiler working in normal condition and improve efficiency. These controllers consist of NARMA controller of ANN and a conventional proportional-integrator-derivative (PID) controller. These parameters are adjusted by built a model and implementation in MATLAB program according to the requisite of the steam power plant and the control objectives. The results show a neural network is best controlled and superior performances of power plant from PID controller artificial neural network and PID have been applied in Al–Dura power plant in Baghdad. Therefore, neural networks have been extensively utilized in many industrial applications.

Keywords: Artificial Neural Network, control, PID, NARMA controller.

1 Introduction

The control system is an important part of steam power plant. When a control system is weakening lead to damage and shutdown of boiler for this reason design modeling of control systems and applied of different types of controllers of industrial plants. Applications of steam generation modeling to control systems can classify into ANN and PID. Many authors have suggested system controller and models by using intelligent technique such as applied Artificial neural network (ANN) to obtain the relationships between input and output data variables of the system. The neural network controllers are extensively used for their suppleness for completion on many systems and good reference track capacity [1]. The authors applied dynamic artificial neural network base on genetic algorithm (GA) to control and identify the advantages and disadvantages of ANN trained by GA. a genetic algorithm utilzed to train a Layer-Recurrent Network, Focused Time-Delay Neural Network, a Elman Network, and Nonlinear Autoregressive Network with exogenous inputs. The results of simulation provide a good accuracy of model the generalization by a nonlinear system of neural network. The training time is shorter of dynamic neural networks and faster of convergence speed. Also the generalization of the Elman network and the NARX network are better than the FTDNN and the LRN networks and the training error of the LRN network is the smallest among the DNNs. The NARX and the Elman network may be describe the complex system because of the back-forward in the DNN. Arrange of the system will be set before the training because the FTDNN network is the feed-forward multilayer [2]. This study obtained application of neural network for control of solar plants. This plant consists of a hybrid diagram combining the possibilities of neural networks for estimate purposes with the well-know hypothesis and general industrial application of PID techniques. The neural network is training base on data that measured from the plant provided that a way of development between a set of PID controllers and verify the use of several local linear controllers to cope with changes in the plant behavior induce by different operating conditions. Experimental results show the neural networks are able to learn by data systems this data collected at "Platforma Solar de Almeria" (Spain), neural network is see as an extension rather than substitute of linear identifiers and controllers that can be previously working and applied to a plant model and the computational requirements with a small initial knowledge .the results were obtained from this control strategy [3]. In this study present use of Artificial Intelligent and PI Controller to analysis dynamic performance and control methodology developed by Load frequency control of number of areas interconnected hydrothermal power reheat system. three areas interconnected consists of steam plant in three areas consists of hydro plant, the arrangement of most complex system like hydro plant and steam plant with reheat are interconnected that increases the nonlinearity of system. This model of technique is built in Simulink \ MATLAB. The results show a conventional controller and intelligent with the addition of slider gain provide a good performance in each area of hydrothermal combination and reduce the oscillation of the frequency variation and the tie line power flow. A comparison of Artificial Intelligence with PI controller illustrates the excellence of proposed ANN based advance more Fuzzy and PI for the conditions. the intelligent control advance using ANN conception is supplementary perfect and more rapidly than the fuzzy and conventional PI controls diagram even for a difficult dynamical system[4]. In this study applied a Neural Network based PI and PID controllers design and simulated of a pneumatic servo actuator to increase the position accuracy. Pneumatic servo actuators in employment systems are usually used in industrial mechanization. In these designs training Neural Network depending on feedback representing change in location error and changes in external load force to present controllers with appropriate gain , these gains must be keep the positional response of overshoot, rise time and steady state error as minimum. The results show the Neural Network based PID controller was more than with PI controller in trained and generate with simpler construction and minimum Mean Square Error [5].

The aim of this research is to control of variables pressure and temperature of boiler of Al-Dura power plant in Baghdad which affected of maximum generated power and plant performance by intelligent technique and compared between them.

2 Research Methodology

2.1 Artificial neural networks

The first time of appear artificial neural network by Bernard Widrow in 1950's [6]. An artificial neural network is a computing structure that is made up of a assembly of simple, very much interconnected by neurons with transfer functions. The Neurons are including input layer, hidden layer and output layer. The system dynamic complexity is determined by the number of hidden layer and neurons in layers for ANN model. ANN learns by training .all inputs of ANN has its own weight. The Weights are determined during network training process. Neural network attempted to look like the human brain to resolve difficult problems in many applications in the field of engineering. Figure 1 shows a simple structure of a ANN with one input, one outputs and Figure 2 shows multiple-input neuron structures where p, w, b, f, and a are input, weight, bias, transfer function, and output correspondingly. Formula 1 allows calculating the neuron output:

$$a = f(w \cdot p + b). \tag{1}$$

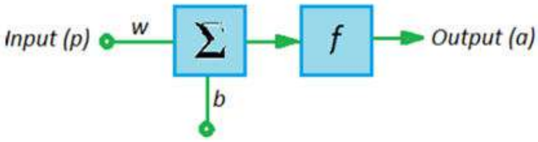

Figure 1 – Single-input neuron structure [7]

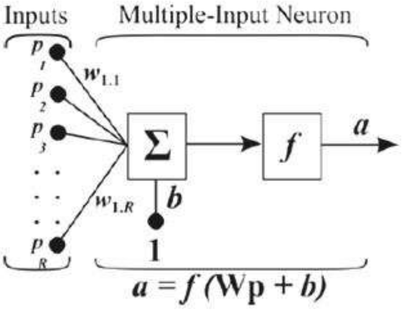

Figure 2 – Multiple-input neuron structure [7]

The variables w and b can be determined by learning rules so that the relation between the input and output meet the predictable aim [7].

Training of ANN can be classified in to types supervised and unsupervised. In supervised learning means that inputs and targets are known, but in unsupervised learning the inputs are known but unknown targets and the underlying relation within the data sets have to be disclose by the ANN utilized the data cluster method.

The training procedure of neural network involves the variation of parameters. So, it is needed to adjust the number of neurons in the hidden layer so as to reach the greatest converging network. A true process of training ANN is generally base on an iterative estimate in which the variables are in succession updated in numerous steps. Such a step can be based on a single information item, on a set of them, or on all obtainable data points. In each step, the desired outcome is compare with the real one and using the data of the architecture, all variables are changed slightly such that the error for the presented data points decreases [8]. Artificial neural networks (ANN) are useful in many fields of science, knowledge and technology. They provide an alternative approach to the simulation of complex, ill-defined and uncertain systems [9–11].

2.2 PID control

The widely utilized in industrial control systems is a proportional-integral-derivative (PID) controller due to their suppleness for give the designer on the system dynamics. it was introduced to industry in 1939. PID is a generic feedback control system that objective is to minimize the values of a measured and a desired difference by adjusting the process control inputs this called error. The PID controller consist of three coefficients the proportional P, the integral I and the derivative D values that can be translate in terms of time. The controller PID can present the requisite control action designed for a exact process by regulate present error, accumulation of past errors, and calculation of future errors [12]. It is also usual to use just PI, PD, P or I controllers. The formula 2 shows the algorithm of PID:

$$u(t)=K_p\left[e(t)+\frac{1}{T_i}\int_0^t e(\tau)d\tau+T_d\frac{de(t)}{dt}\right], \qquad (2)$$

where u – control signal; e – control error; K_p – proportional gain; T_i – integral time, and T_d – derivative time.

The amount of three parameters including P, I and D acts control signal [13].

Figure 3 shows the block diagram of PID controller, where y and r are the measured process and reference parameters.

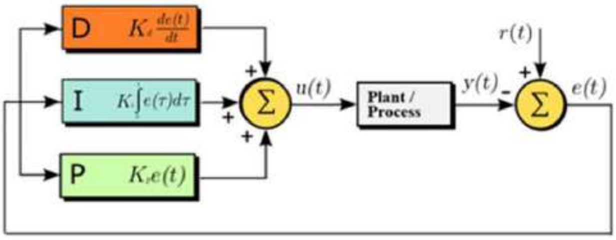

Figure 3 – Block diagram of PID controller [7]

2.3 Modeling of boiler using PID and neural network

The Simulink-MATLAB is used to design and implement an artificial neural network and PID controller. Adjust the gain of PID according to tuning algorithm in MATLAB to obtain a excellent balance between performance and robustness, and saving the system working in . The type of artificial neural network controller using is the nonlinear autoregressive moving average (NARMA) are designed and employed to control of pressure and temperature of boiler of steam power plant. NARMA implement in the ANN toolbox of simulation MATLAB. In system identification of ANN model of the plant is developed. Controller block of NARMA is shown in Figure 4.

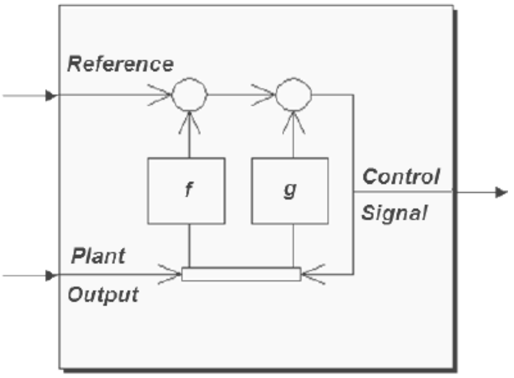

Figure 4 – Controller block of NARMA

The scheme of plant identification for the NARMA of boiler model is working by adjusted parameters for generating data by insert, min and max values for the plant input and output ,min and max interval values. The size of the hidden layer, the number of delayed plant inputs and outputs, the sampling interval and finally the training function is the Levenberg-Marquardt Training Algorithm (TrainLM). The training network then select by the response of the resulting plant model was display. Separate plots for validation data, training data and testing data that's shown in Figures 5–7. The performance of neural net work and regression is shown in Figures 7, 8. The block controller of PID is shown in Figure 9, as well as the model of boiler using PID and Neural network is shown in Figure 10.

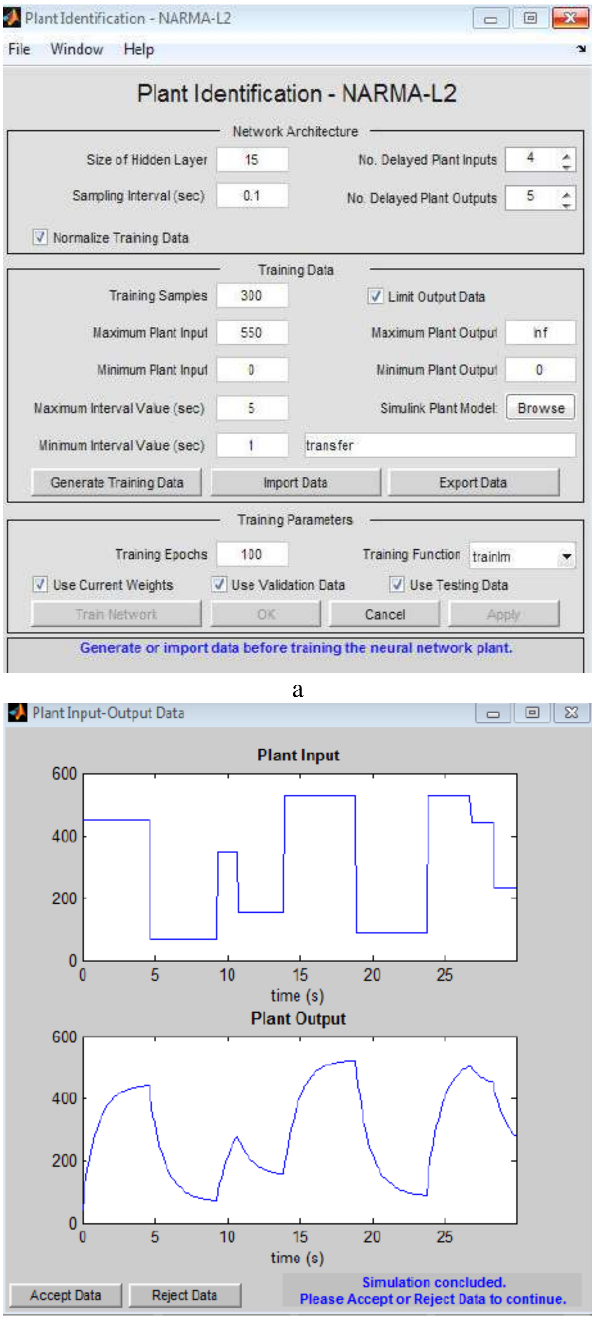

Plant Identification - NARMA-L2

Network Architecture

Size of Hidden Layer: 15
No. Delayed Plant Inputs: 4
Sampling Interval (sec): 0.1
No. Delayed Plant Outputs: 5
☑ Normalize Training Data

Training Data

Training Samples: 300
☑ Limit Output Data
Maximum Plant Input: 550
Maximum Plant Output: Inf
Minimum Plant Input: 0
Minimum Plant Output: 0
Maximum Interval Value (sec): 5
Simulink Plant Model: Browse
Minimum Interval Value (sec): 1
transfer

Training Parameters

Training Epochs: 100
Training Function: trainlm
☑ Use Current Weights
☑ Use Validation Data
☑ Use Testing Data

Generate or import data before training the neural network plant.

a

Simulation concluded.
Please Accept or Reject Data to continue.

b

Figure 5 – Plant identification of NARMA (a) and generate data (b)

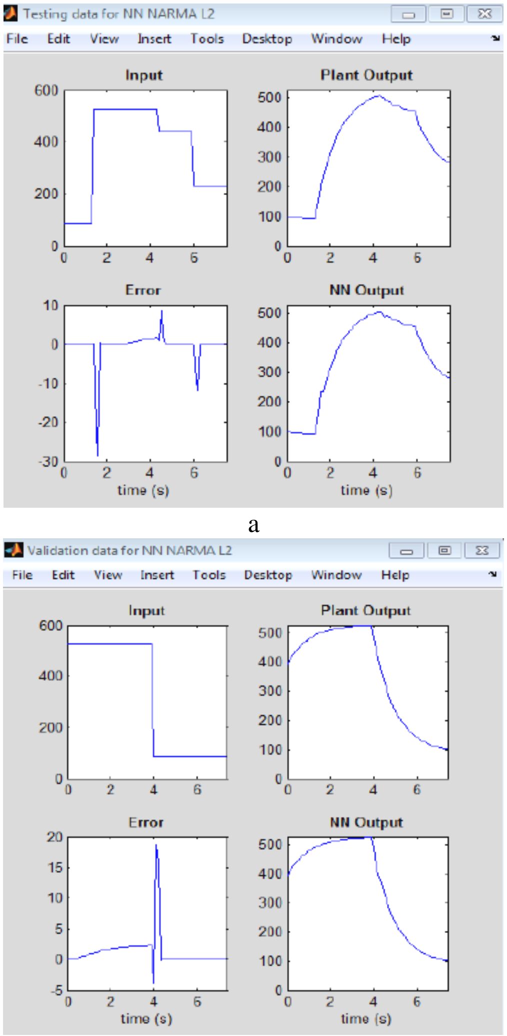

a

b

Figure 6 – Testing (a) and validation data (b)
of neural network

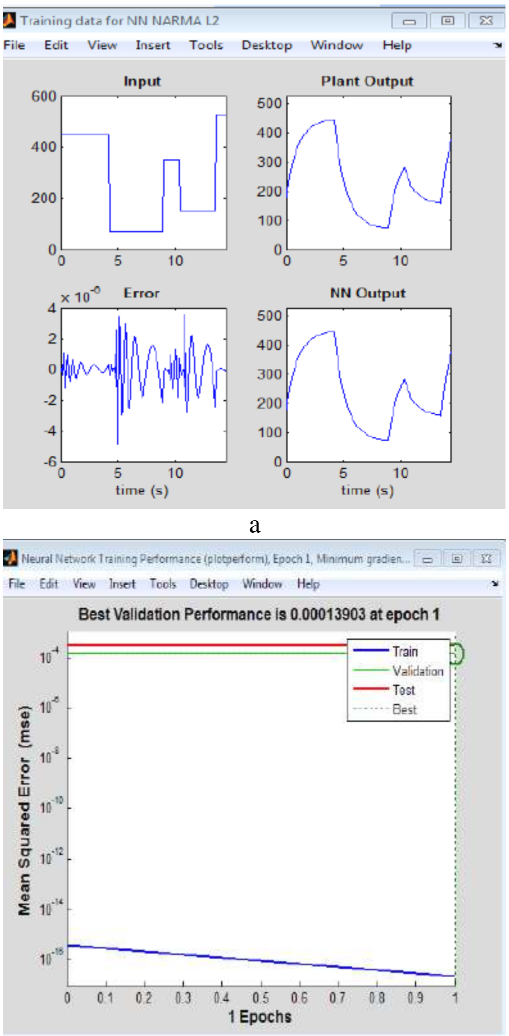

a

b

Figure 7 – Training data (a) and performance (b)
of neural network

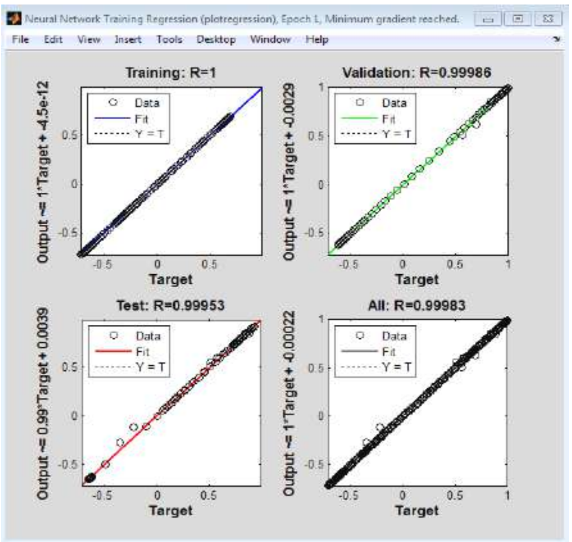

Figure 8 – Regression of neural network

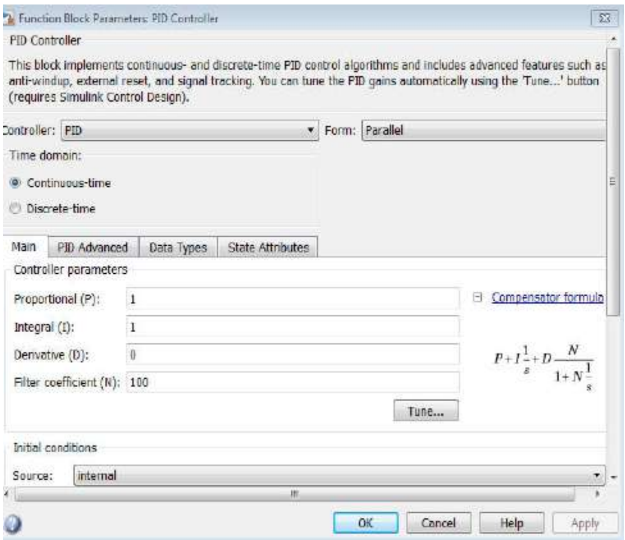

PID Controller

This block implements continuous- and discrete-time PID control algorithms and includes advanced features such as anti-windup, external reset, and signal tracking. You can tune the PID gains automatically using the 'Tune...' button (requires Simulink Control Design).

Controller: PID

Form: Parallel

Time domain:

● Continuous-time

○ Discrete-time

Controller parameters

Proportional (P): 1

Integral (I): 1

Derivative (D): 0

Filter coefficient (N): 100

$$P+I\frac{1}{s}+D\frac{N}{1+N\frac{1}{s}}$$

Initial conditions

Source: internal

Figure 9 – Block controller of PID

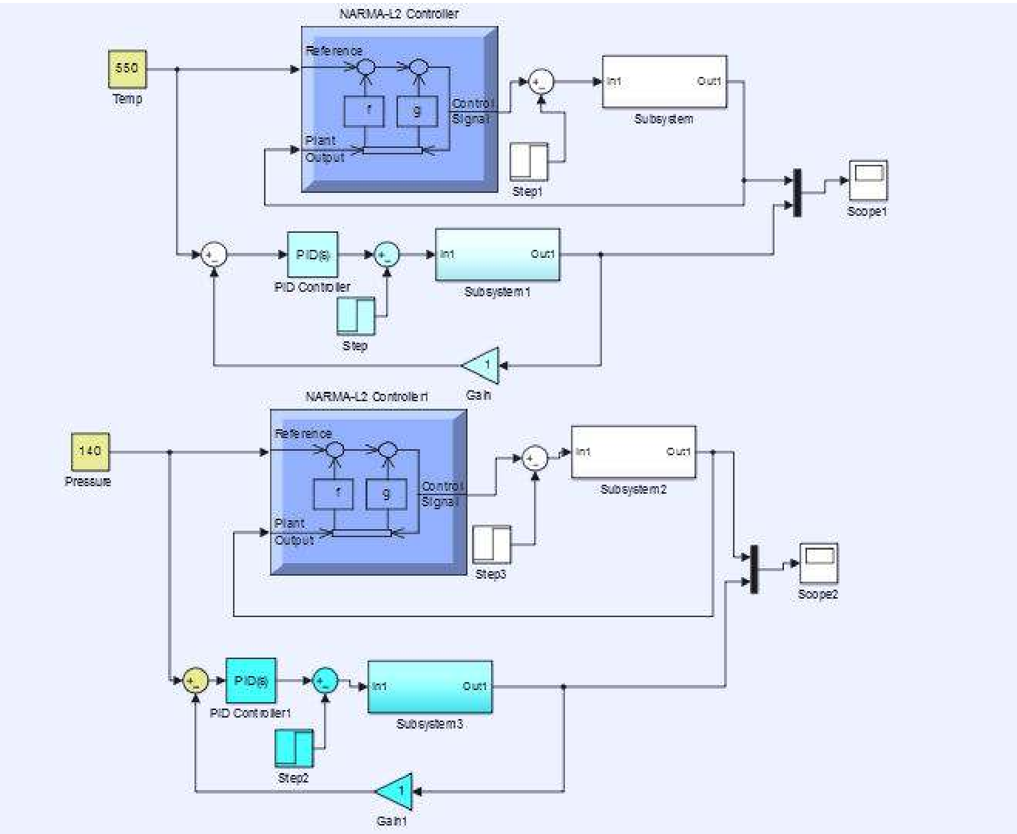

Figure 10 – Block diagram of boiler design using NARMA and PID

3 Results and Discussion

The combination of two or more of intelligent techniques produces a strong system of high efficiency and effectiveness. Intelligent techniques are very useful in the modeling and predicting of high complex systems having nonlinearity and uncertainty in their models. In some applications of more than one part in their systems, it is very difficult to evaluate or drive such mathematical models which can identify these systems, however, by obtaining some data for the inputs and outputs of system.

When implementation Simulink model of whole system, the results shown in Figure 11 allow obtaining the responses of pressure and temperature of model. As it can be see from these figures the response of the controller using neural network is rapid and after about 7 second it is stabilized but when using PID the response of the controller is stabilize after 18 second. From this result show the artificial neural network response is better than PID. These advantages are because of the special construction and algorithm of the network. Neural network method can be a suitable alternative to standard modelling techniques as obtain data sets show nonlinearities in the structure. It has established ability to solve combinatorial optimization troubles in engineering plants.

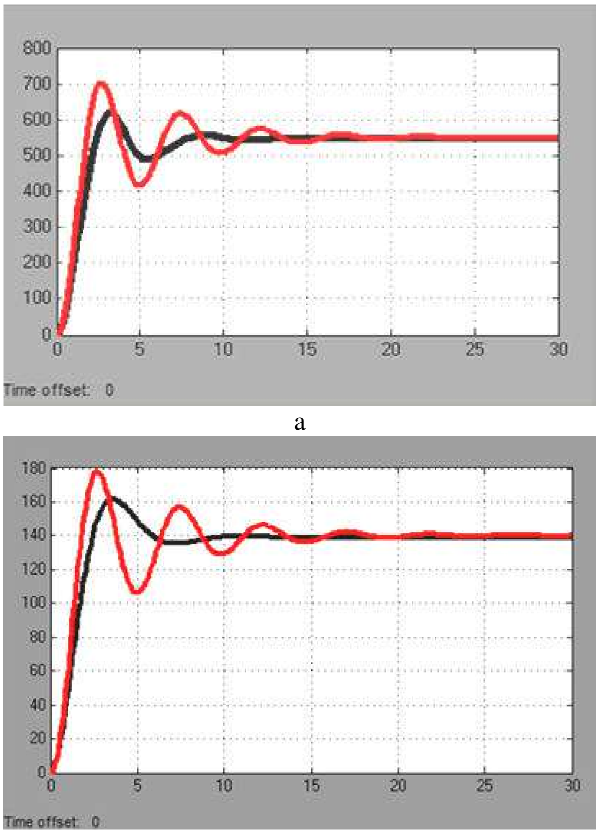

a

b

Figure 11 – The responses of temperature (a) and pressure (b) of a model

4 Conclusions

This paper developed two types of controller structures for two significant outputs from the models and their matching values from the measured information sets temperature and pressure of boiler steam generation . These controllers of steam generation are NARMA of Artificial neural network controller and PID conventional controller. These controllers applied and adjusted their parameters and tune in Simulink\MATLAB according to the requirement of the steam generation structure and the control object. Finally compared and explored the performances of the Artificial neural network and PID conventional controllers .The result obtained that NARMA give a higher performance to PID controllers in this study. The response of rise, settling time, and maximum overshoot of NARMA is less than the for the PID controller. In general, the physical behaviour is well to hold by the NARMA models. It is also shown that neural networks are considered a reliable alternative to PID for identification and modelling systems.

References

1. Junghui, C., & Tien-Chih, H. (2004). Applying Neural Networks to On-Line Updated PID Controllers for Nonlinear Process Control. *Journal of Process Control*, Vol. 14 (2), pp. 211–230.
2. Khalil, R. A. (2012). Comparison of Four Neural Network Learning Methods Based on Genetic Algorithm for Non-Linear Dynamic Systems Identification. *Al-Rafidain Engineering*, Vol. 20 (1).
3. Henriques, J., Gil, P., Cardoso, A., & Dourado, A. (2002). *Scheduling Of PID Controllers by Means of a Neural Network with Application to a Solar Power Plant*. IEEE-IJCNN.
4. Prakash, S., & Sinha, S. K. (2011). Load Frequency Control of Three Area Interconnected Hydro-Thermal Reheat Power System Using Artificial Intelligence and PI Controllers. *International Journal of Engineering, Science and Technology*, Vol. 4 (1), pp. 23–37.
5. Hassan, M. Y., & Kothapalli, G. (2010). Comparison Between Neural Network Based PI And PID Controllers. *International Multi-Conference on Systems, Signals and Devices*, pp. 1–6.
6. Asgari, H., Chen, X. Q., & Sainudiin, R. (2012). Application of Artificial Neural Networks to Rotating Equipment. *3rd Conference on Rotating Equipment in Oil and Power Industries*.
7. Hagan, M. T., Demuth, H. B., & Jesus, O. D. (2002). An Introduction to the Use of Neural Networks in Control Systems. *International Journal of Robust and Nonlinear Control*, Vol. 12 (11), pp. 959–985.
8. Beale, M. H., Hagan, M. T., & Demuth, H. B. (2011). *Neural Network Toolbox™ User’s Guide*. Mathworks.
9. Pallares, D., Johnsson, F. (2006). Macroscopic modelling of fluid dynamics in large-scale circulating fluidized beds. *Progress in Energy and Combustion Science*, Vol. 32 (5), pp. 539–569.
10. Zhao, C., Dun, L., Zhou, W., Chen, X., Zeng, D., Flynn, T., & Kraft, D. (2012). Coal combustion characteristics on an OXY-CFB combustor with warm flue gas recycle. *Proceedings of the 21st International Conference on Fluidized Bed Combustion*, pp. 3–6.
11. Kesgin, U. (2004). Genetic algorithm and artificial neural network for engine optimisation of efficiency and NO_x emission, *Fuel*, Vol. 83 (7), pp. 885–895.
12. Araki, M. (1984). PID Control. *Control, Systems, Robotics, and Automation*, Vol. 2.
13. Astrom, K. J. (2002). PID Control. *Control System Design*, pp. 216–251.

Порівняльний аналіз застосування пропорційно-інтегрально-диференціального регулятора і штучної нейронної мережі для керування паровим котлом електростанції

Салім Х., Султан Х. Ф., Джавад Р.*

Технологічний університет, вул. аль-Сінаа., 10066, м. Багдад, Ірак

Анотація. У статті представлено розроблену методику проведення порівняльного аналізу застосування нейронних мереж і контролерів для традиційних котлів парових електростанцій. Представлені схеми двох різних контролерів для тиску і температури для підтримки роботи котла в нормальному стані та підвищення ефективності. Ці контролери складаються з нелінійного NARMA-контролера штучної нейронної мережі та традиційного пропорційно-інтегрально-диференціального регулятора. Ці параметри коригуються шляхом побудови моделі та подальшої реалізації у програмі MATLAB відповідно до вимог парової електростанції та цілей управління. Результати свідчать, що нейронна мережа контролюється краще, а на електростанції Аль-Дюра у м. Багдад застосовуються характеристики відповідної моделі електростанції з використанням PID-контролера і штучної нейронної мережі, що може бути черговим підтвердження ефективності застосування нейронних мереж у багатьох галузях промисловості.

Ключові слова: штучна нейронна мережа, керування, PID-контролер, NARMA.

JOURNAL OF ENGINEERING SCIENCES
ЖУРНАЛ ІНЖЕНЕРНИХ НАУК
ЖУРНАЛ ИНЖЕНЕРНЫХ НАУК

Web site: http://jes.sumdu.edu.ua

DOI: 10.21272/jes.2019.6(1).e3 Volume 6, Issue 1 (2019)

UDC 681.3.05

Increasing the Speed of Fractal Image Compression Using Two-Dimensional Approximating Transformations

Maydaniuk V. P., Arseniuk I. R., Lishchuk O. O.

Vinnytsia National Technical University, 95 Khmelnitsky Rd., 21021 Vinnytsia, Ukraine

Article info:

Paper received:	October 26, 2018
The final version of the paper received:	January 20, 2019
Paper accepted online:	January 29, 2019

***Corresponding Author's Address:**
igrosars@gmail.com

Abstract. Fractal image compression algorithm is known for allowing very high compression rates (the best examples – up to 1 000 times with acceptable visual quality) for real photos of natural objects, which is not possible for other lossy compression methods. The main disadvantage of the fractal method is the low rate of encoding, which is due to the fact that in order to obtain high image quality for each rank block, it is necessary to perform a search of all domain blocks, and for each domain block, at least eight affine transformations must be performed. Despite the large number of works devoted to increasing the speed of fractal images compression, it is worth noting that this problem remains very relevant. The aim of the work is to find methods for increasing the speed of fractal image compression. Based on the analysis of known approaches of increasing the fractal compression rate, a proposed method is based on the representation of rank and domain blocks in the form of coefficients of two-dimensional linear approximation, which allows for each rank block to perform a rapid pre-selection of blocks by three approximation coefficients. With the selected blocks, the transformations that are characteristic for fractal compression are performed. Since the quantity of the selected blocks is considerably less than the total number of domain blocks, one should expect a significant gain in the sealing speed. The simulation done in the Python programming language showed that the proposed method can increase the fractal image compression rate by on average of 10 times compared to Arnaud Jacquin's method without significant loss of image visual quality.

Keywords: image compression, fractal encoding, two-dimensional approximation, image fractal properties.

1 Introduction

Images that are presented in digital form must be stored on media and transmitted by communication channels. To save memory and make more efficient use of system resources, special encoding algorithms are creates [1, 6]. The image is a special kind of data that has redundancy in two dimensions, which provides additional opportunities for compression [1, 4]. One of the promising methods of image compression is a fractal method [1]. Fractal encoding is a mathematical process for encoding raster images that contain a real image in a set of mathematical data that describes the fractal properties of an image. This type of encoding is based on the fact that all natural and most artificial objects contain excessive information in the form of identical image blocks that are repeated. They got the name fractals. Fractal is a structure that consists of similar shapes and drawings that can be in different sizes.

2 Literature Review

The fractal compression algorithm is known for allowing very high densification factors (best examples – up to 1 000 times with acceptable visual quality) for real photographs of natural objects that can not be used for other lossy compression algorithms [2, 3].

The main disadvantage of the fractal method is the low rate of encoding, which is due to the fact that in order to obtain high image quality for each rank block, it is necessary to perform a search of all domain blocks, and for each domain block, at least eight affine transformations must be performed [7–9]. One of the possible efficient and fast image coding schemes by fractal method was proposed by Arnaud Jacquin [7]. But if you count the number of multiplication operations to find the coefficients of affine transformations of one rank block in the image in grayscale grays of 512×512 ($4^{4.5} = 512$, $k = 4.5$) pixels with the size of the rank block 4×4 ($n = 4$), the domain 8×8 and step of the choice of domain blocks 2, then even for the algorithm proposed by Jacquin, the total number of operations of multiplication will be quite large and will be [1]:

$$M = 8\cdot[4n^{k+1}(n^{k-1}-3)+9n^2] =$$
$$= 8\cdot[4\cdot 4^{5.5}\cdot(4^{3.5}-3)+9\cdot 4^2] = 8.2\cdot 10^6.$$

Consequently, the purpose of increasing the rate of compression of images by the fractal method is very relevant. With improved performance, the fractal compression algorithm can become one of the most effective image compression algorithms [1].

3 Research Methodology

3.1 Mathematical model of encoding-decoding of images by fractal method

From a physical point of view, fractal encoding is based on the assertion that the image contains affinity redundancy. The mathematical model used in fractal image compression is called Iterated Function Systems (IFS). IFS contain a set of compression transformations that can be set for the image *S* as follows [1, 8]:

$$W(S) = w_i(S). \tag{1}$$

According to the Banach theorem, there exists a certain class of mappings called pressing ones, and the following statement holds true for them: if, to some image f_0, we begin to repeatedly apply the mapping *W* in such a way that:

$$f_1 = W(f_0), f_i = W(f_{i-1}), \tag{2}$$

then with *"i"* going to infinity we get the same image no matter what image we took for f_0:

$$f = \lim_{i\to\infty} f_i \tag{3}$$

The image *f* is called a fixed conversion point *W* or attractor.

As transformations w_i affinity mapping is used:

$$w_i\begin{pmatrix}x\\y\\z\end{pmatrix} = \begin{bmatrix}a_i & b_i & 0\\ c_i & d_i & 0\\ 0 & 0 & S_i\end{bmatrix}\begin{bmatrix}x\\y\\z\end{bmatrix} + \begin{bmatrix}dx\\dy\\O_i\end{bmatrix}, \tag{4}$$

where a_i, b_i, c_i, d_i – affine coefficients of deformation, compression, rotation; d_x, d_y – coefficients of move; *x, y* – the coordinates of the point that is converted; *z* – its intensity. Parameter S_i controls contrast, and O_i – brightness of the image. Knowing the coefficients of these transformations, we can restore the original image.

The fractal image coding algorithm can be described as follows. The process of compression begins with the fact that the image is initially divided into non-overlapping (ranked areas), and then in the domain blocks that can overlap, as shown in Figure 1 [7].

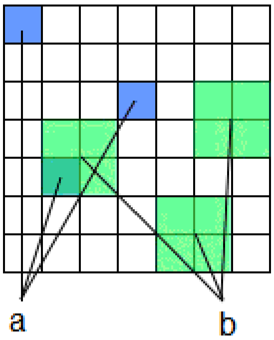

Figure 1 – Selection of blocks in the image:
a– rank, b – domain

Domains must have distinctive fragments that are then used to construct the decoded image. After that, the image encoding begins by selecting for each domain region of the most relevant domain, by which the brightness distribution in the ranked region can be approximated by the distribution of brightness in the domain. In order to get the best approximation, the domains are subjected to affine transformations, which result in not only their geometric deformation, but also changes in contrast and brightness. If the brightness distribution in the converted domain fails to achieve a satisfactory approximation of the brightness distribution in the rank region, the rank region is divided into four parts and the process is repeated. The quality of the required approximation is given in the form of an acceptable value of the average square of the approximation error (the mean square of the discrepancy). Domain numbers used in the encoding of each rank domain, as well as affinity overflow coefficients, are written to a file. The compressed image file contains a heading with information about the location of ranked domains and domains, as well as a table of effectively packed affine coefficients for each rank domain.

One of the possible patterns of image encoding by the fractal method, proposed by Arnaud Jacquin, contains the following steps [1, 8]:

– the image is divided into areas adjacent to each other by the size of *N*×*N* (ranked areas);

– a set of domain scopes is specified. Domain areas can overlap, they do not have to cover the entire surface of the image. The size of domain areas is *2N*×*2N*;

– the domain, which after affine transformations, most closely approximates the rank region is chosen for each rank. In practice, eight variants of mapping one square to another with usage of affine transformations are applied. These are turns of the image at angles 0°, 90°, 180°, and 270° relative to its center and symmetry transformation relative to the orthogonal axes, which pass through the center of the fragment, perpendicular to its sides.

The accuracy of the approximation *F* is determined by means of the mean square criterion:

$$F = \sum_{i,j}(Sd_{ij} + O_{ij} - r_{ij})^2, \tag{5}$$

where d_{ij} – values obtained as a result of averaging fragments with dimensions of 2×2 of the domain's region elements, that leads it's size to the size of the rank region; r_{ij} – values of elements of the rank region. The displacement O_{ij} can be either a constant, or described by polynomials of the first, second, third order.

By equating partial derivatives of the expression S and O to zero:

$$\frac{\partial F}{\partial S} = 0, \quad \frac{\partial F}{\partial O} = 0, \tag{6}$$

Let's find the values S and O, at which the minimum of the expression is reached:

$$O = \frac{1}{n^2} \cdot \left(\sum_{i,j}^{n} r_{ij} - S \sum_{i,j}^{n} d_{ij} \right), \tag{7}$$

$$S = \frac{n^2 \sum_{i,j}^{n} r_{ij} d_{ij} - \sum_{i,j}^{n} r_{ij} \sum_{i,j}^{n} d_{ij}}{n^2 \sum_{i,j}^{n} d_{ij}{}^2 - (\sum_{i,j}^{n} d_{ij})^2}. \tag{8}$$

Domain blocks are usually chosen with step $n/2$ at $n = 4$. The following parameters are written to the output file:

1) coordinates of the domain area with the lowest value of F;

2) values for O and S, obtained according to the formulas (7), (8);

3) number of affine transformation.

The decoding algorithm consists in the fact that two instances of the same image A and B are taken, the distribution of brightness in which is irrelevant. The areas whose boundaries coincide with boundaries of ranks and domains areas are selected on these images and then, using known values of affine coefficients, by the domains selected in image B brightness distributions in the rank areas of image A are found. After that, images A and B change places and the operation is repeated. It can be shown that with many repetition of this operation, the brightness distribution in images A and B will be closer to the brightness distribution in the original image. Let's pay attention to the fact that the algorithms of compression and decompression are asymmetric. It is also worth noting that the compression process takes much longer than the decompression process. Decoding of the compressed image is iterative and consists of the following steps:

1) two images of the same size A and B are created. The size of these images does not necessarily equal the size of the original image; the initial drawing of areas A and B does not matter;

2) the image B is divided into rank areas, as in the first stage of the compression process. For each rank area of image B an affine transformation of the corresponding domain area of image A is performed and the result is placed in B.

3) performed operations are identical to the previous item, only the images A and B swap places;

4) the second and third steps are repeated repeatedly until the images A and B do not become indistinguishable.

The main disadvantage of the fractal method is the low rate of encoding, which is due to the fact that in order to obtain high image quality for each rank block, it is necessary to go through all domain blocks and at least eight affine transformations must be performed for each domain block [5].

3.2 Known methods to increase the rate of fractal image compression algorithm

To improve the speed and efficiency of fractal image encoding, a number of optimization methods are used. The simplest and slowest way of fractal encoding is to check each domain block and perform calculations according to the expressions (5), (7), (8). This method is called an exhaustive search. When encoding images of natural origin, you can increase the coding speed by taking $S = 1$, since, taking into account the image statistics, there is always a domain block that approximates a given rank block with the required precision. Then from the expressions (5), (7) we get:

$$F = \sum_{i,j} (d_{ij} + O_{ij} - r_{ij})^2, \tag{9}$$

$$O = \frac{1}{n^2} \cdot \left(\sum_{i,j}^{n} r_{ij} - \sum_{i,j}^{n} d_{ij} \right). \tag{10}$$

The contrast of the decoded image can be restored by other methods. This simplification allows you to reduce the number of arithmetic operations by 60 % and, accordingly, increase the compression speed.

The most popular methods for increasing the speed of encoding images by fractal method are as follows [10]:

1) search for domain blocks that do not exceed the specified value;

2) local and sub-local search;

3) isometric prediction;

4) classification of domain and rank blocks, the ranked compares with domain blocks of the same class.

Among the methods should be noted the classification proposed by Arnaud Jacquin [1, 8]. It is based on the block topology and involves:

– blocks without contours;

– blocks, invariant to the orientation (texture blocks);

– contour blocks (exhaustive search).

3.3 Increasing the rate of the fractal image compression by two-dimensional approximation

To increase the speed of image compression under the Arnaud Jacquin scheme, it is proposed to perform a preliminary selection of domain blocks based on the approximation coefficients [7].

In the case of linear approximation, the pixel value for a two-dimensional image is determined as follows:

$$f(x, y) = ax + by + c. \tag{11}$$

In the general case, the values of $f(x, y)$ differ from the value of the pixel zxy. The minimum distance value is achieved with a minimum value of the sum of squares of distances, that is:

$$S=\sum_{x=1}^{N}\sum_{y=1}^{M}(ax+by+c-z_{xy})^2=Min, \tag{12}$$

where M, N – image size; z_{xy} – pixel value at the point of the image with the coordinates x, y.

The function S has a minimal extremum at the point where partial derivatives of the coefficients are zero:

$$\frac{\partial S}{\partial a}=0,\ \frac{\partial S}{\partial b}=0,\ \frac{\partial S}{\partial c}=0. \tag{13}$$

Thus, we obtain a system of three equations for three unknowns. For ranked blocks with a size $n = 4$, the system of equations is as follows:

$$\begin{cases} 120a+100b+40c=\sum_{y=1}^{4}\sum_{x=1}^{4}z_{xy}x \\ 100a+120b+40c=\sum_{y=1}^{4}\sum_{x=1}^{4}z_{xy}y \\ 40a+40b+16c=\sum_{y=1}^{4}\sum_{x=1}^{4}z_{xy} \end{cases} \tag{14}$$

Having solved the system of equations (14), it is possible for each rank and domain blocks to determine the coefficients of approximation a, b, c.

Therefore, the encoding process will have the following additional steps:

1. Each domain and rank block is presented in the form of coefficients of approximation. For $n = 4$, the approximation coefficients from (14) are calculated as follows:

$$b=\frac{-3\sum_{x=1}^{4}\sum_{y=1}^{4}z_{xy}+1{,}2\sum_{x=1}^{4}\sum_{y=1}^{4}z_{xy}y}{24}; \tag{15}$$

$$c=\frac{3\sum_{x=1}^{4}\sum_{y=1}^{4}z_{xy}-\sum_{x=1}^{4}\sum_{y=1}^{4}z_{xy}x-20b}{8}; \tag{16}$$

$$a=\frac{3\sum_{x=1}^{4}\sum_{y=1}^{4}z_{xy}-\sum_{x=1}^{4}\sum_{y=1}^{4}z_{xy}y-8c}{20}. \tag{17}$$

2. For each rank block, pre-selection of domain blocks is performed by three coefficients of approximation, for example, by quadratic deviation:

$$\begin{aligned} S_{rd1}&=(a_r-a_d)^2+(b_r-b_d)^2+(c_r-c_d)^2; \\ S_{rd2}&=(a_r-b_d)^2+(b_r-a_d)^2+(c_r-c_d)^2, \end{aligned} \tag{18}$$

where a_r, b_r, c_r – coefficients of approximation for the rank block; a_d, b_d, c_d – coefficients of approximation for the domain block.

With the selected blocks, the transformations characteristic of fractal compaction by the Jacquin method are performed. Since the selected blocks number is considerably less than the total number of domain blocks, one should expect a significant gain in speed.

4 Results

The simulation executed in the Python programming language showed that the proposed method for increasing the speed of fractal image compression can achieve acceleration of 5–10 times compared to the Arnaud Jacquin's method (exhaustive search) without serious loss of image visual quality (Figure 2).

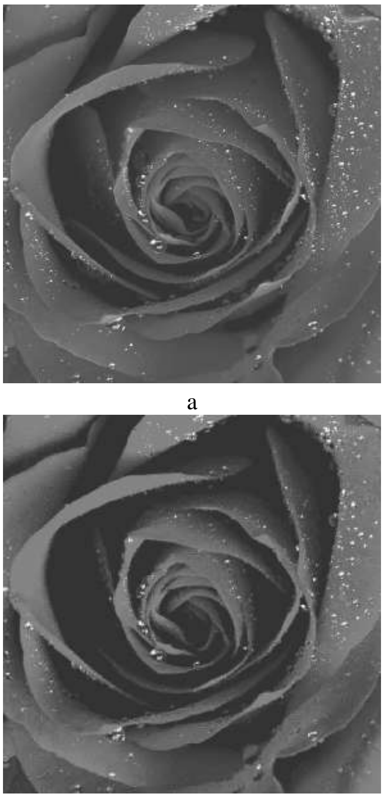

a

b

Figure 2 – Results of simulation of high-speed fractal compression: a – original image; b – image restored after encoding by the proposed method

For example, on the same computer, it takes about 52 minutes to encode an image of 512×512 by the method proposed by Arno Jacquin, and for encoding the image according to the method proposed above – only 5 min, that is, the encoding speed increased by 10 times.

To compare the proposed method and Arnaud Jacquin's method in Table 1, results are presented for images of different sizes. The larger size of the image, the better results are provided by the proposed method, since the pre-selection reduces the space for finding domain blocks for each rank block.

Table 1 – Comparison of the encoding time of images of various sizes

Image size	exhaustive search tg, s	proposed method ts, s	Acceleration rate, tg/ts
128×128	9.7	1.4	6.9
256×256	196	24	8.3
512×512	3 125	302	10.3
1024×1024	19 333	1 588	12.2

5 Conclusions

The main disadvantage of the fractal method is the low rate of encoding, which is due to the fact that in order to obtain high image quality for each rank block, it is necessary to go through all domain blocks and at least eight affine transformations must be performed to each domain block. The method for increasing the fractal compression speed by proposing rank and domain blocks in the form of coefficients of approximation is proposed. This allows to perform a quick pre-selection of domain blocks, which ultimately increases the fractal seal speed on average by 10 times.

REFERENCES

1. Welstead, S. (1999). *Fractal and wavelet image compression techniques*. Bellingham, SPIE Optical, Engineering Press.
2. Fisher, Y., Jacobs, E. W., & Boss, R. D. (1991). *Fractal image compression using iterated transform*.
3. Jacquin, A. (1992). Image coding based on a fractal theory of iterated contractive image transformations. *IEEE Transactions on Image Processing*, pp. 18–30.
4. Ghosh, S. K., Mukherjee, J., & Das, P. P. (2004). Fractal image compression: a randomized approach. *Pattern Recognition Letters*, Vol. 25, pp. 1013–1024.
5. Thomas, L., & Deravi, F. (1995). Region-based fractal image compression using heuristic search. *IEEE Transactions on Image Processing*, Vol 4, pp. 832–838.
6. Maydanyuk, V. P. (2001). *Metody i zasoby komp'yuternykh informatsiynykh tekhnolohiy. Koduvannya zobrazhen'*. Vinnytsya: VDTU [in Ukrainian].
7. Kozhem'yako, V. P., Maydanyuk, V. P., Zhukov, K. M., Khamdi, R. R., & Pika, S. O. (1999). Fraktal'ne stysnennya zobrazhen' pryrodnoho pokhodzhennya. *Vymiryuval'na ta Obchyslyuval'na Tekhnika v Tekhnolohichnykh Protsesakh*, Vol. 2, pp. 50–54.
8. Kozhemiako, V. P., Maidanuk, V. P., Pika, S., & Zhukov, K. M. (2001). Speeding up of fractal image compression. *Proceeding of SPIE*, Vol. 4425, pp. 9–16.
9. Maydanyuk, V. P., Lishchuk, O. O., & Korol', D. C. (2017). Aspekty optymizatsiyi shvydkosti fraktal'noho ushchil'nennya zobrazhen'. *Optyko-Elektronni Informatsiyno-Enerhetychni Tekhnolohiyi*. Vol. 1(33), pp. 24–32 [in Ukrainian].
10. Maydanyuk, V. P., & Lishchuk, O. O. (2018). Pidvyshchennya shvydkosti fraktal'noho metodu ushchil'nennya zobrazhen' za rakhunok aproksymatsiyi. *Internet – Education – Science*, pp. 7–9 [in Ukrainian].

Підвищення швидкості фрактального ущільнення зображень з використанням двовимірних апроксимуючих перетворень

Майданюк В. П., Арсенюк І. Р., Ліщук О. О.

Вінницький національний технічний університет, вул. Хмельницьке Шосе, 95, 21021, м. Вінниця, Україна

Анотація. Алгоритм фрактального ущільнення зображень відомий тим, що у деяких випадках дозволяє отримати дуже високі коефіцієнти ущільнення (найкращі приклади – до 1000 разів за прийнятної візуальної якості) для реальних фотографій природних об'єктів, що є неможливим для інших алгоритмів ущільнення зображень із втратами. Основним недоліком фрактального методу є низька швидкість кодування, яка пов'язана з тим, що для отримання високої якості зображення для кожного рангового блоку необхідно виконати перебір усіх доменних блоків, і для кожного доменного блоку необхідно виконати не менше восьми афінних перетворень. Незважаючи на велику кількість праць, присвячених підвищенню швидкості фрактального ущільнення зображень, варто констатувати, що дана проблема залишається актуальною. Метою роботи є пошук методів підвищення швидкості фрактального ущільнення зображень. На основі аналізу відомих підходів підвищення швидкості фрактального ущільнення запропоновано метод, який грунтується на поданні рангових та доменних блоків у вигляді коефіцієнтів двовимірної лінійної апроксимації, що дозволяє для кожного рангового блоку виконати швидкий попередній відбір доменних блоків за трьома коефіцієнтами апроксимації. З відібраними блоками виконуються перетворення, характерні для фрактального ущільнення. Оскільки обраних блоків значно менше загальної кількості доменних блоків, то слід очікувати значного збільшення швидкості ущільнення. Моделювання, виконане із застосуванням мови програмування Python, показало, що запропонований метод дозволяє підвищити швидкість фрактального ущільнення зображень у середньому в 10 разів порівняно з методом за схемою А. Жакена без суттєвих втрат візуальної якості зображення.

Ключові слова: ущільнення зображень, фрактальне кодування, двовимірна апроксимація, фрактальні властивості зображення.

JOURNAL OF ENGINEERING SCIENCES
ЖУРНАЛ ІНЖЕНЕРНИХ НАУК
ЖУРНАЛ ИНЖЕНЕРНЫХ НАУК
Web site: http://jes.sumdu.edu.ua
DOI: 10.21272/jes.2019.6(1).e4
Volume 6, Issue 1 (2019)

UDC 629.113

Optimum Choice of the Front Suspension of an Automobile

Belkhode P. N.

Laxminarayan Institute of Technology, R.T.M. Nagpur University, 440033 Nagpur, India

Article info:
Paper received: December 21, 2018
The final version of the paper received: February 4, 2019
Paper accepted online: February 9, 2019

***Corresponding Author's Address:**
pramodb@rediffmail.com

Abstract. The paper details the optimum choice of the front suspension of an automobile. The influence of suspension on the steering geometry is studied by considering the various combinations of joints at the four-bar mechanism of the front suspension. The purpose of the suspension is to make the job easier for the tires and give a predictable behavior so that the driver will have control of the car. The most common suspension used is double wishbone. The performance of the steering geometry depends upon the performance of various steering parameters such as kingpin angle, caster angle, camber angle, toe in and out and scrub radius. This steering geometry depends upon the position of kingpin axis an imaginary line passing through the knuckle pin. The steering geometry is a function of vehicle speed, link lengths, and road condition. The selection of the optimum choice of the suspension makes the benefit the comfort for driving and controlling the vehicle conditions.

Keywords: suspension, steering geometry, front suspension, optimum, mechanism.

1 Introduction

The suspension of the front wheels is more complicated than the suspension of the rear wheels. This is because the front wheels move up and down. Front suspension changes the orientation of wheel with respect to the road, affecting the steering behavior and tire. The most common suspension used is double wishbone. As this suspension locates the wheels and controls the geometry of their movement, over bumps. Unequal length wishbones are preferred because they separate the effects of the springs more effectively and controls wheel movement better. The upper wishbone is shorter than the lower one for superior camber control. Therefore, it is also called as SLA which stands for Short Long Arm. It is easily recognized that an SLA suspension is a three-dimensional four bar mechanism [1–2].

Ball joints provide key pivot points in the front independent suspension set up. In operation the swiveling action of the ball joints allows the wheel and spindle assemblies to be turned left or right and to move up and down with changes in road surface geometry. Four control arms are connected with spherical joints, lower ones and upper ones [3]. The other ends of these control arms are connected to the vehicle frame via revolute joints. Various types of mechanisms with two spherical pairs along with revolute pairs and cylindrical pairs were formed by changing the position of various joints [4]. These mechanisms are analyzed for the optimum choice of a front suspension. It also presents the steering geometry parameters along with the measuring techniques. This exercise can be looked upon as a type synthesis of suspension mechanism [5].

2 Research Methodology

2.1 Steering geometry parameters

Presently steering geometry parameters kingpin inclination angle, caster angle, camber angle, toe angle are measured using alignment equipment, caster / camber gauge, a set of turntable and bubble gauges. The steering wheel should be centered while measuring the steering performance. Turn the steering wheel completely to the right then turn the wheel completely to the left and count the number of turns of the steering wheel. After following the complete procedure steering geometry performance parameters are measured and adjusted.

On the basis of six included angles of the 3D front suspension mechanism, one at each revolute joints and two at each spherical joints of this four bar chain, the position of kingpin axis is determined. Steering performance depends on the position of a kingpin axis. Depending on the position of the kingpin axis, caster angle, camber angle, kingpin angle, and toe angle of the four-wheel vehicle are decided.

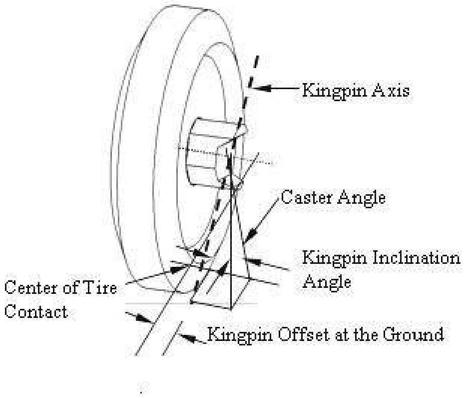

Figure 1 – Steering geometry parameters [6]

The position of the kingpin axis is determined using the Denavit Hartenberg Principle [6–7].

Joint O1 and O2 are revolute joints and joints A and B are Spherical joints as shown in Figure 2. The relative orientation of two links connected at je joint can be decided in terms of magnitudes of included angles which in turn can be measured by the potentiometer and associated electronic instrumentation [8].

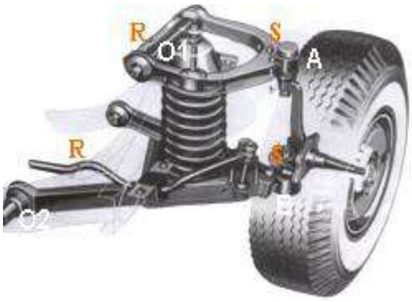

Figure 2 – The front suspension of an automobile
(A-arm front suspension) [6]

2.2 Selection of the "Revolute-Spherical-Sherical-Revolute" mechanism

The front suspension is a three-dimensional four-bar mechanism having four control arms. These arms are connected with four joints, lower ones, and upper ones. Various types of mechanisms with two spherical pairs along with revolute pairs and cylindrical pairs were formed by changing the position of various joints for linear motion and rotational motion. Linear and rotational motion completely defines the relative position of the control arms. Table 1 shows the formulation of various combinations of mechanisms by changing the joints, where S – "spherical", R – "revolute", C – "cylindrical" signs; X indicates that motion is restricted in columns 2, 3 and 5, whereas X indicates in column 4 that motion is permitted.

The analysis of different combinations of mechanism is done by the Denavit Hartenberg notation [9–11]. The analysis of RSSR, RRSS, and SRRS out of 24 mechanisms of table 1 is shown below [12–14].

Table 1 – Formulation of various combinations of mechanisms

Type synthesis of O1-A-B-O2 (1-2-3-4)	Rotation of knuckle link	Vertical movement of knuckle link	Motion of upper and lower arms in Y direction	Motion of both arms O1-A and O2-B due to link AB
SSCR	–	–	×	–
SSRC	×	–	×	–
CSSR	–	–	–	–
RSSC	–	–	–	–
CRSS	×	×	×	–
RCSS	–	–	×	–
SCRS	×	×	×	–
SRCS	×	×	×	–
SSRR	×	×	×	–
RSSR	–	–	–	–
RRSS	×	×	×	–
SRRS	×	×	×	–
SSCC	–	–	×	–
CSSC	–	–	–	–
CCSS	–	–	×	–
SCCS	–	–	×	×
RSSS	–	–	×	–
SRSS	×	×	×	–
SSRS	×	×	×	–
SSSR	–	–	×	–
CSSS	–	–	×	–
SCSS	–	–	×	–
SSCS	–	–	×	–
SSSC	–	–	×	–

3 Results

The design schemes proposed in the research [6] are presented in Figures 3–5 and described below.

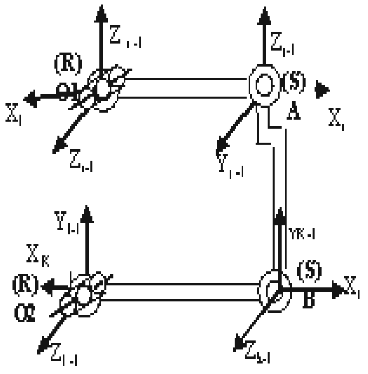

Figure 3 – RSSR ("Revolute-Spherical-Spherical-Revolute")

1. Rotation of link AB is free to rotate about the vertical axis in the clockwise and anticlockwise directions. This makes steering easy. Therefore X is not marked in column 2 of Table 1 as motion is not restricted.

2. Vertical movement of knuckle link AB is possible. Since joint A and joint B is spherical joints. Therefore X is not marked in column 3 of Table 1 for not restricted motion.

3. Since the joint O1 and joint O2 are revolute joints, motion in Y direction of upper arm O1-A and motion of lower arm O2-B is restricted. Therefore X is not marked in column 4 of Table 1 for restricted motion.

4. Upper arm O1A and lower arm O2-B are moved by motion getting from link AB. Therefore X is not marked in column 5 of Table 1 as motion is not restricted [15].

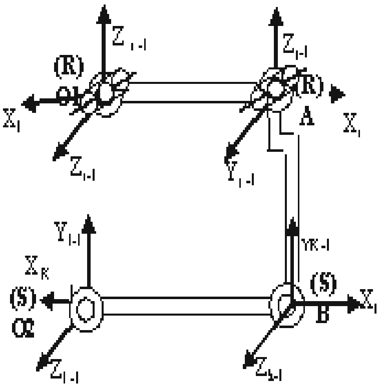

Figure 4 – RRSS ("Revolute-Revolute-Spherical-Spherical")

1. Rotation of link AB is not free to rotate about the vertical axis in the clockwise and anticlockwise directions. This makes steering difficult. Therefore X is marked in column 2 of Table 1 as motion is restricted.

2. Vertical movement of knuckle link AB is not possible. Since joint A is revolute joint and joint B is spherical. Therefore X is marked in column 3 of Table 1 for restricted motion.

3. Since the joint O1 is revolute and joint O2 is spherical Joint, motion in the Y direction of upper arm O1-A is restricted whereas the motion of lower arm O2-B is permitted. Therefore X is marked in column 4 of Table 1 for permitted motion.

4. Upper arm O1A and lower arm O2B are moved by motion getting from link AB. Therefore X is not marked in column 5 of Table 1 as motion is not restricted.

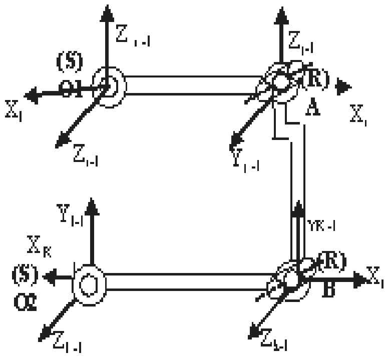

Figure 5 – SRRS ("Spherical-Revolute-Revolute-Spherical")

1. Rotation of link AB is not free to rotate about vertical axis in clockwise and anticlockwise direction. This makes steering difficult. Therefore X is marked in column 2 of Table 1 as motion is restricted.

2. Vertical movement of knuckle link AB is not possible. Since joint A and joint B is the revolute joint. Therefore X is marked in column 3 of Table 1 for restricted motion.

3. Since the joint O1 and joint O2 are spherical joints, motion in the Y direction of upper arm O1-A and motion of lower arm O2-B is permitted. Therefore X is marked in column 4 of Table 1 for permitted motion.

4. Upper arm O1A and lower arm O2-B are moved by motion getting from link AB. Therefore X is not marked in column 5 of Table 1 as motion is not restricted.

4 Conclusions

The complete analysis of these 24 combinations of mechanisms concluded that four types CSSR, RSSC, RSSR, and CSSC are usually selected. From the safety and maintenance point of view CSSR, RSSC and CSSC are avoided due to axial movement of cylindrical joints. Finally, the RSSR ("Revolute-Spherical-Spherical-Revolute") is considered to be the best for giving the complete motion performed by the suspension.

5 Acknowledgments

The author sincerely thank Professor Dr. J. P. Modak, Ex-Professor VNIT, Nagpur, and Dean (R&D), PCE, Nagpur for discussion and reading during manuscript preparation.

References

1. Belkhode, P. N. (2017). Mathematical Modelling of Liner Piston Maintenance Activity using Field data to Minimize Overhauling Time and Human Energy Consumption. *Journal of the Institution of Engineers, Series C, Springer Publication*, pp. 1–9.
2. Belkhode, P. N., & Vidyasagar, V. (2014). Mathematical Model for Face Drilling in underground mining operation. *IJERST International Journal of Engineering Research and Science Technology*, Vol. 3(2).
3. Belkhode, P. N., & Borkar, K. (2013). Modelling and Analysis of Overhauling of Crankshaft in Locoshed. *International Journal of Engineering Research and Technology. ESRSA Publication*, Vol. 2(11).
4. Belkhode, P. N., & Borkar, K. (2014). Maintenance Activity for Locomotive Crankshaft by using FDBM Approach for Saving the Resources. *International Journal of Engineering and Technical Research, ER Publications*, Vol. 2(9).

5. Gillespie, T. D. (1992). *Fundamentals of Vehicle Dynamics*. Society of Automotive Engineers, Warrendale Inc., PA.
6. Suh, & Redcliff (1978). *Kinematics Design of Mechanisms*, John Wiley & Sons, New York.
7. Denavit, & Hertenberg (1955). A Kinematic Notation for Lower Pair Mechanisms Based on Matrices. *ASME Transaction, Journal of Applied Mechanics*, pp. 215–221.
8. Rill, G. (2007). *Vehicle Dynamics*. Fachhochschule Regensburg, University of Applied Sciences, Hochschule for Technik Wrtschaft Soziales.
9. Fu, K. S., Gonzalez, R. C., & Lee, C. C. G. (1987). *Robotics: Control Sensing, Vision and Intelligence*. Mc Graw Hill International Edition, Signapore.
10. Lin, P. D., & Hsich, J. F. (2007). A New Method to Analyze Spatial Binary Mechanism with Spherical Pairs. *Journal of Mechanical Design*, Vol. 129, pp. 455–458.
11. Gao, J., Case, K. W., & Magle, S. P. (1995). *General 3D-Tolerance Analysis of Mechanical Assemblies with small Kinematic Adjustments*. ADCATS Report No. 94-2.
12. Tao, D. C. (1964). *Applied Linkage Synthesis*. Addison–Wesley Publishing Company Inc., London.
13. Theander, A. (2004). *Design of a Suspension for a Formula Student Race Car, Vehicle Dynamics Aeronautical and Vehicle Engineering*. Royal Institute of Technology, Sweden.
14. Singh, K. (2003). *Automobile Engineering*. Standard Publishers Distributors, Delhi.
15. Ramalingam, K. K. *Automobile Engineering – Theory and Practice*. SciTech Publications, Pvt. Ltd., Chennai, India.

Оптимальний вибір передньої підвіски автомобіля

Белходе П. Н.

Лаксмінарайський технологічний інститут, Університет м. Нагпур, 440033, м. Нагпур, Індія

Анотація. У статті розглядається процедура вибору оптимальної геометрії передньої підвіски автомобіля. Досліджується вплив підвіски на геометрію керма з урахуванням різних комбінацій шарнірів чотирьохбалкового механізму передньої підвіски. Метою підвіски є полегшення роботи шин і надання передбачуваної поведінки для того, щоб водій мав контроль над автомобілем. Найбільш уживаною підвіскою є подвійна поперечина. Ефективність геометрії керма залежить від виконання різних параметрів керування, таких як кут зчеплення, кут конуса, кут розвалу, тощо. Ця геометрія керма залежить від положення осі шпильки як уявної лінії, що проходить крізь штифт. Геометрія рульового керування є функцією швидкості транспортного засобу, довжини ланки та стану доріг, тому вибір оптимального вибору підвіски надає перевагу комфорту для керування та контролю умов використання автомобіля.

Ключові слова: підвіска, геометрія керма, передня підвіска, оптимум, механізм.

JOURNAL OF ENGINEERING SCIENCES
ЖУРНАЛ ІНЖЕНЕРНИХ НАУК
ЖУРНАЛ ИНЖЕНЕРНЫХ НАУК
Web site: http://jes.sumdu.edu.ua
DOI: 10.21272/jes.2019.6(1).e5 Volume 6, Issue 1 (2019)

UDC 621.671:621.668:532.528

Influence of an Inlet Rotating Axial Device on the Cavitation Processes in a Low Specific Speed Centrifugal Pump

Moloshnyi O. M.[1*], Szulc P.[2], Sotnyk M. I.[1]

[1] Sumy State University, 2 Rymskogo-Korsakova St., 40007 Sumy, Ukraine;
[2] Wroclaw University of Science and Technology, 27 Wybrzeze Wyspianskiego St., 50-370 Wroclaw, Poland

Article info:
Paper received: December 1, 2018
The final version of the paper received: March 21, 2019
Paper accepted online: March 26, 2019

***Corresponding Author's Address:**
o.moloshnyi@outlook.com

Abstract. The paper is devoted to the analysis of the cavitation processes in the flow section of the low specific speed centrifugal pump. A new conception of double-entry hermetic pump leads to the application of special shaped inlet device, which is a part of an electrical motor rotating element. Four flow geometrical models of the axial inlet device were taken into consideration. The first model, treated as referential and basic, has a cylindrical shape with small diffuser and a cone in front on the impeller. Other three models consist of the motionless cone, which was part of the housing, straight pipe, and diffuser section rotating analogously to the impeller and a spherical fairing. The research was conducted using physical experiments and numerical simulations of the workflow in the ANSYS CFX software environment. The analysis of the results shows that the pump with the basic model of the inlet device has NPSH 3 % above the average values. The comparison between CFD and experiment of the cavitation curves shape showed its similarity but determined by means of the physical experiment have higher values. Cavitation in the impeller starts earlier than in the axial inlet device. The zones of the cavitation in the axial inlet device are located after the cone, at the beginning of the diffuser section and near the fairing at the outlet of the diffuser section. The cavitation zone, which is located after the cone, is separated from the walls of the axial inlet device. The value of the NPSH 3 % increases, when the diameter of the axial inlet device decreases, as the result of the raise of head loses in the inlet structure.

Keywords: inlet chamber, inlet nozzle, intake section, suction casing, cone, diffuser, CFD, NPSH, cavitation performance.

1 Introduction

Cavitation is a negative phenomenon that can occur in a pump. Its appearance in the preliminary phase leads to the increasing of the pulsation of a pressure, as well as the raise of the vibration and noise. Further development of the cavitation reduces the head and the efficiency of the pump. A consequence of the long cavitation process, the destruction of the impeller material could be observed. Therefore, scientists and engineers are devoting a lot of attention to the study and understanding of the cavitation phenomenon and ways to reduce the likelihood of its occurrence in rotating machinery.

As it is known, the greatest influence on the appearance of cavitation has the pressure at the impeller inlet and the temperature of the water. Moreover, the structure of the flow at the impeller inlet has also significant impact on the cavitation performances of the pump. It is determined by the shape and geometrical parameters of the inlet device, the inlet part of the impeller, the leading edges of the blades, the design of an inducer (if it is) and, of course, of the rotating speed.

2 Literature Review

The most popular method for eliminating cavitation in the impeller is the addition of the inducer [1]. However, in this case, cavitation may occur on the inducer blades. To weaken the cavitation processes Jiang et. al [2] proposed additional flow jets in front of the inducer. Tkach [3] demonstrated the benefits of using a stator sleeve with ribs around the inducer to reduce the cavitation erosion.

Si et. al [4] presented a method for improving the cavitation performances of the centrifugal pump by introducing a jet flow into the pump inlet device. However, the cavitation performances of the pump deteriorated with the increase of the flow rate.

Tan et. al [5, 6] discovered, that the cavitation performances deteriorate when the pump is regulated by prewhirl of the flow by inlet guide vanes in front of the impeller. At the same time, there was a slight increase in pressure and efficiency. Skerlavaj et. al [7] discovered a decrease in the cavitation area on the suction side of the blades when the fluid is swirled in the symmetric inlet casing. However, Nagahara et. al [8] discovered that a large swirling of the flow in the inlet device of the vertical pump led to the formation of a cavitation vortex.

According to the results of the experiment conducted by Sikora et. al [9] the process of the appearance of the cavitation bubbles in a direct inlet pipe was accompanied by a decrease in volume flow. Cucha et. al [10] presented a comparison of the results of a numerical and an experimental study of cavitation in the nozzle. The cavitation zone occurs immediately after a sudden entry into the nozzle and is stretched under the walls.

Hergt et. al [11] found that the diffuser before the impeller reduces the length of the recirculation zone and reduces the risk of the cavitation. In turn, Gulich [12] noted the efficiency of using the diaphragm to reduce the cavitation. Limbach [13] analyzed the pump with the diffuser but did not describe its effect on the cavitation phenomena and performances. Moloshnyi et. al [14] analyzed the cavitation processes in a pump with the similar shape of inlet device and found the cavitation zone in the diffuser. Using the sudden expansion at the outlet of the diffuser decreases their area.

The literature review shows that the influence of the change in the cross-sectional area of the inlet device and the rotation of its walls on cavitation processes in the pump are not sufficiently described.

To determine the influence of the diameter of the passage channel in the axial inlet device (AID) with rotating walls on the cavitation performances of the pump and the structure of the cavitation zones in the AID and impeller.

3 Research Methodology

3.1 Object of a study

The object of the study is a low specific speed close coupled centrifugal pump, which corresponds to half of double entry pump. Nominal flow rate Q_{nom} = 16 m^3/h, head H =10 m, rotational speed n = 1450 rpm, specific speed $n_q = n \cdot Q^{0.5}/H^{0.75} \approx 17.5$ rpm. Impeller eye diameter D_0 = 63 mm, impeller outer diameter D_2 = 192 mm, the number of impeller blades z = 7.

Four structures of the AID were dedicated for consideration and research. The construction of AID 0 was a cylindrical shape with a slight diffuser and a cone in front of the impeller (Fig. 1). The AIDs 1,2,3 were designed as an inlet device of the double entry pump. The fluid flows into the cavity of the pump shaft, which additionally is a part of the inlet device. The AIDs 1, 2, and 3 have a motionless cone at the inlet which is part of the housing, straight and diffuser sections, which are rotating with the rotational speed of the pump shaft, and also a spherical fairing. The diameter of the cylindrical section (d) for AIDs 1, 2, 3 was respectively 44 mm, 40 mm, and 36 mm. The diameter of the inlet pipe (D_{in}) was 65 mm. The total length of all AID (L) was 260 mm and the rotating AIDs section length (l_{rot}) was 207 mm. The length of the cone (l_{con}) and the diffuser section of the AIDs (l_{dif}) was 33 mm and 51 mm, respectively. The inner diameter of the outlet from the AIDs (d_{out}) was 20 mm. Overall dimensions of analyzed AIDs were limited by the dimensions of the pump housing. The maximum diffuser angle (ϑ) for organizing the uniform flow out of the diffuser was calculated by the formula given in [12]:

$$\vartheta = 16{,}5[d/(2l_{dif})]^{0.5} = 16.5 \cdot [44/(2 \cdot 51)]^{0.5} = 10.8°.$$

Diffuser angle of the AID 1 was assumed as 10.5°, which is permissible, but for other investigated AIDs, it exceeded this value.

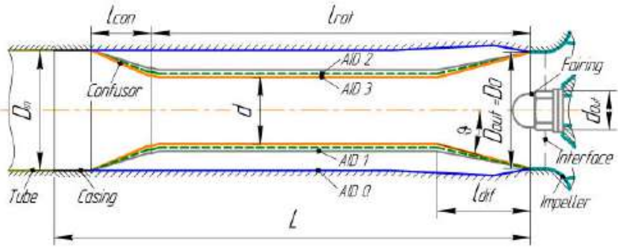

Figure 1 – Scheme of the AID models

3.2 Physical experiment

The physical experiment, to determine the cavitation performances of the pump with different AID structures, was conducted on a special prepared test rig (Fig. 2).

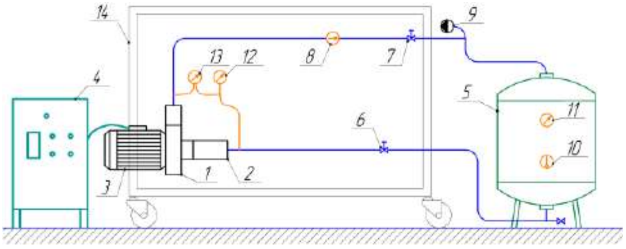

Figure 2 – Principal scheme of the experimental stand:
1 – researched pump; 2 – housing of the AID; 3 – electric motor; 4 – frequency converter with integrated powermeter; 5 – tank; 6, 7 – valves; 8 – electromagnetic flowmeter; 9 – vacuum pump; 10 – thermometer; 11 – pressure gauge; 12 – electronic pressure-and-vacuum gauge; 13 – electronic differential pressure gauge; 14 – mounting frame of the stand

Analysed pump reproduces half of the flow part of the double entry pump (Fig. 3 a). The AID, the impeller and the spiral with guide vanes of the researched pump were made from plastic using 3D-printing method (Fig. 3 b). As the material for printing PETG (Polyethylene Terephthalate Glycol) was used. The test was conducted according to ISO 9906:2012(E) Rotodynamic pumps – Hydraulic performance acceptance tests. Accuracy classes of applied measuring devices were: the electronic pressure and vacuum gauge and electronic differential pressure gauge – 0.5, powermeter – 0.5 and electromagnetic flowmeter – 0.5. The pumping fluid during the test was pure water at temperature 25 °C. The physical experiment was carried out for the AIDs 0, 1, and 2. During the test, the decrease of the pressure at the inlet was made by means of the vacuum pump.

3.3 Numerical simulation

The model of a fluid computational domain of the researched pump was constructed at the beginning (Fig. 3 a). It contains the suction and discharge pipes, the AID, the impeller and the spiral with guide vanes. Simplification of the flow domain was made by assuming that there are no sinuses in the pump, to reduce the complexity of the grid and increase the speed of the calculation. According to comparative calculations, such assumptions influenced no the results of the final calculation within 1 %. Numerical simulation of the flow were carried out for 4 models of the AID.

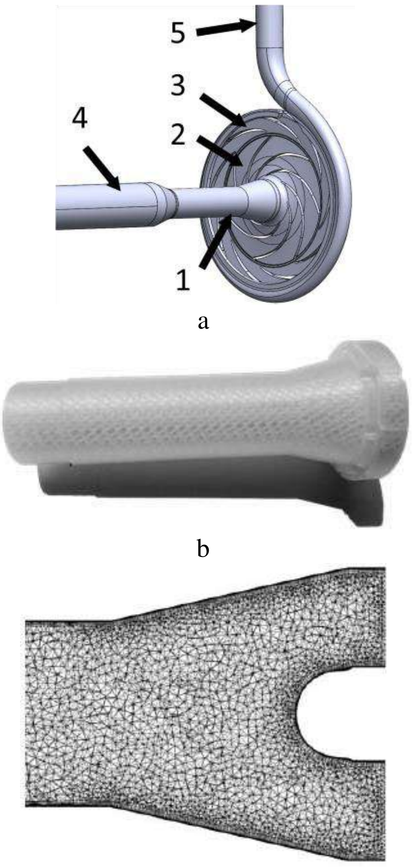

a

b

c

Figure 3 – Investigated model: a – solid model of flow parts of the pump: 1 – axial inlet device (AID); 2 – impeller; 3 – the spiral with guide vanes; 4 – suction pipe; 5 – discharge pipe; b – the plastic rotating part of the AID 2; c – the mesh of the diffuser section with fairing of the AID 2

The numerical simulation of fluid flow in the components of the pump was conducted using the ANSYS CFX software. The Rayleigh–Plesset equation, the standard k–ε turbulence model and the Reynolds equation was used. Boundary conditions were: the total pressure at the pump inlet and the mass flow rate at the pump outlet. Working fluids were water and water–vapor at temperature 25 °C. The saturated steam pressure was set as 3167 Pa. The surface roughness of the printed elements was assumes as 25 μm. The numerical calculation was carried out at (0.7, 1.0, 1.3)·Q_{nom}.

An unstructured mesh was generated using software ICEM–CFD (Fig. 3 c). Elements size was selected via mesh independence research. Layers of prismatic elements were created near solid walls in the boundary layer. The total number of nodes of the pump model was 3.3 mln. The inlet device, the impeller and the spiral contain 0.5 mln, 1 mln and 1.25 mln nodes, respectively.

4 Results and Discussion

The cavitation performances of the pump for (0.7, 1.0, 1.3)·Q_{nom} are determined (Fig. 4). The value of the Net Positive Suction Head (NPSH) is determined by the drop of the head value by 3 % (NPSH 3 %). The basic AID has the lowest cavitation performances. According to the results of the numerical experiment NPSH 3 % is 0.3 m at Q_{nom}. The maximum NPSH3% was achieved for the AID 3 – 1.2 m at Q_{nom}. The value of the NPSH 3 % increases, when the diameter of the AID decreases. This is caused by an increase of the losses in the AID and the change in the structure of flow at the impeller eye.

A sharp drop of the pump head in course of the raise of the intensification of the cavitation phenomena is characteristic of the pumps with a low value of the specific speed. The smallest area of the passage channel relative to other places of the impeller is located between leading edges of neighboring blades. In the process of the developing cavitation, the vapor quickly occupies the passage between blades and leads to a breakdown of the working process of the pump. The increase of the flow rate leads to the raise of NPSH 3 %, which is typical for the low specific speed pumps.

The value of the NPSH 3 % received during the physical experiment has higher values that the values obtained by the numerical simulation. NPSH 3 % for AIDs 0, 1, 2 at Q_{nom} were 0.7 m, 0.95 m, and 1.4 m. However, the shape of curves constructed using the results of a physical experiment and a numerical simulation are similar. Some deviations between the quantity character in obtained results (numerical simulation and experimental test) are widespread in [5, 13]. Possible causes are different roughness of the walls in the numerical model and the real elements, due to features of printing technology. The surface has a micro groove in the plane perpendicular to the rotation axis, which is not taken into account in the numerical model. Additional, the numerical model was the simplification of the real pump and the volumetric losses was not simulated, which can be bigger than normal in case of non–symmetrical clearance in the seals. That is why the results can be considered as accepted.

An important criterion for evaluating the occurrence of cavitation in the pumps with geometrically non-similar inlet device is the suction specific speed n_{ss}. It is defined as [12]:

$$n_{ss} = n\frac{\sqrt{Q_{nom}/f_q}}{NPSH_3^{3/4}},$$

where f_q is the number of the impeller eyes per impeller.

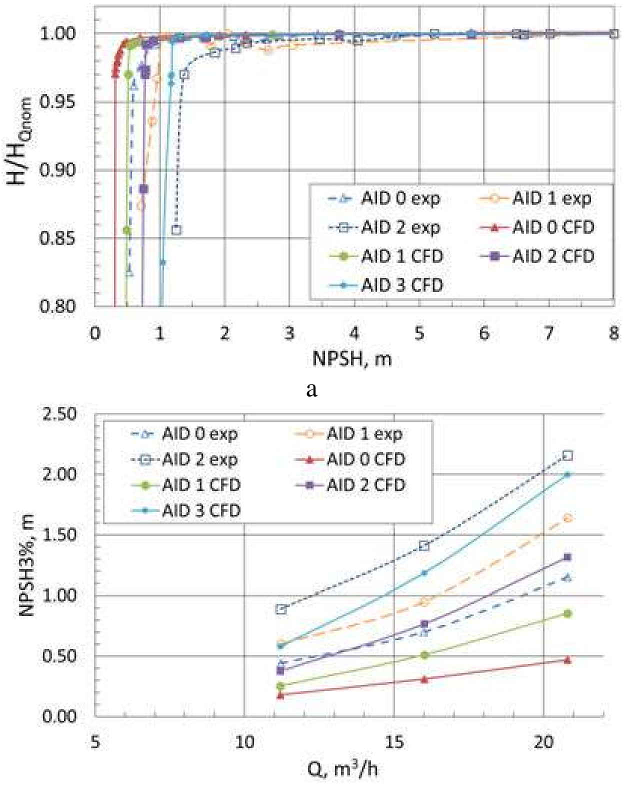

Figure 4 – Comparison of the cavitation performances curves: a – head–drop curves at Q_{nom}; b – NPSH 3 % curves at (0.7; 1.0; 1.3)·Q_{nom}

The calculated value of the suction specific speed at Q_{nom} for AIDs 0,1,2,3 is respectively 231, 160, 118, and 85. Typical values for centrifugal pumps with a standard impeller and an axial or semi–spiral inlet device are in the range of 160–220 [12]. That is, the AID 0 has better performance than standard pumps, AID 1 has a permissible value and AIDs 2, 3 have understated. However, it should be noted that the baseline for comparison is taken for pumps with a higher specific speed than the considered pump.

The AID 2 has a good head, energy, cavitation performances and also has the most optimal dimensions in terms of design features. More could be found in [15]. For further analysis, the *AID 2* was adopted.

The first occurrence of the cavitation was observed in the impeller at the suction side of the blades (near the leading edge) (Fig. 5 a). It is caused due to the flowing around the blades and the deviation of the direction of the flow. That means, the blade angle is too large and real Q_{nom} at bigger value is approximately 17 m^3/h. This is confirmed by Limbach [13]. These zones are larger in the AID 0 than in the AID 2 for *NPSH* = 3.76 m at Q_{nom}. However, their size does not affect the change in the pump head.

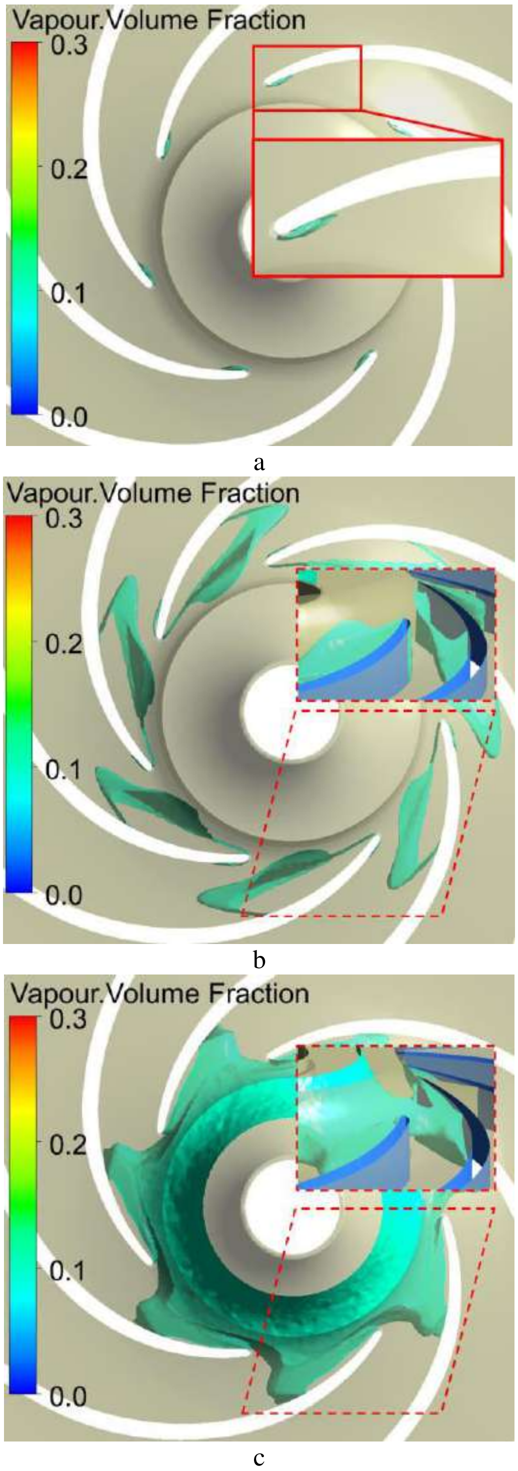

Figure 5 – The cavitation structure in the impeller at Q_{nom}: a – AID 2 *NPSH* = 1.71 m; b – AID 0 *NPSH* 3 % = 0.31 m; c – AID 2 *NPSH* 3 % = 0.77 m

The size of the cavitation zones and the content of water vapor increase, with the decreasing of the NPSH value. There is the uniform "growth" of the cavitation zone on the blades surface for the AID 0 (Fig. 5 b). There is a significant zone of the cavitation on the suction side of the blades, which occupies and overlaps about 2/3 area of the passage between leading edges of neighboring blades at the NPSH 3 % for the AID 0.

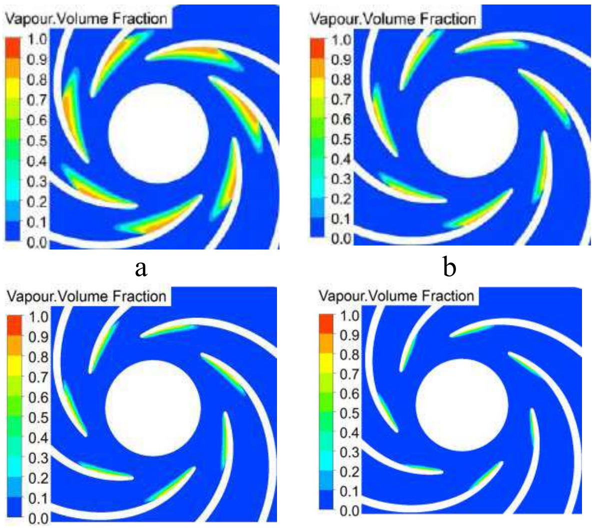

a b c d

Figure 6 – The vapour volume fraction distribution in the impeller cross section at a distance of *3/4* width of the blade from the front shroud at the leading edges at Q_{nom}:
a – AID 0 *NPSH* 3 % = 0.31 m; b – AID 1 *NPSH* 3 % = 0.51 m;
c – AID 2 *NPSH* 3 % = 0.77 m; d – AID 3 *NPSH* 3 % = 1.19 m

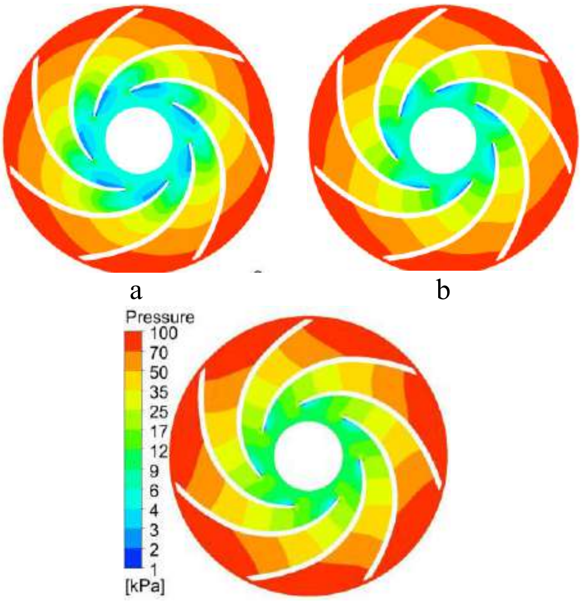

a b c

Figure 7 – The pressure distribution in the impeller cross section at a distance of 3/4 width of the blade from the front shroud at the leading edges at Q_{nom} for the AID 2: a – 0.7·Q_{nom} *NPSH* 3 % = 0.38 m; b – Q_{nom} *NPSH* 3 % = 0.77 m;
c – 1.3·Q_{nom} *NPSH* 3 % = 1.31 m

In the cases, for AIDs 1, 2, 3, there are larger cavitation zones in the impeller eye at the NPSH 3 % than in the AID 0, which differs significantly in shape. They are located near the suction side of the blades and close to the front shroud (Fig. 5 c). Mentioned zones overlap 1/2 area of the passage between leading edges of neighboring blades. This was caused by the union of the cavitation zone of the diffuser with the cavitation zone in the impeller and the change in the direction of the absolute velocity at the impeller inlet. The reduction of the diameter of the AID causes the displacement of the cavitation zone in the impeller to the front shroud.

The vapour distribution in the impeller cross section at a distance of 3/4 width of the blade from the front shroud at the leading edges demonstrates a decrease in the cavitation zone (Fig. 6), but really the cavitation zone just shifts to the front shroud. This confirms the above presented conclusions regarding the change in the cavitation zone (Fig. 5 b, c).

The distribution of the absolute pressure in the impeller at (0.7, 1.0, 1.3)·Q_{nom} is qualitatively similar (Fig. 7). However, larger areas of low pressure at the suction side of the blades near the leading edges are observed for a smaller value of the flow rate. This causes an increase in cavitation zones.

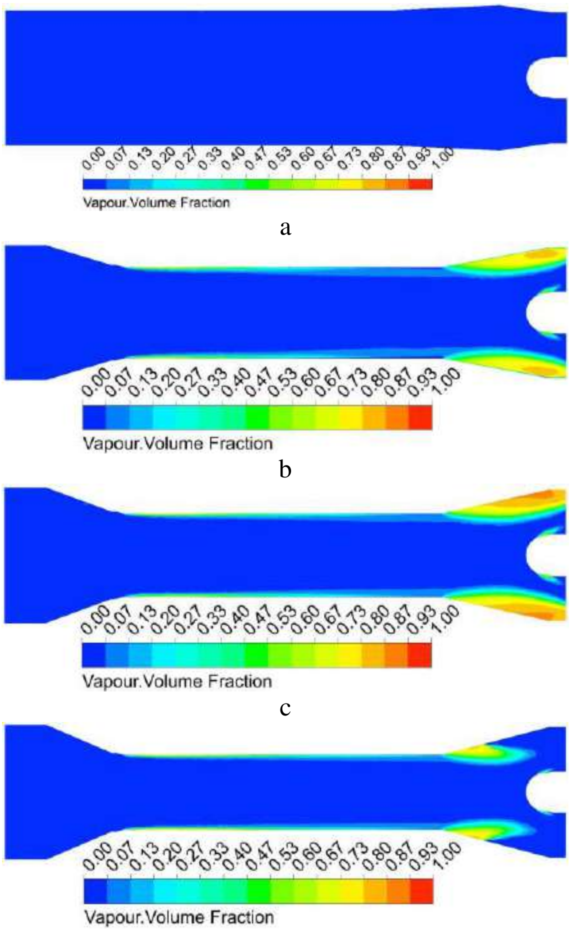

a b c d

Figure 8 – The vapour volume fraction distribution in a longitudinal section of the AID at Q_{nom}:
a – AID 0 *NPSH* 3 % = 0.31 m; b – AID 1 *NPSH* 3 % = 0.51 m;
c – AID 2 *NPSH* 3 % = 0.77 m; d – AID 3 *NPSH* 3 % = 1.19 m

Cavitation in the *AID 0* does not occur under the considered conditions (Fig. 8). There is an increase in the area of the cavitation zones in the diffuser section of the *AID*, when the diameter is reduced and the diffuser angle is simultaneously increased, which is a consequence of the strengthening of the detachment process. It should be noted, that cavitation in the impeller begins earlier than in the *AID*. At the same time, the value of the required NPSH (*NPSHR* = 1.3·*NPSH* 3 %) coincides with the first occurrence of cavitation in the AID and rather large cavitation zones in the impeller. That is, first of all, the destruction of the material through cavitation will be in the impeller. It should be noted, that there are significantly smaller zones of cavitation in the diffuser of the AID 3 compared AIDs 0, 1, 2, but there is an essential decrease in pressure.

Places of appears and structure of the cavitation zones are illustrated by the example of the AID 2 (Fig. 9). Cavitation almost simultaneously appears in two zones (Fig. 9 a). The first zone is after cone at the beginning of the straight section. The second zone is at the beginning of the diffuser section of the AID. The cavitation zones are similar in the AIDs 1, 2, and 3. These zones are rapidly increasing by area with decreasing NPSH value (Fig. 9 b). In addition, cavitation appears in the third zone, located near the fairing at the outlet of the diffuser section. The cavitation zone increases and overlaps bigger area at the impeller eye, which leads to the decrease of the flow diameter of the AID.

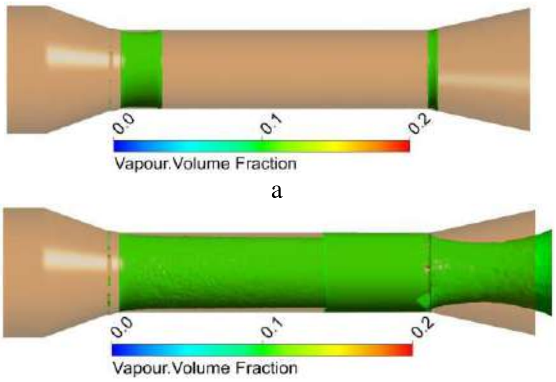

a

b

Figure 9 – The cavitation structure in the *AID 2* at Q_{nom}:
a – *NPSH* = 0.79 m; b – NPSH 3 % = 0.77 m

In general, Cucha et.al [10] described a similar process of cavitation occurrence like in the first zone. However, rotation of the walls causes its “blurring” and stretching of the vapor along the *AID* (Fig. 8, 9, 10), which is likely caused by the presence of a circular component of absolute velocity near the inner surface of the *AID*. “Blurring” is more prominent, with a larger diameter and, respectively, a larger circular component of the absolute velocity. Its intensity decreases, when decreasing the flow rate, which could be explained by the reduction in the axial component of the absolute velocity. This phenomenon is described in more detail at the publication [14].

The decrease of the flow rate causes the increase in the area of the cavitation zones in the AIDs 1,2,3 due to the increase of the absolute pressure in the outlet of diffuser and vice versa (Fig. 10).

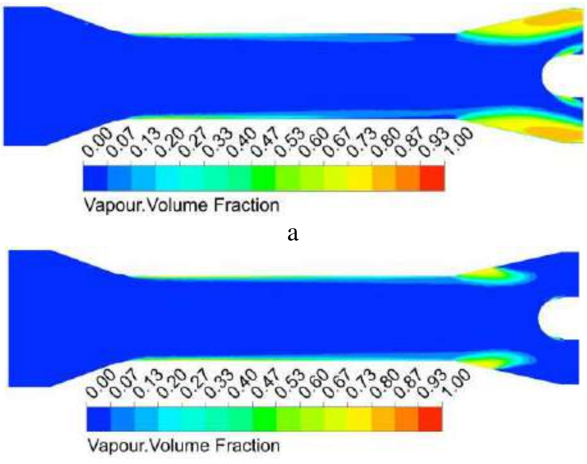

a

b

Figure 10 – The vapour volume fraction distribution
in a longitudinal section of the AID 2:
a – 0.7·Q_{nom} *NPSH* 3 % = 0.38 m;
b – 1.3·Q_{nom} *NPSH* 3 % = 1.31 m

The pictures of the absolute pressure distribution in the AIDs show the zones of the reduced pressure (Fig. 11), which correspond to the zones of the cavitation emergence. The first zone is after cone, the second zone is at the beginning of diffuser section, the third one is located near the fairing at the outlet of the diffuser section. These are the zones of the velocity increasing (due to the change in the cross–sectional area of the passage channel) and changes of the fluid flow direction. There is no zone with pressure below saturated vapor pressure in the AID 0. The absolute pressure distribution is similar for the AIDs 1, 2, and 3.

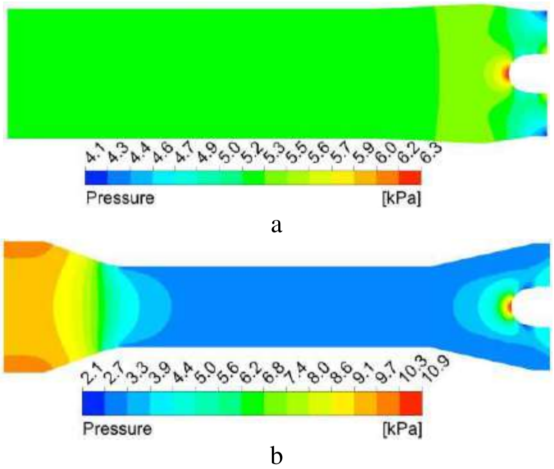

a

b

Figure 11 – The pressure distribution in a longitudinal section
of AID at Q_{nom}: a – AID 0 *NPSH* 3 % = 0.31 m;
b – AID 2 *NPSH* 3 % = 0.77 m

A possible way of eliminating the first and the second zones of absolute pressure reduction is to use a curvilinear wall profile of the cone and diffuser. They have to ensure a smooth change in the diameter of the passage channel and, as a consequence, smooth flow around the walls. To remove the third zone, it is necessary to change the shape of the fairing, giving it a more conical shape.

5 Conclusion

The analysis of the presented results of the numerical simulations of the working process in the centrifugal pump and the physical experiments under the condition of alteration of the geometric parameters (diameter and, respectively, the angles of the cone and the diffuser) of the AID with rotating walls make it possible to do the following conclusions.

The curves of the cavitation characteristics of the analyzed pump have a similar shape, but determined by means of the experiment have higher values compare to CFD. This can be explained by different roughness (and it structure) of walls in numerical model and experimental and disregard volume losses.

The best cavitation performance has the pump with the basic AID. According to the results of the numerical experiment its equals NPSH 3 % = 0.3 m at Q_{nom}. The value of the NPSH 3 % increases with decreasing diameter of the AID and proportional to the change of the flow rate. The maximum value of the NPSH 3 % is 1.2 m for AID 3 at Q_{nom}.

The calculated values of the suction specific speed at Q_{nom} for AID 0, 1, 2, and 3 are respectively 231, 160, 118, and 85. The base AID has better performance than standard pumps, AID 1 has a permissible value and AID 2, and 3 have understated.

The cavitation in the impeller beginning earlier than in the AID. That is, the proposed design of the AID will not be endangered to the destruction if the pump is operating with pressure above the NPSHR.

The value of the NPSH 3 % increases and the shape of the cavitation zones substantially change with the decrease in the diameter of the cylindrical section of the AID. The cavitation zones shifts to the suction side of the blades and the front shroud, while occupies to ½ of the cross–sectional area of the passage between blades near leading edges. This is caused by the union of the cavitation zone of the diffuser with the cavitation zone in the impeller and the change in the direction of absolute velocity at the inlet to the impeller.

The rotation of the AID causes swirling flow character near its walls and, as a result, the separation from the walls and the "blurring" of the cavitation zones occurs. "Blurring" is more prominent, with a larger diameter and, respectively, a larger circular component of the absolute velocity. Its intensity decreases, when decreasing the flow rate, which is explained by the decrease in the axial component of absolute velocity.

The results of the conducted research show that in order to improve the cavitation performances of the AID of the centrifugal pump in the considered structure, it should be avoided abrupt transitions from cone to the cylindrical section, and then to the diffuser section of the AID. It is better to use curvilinear wall profile of the cone and diffuser.

References

1. Guo, X., Guo, X., Zhu, Z., Cui, B., & Li, Y. (2012). Analysis of cavitation performance of inducers, centrifugal pumps. *Centrifugal Pumps*, doi: 10.5772/26744.
2. Jiang, J., Sun, Q., Liu, Y., Chen, Y., & Yi, W. (2015). Numerical simulation of cavitation performance on a high-speed centrifugal pump with a variable pitch inducer. *The 13th Asian International Conference on Fluid Machinery*, Tokyo, Japan, September 7–10, 2015.
3. Tkach, P. Y, (2017). Influence of geometry parameters of inducer bush design on cavitation erosion characteristics of centrifugal inducer stage of pump. *IOP Conference Series: Materials Science and Engineering*, Vol. 233, doi: 10.1088/1757-899X/233/1/012012.
4. Si, Q., Yuan, S., Yuan, J., & Bois, G. (2016). Investigation on the influence of jetting equipment on the characteristics of centrifugal pump. *Advances in Mechanical Eng*, Vol. 8(8), pp. 1–11, doi: 10.1177/1687814016660287.
5. Tan, L.., Zhu, B., Cao, S., Wang, Y., & Wang, B. (2014). Influence of prewhirl regulation by inlet guide vanes on cavitation performance of a centrifugal pump. *Energies*, Vol 7, pp. 1050–1065, doi: 10.3390/en7021050.
6. Tan, L., Zha, L., Cao, S. L., Wang, Y. C., & Gui, S. B, (2015). Cavitation performance and flow characteristic in a centrifugal pump with inlet guide vanes. *International Symposium of Cavitation and Multiphase Flow (ISCM 2014) IOP Conference Series: Materials Science and Engineering*, Vol. 72, http://iopscience.iop.org/1757-899X/72/3/032028.
7. Skerlavaj, A., & Pavlin, R. (2014). Effect of vortical structures on cavitation on impeller blades in pumps with suction chambers. *IOP Conference Series: Earth and Environmental Science, 27th IAHR Symposium on Hydraulic Machinery and Systems,* Vol. 22, doi: 10.1088/1755-1315/22/5/052002.
8. Nagahara, T., Sato, T., & Okamura, T. (2003). Measurement of the flow around the submerged vortex cavitation in a pump intake by means of PIV. *Fifth International Symposium on Cavitation (cav2003).*
9. Sikora, R., Burecek, A., Hruzik, L., & Vasina, M. (2015). Experimental investigation of cavitation in pump inlet. *EPJ Web of Conferences*, Vol. 22, doi: 10.1051/epjconf/20159202081.
10. Cunha, M. A. R., & Nova, H. F. V. (2013). Cavitation modelling of a centrifugal pump impeller. *22–nd International Congress of Mechanical Engineering*, San Paulo, Brazil, pp. 1633–1644.

11. Hergt, P., Nicklas, A., Mollenkopf, G., & Brodersen, S. (1996). The suction performance of centrifugal pumps possibilities and limits of improvements. *Proceedings of the International Pump Users Symposium, Texas A&M University System,* pp. 13–26.
12. Gulich, J. F. (2014). *Centrifugal Pumps*. *Springer*, Berlin, Heidelberg, New York, doi: 10.1007/978-3-642-40114-5.
13. Limbach, P., Muller, T., Blume, M., & Skoda R. (2016). Numerical and experimental investigation of the cavitation flow in a low specific speed centrifugal pump and assessment of the influence of surface roughness on head prediction. *International Symposium on Transport Phenomena and Dynamics of Rotating Machinery*, Hawaii.
14. Moloshnyi, O., & Sotnyk, M. (2017). Cavitation in centrifugal pump with rotating walls of axial inlet device. *IOP Conference Series: Materials Science and Engineering*, Vol. 233, doi: 10.1088/1757-899X/233/1/012007.
15. Moloshnyi, O., & Sotnyk, M. (2018) Influence of geometric dimensions of inlet device on the operating process of the pump. *Industrial Hydraulics and Pneumatics*, Vol 3(61) [in Ukrainian].

Вплив підвідного обертового осьового пристрою на кавітаційні процеси у відцентровому насосі

Молошний О. М.[1], Шульц П.[2], Сотник М. І.[1]

[1] Сумський державний університет, вул. Римського-Корсикова, 2, 40007, м. Суми, Україна;
[2] Вроцлавський університет науки і техніки, вул. Берег Вишпянскєго, 27, 50-370, м. Вроцлав, Польща

Анотація. Робота присвячена аналізу кавітаційних процесів у проточній частині відцентрового насоса. Нова концепція двопотічного герметичного насоса потребує застосування спеціального підвідного пристрою, що входить до складу обертаючих елементів електродвигуна. Проаналізовано чотири моделі осьового підвідного пристрою. Перша є базовою і має циліндричну форму з незначною дифузорністю та конусом перед робочим колесом. Інші три мають нерухомий конус, який є частиною корпусу, а також прямолінійну і дифузорну ділянки, що обертаються з частотою обертання вала насоса, а також обтічник сферичної форми. Дослідження проведено за допомогою фізичного експерименту і числового моделювання. Аналіз результатів показує, що насос із базовим підвідним пристроєм має кавітаційний запас вище середньостатистичного для подібної геометрії. Кавітаційні характеристики насоса, отримані числовим моделюваням і шляхом проведення фізичного експерименту, мають подібні форми, проте останні мають вищі значення. Кавітація у робочому колесі починається раніше, ніж в осьовому підвідному пристрої. Кавітаційні зони в осьовому підвідному пристрої розташовані після звуження поперечного перерізу – на початку дифузорної ділянки і біля обтічника на виході з дифузора. Кавітаційна зона, що знаходиться після конфузору, відривається від стінок осьового підвідного пристрою. При зменшенні діаметра в осьовому підвідному пристрої через втрати напору в ньому відбувається підвищення значення кавітаційного запасу.

Ключові слова: підвід, вхідний патрубок, робоче колесо, конфузор, дифузор, CFD, кавітаційний запас, кавітаційна характеристика.

JOURNAL OF ENGINEERING SCIENCES
ЖУРНАЛ ІНЖЕНЕРНИХ НАУК
ЖУРНАЛ ИНЖЕНЕРНЫХ НАУК

Web site: http://jes.sumdu.edu.ua

DOI: 10.21272/jes.2019.6(1).e6 Volume 6, Issue 1 (2019)

UDC 536.2:697.1

Dynamic Simulation of Heat Transfer through External Building Constructions

Pitel J.[1], Khovanskyi S.[2], Pavlenko I.[2], Mizakova J.[1*]

[1] Faculty of Manufacturing Technologies with a seat in Presov, Technical University of Kosice,
1 Bayerova St., 080 01 Presov, Slovakia;
[2] Faculty of Technical Systems and Energy Efficient Technologies, Sumy State University,
2 Rymskogo-Korsakova St., 40007 Sumy, Ukraine

Article info:
Paper received: January 20, 2019
The final version of the paper received: April 24, 2019
Paper accepted online: April 29, 2019

[*] **Corresponding Author's Address:**
jana.mizakova@tuke.sk

Abstract. In the paper, some approaches to dynamic modeling of heat transfer through external building constructions are presented. The model of heat transfer dynamics through a wall was designed on the base of mathematical describing of an energy balance for the elementary layer of a plane wall. The wall was considered as a continuum with continuously distributed thermal resistance and capacity. Based on the designed analytical mathematical model, a simulation model in MATLAB/Simulink environment was developed. These dynamic models of heat transfer through the wall with real materials parameters and also through the window with real thermal parameters were simulated and some simulation results are presented in the paper.

Keywords: dynamic modeling, mathematical model, heat transfer.

1 Introduction

Heating, cooling, and lighting are the primary energy consumers in buildings, but heating is predominant [1]. To improve energy efficiency and reduce energy consumption, it is highly important to obtain patterns of energy use, climatic conditions, heat transfer characteristics, and ventilation requirements.

Heating models can be installed on the basis of system identification and statistical methods to assess the energy consumption of buildings by combining existing data. Since the interior of the building is not always meet the requirements of comfort, the reaction of the building should be corrected through the heating or air-conditioning systems that act as controlled heat or cold sources [2].

Due to a high number of insulating materials are widely used in new construction and modern building envelope has more complicated internal and external structures [3], the problem of dynamic simulation of heat transfer through external building constructions is the urgent scientific problem.

Previously developed simplified models are able to describe existing building systems with the aim of prediction for air-conditioning system optimal control [4]. However, these models need to be supplemented by detailed physical models of heat transfer.

2 Literature Review

A number of research works are aimed at ensuring the precise dynamic simulation of heat transfer through external building constructions. Particularly, the paper [5] presents the analysis of energy demand in residential buildings for different climates by means of dynamic simulation.

The paper [6] presents a solution of the problem of heat transfer through walls for energy independent building applications in the form of an optimized, thermally controlled storage using phase change materials integrated to building walls.

Thermal dynamic modeling and simulation of a heating system for a multi-zone office building equipped with demand controlled ventilation using MATLAB/Simulink is presented in the paper [7].

Using the CFD methods for numerical simulation of the heat and mass transfer processes is proposed in the articles [8, 9].

Modeling of conduction transfer functions for typical thermal bridges identified in BIM data is proposed in the paper [10].

Comparison of steady-state and dynamic building energy simulation programs is discovered in the research work [11].

3 Research Methodology

3.1 Mathematical description of heat transfer dynamics through a wall

For the design of the mathematical model of heat transfer dynamics through the wall, we have considered a single-layered plane wall, where the wall has been considered as a continuum with continuously distributed thermal resistance and capacity. We have chosen elementary layer with following parameters, m (Figure 1):

dy – thickness of an elementary layer in a plane wall; d_i – thickness of the whole single-layered plane wall; *y* – a distance of elementary layer from the heated surface.

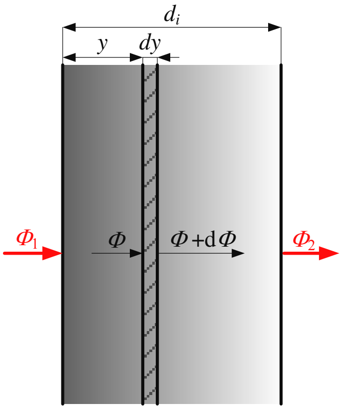

Figure 1 – Single-layered plane wall

Let's others variable has been used for mathematical description: Φ_1 – heat flow supplied into the heated wall surface, W; Φ_2 – heat flow taken away from the cooled wall surface, W; Φ – heat flow inputs into unit surface of layer *dy*, and heat flow ($\Phi + d\Phi$) outputs from it, W.

Material parameters of a single-layered plane wall which have been used for mathematical description: *c* – specific heat capacity, J/(kg·K); ρ – volume weight, kg/m^3; λ – heat conductivity of wall material, W/(m·K).

If a wall of the real building is considered, which consists of several layers (Figure 2) with various parameters of each material, the materials parameters and the temperatures on both sides of such wall can be denote as follows: θ_{w1} – temperature of the heated wall surface, K; θ_{w2} – temperature of the cooled wall surface, K; θ_w – temperature of elementary layer, K; d_i – i-layer thickness, m; λ_i – heat conductivity of i-layer material, W/(m·K).

The parameters of the multi-layered wall are calculated as follows: $R_i = d_i/\lambda_i$ – thermal resistance of i-layer with thickness d_i, K·m^2/W; $d_w = \sum_{i=1}^{n} d_i$ – thickness of multi-layered wall, which consists from layers with thickness d_i, m; $R = \sum_{i=1}^{n} R_i$ – thermal resistance of multi-layered wall, which consists from layers with thermal resistance R_i, K·m^2/W; $U = 1/R$ – heat transfer coefficient, W/(m^2·K).

According to [12] the heat energy does not originate either does not dissolve in considering an elementary layer of the wall. Then the difference of input heat and output heat in the layer has to be equal to the time variation of the energy in a layer.

Let's *c* is a specific heat capacity and ρ is a volume weight of the wall material, then:

$$\Phi - (\Phi + \mathrm{d}\Phi) = \frac{\partial}{\partial t}(c \cdot \rho \cdot \theta_w \cdot \mathrm{d}y), \tag{1}$$

where heat flow $d\Phi$ is:

$$\mathrm{d}\Phi = \frac{\partial \Phi}{\partial y}\mathrm{d}y. \tag{2}$$

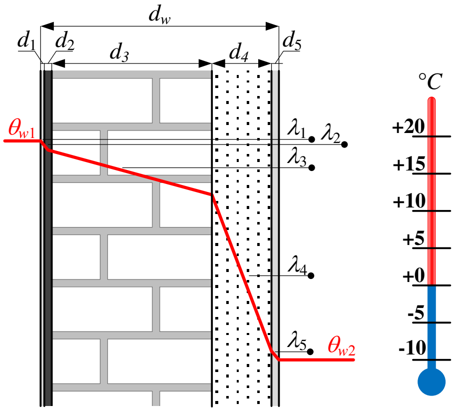

Figure 2 – Multi-layered plane wall

If specific heat capacity *c* and volume weight ρ of the used wall material are constant, then:

$$-\frac{\partial \Phi}{\partial y} = c \cdot \rho \cdot \frac{\partial \theta_w}{\partial t}. \tag{3}$$

According to Fourier's law, the heat flow is directly proportional to the temperature gradient

$$\Phi = -\lambda \frac{\partial \theta_w}{\partial y}, \tag{4}$$

where λ is the heat conductivity coefficient of the used wall material.

These partial differential equations (3) and (4) with relevant initial and border conditions completely describe non-stationary one-dimensional heat flow. After expression of dependent variables by their values and increments and their conversion to non-dimensional form [13, 14] we have got partial differential equations system of heat transfer dynamics through a wall:

$$\frac{\partial x_\Phi}{\partial y} + c \cdot \rho \cdot \frac{d_w}{\lambda}\frac{\partial x_{\theta w}}{\partial t} = 0; \tag{5}$$

$$x_\Phi + d_w \frac{\partial x_{\theta w}}{\partial y} = 0. \tag{6}$$

This system describes the dependence of non-dimensional variables x_{Φ} for heat flows Φ and $x_{\theta w}$ for temperatures θ_w, but it still needs to be supplemented by equations of heat transfer on both sides of the wall surfaces. In dimensionless form for the indoor surface area it is valid:

$$x_{\Phi1} = x^*_{\Phi1} - \kappa_1 \cdot x_{\theta w1} = \left(x_{\theta a2} - x_{\theta w1}\right) \cdot h_1 - \kappa_1 \cdot x_{\theta w1}, \quad (7)$$

where $x^*_{\Phi1}$ includes also external effects on the heat flow transfer into the wall, $x_{\theta a2}$ is the temperature of air warming the wall, $\kappa_1 = h_1 \cdot d_w / \lambda$, and h_1 is heat transfer coefficient between air and wall surface, W/(m^2·K).

Similarly, for the outdoor surface area it is valid:

$$x_{\Phi2} = x^*_{\Phi2} + \kappa_2 \cdot x_{\theta w2} = \left(x_{\theta w2} - x_{\theta o}\right) \cdot h_2 + \kappa_2 \cdot x_{\theta w2}, \quad (8)$$

where $x^*_{\Phi2}$ includes external conditions of the heat flow transfer from the wall, $x_{\theta o}$ is the temperature of air cooling the wall, $\kappa_2 = h_2 \cdot d_w / \lambda$, and h_2 is heat transfer coefficient between the wall surface and air W/(m^2·K).

Using Laplace transform and some substitutions (detailed described in [15]) we have got equations:

$$\overline{X}_{\Phi2}(p) = G_1(p) \cdot \overline{X}_{\Phi1}(p) - G_2(p) \cdot \overline{X}_{\theta w2}(p); \quad (9)$$

$$\overline{X}_{\theta w1}(p) = G_3(p) \cdot \overline{X}_{\Phi1}(p) + G_1(p) \cdot \overline{X}_{\theta w2}(p), \quad (10)$$

where:

$$G_1(p) = \frac{1}{ch\sqrt{p}}; \quad (11)$$

$$G_2(p) = \sqrt{p} \cdot \mathrm{th}\sqrt{p}; \quad (12)$$

$$G_3(p) = \frac{\mathrm{th}\sqrt{p}}{\sqrt{p}}. \quad (13)$$

Then using substitution solved in [15] and substitution $p = T_s \cdot s$, we have got transfer functions:

$$G_1(p) = \frac{24}{24 + 12p + p^2} = \frac{24}{24 + 12T_s s + (T_s s)^2}; \quad (14)$$

$$G_2(p) = \frac{4\left(6p + p^2\right)}{24 + 12p + p^2} = \frac{4\left[6T_s s + (T_s s)^2\right]}{24 + 12T_s s + (T_s s)^2}; \quad (15)$$

$$G_3(p) = \frac{120 + 20p + p^2}{5\left(24 + 12p + p^2\right)} = \frac{120 + 20T_s s + (T_s s)^2}{5\left[24 + 12T_s s + (T_s s)^2\right]}, \quad (16)$$

where $T_s = d_s^2 \cdot \rho \cdot c / \lambda$ is constant, which is depended on wall properties d_w and

$$\lambda = d_w \cdot R = d_w \cdot \sum_{i=1}^{n} R_i = d_w \cdot \sum_{i=1}^{n} \frac{d_i}{\lambda_i}. \quad (17)$$

Based on equations (7)–(10) block diagram of heat transfer dynamics through a wall was designed and it is shown in Figure 3.

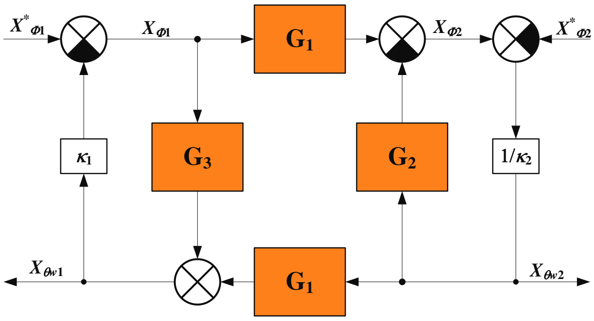

Figure 3 – Block diagram of heat transfer dynamics through a wall

3.2 Simulation model of heat transfer dynamics

In Figure 4, there is presented dynamic simulation model of heat transfer through a wall developed in MATLAB/Simulink environment. This model was designed on the base of the block diagram of heat transfer dynamics through a wall (Figure 3) corresponding to transfer functions (14)–(16) of partial differential equation system (9), (10).

According to (9) and (10), temperature θ_{w1} of the heated wall surface and heat flow Φ_2 taken away from cooled wall surface is calculated from heat flow Φ_1 supplied into the heated wall surface and from temperature θ_{w2} of the cooled wall surface. Heat flow Φ_1 supplied into the heated wall surface is calculated using equation (7) with two inputs: temperature θ_{a2} of air warming the wall and temperature θ_{w1} of the heated wall surface. The temperature of the cooled wall surface θ_{w2} is calculated using equation (8) and it serves as input into main parts of the model.

The main part of the model is Transfer Fcnblocks $G_{1a} = G_{1b} = G_1$, G_2, and G_3, which determine the dynamics of the system. Another important part of the model is hierarchical blocks named “standardize”, which serve for calculation of main variables in the model.

4 Results

Using the model in Figure 4 we have simulated heat transfer through the real wall and through the real window, to compare different materials of multi-layered wall, thermal parameters, energy losses, etc.

Firstly, heat transfer through the real wall was simulated (Figure 5) with following real parameters, which have corresponded to parameters measured on typical building wall with thickness $d_w = 0.520$ m, where the wall has consisted of an internal plaster with thickness 0.015 m, external plaster with thickness 0.015 m, internal isolation layer 0.150 m, external isolation layer 0.050 m, and finally brick layer thickness layer 0.290 m. The wall material volume weight was $\rho = 1\,400$ kg/m^3, and its specific heat capacity $c = 840$ J/(kg·K). Thermal conductivity λ, W/(m·K), has been calculated as

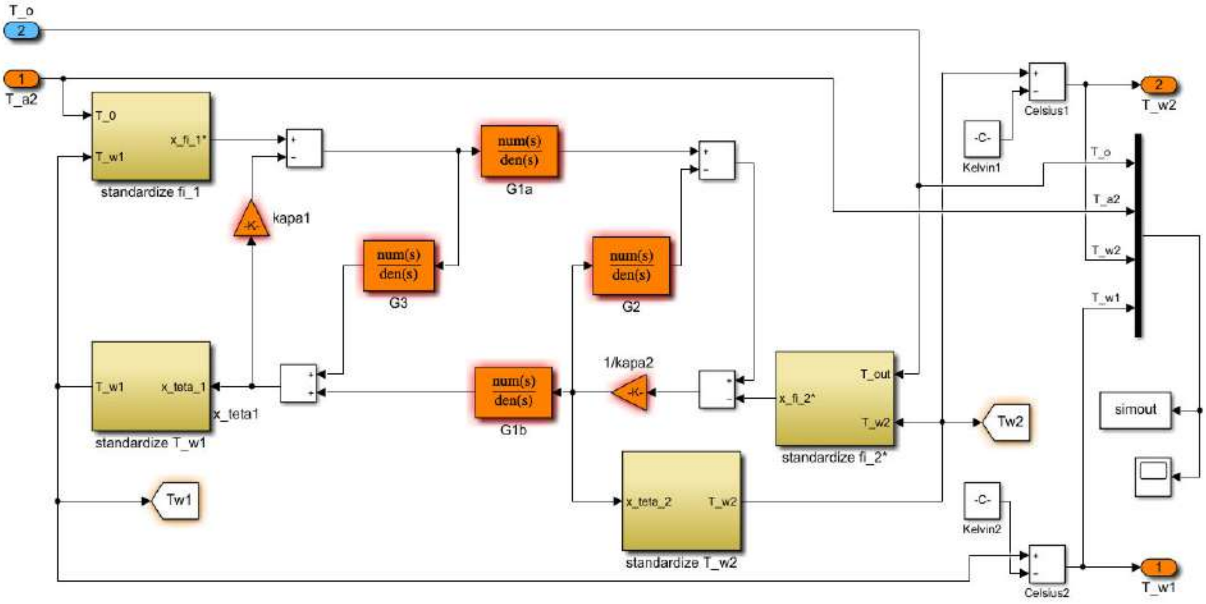

Figure4 – Dynamic simulation model of heat transfer through a wall

$$\lambda = \frac{d_w}{R}, \tag{18}$$

where R is thermal resistance obtained by formula (for the case of the total number of layers $n = 5$):

$$R = \sum_{i=1}^{5} \frac{d_i}{\lambda_i}. \tag{19}$$

Thermal conductivities of the individual wall layers, W/(m·K): $\lambda_1 = 0.70$, $\lambda_2 = 0.03$, $\lambda_3 = 0.52$, $\lambda_4 = 0.04$, and $\lambda_5 = 0.87$.

So, thermal conductivity of the simulated multi-layered wall is $\lambda = 0.15$ W/(m·K).

Outdoor temperature θ_o has been simulated as a sine wave with period 86 400 s (i. e. 24 hours), and amplitude 5 °C. The temperature of heating water θ_{b1} has been 50 °C.

Next, heat transfer through the real wall was simulated (Figure 6) with the following real parameters: thermal resistance $R = 1$ K·m^2/W, $d_w = 0.030$ m. Outdoor temperature θ_o has been simulated again as a sine wave with period 86 400 s (i. e. 24 hours) and amplitude 5 °C. The temperature of heating water θ_{b1} has been 50 °C.

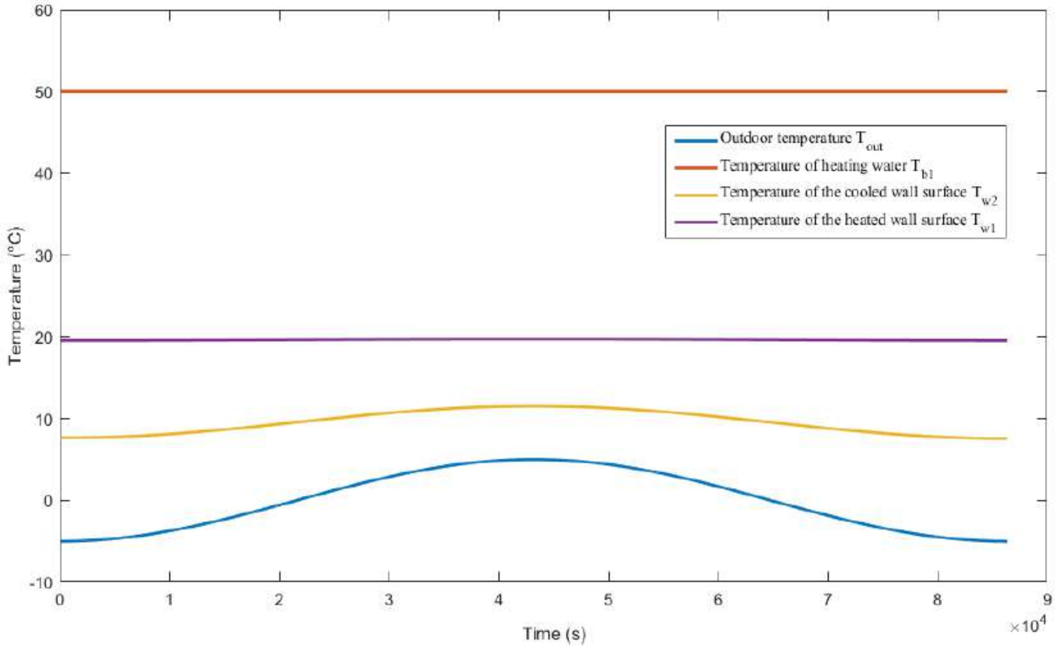

Figure 5 – Simulation results of heat transfer through the real wall: temperature of the heated wall surface θ_{w1} (T_{w1}), and temperature of the cooled wall surface θ_{w2} (T_{w2})

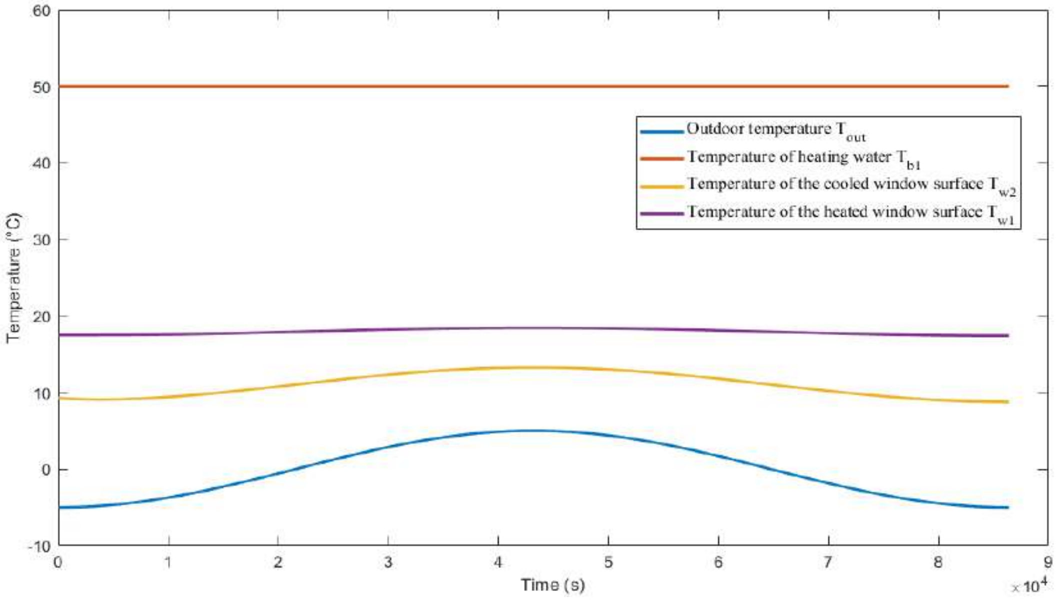

Figure 6 – Simulation results of heat transfer through the real window: temperature of the heated window surface θ_{w1} (T_{w1}), and temperature of the cooled window surface θ_{w2} (T_{w2})

5 Conclusions

To summarize, the described mathematical model of heat transfer dynamics through a plane wall has led to the system of partial differential equations which second-order transfer functions were derived. Model parameters of single-layered and multi-layered plain walls were also described in the paper. Based on the designed analytical model of heat transfer through a wall, a dynamic simulation model in MATLAB/Simulink environment was developed. This model has been tested for different real wall material parameters, for example, a brick wall, insulated wall, etc. The tested model was also used for simulation of heat transfer through the real window.

Comparison of simulation results in Figures 5, 6 shows that the temperature of the heated wall surface is higher than the temperature of the heated window surface. Conversely, the temperature of the cooled wall surface is lower than the temperature of the cooled window surface. It shows that heat losses through the window with worse thermal properties are higher than through the wall with better thermal properties. So, the achieved simulation results have confirmed the right approach to model design.

From the point of view of model dynamics, it can be stated that the dynamic change in the outdoor temperature had an impact especially on the temperature of the cooled wall or window surface. This impact is with time delay given by system time constant. The achieved simulation results are in line with theoretical assumptions.

The designed and tested dynamic model of heat transfer through external building constructions is needed for simulation of the heating process control based on outdoor temperature compensation. So in the future work, this model will be implemented into a dynamic simulation model of the heating system containing model of heating body and a model of heating curves.

6 Acknowledgments

This work was supported by the Slovak Research and Development Agency under the contract No. APVV-15-0602.

The achieved results were partially supported by the Ministry of Education and Science of Ukraine under the research project No. 0117U003931.

References

1. Perera, D. W. U., Pfeiffer, C. F., & Skeie, N.-O. (2014). Modelling the heat dynamics of a residential building unit: Application to Norwegian buildings. *Modeling, Identification and Control*, Vol. 35(1), pp. 43–57, doi: 10.4173/mic.2014.1.4.
2. Missoum, A., Elmir, M., Bouanini, M., & Draoui, B. (2016). Numerical simulation of heat transfer through the building facades of buildings located in the city of Bechar. *International Journal of Multiphysics*, Vol. 10(4), pp. 441–450.
3. Gao, Y., Roux, J. J., & Zhao, L. H. (2007). A low-order thermal bridge dynamic model for building simulation. *Proceedings: Building Simulation*, pp. 281–286.
4. Xu, X., & Wang, S. (2008). A simplified dynamic model for existing buildings using CTF and thermal network models. *International Journal of Thermal Sciences*, Vol. 47(9), pp. 1249–1262, doi: 10.1016/j.ijthermalsci.2007.10.011.

5. Bianco, V., Rosa, M., Scarpa, F., & Tagliafico, L. A. (2016). Analysis of energy demand in residential buildings for different climates by means of dynamic simulation. *International Journal of Ambient Energy*, Vol. 37(2), pp. 108–120, doi: 10.1080/01430750.2014.907207.
6. Wegmueller, R., Magnin, G., Robadey, J., & Niederhauser, E.-L. (2018). Controlled active thermal storage in smart PCM walls for energy independent building applications. *IEEE 5th International Conference on Renewable Energy: Generation and Applications*, 17703462, doi: 10.1109/ICREGA.2018.8337575.
7. Behravan, A., Obermaisser, R., & Nasari, A. (2017). Thermal dynamic modeling and simulation of a heating system for a multi-zone office building equipped with demand controlled ventilation using MATLAB/Simulink. *IEEE International Conference on Circuits, System and Simulation*, pp. 103–108, doi: 10.1109/CIRSYSSIM.2017.8023191.
8. Svoboda, Z., & Kubr, M. (2011). Numerical simulation of heat transfer through hollow bricks in the vertical direction. *Journal of Building Physics*, Vol. 34(4), pp. 325–350, doi: 10.1177/1744259110388266.
9. Varukha, D. A., Smirnov V. A., Edl M., Demianenko M. M., Yukhymenko M. P., Pavlenko I. V., & Liaposhchenko O. O. (2018). Simulation of separation and air classification processes of aerodisperse systems in the shelving device. *Journal of Engineering Sciences*, Vol. 5(1), pp. F5–F9, doi: 10.21272/jes.2018.5(1).f2.
10. Narowski, P., Stasierski, J., & Wereszczynski, P. (2011). Modelling of conduction transfer functions for typical thermal bridges identified in BIM data. *Proceedings of Building Simulation 2011: 12th Conference of International Building Performance Simulation Association*, Vol. 12, pp. 1320–1327.
11. Veken, J., Saelens, D., Verbeek, G., & Hens. H. (2004). Comparison of steady-state and dynamic building energy simulation programs. *Buildings*, Vol. IX, pp. 1-11
12. Cermak, J., Peterka, V., & Zavorka, J. (1968). *Dynamika Regulovaných Soustav v Tepelné Energetice a Chemii*. Academia, Praha, Czech Republic [in Czech].
13. Piteľ, J. (2007). Matematický model prestupu tepla stenou pre simuláciu riadenia procesu vykurovania. *Acta Metallurgica Slovaca*, Vol. 13(3), pp. 296-300 [in Slovak].
14. Mizakova, J., & Piteľ, J. (2017). An analytical dynamic model of heat transfer from the heating body to the heated room. *MATEC Web of Conferences*, Vol. 125, pp. 1–5.
15. Mizakova, J., Piteľ, J., & Hrehova, S. (2014). Some simulation results of heat transfer through the wall model. *International Journal of Mathematical Models and Methods in Applied Sciences*, Vol. 8(1), pp. 1–8.

Динамічне моделювання теплообміну через зовнішні будівельні конструкції

Пітель Я.[1], Хованський С.[2], Павленко І.[2], Міжакова Я.[1]

[1] Факультет виробничих технологій у м. Прешов, Технічний університет м. Кошице,
вул. Баєрова, 1, 080 01, м. Прешов, Словаччина;
[2] Факультет технічних систем та енергоефективних технологій, Сумський державний університет,
вул. Римського-Корсакова, 2, 40007, м. Суми, Україна

Анотація. У статті представлені теоретичний і числовий підходи до динамічного моделювання теплообміну через зовнішні будівельні конструкції. У результаті розроблено модель динаміки теплопередачі через стіну на основі математичного моделювання енергетичного балансу елементарного шару плоскої стінки. Стіна розглядалась як суцільне середовище з безперервно розподіленим тепловим опором і ємністю. На основі розробленого аналітичного підходу, що реалізує запропоновану математичну модель, розроблено імітаційну модель із застосуванням середовища MATLAB/Simulink. Продемонстровано динамічну модель теплопередачі через стіну з параметрами реальних матеріалів, а також через вікно з реальними тепловими параметрами. Результати моделювання представлені графічно.

Ключові слова: динамічне моделювання, математична модель, теплообмін.

JOURNAL OF ENGINEERING SCIENCES
ЖУРНАЛ ІНЖЕНЕРНИХ НАУК
ЖУРНАЛ ИНЖЕНЕРНЫХ НАУК
Web site: http://jes.sumdu.edu.ua
DOI: 10.21272/jes.2019.6(1).f1 Volume 6, Issue 1 (2019)

UDC 66.074-911.69:66.022.62

Solving the Nonstationary Problem of the Disperse Phase Concentration during the Pneumoclassification Process of Mechanical Mixtures

Pavlenko I. V.[1], Yukhymenko M. P.[1*], Lytvynenko A. V.[1], Bocko J.[2]

[1] Sumy State University, 2 Rymskogo-Korsakova St., 40007 Sumy, Ukraine;
[2] Technical University of Kosice, 1/9 Letna St., 040 01 Kosice, Slovak Republic

Article info:
Paper received: July 10, 2018
The final version of the paper received: December 18, 2018
Paper accepted online: December 23, 2018

[*]Corresponding Author's Address:
yukhimenko@pohnp.sumdu.edu.ua

Abstract. The article dials with studying of the gas-dispersed systems classification process in gravitation pneumoclassifiers of prismatic shape. The aim of the research is to determine operating parameters of the investigated process. Recent research is based on the previously developed mathematical model of hydrodynamics for a gas-dispersed flow in a vertical channel with variable cross-section. As a development of this study, a physical model based on the process of kinetic removal from the mixture was used. This process is caused by the removal of fine particles from the weighed layer in the case of theirs low velocities in comparison with the average gas flow velocity. This model also considers the inertial effect due to the kinetic energy of fine particles removed from the surface of the weighted later. The first order linear nonhomogeneous partial differential equation describing the unsteady process of changing the dispersed phase concentration in the gas-mechanical mixture by channel height was solved by mathematical modeling using the combination of direct and inverse Laplace transforms. As a result, for the first time the general solution was obtained for for non-trivial boundary and initial conditions. This fact allowed developing the mathematical model of the nonstationary problem for the disperse phase concentration during the pneumoclassification process of mechanical mixtures in pneumoclassifiers. The model allows determining the concentration of fine fraction of the gas-dispersed mixture by channel height in operating volume of the device, as well as evaluating time of the pneumoclassification process. Particularly, it was found that the dispersed phase concentration decreases by the height of the apparatus with respect to time. This fact proves the possibility of effective separation of components in gas-mechanical mixtures. Finally, the achieved results allow proposing the engineering technique for calculations of vertial-type gravitation pneumoclassifiers.

Keywords: pneumoclassifier, weighted layer, fine particles, agglomeration, mathematical modeling, Laplace transform, Heaviside step function.

1 Introduction

The increase of the efficiency of chemical, heat and mass transfer processes for heterogeneous systems is mainly achieved using powdering of solid materials with a given granulometric composition. Therefore, in technological lines, pneumoclassifiers are installed to separate the solid phase of gas-liquid mixtures into two fractions with a predominant content of fine particles. If the dust content is less than 15–20 %, pneumoclassifiers are effectively used as separators for the decomposition of mixtures. When separating of binary mixtures with the equal content of fine and coarse fractions, traditionall pneumoclassifiers ensure the purity of the resulting fractions up to 70–75 %. Due to the existence of technologies requiring clean separation products not less than 95 %, it is the development of new designs of separation equipment is needed realizing fundamentally different organization of the pneumoclassification process and pneumatic enrichment of gas-mechanical mixtures to obtain clean separation products. In this case, mathematical modeling of the separation process in a gravitational pneumoclassifier is an urgent problem, which is essential for the study of chemical technology processes. The scientific novelty of the research confirms the need to solve the insufficiently solved problem of investigating the pneumatic classification and enrichment processes for mechanical mixtures. The practical significance of the achieved results is to improve up-to-date scientifically based methods for calculations of main technological parameters and related characteristics of pneumoclassifiers.

2 Literature Review

The first ways for improvement of pneumoclassifiers were proposed in the research works [1, 2]. As a result, modifications of classifier designs with mobile inclined grid were proposed for increasing of the operating process efficiency.

The investigation of the classification process for polydisperse materials in the gravitational air classifier was considered within the previous research [3]. As a result, the problem of the separation efficiency was solved for polydisperse materials, as well as methods for increasing the separation quality are proposed. Additionally, the results of experimental research and computer simulation were obtained and analyzed. Based on the achieved data, the possibility of increasing gas flow influence to polydispersed materials were found.

The effect of particle concentration on fluctuating velocity of the disperse phase for turbulent pipe flow was investigated in the paper [4]. As a result, experimental investigations of the fluctuation velocity distributions of solid particles were presented for the gas turbulent pipe flow. An influence of the particle concentration on the increasing of axial fluctuation velocity in the pipe wall region was observed.

In the paper [5], a concentrated suspension flow of solid spherical particles was modelled using numerical experiment. As a result, the self-diffusion coefficient was obtained. It was shown that spheres at volume fraction about 13 % form a percolation cluster. Finally, the dependence of the self-diffusion coefficient on volume fraction of particles was investigated.

The research papers [6–9] dials with the process of agglomeration as a common phenomenon in separation and pneumiclassification processes. As a result of using the Rumpf model [6] and related numerical simulations, it is proved that the mechanical properties of agglomerates depend on their structures. It was proved that the acoustic agglomeration technology can be applied for removal of fine particles [7]. Comparison of agglomeration behavior of fine particles in during mixing is presented in the paper [8]. Finally, ways for experimental evaluation of chemical agglomeration of fine particles in gas-mechanical mixtures are presented in the research work [9].

3 Research Methodology

Previously obtained equations [3] allows determining the velocity field of the two-phase flow, as well as evaluating changes of particles velocities of mixed material by the width and height of pneumoclassifier's housing depending on the gas flow action.

It should be noted that the action of friction forces on the particles, flow compression and bending forces between particles significantly impact on the redistribution of particle velocity in the separated flow. At the same time, the gas flow rate decreases due to the additional hydraulic resistance as a result of aggregation of the bulk material in agglomerates.

Due to abovementioned, the process of fine fracture concentration changing in a pneumoclassifier of the prismatic form with veriable cross-sections is considered with respect to time and spatial position of particles (Figure 1).

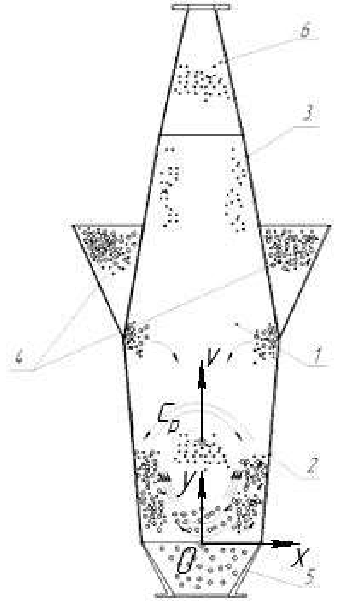

Figure 1 – Design scheme of the pneumoclassifier:
1 – separation zone; 2 – housing; 3 – accelerating zone;
4 – loading hopper; 5 – discharge pipe for a coarse fraction;
6 – discharge pipe for a fine fraction

In the case of unchangeable physical parameters in a transverse direction ($\partial/\partial x = 0$) and relatively insufficient transverse velocity component ($|dx/dt| << |v(y)|$), the equation describing the operating process takes the following form [10]:

$$\frac{\partial c_p(y,t)}{\partial t} = v(y)\frac{\partial c_p(y,t)}{\partial y} + k_y\left[c_* - c_p(y,t)\right], \qquad (1)$$

where t – time, s; x, y – transverse and vertical coordinates, m; v – vertical component of flow velocity, m/s; c_p – concentration of fine particle in a flow, kg/kg; c_* – equilibrium concentration of fine fraction in a weighted mode, kg/kg; k_y – removal ratio determining experimentally, s^{-1}.

Abovementioned simplifications are argued due to the fact, that the width of the pneumoclassifier is much less than its height. Additionally, the velocity of solid particles in the horizontal direction (from the x axis of the apparatus to the walls) significantly decreases due to the inhibitory effect. Therefore, the gas flow in the transverse direction does not significantly impact on the separation of particles by their size.

The equation (1) defines the removal of fine particles from the weighed layer in the case of theirs low velocities in comparison with the average gas flow velocity. In the case of the relatively constant velocity v, this equation has the precise analytical solution, which can be obtained using the Laplace transform [11] with respect to time *t*. The corresponding originals and their mappings can be given in the following forms:

$$L[c_p(y,t)] = C_p(y,s);\ L(c_*) = \frac{c_*}{s},$$
$$L\left[\frac{\partial c_p(y,t)}{\partial t}\right] = sC_p(y,s) - c_{p0}(y), \tag{2}$$

where Y, s – new parameters of the vertical coordinate y and time t respectively; C_p – reflecting function for the fine fraction concentration; $c_{p0}(y)$ – distribution function of the initial concentration.

After applying transformations (2), the equation (1) takes the following form:

$$sC_p(y,s) - c_{p0}(y) = v\frac{\partial C_p(y,s)}{\partial y} + k_y\left[\frac{c_*}{s} - C_p(y,s)\right]. \tag{3}$$

Identical transformations allow obtaining the following first-order heterogeneous ordinary differential equation with respect to the vertical coordinate y:

$$C_p^{/} + \frac{s-k}{v(y)}C_p = \frac{1}{v(y)}\left[c_{p0}(y) - \frac{k_y c_*}{s}\right]. \tag{4}$$

Previous research of the two-phase flow indicates the fact, that the trajectories of fine particles are aligned by the channel height. Consequently, the gas flow does not significantly affect the shearing of particles to the wall. In this case, considering $v = \text{const}$, $c_{p0} = \text{const}$, the differential equation (4) has the following general solution:

$$C_p = \frac{1}{s-k}\left(c_{p0} - \frac{kc_*}{s}\right) + A\cdot\exp\left(-\frac{s-k}{v}z\right), \tag{5}$$

where A – the integration constant determined from the boundary condition:

$$c_p(0,t) = c_p^{in}, \tag{6}$$

which can be rewritten after the direct Laplace transform in the following form:

$$C_p(0,s) = L[c_p(0,t)] = \frac{c_p^{in}}{s}. \tag{7}$$

The last two formulas contain the initial concentration c_p^{in} of the disperse phase.

The substitution of the boundary condition (7) into the formula (5) allows obtaining the following expression for the integration constant:

$$A = \frac{c_p^{in}}{s} - \frac{1}{s-k}\left(c_{p0} - \frac{kc_*}{s}\right). \tag{8}$$

Hence, the general solution (5) takes the following form:

$$C_p = \frac{c_p^{in}}{s}e^{-\frac{s-k}{v}z} + \left(\frac{c_*}{s} + \frac{c_{p0}-c_*}{s-k}\right)\left(1 - e^{-\frac{s-k}{v}z}\right). \tag{9}$$

Using the inverse Laplace transform to elements of the obtained expression:

$$L^{-1}\left(\frac{c_p^{in}}{s}e^{-\frac{s-k}{v}}\right) = c_p^{in}e^{-\frac{k}{v}y}H\left(t - \frac{y}{v}\right);$$
$$L^{-1}\left(\frac{c_*}{s}\right) = c_*;\ L^{-1}\left(\frac{c_{p0}-c_*}{s-k}\right) = (c_{p0} - c_*)e^{-kt}; \tag{10}$$
$$L^{-1}\left(\frac{c_{p0}-c_*}{s-k}e^{-\frac{s-k}{v}}\right) = (c_{p0} - c_*)e^{-kt}H\left(t - \frac{y}{v}\right),$$

where $H(t)$ – Heaviside step function, allows finally obtaining the expression for the distribution function of the disperse phase concentration:

$$c_p(y,t) = c_* + (c_p^{in} - c_*)e^{-\frac{k}{v}y}H\left(t - \frac{y}{v}\right) +$$
$$+ (c_0 - c_*)e^{-kt}\left[1 - H\left(t - \frac{y}{v}\right)\right]. \tag{11}$$

4 Results and Discussion

A general solution of the nonstationary problem of the disperse phase concentration during the pneumoclassification process of mechanical mixtures can be obtained ubder the condition $c_p^{in} = c_{p0}$:

$$c_p(y,t) = c_* + (c_{p0} - c_*)\left\{\exp\left(-\frac{k}{v}y\right)H\left(t - \frac{y}{v}\right) +\right.$$
$$\left. + \exp(-kt)\left[1 - H\left(t - \frac{y}{v}\right)\right]\right\}. \tag{12}$$

It should be noted that this solution approaches the following curve asymptotically with respect to time:

$$c_{p\infty}(y) = \lim_{t\to\infty} c_p(y,t) = c_* + (c_{p0} - c_*)\exp\left(-\frac{k}{v}y\right). \tag{13}$$

This equation describes the equilibrium state as a result of the solution of stationary problem of fine particles concentration.

Introducing the dimensionless coordinates

$$\eta = \frac{ky}{v};\ \tau = \frac{vt}{y} \tag{14}$$

and criteria

$$\bar{c}_p = \frac{c_p}{c_{p0}};\ \alpha = \frac{c_*}{c_{p0}};\ \bar{c}_{p\infty} = \frac{c_{p\infty}}{c_{p0}} \tag{15}$$

allows rewriting the dependencies (12) and (13) in the following universal forms:

$$\bar{c}_p(\eta,\tau) = \alpha + (1-\alpha)\left\{e^{-\eta}\, H(\tau-1) + \right.$$
$$\left. + e^{-\eta\tau}\,[1 - H(\tau-1)]\right\}; \tag{16}$$

$$\bar{c}_{p\infty}(\eta) = \alpha + (1-\alpha)e^{-\eta} \tag{17}$$

presented graphically in Figures 2, 3.

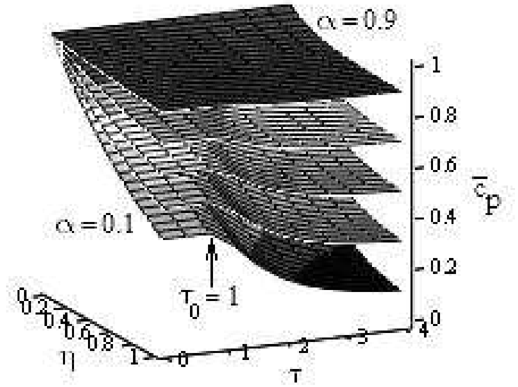

Figure 2 – The surface of changing the fine particles concentration in a weighed layer by the height of the apparatus and time for different values of equilibrium concentration

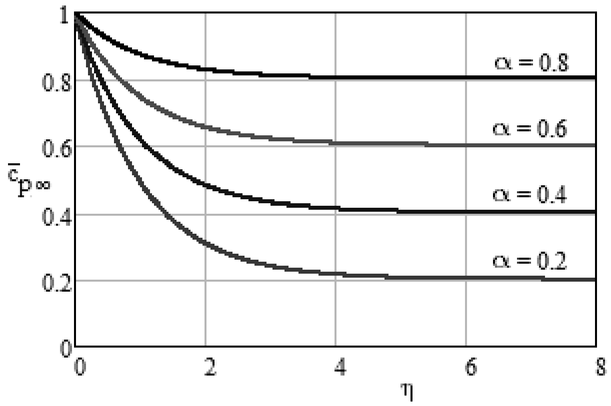

Figure 3 – Universal characteristics of changing the fine particles concentration in a weighed layer by the height of the apparatus for the equilibrium state

Figure 2 discovers the existence of the dimensionless time $\tau_0 = 1$ as a limit value, when the concentration decreases by the height. Consequently, due to the dependencies (14), the related time is determined by the following formula:

$$t_0 = \left.\frac{y\tau}{v}\right|_{\tau=\tau_0=1} = \frac{y}{v}. \tag{18}$$

5 Conclusions

Mathematical model of the pneumoclassification process is developed. As a result, the nonstationary problem of investigating the operating processes in gravitational pneumoclassifiers is solved. The analytical dependence for the fine particles concentration is obtained. As a partial result of the solution of stationary problem, the expression for equilibrium concentration is determined. Additionally, the critical time is discovered, when the concentration decreases by the height, as well as the related expression for its calculation is obtained. Overall, the possibility of effective separation of components in gas-mechanical mixtures is proved.

The results of the abovementioned research allow proposing the engineering technique for calculations of vertial-type gravitation pneumoclassifiers.

The further research will be aimed at the implementation of the developed mathematical model in the process of designing the module separation equipment.

6 Acknowledgements

The main theoretical results was obtained within the research project of the Faculty of Technical Systems and Energy Efficient Technologies of Sumy State University “Development and implementation of energy efficient modular separation devices for oil and gas purification equipment” (State reg. No. 0117U003931) ordered by the Ministry of Education and Science Ukraine.

The numerical calculations were realized within the research collaboration between Sumy State University and Technical University of Kosice.

References

1. Makarenko, E. S. (1992). Improvement pneumoclassifier with inclined mobile grid. *Koks i Khimiya*, Vol. 1, pp. 31–32.
2. Kasimov, A. M., Makarenko, E. S., Shuvalov, E. A. (1992). Modification of pneumoclassifier with inclined air distributive grid for strong materials. Ogneupory, Vol. 3, pp. 33.
3. Varukha, D. A., Smirnov, V. A., Edl, M., Demianenko, M. M., Yukhymenko, M. P., Pavlenko, I. V., & Liaposhchenko, O. O. (2018). Simulation of separation and air classification processes of aerodisperse systems in the shelving device. *Journal of Engineering Sciences*, Volume 5(1), pp. F5–F9.
4. Varaksin, A. Yu., Polezhaev, Yu. V., & Polyakov, A. F. (2000). Effect of particle concentration on fluctuating velocity of the disperse phase for turbulent pipe flow. *International Journal of Heat and Fluid Flow*, Vol. 21(5), pp. 562–567.
5. Lukyanov, A., Andreev, V., & Pozdyshev, V. (1990). Influence of disperse phase concentration on character of Brownian motion of particles. *Journal of Colloid And Interface Science*, Vol. 137(1), pp. 111–119.

6. Yang, R. Y., Yu, A.B., Choi, S. K., Coates, M. S., & Chan, H.K. (2007). Agglomeration of fine particles subjected to centripetal compaction. *Powder Technology*, Vol. 184(1), pp. 122–129.
7. Shi, C.-H., Zhang, J., Zhao, Y., & Liang, J. (2017). Acoustic Agglomeration Process of Fine Particles in a Resonance Structure. *IOP Conference Series: Earth and Environmental Science*, Vol. 78, 012001, doi: 10.1088/1755-1315/78/1/012001.
8. Sumimoto, S., Yoshimoto, K., Uddin, A., & Kato, Y. (2017). Comparison of Agglomeration Behavior of Fine Particles in Liquid among Various Mixing Operations. *ISIJ International*, Vol. 58(1), pp. 1–9.
9. Guo, Y., Zhang, J., Zhao, Y., Wang, S., Jiang, C., & Zheng, C. (2017). Chemical agglomeration of fine particles in coal combustion flue gas: Experimental evaluation. *Fuel*, Vol. 203, pp. 557–569.
10. Kafarov, V. V., Dorokhov, I. N. (2018). *Systematic analysis of the chemical technologies processes: Fundamental strategies*. Urait, Moscow [in Russian].
11. Rodrigo, M. R., & Worthy, A. L. (2016). Solution of multilayer diffusion problems via the Laplace transform. Journal of Mathematical Analysis and Applications, Vol, 444(1), pp. 475–502.

Розв’язання нестаціонарної задачі про визначення концентрації дисперсної фази у процесі пневмокласифікації механічних сумішей

Павленко І. В.[1], Юхименко М. П.[1], Литвиненко А. В.[1], Боцко Й.[2]

[1] Сумський державний університет, вул. Римського-Корсакова, 2, 40007, м. Суми, Україна;
[2] Технічний університет м. Кошице, вул. Літня, 1/9, 040 01, м. Кошице, Словаччина

Анотація. Робота присвячена дослідженню процесу класифікації газодисперсних систем у гравітаційних пневмокласифікаторах призматичної форми. Метою роботи є встановлення робочих параметрів досліджуваного процессу, в основі якого є попередньо розроблена математична модель гідродинаміки руху газодисперсного потоку у вертикальному каналі змінного перерізу. Як розвиток цього дослідження, застосовано фізичну модель, засновану на процесі кінетичного винесення суміші, обумовленого винесення дрібних частинок взваженого шару, швидкість яких менша за швидкість газового потоку. Ця модель також ураховує інерційний ефект, обумовлений кінетичною енергією дисперсної фази, що виноситься з поверхні зваженого шару. Шляхом математичного моделювання із застосуванням комбінації прямого і оберненого перетворень Лапласа розв’язано лінійне неоднорідне диференціальне рівняння першого порядку у частинних похідних, що описує нестаціонарний процес зміни концентрації дисперсної фази газомеханічної суміші по висоті каналу. У результаті для нетривіальних граничних і початкових умов вперше отримано загальний розв’язок, що дозволило розробити математичну модель нестаціонарної задачі про визначення концентрації дисперсної фази у пневмокласифікаторах. Розроблена математична модель дозволяє встановити зміну концентрації дрібної фракції газодисперсної суміші по висоті робочого об’єму апарата, а також оцінити час процесу пневмокласифікації. Зокрема, встановлено, що концентрація дисперсної фази з часом зменшується по висоті апарату, що свідчить про можливість ефективного розділення компонентів газомеханічної суміші. Таким чином, отримані результати дозволяють створити інженерну методику розрахунку вертикальних гравітаційних пневмокласифікаторів призматичної форми зі змінним поперечним перерізом.

Ключові слова: пневмокласифікатор, взважений шар, дрібна фракція, агломерація, математичне моделювання, перетворення Лапласа, функція Хевісайда.

JOURNAL OF ENGINEERING SCIENCES
ЖУРНАЛ ІНЖЕНЕРНИХ НАУК
ЖУРНАЛ ИНЖЕНЕРНЫХ НАУК
Web site: http://jes.sumdu.edu.ua
DOI: 10.21272/jes.2019.6(1).f2 Volume 6, Issue 1 (2019)

UDC 631.371:620.92

Improvement of the Vacuum Cooling System for Biodiesel Production

Sharapov S.[1*], Starchenko M.[1], Protsenko M.[2], Panchenko V.[1], Kovtun V.[1]

[1] Sumy State University, 2 Rymskogo-Korsakova St., 40007 Sumy, Ukraine;
[2] Academy of Management and Administration in Opole, 18 M. Niedzialkowskiego St., 46020 Opole, Poland

Article info:
Paper received: October 16, 2018
The final version of the paper received: February 3, 2019
Paper accepted online: February 8, 2019

***Corresponding Author's Address:**
s.sharapov@kttf.sumdu.edu.ua

Abstract. The article deals with the actual problem of improving the vacuum cooling efficiency systems during the biodiesel production by using vacuum devices account for the liquid-vapor ejector, which operates on the principle of jet thermal compression. The purpose of this study is the feasibility of using vacuum devices, that based on the liquid-vapor ejector, and takes as a basis the principle of jet thermal compression in vacuum cooling systems of biodiesel production units. This article describes the basic scheme of the cooling system devices during the biodiesel production, which includes a three-stage steam-jet ejector and the proposed scheme based on the liquid-vapor ejector. A comparative analysis of the vacuum cooling systems during biodiesel production units was realized, where the schemes were compared on the basis of existent three-stage steam-jet ejectors and a new single-stage vacuum unit based on a liquid-vapor ejector. An exergy method of assessing the effectiveness of the proposed equipment was used as a comparison, because in the working process there is a transformation of two energy types: electric for the pump drive and heat for heating the working fluid of the active flow in the exchanger-heater. The intermediate pressure between the liquid-vapor ejector and the liquid-ring vacuum pump can help to achieve the highest characteristics of the new technology on the optimization parameters.

Keywords: vacuum cooling system, liquid-vapor ejector, biodiesel production, exergy efficiency.

1 Introduction

At the present stage of industrial development of the European Union and North America countries, renewable energy sources are widely used, in particular, the replacement of traditional fossil carbon energy sources with products of plant and natural origin. A price increasing on oil and natural gas, poses a challenge to modern science to find environmentally friendly fuel, which would be a relatively cheap alternative to existing but would not pollute the environment.

In particular, biodiesel belongs to this sort that lately is becoming more widely used. Thus, in 2010, in the European Union countries for its production was about 6 % of all fuel, and in 2020 this figure will increase to 20–25 %.

An integral part of the biodiesel production is the process of purification of its raw materials from odorants, which is carried out at a pressure below atmospheric pressure. The world's leading manufacturers still use multistage vacuum units based on steam-jet ejectors with intermediate condensers, often in combination with liquid-ring vacuum pumps, which are unproductive(only 2–10 %).

Therefore, at this stage it is very important to use significantly liquid-vapor ejectors (LVE), which are based on the principle of jet thermal compression. These units are much more efficient due to a better workflow and can significantly simplify the design of the installation, as there is usually a single-stage.

2 Literature Review

The working process of the liquid-vapor ejector, which operates on the principle of jet thermal compression is quite complex, but today a more reliable technique has been obtained, which allows to determine its regime and geometric parameters as close as possible to reality [1].

The authors have successfully conducted theoretical and experimental studies and modeling the working process of the liquid-vapor ejector in the ANSYS CFX software package on different operating parameters of the pumped passive flow and various structural designs with the definition of achievable indicators of its efficiency [2–4], which are significantly higher than in similar steam.

Also, the results of theoretical and experimental studies about the feasibility the using of the liquid-vapor ejector for other purposes, in particular, in the food, chemical and engineering industries [5].

To assess the energy efficiency of a vacuum unit based on the liquid-vapor ejector operation, the most correct method is to use the exergy method of thermodynamic analysis. Using this method makes it possible to uniquely express and distribute heterogeneous energy flows in thermomechanical systems.

Exergy evaluation of the perfection energomonitoring-degree in the vacuum system study is based on modern terminology and regulations that you laid in the works [6–8].

3 Research Methodology

3.1 The basic diagram of a vacuum cooling system unit for biodiesel production

A traditional installation of biodiesel production by “Körting” (Hanover, Germany) (Figure 1) is a multi-stage vapor vacuum system, which consists of two boosters (two large steam-jet ejectors, that are connected in series), the main mixing condenser, a small intermediate ejector with a mixing condenser for pumping air, as well as a water-ring vacuum pump of the final stage.

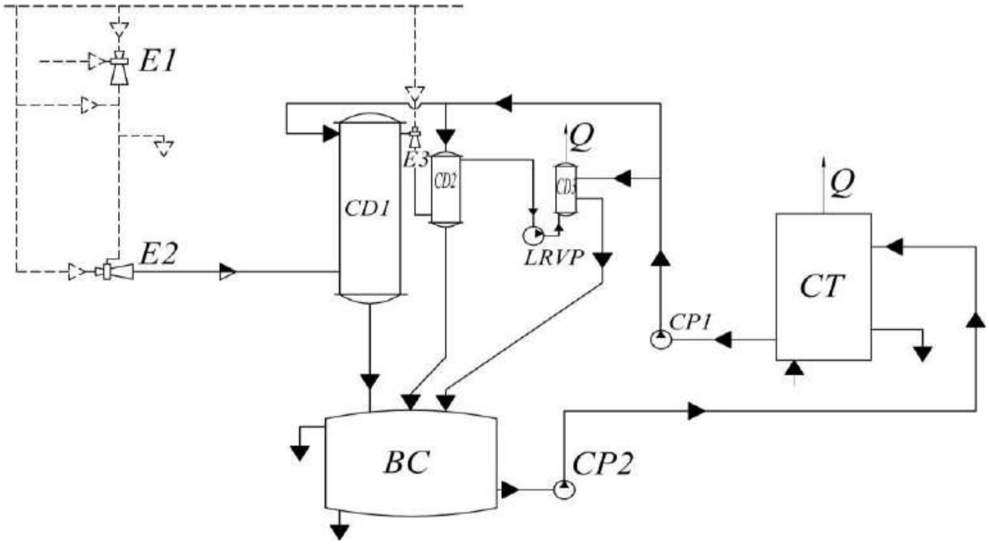

Figure 1 – The basic scheme of a vacuum cooling system unit for biodiesel production: LRVP–liquid ring vacuum pump; E1, E2, E3 – ejectors; CD1, CD2, CD3 – condensers; CP1, CP2 – coolant pumps; CT – cooling tower; BC – barometric capacity

The productiveness of the basic unit is 220 kg/h of water vapor 8 kg/h of air 5 kg/h of free fatty acids. Deodorization technology involves the extraction of fatty acids (odorants) by bubbling hot water vapor through a processed fuel ball at a pressure of 2 kPa. Maintaining this level of vacuum increases the volatility of odorants and their vapors diffuse into water vapor bubbles.

The bubbling steam condensation and the pressure maintenance at a certain level is ensured by the supply of cooling water, which circulates in the cooling circuit through the cooling tower.

The working pressure of the boiler steam, that is used by the steam jet ejectors as the working jet of the active flow is 9 bar, the cooling water temperature at the inlet is 33 C.

The working steam condensate, that supplied to the nozzle of the active flow in steam-jet ejectors is polluted the components, which contained in the pumped flow with the bubbling steam and doesn’t return to the unit. For surface-type capacitors, which are used in this unit, it is necessary to pump out the condensate, as the condensation pressure is less than atmospheric.

This type of vacuum systems combines the advantages, when steam-jet ejectors and water ring vacuum pumps are working together. This means, that the bubbled steam is compressed only by steam-jet ejectors (so-called boosters) to the first possible stage of condensation. And after the first stage, behind the main mixing condenser, combinations of steam-jet ejectors and water ring pumps are possible.

3.2 A vacuum cooling system’s scheme of biodiesel production unit, that is based on liquid-vapor ejector

The alternative circuit solution, which is proposed (Figure 2), minimizes the consumption of boiler steam in the vacuum system. Pumping of the vapor-gas mixture is provided by a liquid-vapor ejector (LVE), operating as a part of the vacuum unit.A condenser unit is provided for the vapor phase condensation of the mixing flow after the separator and return the working fluid to the circulation circuit of the vacuum unit, including a condenser, a water ring vacuum pump and a cooling system for circulating water.

The use of a mechanical vacuum pump as a forvacuum unit in this case is advisable from the standpoint of ensuring higher energy efficiency of the vacuum system.

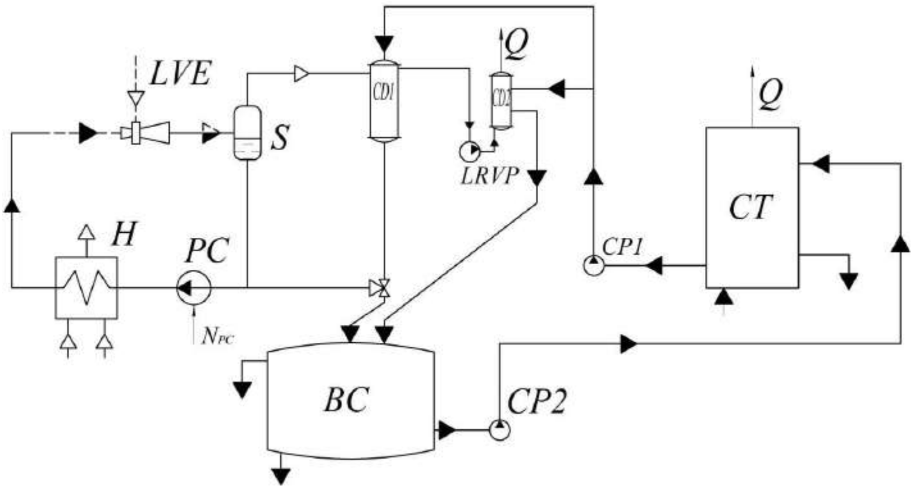

Figure 2 – A vacuum cooling system's scheme of biodiesel production unitbased on LVE: LVRP– liquid ring vacuum pump; LVE – liquid-vapor ejector; H – heater; PC – circulation pump; S – separator; CD1, CD2– condensers; CP1, CP2– coolant pump; CT – cooling tower; BC – barometric capacity

3.3 An exergy analysis of new equipment effectiveness use

An exergy analysis is executed with such step-by-step procedures:

– choose limits of the system;

– make a formalized scheme of exergy transformations in general and the system components;

– calculate the value of exergy flows crossing the system boundaries or components;

– perform classification of exergy flows in the categories, such as: "fuel", "product", "destruction", "loss";

– determine the indicators (criteria) of the exergy analysis;

– determine the optimization directions of the system as a whole or its individual components.

The scheme of exergy transformations, that occur in the basic and alternative schemes, is shown in Figure 3.

According to this methodology, during comparing circuit solutions the main indicator is the exergy efficiency value ε_{in}:

$$\varepsilon_{in} = E_p / E_F ,$$

where E_P – system exergy of the product stream; E_F – system exergy of the fuel stream.

A value difference E_F and E_P gives a destruction value E_D and exergy losses E_L in the energy transformation processes of the system, that is

$$E_D + E_L = E_F - E_P . \tag{1}$$

It should be noted that$E_D$value characterizes the level of dissipative losses due to internal irreversibility, and$E_L$is due to the presence of external heat exchange of system components with the environment.

When we use this type of the exergy analysis does not require an entropy analysis to calculate the total destruction and loss of exergy in the system, as follows from equation (1).

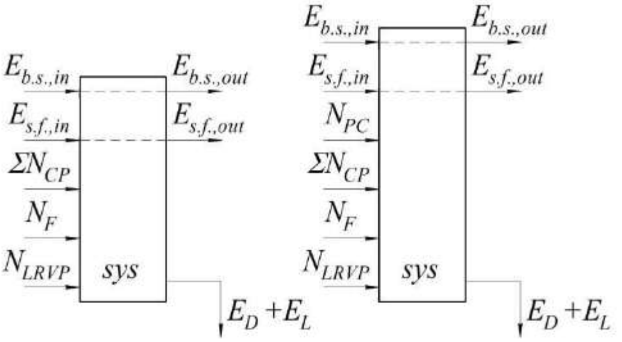

Figure 3 – The scheme of exergy transformations in the basic (a) and alternative (b) schemes

In determining E_P and$E_F$for the vacuum systems under consideration, some assumptions have been made to make significant simplifications in the calculations, namely:

– condensate flows that are removed from the system to the environment after the condensation pumps, taking into account their further non-use as energy sources, are classified as exergy losses;

– a similar approach is adopted for the mixture flows at the outlet from E3 ejector for the basic scheme and at the outlet of the liquid separator according to an alternative scheme;

– the heat flux, which is transmitted to the environment after the cooling tower is also classified as exergy losses;

– the change in the exergy of air leaks is neglected.

Taking into account the above assumptions for the basic scheme, we have:

$$E_{P1} = m_{s.f.} \left(e_{s.f.,out} - e_{s.f.,in} \right);$$

$$E_{F1} = \left(m_{b.s.} \right)_e \cdot e_{b.s.,in} + \sum N_{CP} + N_F + N_{LRVP} .$$

For the scheme with LVE:

$$E_{P2} = m_{s.f.}\left(e_{s.f.,out} - e_{s.f.,in}\right);$$
$$E_{F2} = \left(m_{b.s.}\right)_H \cdot e_{b.s.,H} + N_{PC} + \sum N_{CP} + N_F + N_{LRVP},$$

where $m_{s.f.}$ – mass flow rate of the secondary flow, kg/s; $\left(m_{b.s.}\right)_e$ – a total mass flow rate of boiler steam to the base circuit ejectors, kg/s; $\left(m_{b.s.}\right)_H$ – a mass flow rate of boiler steam through the circulation flow heater, kg/s; $e_{s.f.,in}$, $e_{s.f.,out}$ – specific exergy of secondary flow under the conditions of inlet and outlet in the vacuum system, *kJ/kg*; $e_{b.s.,in}$ – specific exergy of boiler steam at the ejector inlet in the basic scheme, kJ/kg; $e_{b.s.,H}$ – specific exergy of boiler steam at the entrance to the heater circuit based on the liquid-vapor ejector, kJ/kg; $\sum N_{CP}$ – total power consumption of coolant pumps, kW; N_{PC} – power consumption of circulating circuit pump, that is based on the liquid-vapor ejector, kW; N_F – a power consumption of cooling tower fan, *kW*; N_{LRVP} – a power consumption of liquid ring vacuum pump, kW.

After the exergy transformation of these values for the basic scheme, we obtain:

$$E_{P1} = m_{s.f.} \cdot \left[\begin{array}{l} c_p \cdot \left(T_{s.f.,out} - T_{s.f.,in}\right) - \\ -T_{env.} \cdot \left(c_p \cdot \ln\dfrac{T_{s.f.,out}}{T_{s.f.,in}} - R \cdot \ln\dfrac{P_{s.f.,out}}{P_{s.f.,in}}\right) \end{array}\right],$$

$$\begin{gathered} E_{F1} = \left(m_{b.s.}\right)_e \cdot \left[\left(h_{in} - h_{out}\right) - T_{env.} \cdot \left(s_{in} - s_{out}\right)\right] + \\ + \sum N_{CP} + N_F + N_{LRVP} \end{gathered}.$$

For the scheme, which is based on the liquid-vapor ejector:

$$E_{P2} = m_{s.f.} \cdot \left[\begin{array}{l} c_p \cdot \left(T_{s.f.,out} - T_{s.f.,in}\right) - \\ -T_{env.} \cdot \left(c_p \cdot \ln\dfrac{T_{s.f.,out}}{T_{s.f.,in}} - R \cdot \ln\dfrac{P_{s.f.,out}}{P_{s.f.,in}}\right) \end{array}\right],$$

$$\begin{gathered} E_{F2} = \left(m_{b.s.}\right)_H \cdot \left[\left(h_{in} - h_{out}\right) - T_{env.} \cdot \left(s_{in} - s_{out}\right)\right] + \\ + N_{PC} + \sum N_{CP} + N_F + N_{LRVP} \end{gathered}.$$

where c_p – specific heat of passive flow at medium temperature $\dfrac{T_{s.f.,in} + T_{s.f.,out}}{2}$, kJ/(kg·K); $T_{s.f.,\,in}$ – temperature of the secondary flow at the inlet of the ejector of the 1st degree of the base circuit and the heat exchanger-heater circuit, which is based on LVE, K; $T_{s.f.,\,out}$ – secondary flow temperature at the condenser outlet after the liquid ring vacuum pump, K; $T_{env.}$ – ambient temperature, K; R – gas specific matter of secondary flow, kJ/(kg·K); $P_{s.f.,\,in}$ – secondary flow pressure at the ejector inlet, Pa; $P_{s.f.,\,out}$ – secondary flow pressure at the condenser outlet after the liquid-ring vacuum pump, Pa; h_{in} – boiler steam enthalpy at the ejector inlet of the 1st degree on the basic scheme and the heat exchanger-heater of the scheme with LVE, kJ/kg; h_{out} – boiler steam enthalpy at the ejector outlet of the 3rd degree on the basic scheme and the heat exchanger-heater of the scheme with LVE, kJ/kg; s_{in} – boiler steam entropy at the ejector inlet of the 1st degree on the base circuit and the heat exchanger-heater circuit, that is based on LVE, kJ/(kg·K); s_{out} – boiler steam entropy at the ejector outlet of the 3rd degree on the basic scheme and the heat exchanger-heater of the scheme with LVE, kJ/(kg·K).

To assess the economic effect of the new technology introduction, it is necessary to perform a thermos-economical calculation, which is determined the cost of fuel that is required for the basic and energy-saving scheme.

For the basic fuel scheme is used superheated steam boiler and electricity, which are needed to drive the coolant pump, vacuum pump and cooling tower fan so the total fuel cost is determined by the formula:

$$\begin{gathered} C_{bas} = C_{b.s.,bas} + C_{e/e,\text{баз}} = c_{b.s.} \cdot \left(m_{b.s.}\right)_e \cdot \tau_p + \\ + c_{e/e} \cdot \left(\sum N_{CP} + N_F + N_{LRVP}\right) \cdot \tau_p \end{gathered},$$

where $c_{к.п.}$ – cost of boiler superheated vapor, UAH/(kW·h); τ_p – calculation period of the unit operation, h; $c_{e/e}$ – electricity cost for Ukrainian industrial enterprises UAH/(kW·h).

For the energy-saving scheme a fuel cost is determined as follows:

$$\begin{gathered} C_{LVE} = C_{b.s.,LVE} + C_{e/e,LVE} = c_{b.s.} \cdot \left(m_{b.s.}\right)_H \cdot \tau_p + \\ + c_{e/e} \cdot \left(N_{PC} + \sum N_{CP} + N_F + N_{LRVP}\right) \cdot \tau_p \end{gathered}.$$

The economic effect of a new vacuum cooling system introduction in the biodiesel production unit is:

$$E = C_{bas} - C_{LVE}, UAH$$

The specific price per unit of product (kg) for the basic and alternative scheme is determined by the formulas:

$$p_{G,bas} = \frac{C_{bas}}{m_{s.f.} \cdot \tau_p}, UAH/kg,$$

$$p_{G,\text{РПЕ}} = \frac{C_{LVE}}{m_{s.f.} \cdot \tau_p}, UAH/kg.$$

4 Results and Discussion

Calculation results of regime and energy parameters by comparative schemes are given in Table 1, exergy indicators – in Table 2.

Table 1 – Regime and energy parameters of the circuit solution variants

Parameter	Design scheme	
	basic	with LVE
Initial pressure in the vacuum system, kPa	5	5
Pressure suction of vacuum pump, kPa	40	40
Boiler vapor pressure, kPa	900	900
Boiler vapor temperature, °C	180	180
Mass flow rate of boiler vapor, kg/h	1 535	215
Mass flow rate of secondary flow, kg/h	213	213
Volume flow rate of a coolant, m^3/h	223	109
Mass flow rate of a coolant, kg/h	$2.2 \cdot 10^5$	$1.1 \cdot 10^5$
Power consumption of a coolant pump, kW	6.5	3.2
Power consumption of the pump circulation loop, kW	–	0.1
Power consumption of the vacuum pump, kW	4.0	4.0
Power consumption of the cooling tower fan, kW	3.15	2.1

Table 2. Exergy indexes of schematic variants

Parameter	Design scheme	
	basic	with LVE
Exergy of a product flow, kW	24.5	24.5
Exergy of a fuel flow, kW	336.3	55.6
Exergy efficiency	0.073	0.441

On the basis of the software package for calculating the vacuum unit, which was developed by the author, calculations were performed to assess the impact of the increasing degree in the passive flow pressure with LVE on the injection coefficient and exergy efficiency indicators. On Figure 4 this dependence is presented, allowing the choice of intermediate pressure between compression stages for the vacuuming system.

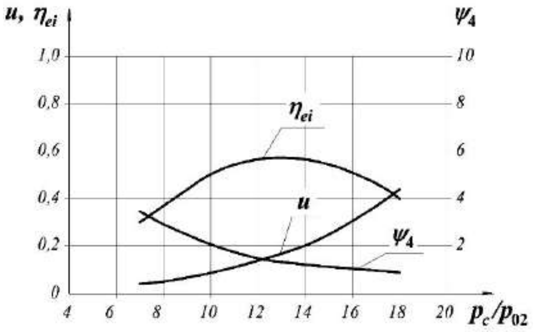

Figure 4 – The dependence graph of the degree of vapor overproduction ψ_4, injection coefficient u and exergy efficient η_{ei} from the increasing value of the passive flow pressure p_c/p_{02} at t_{01} = 121–149 °C, p_{01} = 300–500 kPa, p_{02} = 5 kPa

5 Conclusions

As a result, during the comparative calculation of the evacuation schemes on the basis of a three-stage steam-jet ejector and a liquid-vapor ejector, it can be concluded, if we use LVE, we can make it possible to increase the efficiency of the biodiesel production unit as follows:

– to simplify the design of the installation by switching from a two-stage steam-jet ejector to a single-stage vacuum unit, based on LVE.

– to reduce the initial parameters of the working vapor by switching to more moderate parameters of the working fluid in the active flow with LVE (from 9 bar and 225 °C to 4 bar and 135 °C) and to minimize the consumption of this vapor due to the design features of the vacuum unit, based on LVE, in which the working vapor is consumed not as an active flow of the steam-jet ejector, but only in a small amount for heating the working fluid of the active flow in the heat exchanger-heaters (a vapor reduction).

According to the results of the exergy analysis, we see that the energy efficiency of the vacuum cooling system in the biodiesel production unit, that is based on the liquid-vapor ejector is more than 6 times higher than for the basic scheme.

More accurate optimization of the vacuum system was carried out on the basis of thermo-economic analysis by Tsatsaronis method considering the economic model for the optimization indicator in the value form of the exergy product cost and found, that the fuel cost for the basic scheme is 101 797 UAH, and for energy saving – 64 578 UAH, it follows that the economic effect of the new scheme introduction is 37 219 UAH.

References

1. Sharapov, S. O., Arsenyev, V. M., & Kozin, V. M. (2017). Application of jet thermal compression for increasing the efficiency of vacuum systems. *IOP Conference Series: Materials Science and Engineering*, Vol. 233, 012028.
2. Sharapov, S. O. (2011). Problems of experimental studies of liquid-vapor ejector working process in the vacuum regime and their technical content. *Bulletin of Sumy State Univerity. Series "Technical Sciences"*, Vol. 1, pp. 51–57.
3. Sharapov, S., & Arsenyev, V. (2016). Experimental study of a liquid-vapor ejector with a cylindrical mixing chamber. *Refrigerating Equipment and Technology*, Vol. 52(2), pp. 87–92.
4. Sharapov, S., Arsenyev, V., & Kozin, V. (2016). Experimental investigation of liquid-vapor ejector with conical mixing chamber. *Technology Audit Production Reserves*, Vol. 4, No. 1(30), pp. 50–55.

5. Sharapov, S., Arsenyev, V., & Protsenko, M. (2013). The use of liquid-vapor ejector in vacuum systems. *Science et Tchnique du Foid – Refrigeration Science and Technology*, Vol. 4.
6. Tsatsaronis, J. (2002). *The interaction of thermodynamics and economics to minimize the cost of energy-conversion system*. Negotiant Studio Ltd., Odessa, Ukraine.
7. Morozyuk, T. V. (2006). Theory of cooling and heat pumps. Negotiant Studio Ltd., Odessa, Ukraine
8. Arsenyev, V. M. (2011). *Heat pump energy conservation technology*. Sumy State University, Sumy, Ukraine.

Удосконалення вакуумної системи охолодження установки виробництва біодизельного палива

Шарапов С.[1], Старченко М.[1], Проценко М.[2], Панченко В.[1], Ковтун В.[1]

[1] Сумський державний університет, вул. Римського-Корсакова, 2, 40007, м. Суми, Україна;
[2] Академія управління та адміністрування м. Ополє, вул. М. Нєдзяловського, 18, 46020, м. Ополє, Польща

Анотація. У статті вирішено актуальну проблему підвищення ефективності вакуумних систем охолодження установок виробництва біодизельного палива шляхом застосування вакуумних агрегатів на базі рідинно-парового ежектора, що працює за принципом струминної термокомпресії. Метою даного дослідження є підтвердження доцільності застосування вакуумних агрегатів на базі рідинно-парового ежектора, що працює за принципом струминної термокомпресії, у вакуумних системах охолодження установок виробництва біодизельного палива. Подано опис базової схеми системи охолодження установки виробництва біодизельного палива, яка містить трьохступеневий пароструминний ежектор. Запропоновану схему на базі рідинно-парового ежектора. Виконано порівняльний аналіз вакуумних систем охолодження установок виробництва біодизельного палива, схеми яких порівнювались, у тому числі на базі існуючих триступеневих пароструминних ежекторів і нового одноступеневого вакуумного агрегату на базі рідинно-парового ежектора. Як порівняльний аналіз застосовано ексергетичний метод оцінювання ефективності застосування запропонованого устаткування, оскільки у робочому процесі відбувається перетворення двох видів енергії: електричної (для приводу насоса) і теплової (для підігріву робочої рідини активного потоку у теплообміннику-підігрівачі). У результаті досягнуті більші показники ефективності застосування нової технології за оптимізаційним параметром – проміжним тиском між рідинно-паровим ежектором та рідинно-кільцевим вакуумним насосом.

Ключові слова: вакуумна система охолодження, рідинно-паровий ежектор, біодизельне паливо, ексергетичний коефіцієнт корисної дії.

JOURNAL OF ENGINEERING SCIENCES
ЖУРНАЛ ІНЖЕНЕРНИХ НАУК
ЖУРНАЛ ИНЖЕНЕРНЫХ НАУК
Web site: http://jes.sumdu.edu.ua
DOI: 10.21272/jes.2019.6(1).f3 Volume 6, Issue 1 (2019)

UDC 504.062:66.086.4

Clarification of the Recent Scientific Approaches in Magnetic Water Treatment

Plyatsuk L. D.[1], Roy I. O.[1*], Chernysh Y. Y.[1], Kozii I. S.[1], Hurets L. L.[1], Musabekov A. A.[2]

[1] Sumy State University, 2 Rymskogo-Korsakova St., 40007 Sumy, Ukraine;
[2] M. Auezov South Kazakhstan State University, 5 Tauke-Khan Av., 486018 Shymkent, Kazakhstan

Article info:
Paper received: October 26, 2018
The final version of the paper received: February 9, 2019
Paper accepted online: February 15, 2019

***Corresponding Author's Address:**
i.roy@ecolog.sumdu.edu.ua

Abstract. The paper focused on study of influence magnetic water treatment (MWT) mechanism on physicochemical properties of aqueous solutions taking into account nature of changes in kinetics of chemical reactions. The theoretical analysis of the magnetic field geometry in the hardware equipment of water purification technologies was used. A review of current data on physicochemical processes was carried out for the processes of the influence of magnetic treatment on the properties and structure of aqueous solutions. The determination of the basic mechanisms of MWT was done taking into account the influence of a non-uniform magnetic field on the librational fluctuations of water molecules, followed by their destruction and disruption of the ortho-para ratio towards more chemically active water molecules. The resulting formalized model makes it possible to explain the nature of the complex effects reorganized after exposure of a non-uniform magnetic field to aqueous solutions. Subsequently, this model can be used to optimize the parameters of the mode of the process of water preparation and water purification.

Keywords: mechanisms of influence, magnetic field, chemical activity, librational fluctuations of water molecules, aqueous solution, formalized model.

1 Introduction

According to the UN, about 500 million people live in areas where water consumption exceeds twice locally renewable water resources. The discharge of wastewater causes significant damage to flora and fauna of water bodies and human health. Direct impact includes degradation of aquatic ecosystems and diseases transmitted through water from contaminated freshwater sources, has long-term consequences for the well-being of social and human resources [1]. The research of nonlinear kinetics models of ecosystem processes under the influence of pollutants and distribution organic impurities in the environment also determines need for expansion scientific and theoretical foundations for implementation of water purification methods [2].

Implementation of reverse water supply systems requires improvement quality of purified water and reduction of demand for additional resources (electricity, reagents, etc.). According urgent task is finding ways to intensify existing cleaning methods to improve the efficiency of such systems.

2 Literature Review

The most common methods of treatment intensification areas are using of technologically justified treating schemes, modernization of existing and development new designs of devices, and use physical processing of aqueous solutions (treatment of external fields, ultra-sound, ultraviolet, etc.). The latter becomes of increasing importance in the direction of intensifying purification methods of contaminated water, which is primarily due to their versatility, economy and lack of need for additional reagents.

The magnetic water treatment (MWT) is the one of the perspective physical methods before filing for purification, which based on change in physical and chemical properties of aqueous solutions. Such method characterized by simplicity of implementation, low capital and operating costs [3]. The only disadvantage is lack of knowledge about MWT mechanism [4–6], which limits its widespread implementation. However, positive experience and numerous studies [4–16], proving presence of changes in kinetics of deposition suspended particles in the volume of solution, nature and volume of deposits on heat exchange surfaces, efficiency of ion-exchange processes, kinetics passage of chemical reactions, etc., allows us to confirm promise of its use in processes of environmental protection, which confirms relevance of our research.

The main problem on the path of widespread introduction of MWT is the lack of an integrated approach to studying the mechanism of manifestation of MWT effects, in particular, the effect on the kinetics of chemical reactions in aqueous solutions, which was partially studied in [7–16].

The aim of the paper is theoretical study of influence mechanism MWT on physicochemical properties of aqueous solutions taking into account nature of changes in kinetics of chemical reactions.

The following tasks set and solved in the article:

– to analyze previous studies of MWT mechanisms of impact on structure and properties of aqueous solutions;

– to form a complex model for description the mechanism of influence non-uniform magnetic field on aqueous solutions properties and change kinetics of chemical reactions.

3 Research Methodology

Since all effects of MWT related to change in physical and chemical water properties caused by influence of magnetic field on water solution, it is important to take into account the basic design and mode parameters of MWT devices, which differ in a number of features [17]. One of the main structural parameters is geometry of magnetic field and heterogeneity of distribution magnetic induction B along the pipe for passage of aqueous solution (Figure 1).

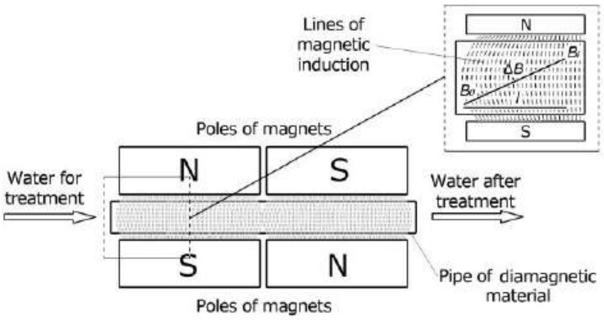

Figure 1 – Typical scheme of elementary plot device MWT: ΔB – value of magnetic induction changes in a non-uniform magnetic field; l – length of MWT device section, where magnetic induction varies from B_0 to B_i; B_0, B_i – minimum and maximum value of magnetic induction, respectively

The geometry of magnetic field in MWT devices depends on several factors, which based on properties of magnets and how to accommodate them. The effect of magnetic field on water occurs on MWT device areas, where magnetic induction varies from B_0 to B_i, its lines necessarily directed perpendicular to the solution motion, and induction difference $\Delta B \neq 0$ T, otherwise MWT effect not observed.

Among regime parameters MWT [4, 6, 18], it is mandatory that the water flows in magnetic field is mandatory, and water velocity is one of the parameters that determines effectiveness of MWT.

The aqueous solution velocity and value of magnetic induction between them are closely interconnected, and their connection must be taken into account when designing MWT devices and selecting optimal operating modes. In view of current developments MWT devices, one of the main drawbacks is incomplete incorporation of MWT parameters, or their inclusion separately from each other, without analyzing their interconnection. The simultaneous consideration of such MWT parameters as the aqueous solution speed and magnetic induction requires further study.

4 Results and Discussion

4.1 Theoretical formalization of the MWT mechanism

The large amount of data associated with MWT have led to determination of various aspects regarding MWT mechanism, which can be conventionally grouped into three approaches: colloidal, ionic and water [4–7, 9, 18, 19–21]. In the table 1 presents groups of MWT mechanism influence according our analysis.

Modern ideas about kinetics of chemical reactions based on the fact that any reaction occurring in aqueous solution includes the step of rearranging solvent molecules to form “cavities” in which located reacting particles, activated complex and reaction products [22]. The rate of water molecule rearrangement for expected activated complex greatly effects on kinetics of chemical reactions and depends on physical and chemical properties of aqueous solutions that are due to presence of hydrogen bonds [23] and their nature, peculiarity of water molecule isomers structure [24] and features of molecules oscillations [25, 26].

Table 1 – Groups of the MWT mechanisms

Impact object	Mechanisms
Colloidal group of approaches	
Colloidal (ferromagnetic) particles	The surface properties of such particles changes and they act as crystallization centers under the magnetic field influence. This group explains the anti-scale effect.
Ionic group of approaches	
Ions that are present in water	Under the influence of a magnetic field, polarization and deformation of ions occur, which are accompanied by their hydration decrease, which affects the course of physicochemical processes in aqueous systems.
Water group of approaches	
Water molecules	This group combines ideas about the possible influence of a magnetic field on the water structure. This influence, on the one hand, can cause changes in the aggregation of water molecules, and on the other hand, changes in the orientation of the nuclear spins of hydrogen in water molecules, etc.

Changing kinetics of reactions in aqueous solutions is possible due to the weakening of interaction water molecules between themselves and with dissolved substances, breaking of hydrogen bonds, or reducing their energy, which facilitates water molecules restructuring for the expected activated complex [23]. The last becomes possible even with MWT, which is confirmed by many studies [3–6, 18, 19], in which appearance of changes in structure and physical and chemical properties of aqueous solutions due to hydrogen bond (density, viscosity, surface tension), changes in hydration of dissolved substances and changes in rate of reaction. However, nature of such impact requires further research.

Given the value of magnetic induction at MWT, external energy entering aqueous solution is not sufficient for direct breaking or weakening of hydrogen bonds [4, 5]. The results obtained in [6] indicate that defining parameter MWT, which more than induction value determines efficiency of MWT, is the heterogeneity of magnetic field. The changes caused by influence of non-uniform magnetic field on the structure of water, may related not so much to discontinuities of hydrogen bonds, but with decrease in their energy, increase in length and change in angle [5, 27]. In this case, structure of water molecules, presence of quantum differences water molecules and nature of their interaction with each other and with dissolved substances has important role [24, 25].

The appearance of quantum differences between water molecules can be explained by states presence librational undamped oscillations in water molecules [25]. Such oscillations cause appearance of hydrogen proton rotation on hydrogen bond line in the directions perpendicular to hydrogen bond line.

The rotation of hydrogen proton around hydrogen bond line has an elliptical trajectory (EPT) whose radius also rotates, as shown in Figure 2.

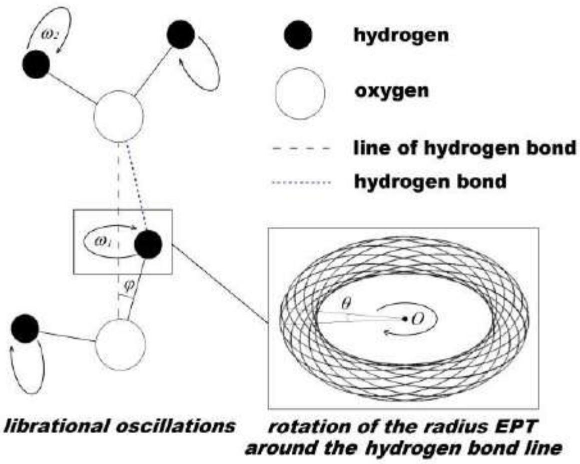

Figure 2 – Rotate proton and electron orbitals of neighboring water molecules connected by hydrogen bonds: ω_i – frequency molecules libration vibrations; φ – angle of proton deviation from hydrogen bond line; θ – phase rotation radius EPT; O –hydrogen bond line

Movement of positively charged hydrogen proton by EPT causes appearance of magnetic and mechanical moment. Magnetic fields formed by rotation of hydrogen protons of one molecule can both coincide in the direction and be opposite directed along molecule axis. In the case of uniform direction of protons rotation, magnetic fields formed and form magnetic field of entire molecule and conversely. Consequently, presence of librational oscillations water molecules is the reason for appearance of quantum differences in water molecules isomers, which mentioned in work [24].

Synchronization of libration oscillations for para-isomers in supramolecular formations is carried out by four hydrogen bonds, and their cooperative nature provides a redistribution of energy received from outside, from collisions with thermal motion [25], which makes possible existence of ice-like structures in aqueous solutions, emergence heterogeneity of water density [26] and the violation of equilibrium ortho/pair ratio in the direction of pair-isomers, more than 2 times [24]. Thus, aqueous solution is a nonequilibrium system that is sensitive to external influences.

The prerequisite for establishing an equilibrium ortho/pair ratio is violation of synchrony librational oscillations in ice structures, where, first of all, weakest hydrogen bonds destroyed, and energy received from outside goes to destruction of ice-like structures. Their destruction leads to "release" of pair-isomers, which, when further collisions with other water molecules, become ortho-isomers [24].

For explain mechanism of appearance pair-ortho conversion under influence of non-uniform magnetic field on aqueous solution, let's consider loss synchronism of libration oscillations under magnetic field influence on hydrogen proton, rotating on EPT. The effect of non-uniform magnetic field on the proton EPT results in precession of EPT radius around hydrogen bonds. Due to structural stiffness of water molecule, appearance precession of one hydrogen proton leads to appearance a similar precession of second proton. EPT precession is not the same as that occurring with electrons orbits, because for EPT precession required rotation the entire water molecule, which is impossible due to presence other hydrogen bonds. EPT precession becomes possible only for those protons, in which plane of EPT is perpendicular to lines of magnetic induction. Since, in case of oscillations, radius proton EPT rotate around hydrogen bond line, appearance of an additional precision with radius EPT changes rotation phase θ of radius EPT, which will be different for two pair-isomers bound by one hydrogen bond due to difference in angle slope plane EPT protons of neighbouring molecules to lines of magnetic induction.

The result of the influence of a non-uniform magnetic field on an aqueous solution is the shift of the phase of rotation of the radius of the EPT of hydrogen protons for neighbouring isomers of water molecules by $\pm \Delta\theta$. Such a phase shift occurs non-uniformly with a certain angular acceleration ε in the direction of the Lorentz force, where the magnitude of the acceleration was found from the second law of Newton:

$$ma = F_L, \tag{1}$$

where m is proton weight, kg; a is acceleration of rotation of the proton EPT radius around the hydrogen bond line, m/s^2; F_L is Lorentz force, N.

$$ma = e\upsilon_m \Delta B \sin\alpha, \tag{2}$$

where e is proton charge, C; υ_m is the speed of "movement" of the magnetic induction lines relative to something (a circuit of EPT), m/s; ΔB is the magnitude by which the magnetic induction changes, T; sinα is the angle between the velocity υ_m and the magnetic induction vector B.

The additional motion of the radius of EPT around the hydrogen bond line in a non-uniform magnetic field is rotational motion with angular acceleration, which, by means of standard transformations of expression (2), is represented as

$$\varepsilon = \frac{e\upsilon_m \Delta B}{mr}. \tag{3}$$

For find the velocity υ_m, an expression was taken from [28] and, having carried out the necessary transformations, we obtain

$$\upsilon_m = \frac{\Delta \Phi}{\Delta B \cdot L \cdot \Delta t}, \tag{4}$$

where $\Delta\Phi$ is magnetic flux, Wb; ΔB is change in magnetic induction, T; L is the length of EPT, m; Δt is the time during which the magnetic induction lines intersect the contour of EPT, s.

The magnetic flux $\Delta\Phi$ can be expressed in terms of the change in the magnetic induction ΔB and the area of the EPT square S, which it intersects:

$$\upsilon_m = \frac{\Delta B \cdot S}{\Delta B \cdot L \cdot \Delta t}. \tag{5}$$

The radius of EPT was taken equal to r for simplicity of writing the formula (5) as:

$$\upsilon_m = \frac{r}{2 \cdot \Delta t}. \tag{6}$$

Thus, the rate of "movement" of magnetic induction lines relative to a proton depends only on the radius of EPT and the time during which the magnetic induction B changes and does not depend on how much the magnetic induction changes. In turn, an increase or decrease in induction affects only the direction of the effect of the F_L force. Having made the necessary transformations of expressions (3) and (6):

$$\varepsilon = \frac{e}{2m}\frac{\Delta B}{\Delta t}. \tag{7}$$

The change θ-phase of radius EPT in a non-uniform magnetic field is due to influence Lorentz force on proton (Figure 3 a). It has two components, where the first component F_{L1} arises from proton motion in a magnetic field at velocity υ, which is due by librations oscillations. The component F_{L1}, for each proton position on EPT, is oriented perpendicularly to proton movement, and as can we see from Figure 3 a (position 1 and 2), compensates for itself and does not cause shift of turn phase θ. In addition, hydrogen bond formed by electrostatic forces much larger than F_{L1}, so radius EPT remains "rigid" and angular velocity of proton rotation remains unchanged.

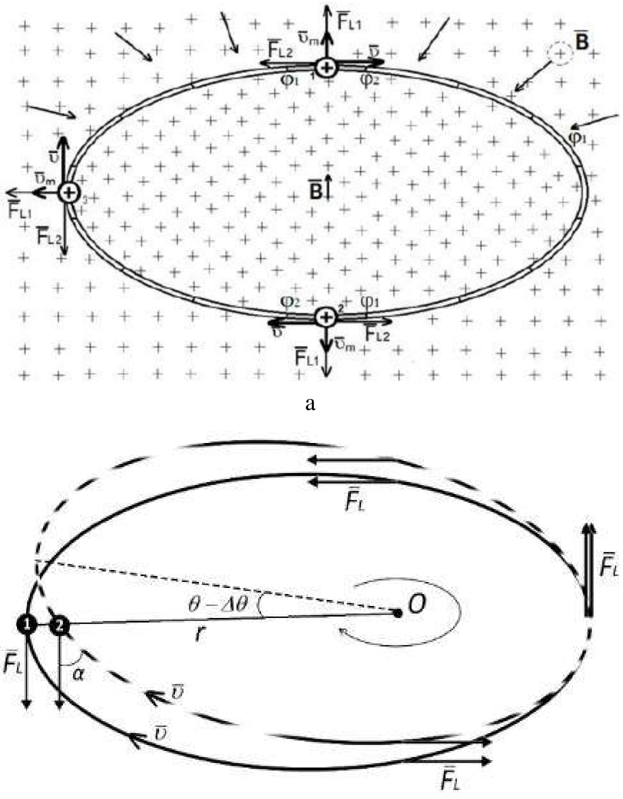

Figure 3 – Displacement phase of EPT rotation hydrogen proton in a non-uniform magnetic field (magnetic induction lines directed from us): B – magnetic induction; F_{L1} – first component of Lorentz force; F_{L2} – second component of Lorentz force; υ – proton speed movement by EPT; υ_m – rate intersection of contour EPT by magnetic induction lines; φ_1 and φ_2 – potentials; 1, 2 – position of hydrogen proton on EPT in plane rotation radius EPT, in accordance before and after turning radius EPT; r – radius EPT; α – angle between direction of force F_L and tangent to contour EPT; O – hydrogen bond line; θ – phase of radius EPT rotation; $\Delta\theta$ – shift of turn phase radius EPT

The appearance of second component of Lorentz force F_{L2} becomes possible only in non-uniform magnetic field, which is a prerequisite for MWT. Force F_{L2} directed in one direction at tangent to EPT (Figure 3 a, positions 1, 2, and 3). The process of occurrence electromotive force (EMF) in non-uniform magnetic field isn't considered as the result of appearance vertical electric field, but it's the result of increase in density of magnetic field due to "flow" field lines from surrounding space into magnetic flux through closed circuit. In process of "entering" lines of induction into the contour, they cross contour, causing EMF induction by “mechanism of intersection” [28].

Supposed that closed circuit in Figure 3 a is the region in which fluctuates radius EPT of the hydrogen proton (Figure 2), on which proton moves and creates elemental current in circuit. Conditionally divide contour into n sections that “isolated” from each other. Each section corresponds to certain position of proton and during its movement there is a potential difference. With increase of magnetic induction, its lines “penetrating” into contour, intersect it with velocity υ_m (expressions (6)) in direction to the center. Otherwise, with decrease magnetic induction, its lines move from center to periphery, and Lorentz force F_{L2} changes its direction.

The effect of Lorentz force F_{L2} (further F_L) is shown in Figure 3 b, which depicts elementary act turning radius EPT taken from Figure 2. Additionally, Figure 3 b clearly shows that when $\upsilon_m = \text{const}$, the direction and value of force F_L stored for proton irrespective of its position on EPT, only angle α between vector of force F_L and tangent to EPT changes. Thus, at p.1 angle $\alpha = 0°$, after turning EPT (position 2) angle $\alpha \neq 0^o$. That’s why, with coincidence of basic direction rotation radius EPT and direction of force F_L, it accelerates, and in opposite case, slows rotation radius EPT around hydrogen bond line, changing rotation phase EPT by value $\pm\Delta\theta$ and with prolonged influence of F_L, with each turn EPT displacement phase of the rotation increases.

4.2 Development of a complex model of the influence of a non-uniform magnetic field on the properties of aqueous solutions

Figure 4 shows the formed model of the non-uniform magnetic field impact on the kinetics of chemical reactions in aqueous solutions, which takes into account complex factors that reasoned by this influence.

Thus, influence of non-uniform magnetic field on kinetics chemical reactions in aqueous solutions does not depend on whether induction of magnetic field increases or decreases, result of effect remains the same, an important value becomes value at which magnetic induction changes and time for which this change occurs. The Lorentz force, caused by change in induction value, directed at proton-tangent to EPT and its direction may coincide with direction of rotation proton radius EPT, and be opposite directed. The effect of this force becomes possible only when moving in non-uniform magnetic field, where it shifts the phase of rotation radius EPT by a value of $\pm\Delta\theta$. In turn, because the water molecules in the volume of solution oriented arbitrarily, phase displacement $\pm\Delta\theta$ is not the same for adjacent water molecules in ice structures, which causes asymmetry of libration oscillations pair-isomers and affects their synchronicity and cooperability.

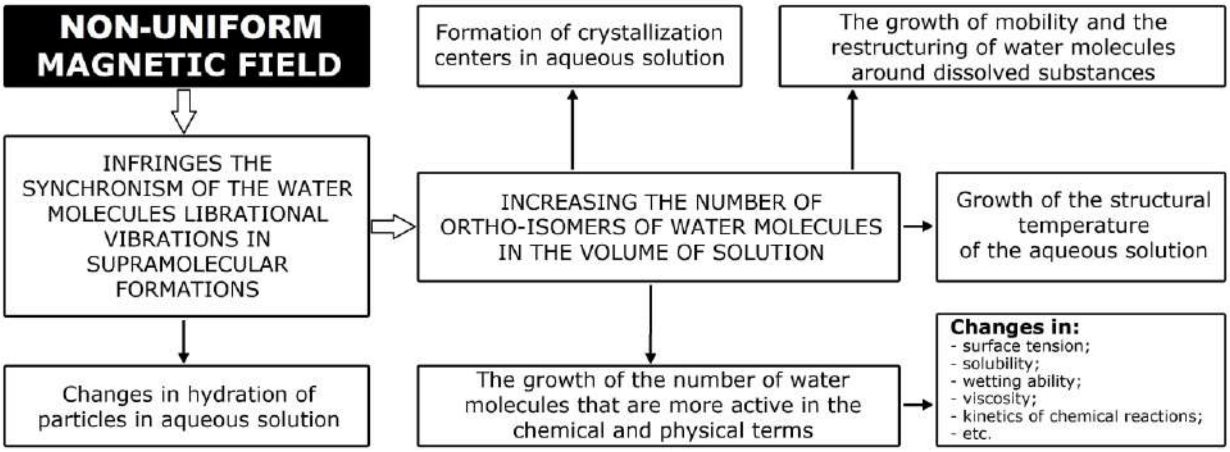

Figure 4 – Complex model of non-uniform magnetic field influence on kinetics chemical reactions in aqueous solutions

Because water is a non-equilibrium system, violation of synchronous oscillations in supramolecular formations, which, due to collisions with other molecules, results in excess energy and collapses, results in conversion of pair-isomers, increase in number of ortho-isomers, causing changes in density, viscosity, in infrared spectrum of water, hydration of dissolved substances, registered after MWT, etc.

5 Conclusions

The analysis of technical realization of MWT allowed establish that one of the main structural parameters is heterogeneity of distribution magnetic induction along the pipe for passage aqueous solution. The groups of MWT mechanisms were formed for interpretations of the physicochemical effects of MWT.

The theoretical model of the complex mechanisms of the influence non-uniform magnetic field was formed for considering quantum differences between two types of water molecule isomers and librational oscillations of water molecules in supramolecular formations. Further research will be directed to use the complex model of magnetic field influence for regime parameters rationalization of water preparation and purification processes.

References

1. The United Nations World Water Development Report (2017). *Statistical Information.* Retrieved from: http://www.unwater.org/publications/world-water-development-report-2017.
2. Plyatsuk, L., & Chernish, Ye. (2016). Formalization of non-linear patterns of evolutionary ecosystem processes under anthropogenesis influence. *Eastern-European Journal of Enterprise Technologies*, № 2/4 (80), pp. 25–31.
3. Roy, I., & Plyatsuk, L. (2013). The use magnetic treatment of natural waters for intensification of organic compounds oxidation by ozone. *Ecological Safety*, No. 2 (16), pp. 103–106 [in Ukrainian].
4. Klassen, V. (1982). *Magnetization of Water Systems.* Khimiya, Moskow [in Russian].
5. Minenko, V. (1981). *Electromagnetic treatment of water in power system*. KhGU, Kharkov [in Russian].
6. Baran, B. (2005). *Physical and Chemical Substantiation magnetic field Action on Aqueous Solutions with the Object of Development of the Systems of Technogenetic Ecological Safety*. Khmelnytskiy National University, Khmelnytskyi [in Ukrainian].
7. Lipus, L., & Dobersek, D. (2007). Influence of magnetic field on the aragonite precipitation. *Chemical Engineering Science*, No. 62, pp. 2089–2095.
8. Bali, M., Mabrouk, Y., & Abdelli, N. (2016). Effects of magnetic treatment on scaling power of hard waters. *Separation and Purification Technology*, Vol. 171, pp. 88–92.
9. Chibowski, E., Szcześ, A. (2018). Magnetic water treatment–A review of the latest approaches. *Chemosphere*, Vol. 203, pp. 54–67.
10. Latva, M., Inkinen, J., Ramo, J., Kaunisto, T., et al. (2016). Studies on the magnetic water treatment in new pilot scale drinking water system and in old existing real-life water system. *Journal of Water Process Engineering*, Vol. 9, pp. 215–224.
11. Szcześ, A., Chibowski, E., Holysz, L., & Rafalski, P. (2011). Effects of static magnetic field on water at kinetic condition. *Chemical Engineering and Processing: Process Intensification*, Vol. 50(1), pp. 124–127.
12. Seyfi, A., Afzalzadeh, R., & Hajnorouzi, A. (2017). Increase in water evaporation rate with increase in static magnetic field perpendicular to water-air interface. *Chemical Engineering and Processing - Process Intensification*, Vol. 120, pp. 195–200.
13. Surendran, U., Sandeep, O., & Joseph, E. J. (2016). The impacts of magnetic treatment of irrigation water on plant, water and soil characteristics. *Agricultural Water Management*, Vol. 178, pp. 21–29.
14. Al-Ogaidi, A. A. M., Wayayok, A., Rowshon, M. K., & Abdullah, A. F. (2017). The influence of magnetized water on soil water dynamics under drip irrigation systems. *Agricultural Water Management*, Vol. 180(A), pp. 70–77.
15. Lipus, L. C., Acko, B., & Neral, B. (2013). Influence of magnetic water treatment on fabrics' characteristics. *Journal of Cleaner Production*, Vol. 52, pp. 374–379.
16. Koshoridze, S. I., & Levin, Yu. K. (2014). Model of scale deposition with magnetic water treatment. *Formerly known as nanomechanics science and technology: an international journal*, Vol. 5(1), pp. 51–71.
17. Roy, I., & Plyatsuk, L. (2012). Hardware realization of magnetohydrodynamic sewage treatment. *Environmental intelligence – 2012.* Dnipropetrovsk: Dnipropetrovsk National University of Railway Transport named after Academician V. Lazaryan, pp. 158–159 [in Ukrainian].
18. Dushkin, S., & Evstratov, V. (1986). *Magnetic water treatment at chemical plants*. Khimiya, Moskow [in Russian].
19. Kvartenko, A. (2009). Fundamentals of the modern theory of the influence of a constant magnetic field on changes in the structure of water and the permeability of cell membranes. *Bulletin of the National University of Water and Environmental Engineering*, No. 1(45), pp. 104–115 [in Ukrainian].
20. Usatenko, S., Morozov, V., & Klassen, V. (1977). The effect of magnetic fields on the rotational IR spectra of water. *Colloid Journal*, Vol. 39(5), pp. 1018–1020 [in Russian].
21. Semikhina, L., & Kiselev, V. (1988). The effect of weak magnetic fields on the properties of water and ice. *Russian Physics Journal*, No. 5, pp. 13–17 [in Russian].
22. Kilimnik, A. (2008). *Physical chemistry*. Publisher TSTU, Tambov [in Russian].
23. Entelis, S., & Teager, R. (1973). *Kinetics of reactions in the liquid phase*. Khimiya, Moscow [in Russian].
24. Pershin, S. (2012). Quantum difference of ortho-para spin-isomers H_2O as a physical basis of water anomaly properties. *Nanostuctures. Mathematical physics and Modelling*, Vol. 7(2), pp. 103–120 [in Russian].
25. Malafayev, N. (2015). Power features of oscillations of a two-frequency spherical pendulum in a non-uniform force field. *Science Rise*, No. 10/2(15), pp. 68–75 [in Russian].
26. Zakharov, S., & Mosyagina, I. (2011). *Cluster structure of water (review).* FIAN, Moskow (Preprint) [in Russian].
27. Voloshin, V., Zheligovskaya, E., Malenkov, G., et al. (2001). Structures of hydrogen bond networks and the dynamics of water molecules in condensed water systems. *Russian Chemical Journal*, Vol. XLV(3), pp. 31–37 [in Russian].
28. Kann, K. (2012). *Electrodynamics of common sense*. Lambert Academic Publishing, Dudweiler [in Russian].

Уточнення останніх наукових підходів до магнітної обробки води

Пляцук Л. Д.[1], Рой І. О.[1], Черниш Є. Ю.[1], Козій І. С.[1], Гурець Л. Л.[1], Мусабеков А. А.[2]

[1] Сумський державний університет, вул. Римського-Корсакова, 2, 40007, м. Суми, Україна;
[2] Південно-Казахстанський державний університет ім. М. Ауезова,
просп. Тауке Хана, 5, 486018, м. Шимкент, Казахстан

Анотація. Досліджено механізм впливу магнітної обробки на фізико-хімічні властивості водних розчинів з урахуванням характеру змін кінетики хімічних реакцій. Використано теоретичний аналіз геометрії магнітного поля в апаратному обладнанні технологій очищення води. Проведено огляд сучасних даних про фізико-хімічні процеси, обумовлені впливом магнітної обробки на властивості та структуру водних розчинів. Здійснено розширення концептуальних засад теорії механізму магнітної обробки з урахуванням впливу неоднорідного магнітного поля на лібраційні коливання молекул води з подальшим їх руйнуванням і порушенням орто-пара-відношення у бік більш хімічно активних молекул води. Отримана формалізована модель пояснює природу ефектів, що спостерігаються після впливу магнітного поля на водні розчини та може бути використана для оптимізації режимних параметрів процесів підготовки та очищення води.

Ключові слова: механізм впливу, магнітне поле, хімічна активність, лібраційні коливання молекул води, водний розчин, формалізована модель.

JOURNAL OF ENGINEERING SCIENCES
ЖУРНАЛ ІНЖЕНЕРНИХ НАУК
ЖУРНАЛ ИНЖЕНЕРНЫХ НАУК
Web site: http://jes.sumdu.edu.ua
DOI: 10.21272/jes.2019.6(1).f4 Volume 6, Issue 1 (2019)

UDC 66.06

Hydrodynamics of a Liquid Film Downflow on a Flat Surface in Evaporation Conditions into a Flow of Neutral Gas

Lukashov V. K.*, Kostiuchenko Y. V., Timofeev S. V.

Shostka Institute of Sumy State University, 1 Haharina St., 41100 Shostka, Ukraine

Article info:
Paper received: November 22, 2018
The final version of the paper received: February 25, 2019
Paper accepted online: March 1, 2019

***Corresponding Author's Address:**
khtms@ishostka.sumdu.edu.ua

Abstract. The work is devoted to the study of the gravitational motion of a liquid film under evaporation conditions into a flow of neutral gas as applied to film machines with a plane-parallel nozzle. The aim of the work is to develop a mathematical model of such a process and establish its laws. The model is based on the physical concepts of a liquid film flowing down a flat surface heated from outside under the assumption that the film flows in isothermal conditions under steady-state laminar mode without wave formation and in the absence of friction between the gas and the film. The mathematical description of the film flow down process in these conditions includes the equation of motion and the continuity equation for the liquid film, which are supplemented by the equations of mass transfer, the material balance of the gas phase in the evaporated liquid, the relative content of the vaporized substance in the gas phase and the equation expressing the Dalton's law. As a result of solving this system of equations, dependencies are obtained that make it possible, at known values of the mass transfer coefficient in the gas phase, to carry out calculations and simulate the hydrodynamics of the liquid film flow under conditions of evaporation into a flow of neutral gas. For the water-to-air system, regularities were established in which the film thickness and speed of movement along the surface height were varied for different types of film interaction with the air flow: forward flow, backflow, and cross-flow, as well as with different hydrodynamic and temperature conditions of its flow down under cross interactions conditions of the flows. It has been shown that in all cases a decrease in the thickness and speed of movement of the film is observed, with the largest decrease occurring during cross-interaction, which is associated with an intense removal of the resulting vapor from the film surface. The developed mathematical model can be used to evaluate the operating modes of film machines with a plane-parallel nozzle.

Keywords: film machine, plane-parallel nozzle, cross-interaction, film thickness, mass transfer coefficient, evaporation rate.

1 Introduction

Film machines, whose operation is based on the gravitational flow of a liquid, are widely used for heat and mass transfer processes in the "liquid – gas (vapor)" system. Many of these processes are accompanied by evaporation of the liquid. Introducing a neutral (inert) gas flow with respect to the liquid into the machineand evaporating the liquid into it allows the temperature of such processes to be reduced. This also makes promising the use of film machine with a neutral gas flow for example for the concentration of aqueous solutions of non-volatile liquids (sulfuric acid, glycerin, etc.). Special interest in this case are film apparatuses with flat-sheet nozzles, which allow you to organize cross-phase movement, which makes it possible to increase the driving force of the process at high density irrigation nozzles. However, the theory of such a process has not been developed sufficiently, which makes it difficult to carry out engineering calculations of these apparatuses. The aim of this work is to develop a mathematical model and establish on its basis the laws of the liquid film flow down over a flat surface in the conditions of evaporation into a flow of neutral gas.

2 Literature Review

Literary data show [1] that when carrying out processes accompanied by evaporation of a liquid (separation of liquid mixtures, concentration of solutions, evaporative cooling, etc.), film machines have several advantages compared with other types of machines. These advantages primarily include: a large contact surface of the phases and high intensity of heat and mass transfer, low hydraulic resistance, small residence time of liquid in the machine, which is important for thermolabile materials.

Depending on the design of the machine, a film may form on the surface of different geometries, for example, a number of papers deal with the liquid film flowing down along the inner surface of vertical pipes, the outer surface of horizontal pipes or on surfaces of other geometry (half cylinder, cone, plate) [2–4]. Promising from the point of view of the organization of heat and mass transfer processes is the liquid film flow down on a flat surface [5, 6]. Such a fluid flow is described by equations of motion and continuity which have the following forms:

$$\rho_l \frac{\partial u}{\partial y} u = \rho_l g + \mu_l \frac{\partial^2 u}{\partial y^2}, \qquad (1)$$

$$\frac{\partial u}{\partial y} + \frac{\partial u}{\partial z} = 0, \qquad (2)$$

where ρ_l – the density of the liquid, kg/m^3; μ_l – the dynamic viscosity of the liquid, H·s/m^2; u –component of the liquid rate in the direction of the film flowing, m/s; g – gravitational acceleration, m/s^2, y – transverse coordinate, z – longitudinal coordinate in the direction of the film flow down.

Liquid evaporation from a film to a neutral gas has features that must be taken into account when developing film machines. The introduction of a neutral gas into the liquid-vapor system leads to the fact that during evaporation, conditions close to the action of vacuum are achieved and accordingly allows the process to be carried out at a lower temperature [7]. The effectiveness of such machines increases with evaporation into a neutral gas flow, which also serves as the carrier of the resulting vapor [8, 9]. At the same time, along with the gas flow rate, the nature of the interaction of the gas flow with the flowing down liquid film also influences the liquid evaporation from the film. It can be forward flow, backflow or cross-flow. This can be quite easily organized using a plane-parallel nozzle [10].

However these questions were not sufficiently developed and therefore the following tasks were set to achieve the objectives of this work:

– developing a mathematical model and, on its basis, an algorithm for calculating hydrodynamics of the liquid film flow down on a flat surface under the evaporation conditions into a neutral gas flow;

– using the developed model to establish the effect of the interaction nature of the neutral gas flow with a liquid film, as well as regime parameters on the change in the thickness and movement rate of the film.

3 Research Methodology

3.1 The mathematical description of the process

A mathematical model of the liquid film downflow under the conditions of evaporation into a flow of neutral gas was developed on the basis of the scheme presented in Figure 1.

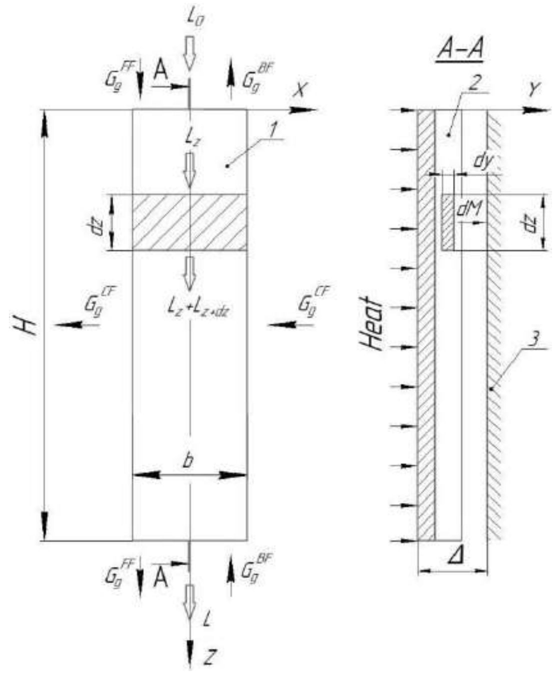

Figure 1 – Calculation scheme for the liquid film flow down: 1 – surface; 2 – film; 3 – bounding wall

According to this scheme the film of liquid 1 moves under the action of gravity along a vertical surface 2, uniformly heated from the outside. With this heating, the heat from the surface is transferred to the liquid, as a result of which the liquid evaporates into the space bounded by the wall 3. A flow of neutral gas enters this space, which traps liquid vapor and carries it outside the surface. Suggesting that the liquid film flow occurs under isothermal conditions, we assume that the temperature of the liquid is constant and equal in the entire volume of the film. Considering the movement of the film at a sufficient distance from the upper edge of the surface, we take it steady and occurring in a laminar mode without wave formation. In this case, the friction between the gas and the liquid, as well as the change in pressure along the height of the surface, is neglected.

Under these conditions, the change in the film thickness of the liquid δ and the speed of the film $\bar{u}$ along the Z axis (surface height) were determined, while the values along the X axis (surface width) were assumed to be unchanged.

The equation of motion of the liquid film (1) can be obtained by considering the selected element in it with the volume $bdydz$ (section A–A in Figure 1). Expressing the frictional forces arising from the movement of liquid on the front and rear faces of an element, through shear stresses, and also using the basic principle of dynamics, the continuity equation in evaporation conditions will differ from equation (2).

The continuity equations were derived by considering the film element with the volume $b\delta dz$ (Figure 1), through the upper face of which passes the mass liquid flow equal to $L_Z = \rho_l b \bar{u} \delta$ and through the lower face – equal to

$$L_{z+dz} = \rho_l b\left(\bar{u} + \frac{\partial \bar{u}}{\partial z}dz\right)\left(\delta + \frac{\partial \delta}{\partial z}dz\right)$$

where u is the velocity of the film (average liquidvelocity in the cross section of the film), m/s; δ – film thickness, m. We believe that changes in the mass flow of a liquid occur due to its evaporation through the surface bdz of the front face of the element. At the same time, the evaporation through the surfaces of its left and right faces is neglected. Then the mass flow of liquid turning into vapor is equal to

$$dL = L_z - L_{z+dz} \tag{3}$$

This flow can be expressed as

$$dL = wbdz \tag{4}$$

where w is the evaporation rate (specific vapor flow), kg/(m^2·s).

Substituting the dependence (4) into (3) and expressing the mass flows through their components, we obtain the continuity equation in the following form

$$\rho_l d(\delta \bar{u}) = wdz \tag{5}$$

Equations (1) and (5) are complemented by the following dependencies:

1) the mass transfer equation from the film surface:

$$dM = \beta(P_{sv} - P_v)Fd\tau \tag{6}$$

where M – the mass of the resulting steam, kg; β – mass transfer coefficient to the gas phase, kg/(m^2·s·Pa); P_{sv} – the saturated vapor pressure of the evaporated liquid, Pa; P_v – partial vapor pressure in the gas phase, Pa; F – evaporation surface, m^2; τ – time, s;

2) material balance equation for gas phase of evaporated liquid:

$$dM = G_g\left(d_g - d_{g0}\right)d\tau \tag{7}$$

where G_g is the neutral gas flow (indices in Figure 1: FF – forward flow; BF – backflow; CF – cross flow), kg/s; d_g, d_{g0} – the current and initial relative contents of the moisture content of the evaporated substance in a neutral gas, kg/kg;

3) the equation of the relative content of the evaporated substance in the gas phase, which is written on the basis of the Clapeyron equations of state for vapor and neutral gas:

$$P_v m_v = d_g P_g m_g \tag{8}$$

where m_v, m_g are the molar masses of evaporated substance and neutral gas, kg/kmol; P_g – the partial pressure of a neutral gas in the gas phase, Pa;

4) an equation expressing Dalton's law:

$$P = P_v + P_g \tag{9}$$

The presented system of equations (1), (5)–(9) describes the hydrodynamics of the flow down of a liquid film over a flat surface under the conditions of evaporation of a liquid into a neutral gas flow.

3.2 Equations solution and calculation algorithm

To solve the equations of motion we use the following approach. If it is assumed that the evaporation of a liquid from the free surface of the film does not affect the distribution profile of the local liquid velocity along the Y axis (in cross sections of the film), then under boundary conditions $y = 0$, $u = 0$ and $y = \delta$, $\partial u/\partial y = 0$ (there is no friction force on the free surface of the film) it can be used the classical solution of the equation of motion:

$$u = \frac{\rho_l g \delta^2}{2\mu_l}\left(1 - \frac{y^2}{\delta^2}\right)$$

Accordingly by averaging the velocity of the liquid over its volume passing per unit time through the cross section of the film we obtain the dependence for determining the velocity of the film

$$\bar{u} = \frac{\rho_l g \delta^2}{3\mu_l} \tag{10}$$

The quantity $\delta\bar{u}$ in equation (5) is a linear (referred to the wetted surface width) watering volume, m2/s. Turning to the linear watering mass $\Gamma = \rho_l(\delta\bar{u})$, we integrate equation (5) in the range from $z = 0$ to the current z and from $\Gamma = \Gamma_0$ to the current value of Γ. As a result, considering the dependence (10), we have

$$\delta = \sqrt[3]{\frac{3\mu_l}{\rho_l^2 g}\left(\Gamma_0 - wz\right)}, \tag{11}$$

where $\Gamma_0 = L_0/b$ is the initial linear watering mass, kg/(m·s); L_0 is the initial mass flow of the liquid, kg/s.

Expressing the evaporation rate as

$$w = \frac{1}{F}\frac{dM}{d\tau},$$

from equation (6) we have

$$w = \beta(P_{vs} - P_v). \tag{12}$$

From equations (8) and (9) we get

$$P_v = \frac{d_g m_g P}{m_v + d_g m_g}. \tag{13}$$

Equating the left sides of equations (6) and (7), after the appropriate transformations with regard to dependence (13), we obtain the quadratic equation

$$d_g^2 + pd_g - q = 0. \tag{14}$$

In this equation, the coefficient p and the free term q depending on the nature of the interaction of the phases and the corresponding expression of the evaporation surface are determined by the following formulas:

1) forward flow:

$$p = \frac{m_v}{m_g} - d_{g0} + \frac{\beta \cdot b \cdot z}{G_Г}(P - P_{sv}).$$

$$q = \frac{m_v}{m_g}\left(d_{g0} + \frac{\beta \cdot b \cdot z}{G_g}P_{vs}\right)$$

2) backflow:

$$p = \frac{m_v}{m_g} - d_{g0} + \frac{\beta \cdot b \cdot (H - z)}{G_g}(P - P_{sv})$$

$$q = \frac{m_v}{m_g}\left(d_{g0} + \frac{\beta \cdot b \cdot (H - z)}{G_g}P_{sv}\right)$$

3) cross-flow:

$$p = \frac{m_v}{m_g} - d_{g0} + \frac{\beta \cdot b \cdot H}{G_g}(P - P_{sv})$$

$$q = \frac{m_v}{m_g}\left(d_{g0} + \frac{\beta \cdot b \cdot H}{G_g}P_{sv}\right)$$

The positive real root of equation (14) is the value of the relative content of the vaporized substance in the gas phase (moisture content for water).

Obtained as a result of solving the system of equations of the above mathematical description of dependencies (10)–(14) allow for known values of the mass transfer coefficient β to carry out calculations and modeling of hydrodynamics of a liquid film flowing down a flat surface under conditions of evaporation into a neutral gas flow. The initial data for the calculation are the following values: v − velocity of neutral gas, m/s; L_0 − the initial mass flow of the liquid , kg/s; b − surface width, m; H − surface height, m; Δ − the distance from the surface to the bounding wall, m; t_l − liquid temperature, − the initial temperature of the neutral gas, °C; t_a − the ambient temperature, °C; φ_a − the relative content of the evaporated substance in the environment, %; B − atmospheric pressure, Pa.

The calculation is carried out in accordance with the following algorithm.

1) take the temperature of the gas phase is equal to

$$t_g = \frac{t_l + t_{g0}}{2}$$

2) using reference data, the t_g value is used to determine the kinematic viscosity of the neutral gas v_g and the vapor diffusion coefficient to-neutral gas necessary to calculate the mass transfer coefficient β, and also P_{vs}. By value t_l we determine the values ρ_l and μ_l, by value t_l we determine the values ρ_l and μ_l, by value of t_a is determined by the value of the partial vapor pressure in the environment P_a. Next, using the known formulas, we calculate the values of the content of the evaporated substance in the environment d_a and the specific volume of the environment containing this substance γ_a;

3) calculating the volume flow rate of neutral gas for forward flow and backflow:

$$V = vb\Delta$$

for the cross-flow

$$V = vH\Delta$$

and its mass flow

$$G_g = \frac{V}{\gamma_a}$$

4) setting the values of the longitudinal coordinate from $z = 0$ to $z = H$, for each value we calculate:

– the relative content of the vaporized substance in the gas phase d_g according to equation (14), having previously determined the coefficient p and the free term q for a specific type of the phases interaction;

– partial vapor pressure of this substance in the gas phase P_v according to equation (13);

– evaporation rate w according to equation (12);

– film thickness δ according to equation (11);

– film speed $\bar{u}$ according to equation (10).

According to the results of the calculation, we establish the change in the thickness and speed of movement of the film along the height of the surface.

4 Results

The study of the regularities of the liquid film flow down on a flat surface under the conditions of evaporation into a flow of neutral gas was carried out using the calculation algorithm described above. In this case, water was taken as a liquid, and air was taken as a neutral gas. The necessary data for calculating the mass transfer coefficient β was determined by the well-known empirical formula of Gilliland and Sherwood [11]. The results were presented in the form of dependences of the change in film thickness and speed on the surface height with different types of film interaction with air flow: forward flow, backflow and cross flow, as well as various hydrodynamic and temperature regimes of its flowing down under cross-interaction conditions.

The analysis of these dependences shows that the film thickness and the rate of its flow down in all cases decrease along the surface height as a result of the water evaporation. From a comparison of these dependences with a different character of film interaction with the air flow (Figure 2), it follows that the decrease in film thickness and speed during cross-interaction is comparable with the backflow and even slightly exceeds it.

Such a feature of cross-flow interaction is associated with the rapid removal of vapor from the film surface, which reduces its partial pressure in the air flow throughout the film's movement path and, accordingly, increases the driving force of the evaporation process.

The influence of hydrodynamic regimes on the film flow patterns (Figure 3) is characterized by a more intense decrease in the film thickness and speed with increasing air rate, which is associated with an increase in the mass transfer coefficient and, accordingly, evaporation rate. With an increase in the mass flow of water entering the film, a decrease in the thickness and speed of movement of the film, on the contrary, is less intense.

The study of the effect of temperature regimes on the regularities of the film flow down was carried out in the absence of water boiling in the film (t_l < 100 °C).

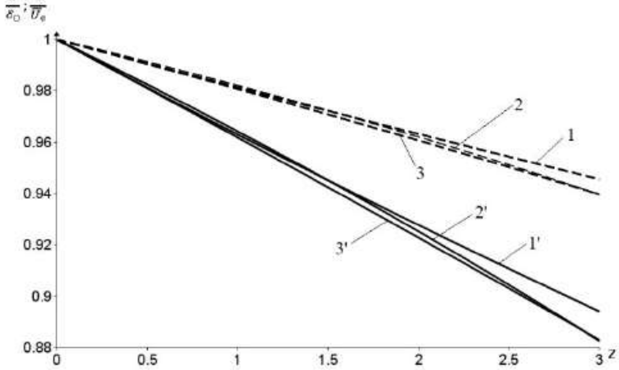

Figure 2 − Effect of the nature of the interaction of the water film with the air flow on thickness changes (dotted lines) and the speed of movement (solid lines) of the film (t_l = 80 C; t_{l0} = 20 °C; v = 10 m/s; L_0 = 0.005 kg/s): 1, $1^/$ – forward flow; 2, $2^/$ – backflow; 3, $3^/$ – cross-flow

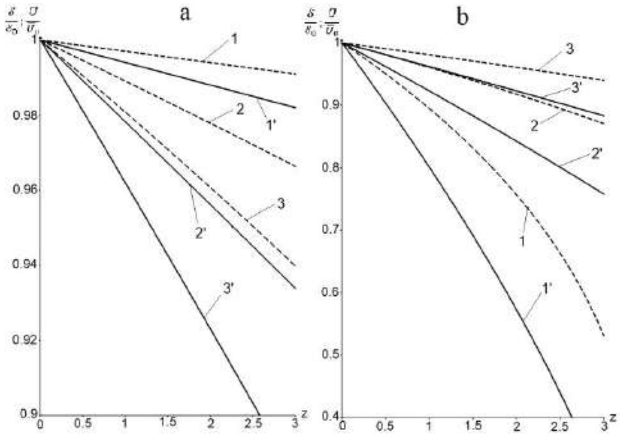

Figure 3 − Influence of hydrodynamic regimes of the flow down process of a water film on the change in its thickness (dotted lines) and speed of movement (solid lines) during cross flow interaction: a − flow rates (t_l = 80 °C; L_0 = 0.005 kg/s; t_{g0} = 20 °C): 1, $1^/$ − v = 1.0 m/s; 2, $2^/$ − v = 5.0 m/s; 3, $3^/$ − v = 10 m/s; b − the initial mass flow of water (t_l = 80 °C; v = 10.0 m/s; t_{l0} = 20 °C): 1, $1^/$ – L_0 = 0.001 kg/s; 2, $2^/$ – L_0 = 0.0025 kg/s; 3, $3^/$ – L_0 = 0.005 kg/s

Calculations show that in this case, an increase in both the water temperature in the film and the temperature of air supplied to the evaporation surface leads to a more intensive decrease in the thickness and movement speed of the film (Figure 4).

It was established that with significant initial air temperatures (t_{g0} > 100 °C) complete water evaporation can be achieved (Figure 4 b). This is due to the increase in the saturated vapor pressure and accordingly the evaporation rate in accordance with equation (11).

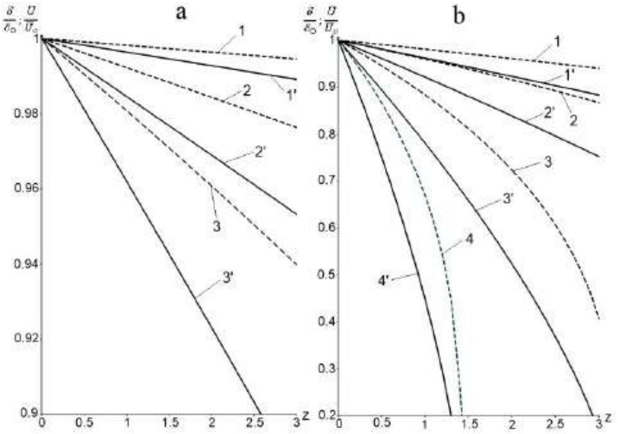

Figure 4 - Influence of temperature regimes of the flow down process of a water film on the change of its thickness (dotted lines) and movement speed (solid lines) during cross flow interaction: a − liquid temperature (v = 10 m/s; L_0 = 0.005 kg/s; t_{g0} = 20 °C): 1, $1^/$ − t_l = 20 °C; 2, $2^/$ − t_l = 50 °C; 3, $3^/$ − t_l = 80 °C; b − gas temperature (t_l = 80 °C; v = 10 m/s; L_0 = 0.005 kg/s): 1, $1^/$ – t_g = 20 °C; 2, $2^/$ – t_g = 50 °C; 3, $3^/$ – t_g = 100 °C; 4, $4^/$ – t_g = 150 °C

5 Conclusions

On the basis of the developed mathematical model, hydrodynamic regularities of a liquid film flowing down along a flat surface are established considering evaporation into a neutral gas flow. These regularities include the influence of the nature of the neutral gas flows interaction with a liquid film, as well as regime parameters on the change in film thickness and speed. It is shown that the film thickness and motion speed of the film decreases most intensively with cross-flow interaction. The intensity of the decrease in the thickness and speed of movement of the film along the surface height increases with an increase in the velocity of the neutral gas, and with an increase in the flow velocity of the liquid decreases. With a significant temperature of neutral gas (t_{g0} > 100 °C) at a certain height of the surface, complete evaporation of the liquid is achieved.

The model can be used to evaluate the operating modes of film machines with a plane-parallel nozzle.

References

1. Olevsky, V. M., Ruchinsky, V. R., et al. (1988). *Film heat and mass exchange equipment*. Moscow, Chemistry [in Russian].
2. Fujita, I., & Hihara, E. (2005). Heat and mass transfer coefficients of falling-film absorption process. *International Journal of Heat and Mass Transfer*, Vol. 48(3), pp. 2779–2786, doi: 10.1016/j.ijheatmasstransfer.2004.11.028.
3. Narvaez-Romo, B., & Simoes-Moreira, J. R. (2017). Falling liquid film evaporation in subcooled and saturated water over horizontal heated tubes. *Heat Transfer Engineering*, Vol. 38(3), pp. 361–376, doi: 10.1080/01457632.2016.1189275.
4. Danilov, Yu. V., & Gavrilichenko, I. G. (2013). Evaporation during the gravitational motion of the film of a solution. Bulletin of NTU "KhPI", No. 55(1028), pp. 148–153 [in Russian].
5. Kuznetsov, V. V., Vitovskiy, O. V., & Krasovsky, V. A. (2007). Experimental study of flow regimes during the evaporation of a liquid on a vertical heating surface. *Thermal Physics of High Temperatures*, Vol. 45(1), pp. 77–84 [in Russian].
6. El Haj Assad, M., & Lampinen, M. J. (2002). Mathematical modeling of falling liquid film evaporation process. *International Journal of Refrigeration*, Vol. 7, pp. 985–991, doi: 10.1016/S0140-7007(01)00064-0.
7. Serafimov, L. A., & Frolkova, A. V. (2008). Observance of the first law of Konovalov in the process of rectification with inert gas. *Review of MITHT*, Vol. 3(2), pp. 45–52 [in Russian].
8. Tsay, Y. L., & Lin, T. F. (1995). Evaporation of a heated falling liquid film into a laminar gas stream. *Experimental Thermal and Fluid Science*, Vol. 11(1), pp. 61–71, doi: 10.1016/0894-1777(94)00112-L.
9. Mohamed, A. B., Orfi, J., Debissi, C., & Ben Nasrallah, S. (2005). The evaporation of a liquid film into a humid air stream under mixed convection condition along a vertical channel and the inversion temperature. *International Journal of Heat and Technology*, Vol. 23(2), pp. 101–108.
10. Gorodilov, A.A. (2016). *Intensification of the process of heat and mass transfer in contact apparatus with a regular nozzle*. Ph.D. Thesis, MSTU MAMI [in Russian].
11. Ramm, V. M. (1966). *Gas absorption*. Moscow, Chemistry [in Russian].

Гідродинаміка стікання плівки рідини по плоскій поверхні в умовах випаровування у потік нейтрального газу

Лукашов В. К., Костюченко Є.В., Тимофіїв С. В.

Шосткінський інститут Сумського державного університету, вул. Гагаріна, 1, 41100, м. Шостка, Україна

Анотація. Робота присвячена дослідженню гравітаційного руху плівки рідини в умовах випаровування у потік нейтрального газу для застосування у плівкових апаратах із плоскопаралельною насадкою. Метою роботи є розробка математичної моделі такого процесу і встановлення його закономірностей. За основу моделі обрано фізичні закономірності стікання плівки рідини уздовж нагрітої ззовні плоскої поверхні за припущень, що стікання плівки відбувається в ізотермічних умовах при сталому ламінарному режимі без хвилеутворення та за відсутності тертя між газом і плівкою. Математична модель процесу стікання плівки в цих умовах містить рівняння руху і нерозривності плівки рідини, доповнені рівняннями масовіддачі, матеріального балансу газової фази за випаровуваною рідиною, відносного вмісту випаровуваної речовини у газовій фазі та рівнянням закону Дальтона. У результаті розв'язання системи рівнянь отримано залежності, що дозволяють (за відомих значень коефіцієнта масовіддачі у газову фазу) здійснювати розрахунки і моделювати гідродинаміку стікання плівки рідини за умов випаровування у потік нейтрального газу. Для системи «вода – повітря» були встановлені закономірності зміни товщини і швидкості руху плівки по висоті поверхні за різного характеру взаємодії плівки з потоком повітря (прямоточного, протитечійного і перехресного), а також за різних гідродинамічних і температурних режимів її стікання в умовах перехресної взаємодії потоків. Показано, що для всіх випадків спостерігається зменшення товщини та швидкості руху плівки, причому найбільше зменшення відбувається при перехресній взаємодії, що пов'язано з інтенсивним відводом утворюваної пари від поверхні плівки. Розроблена математична модель може бути використання для оцінювання режимів роботи плівкових апаратів із плоскопаралельною насадкою.

Ключові слова: плівковий апарат, плоскопаралельна насадка, перехресна взаємодія, товщина плівки, коефіцієнт масовіддачі, швидкість випаровування.

JOURNAL OF ENGINEERING SCIENCES
ЖУРНАЛ ІНЖЕНЕРНИХ НАУК
ЖУРНАЛ ИНЖЕНЕРНЫХ НАУК
Web site: http://jes.sumdu.edu.ua
DOI: 10.21272/jes.2019.6(1).g1
Volume 6, Issue 1 (2019)

UDC 621.436

Compression Ignition Engine Performance as a Function of the Fuel Properties

Towoju O. A.[1], Jekayinfa S. O.[1, 2]

[1] Adeleke University, P.M.B 250, Ede-Osogbo Rd, Ede, Osun State, Nigeria;
[2] Ladoke Akintola University of Technology, P.M.B 4000, Ogbomoso Rd, Ogbomoso, Nigeria

Article info:

Paper received:	June 7, 2018
The final version of the paper received:	December 20, 2018
Paper accepted online:	December 25, 2018

***Corresponding Author's Address:**
olumidetowo@yahoo.com

Abstract. Compression ignition engines have wide application in the transportation, agricultural, construction and industrial sectors which are critical for the economic sustainability of any nation. These engines are powered with petroleum diesel which is however, been threatened by the reality of crude oil going into extinction in some couple of years if new reserves are not discovered, and also the need to reduce global warming; a consequence of the effect of its combustion products. Biodiesel is a renewable fuel with similar properties to petroleum diesel, and can be used purely or in blends without the need for modifying the existing engines. The thermal efficiency of an engine is a very important performance indicator, and researchers would stop at nothing to ensure its improvement. The kinematic viscosity is one of the fuel's properties which contribute to an engine thermal efficiency. This work is thus designed to review some past studies on the use of biodiesels and its blends in engines and find a correlation between the kinematic viscosity and the thermal efficiency. A correlation was established to exist between the fuel kinematic viscosity and the engine thermal efficiency.

Keywords: biodiesels, kinematic viscosity, calorific value, pure biodiesel properties, thermal efficiency.

1 Introduction

The rapid dwindling rate of the world fossil energy reserves has continued to be unmatched by new discoveries. However, the comfortable existence of the present age mankind has been tailored towards his large dependence on generated energy used in transportation from a location to another (air, land, and marine), powering of construction and agricultural equipment, and for electricity generation utilized in powering of household equipment and industrial machines/ equipment.

To meet this energy requirement, the dwindling fossil energy reserves are being continually called into play, as the bulk of the generated energy consumed by man is produced from it and only a fraction, about 13% of the whole is generated from nuclear, wind, solar and hydraulic sources. The generation of energy from fossil energy resources however also comes with an attendant cost of environmental pollution asides the possibility of it getting into extinction in a couple of years if new reserves are not discovered.

The transportation sector and agricultural and construction equipment generate its energy largely from crude oil, while a small fraction of the world's electricity is also generated from it. The major process of converting the inherent energy of crude oil utilized in these sectors employs basically the use of internal combustion engines. Crude oil forms about 38% of the amount of fossil energy used in generating energy for the use of mankind, and is a major contributor to the much talked about climatic change caused by global warming.

In order to continue to meet the huge demand of energy for transportation, agricultural and construction equipment, and electricity generation placed on internal combustion engines while placing a premium on the maintenance of a cleaner environment, alternative energy sources to crude oil are been sought for, and one of such is the use of renewable and bio-degradable biofuels.

Compression ignition engines are known for their heavy-duty applications, and are the preferred engine of choice for agricultural and construction earth moving equipment, marine and rail transportation devices, and electricity generation. These engines rely on the combustion of Automotive Gas Oil (AGO) generally known as diesel for the generation of its energy. In a quest to reduce the environmental impact and maintain a high thermal efficiency with the use of these engines, biodiesels are now increasingly used as a source of fuel because of its applicability to already existing engines without the need for modifications [1].

Researchers are thus busy carrying out studies on the production and use of biodiesels in compression ignition engines, its desired properties and the impact of its combustion products on the environment.

The impact of some of the properties of fuels, biodiesels inclusive such as calorific value on thermal efficiency [2–4] flash point on storage of fuels [5], cetane number on the fuel auto-ignition [6], and viscosity on flow rate and thermal efficiency [7–13].

This study is thus designed to review the literature and find a correlation between the kinematic viscosities of biodiesels / biodiesel blends and engine thermal efficiency.

2 Literature Review

2.1 Kinematic viscosity and thermal efficiency

Kinematic viscosity is the ratio of the fluid dynamic viscosity to its density and has a significant impact on fuel delivery and power output. It determines the rate of flow of the fuel, and too high a value can lead to pumping issues and atomization in the injection system [14].

Thermal efficiency is the fraction of the heat input that is converted into useful work by the device, in other words, it is the percentage of fuel energy converted into useful power output [11, 15]. The thermal efficiency of an engine has a direct relationship to its power output and is inversely proportional to the rate of mass of fuel consumption, hence a high value of thermal efficiency is an indication of better fuel economy and by extension reduced spending and lower exhaust of emission products.

In the quest to investigate the effect of the utilization of biodiesels and petroleum biodiesel blends on engine performance several researchers have conducted experiments using biodiesels produced from different sources and different blend fractions. Biodiesels produced from different sources have their own characteristic physicochemical properties which are a function of the production process and have an impact on the performance of the engine.

Independent studies with the use Karanja oil biodiesel and its blend (B20) with determined kinematic viscosities of 5.35 cSt at 40 °C and 3.04 cSt resulted into engine thermal efficiencies of 32.0 % and 30.2 % respectively [16, 17]. With biodiesel/biodiesel blends of Pongamia origin, kinematic viscosity values of 5.17 (B10), 5.43 (B20), and 5.62 cSt (B30) at 40 °C, the engines thermal efficiency were 26.2 %, 26.8 %, and 26.5 % respectively [10], while with values of 4.56 cSt (B100) at 33 °C and 5.46 cSt (B20) as determined from other studies resulted into engine thermal efficiency values of 26.0 % and 28.0 % respectively [18].

Studies on biodiesels with Canola oil and Honge oil as their origin with kinematic viscosity values of 5.38 and 5.60 cSt respectively measured at 40 °C resulted into thermal efficiency values of 31 % and 25 % respectively [2–8].

Jatropha oil is commonly used as a source of biodiesel in many parts of the world because of its ease of propagation [19]. Several studies have been conducted on the performance and emission characteristics of compression ignition engines using biodiesels produced from Jatropha and its blends with petroleum diesel, some of interest to the authors have been selected. Kinematic viscosity values of 4.38 (B100), 5.84 (B100), 5.21 (B10), 5.64 (B20), 5.97 (B30), 6.61 (B100), and 4.84 cSt (B100) measured at 40 °C as determined by some researchers for Jatropha biodiesel and its blends used in fuelling of an engine resulted into thermal efficiency values of 24.0, 24.0, 26.5, 26.3, 27.2, 22.0, and 31.0 % respectively [7, 8, 10, 15, 20].

Biodiesels with Soybean, Manhua and Palm oil as sources have also been worked upon by researchers. With Soybean oil as source, the use of its biodiesel with kinematic viscosity values of 3.34 (B20), 3.68 (B40), and 4.25 cSt (B100) measured at 40 °C in compression ignition engine resulted to thermal efficiency values of 31.3, 30.5, and 29.5 % respectively [3].

Manhua oil biodiesel with a kinematic viscosity of 5.58 cSt measured at 40 °C gave a thermal efficiency value of 27 % when used to fuel an engine [21]. Studies on biodiesel derived from Palm oil with kinematic viscosity values of 4.56 (B100), 2.82 (B20), and 3.40 cSt for petroleum diesel-palm oil blend in the ratio 1:4 measured at 40 °C resulted into thermal efficiency values of 25, 28 and 27 % respectively [22], while with kinematic viscosity of 4.70 cSt (B100) measured at 30 °C during another study, the thermal efficiency of the fuelled engine was 27 % [23].

Working with biodiesel produced from used and fresh Corn oil, the kinematic viscosity values measured at room temperature were gotten to be 4.70 and 5.86 cSt gave engine thermal efficiency values of 25.5 and 22.5 % respectively [24]. With Neem oil biodiesel having a kinematic viscosity value of 3.20 cSt, the engine's thermal efficiency was found to be 23.0 % [25], and as reported by Tutak et al., the use of B100 as fuel in their test engine with kinematic viscosity value of 4.51 cSt measured at 40 °C gave thermal efficiency value of 27.0 % [26].

A summary of the literature values of kinematic viscosities and the corresponding engine thermal efficiencies is as shown in Table 1 below.

Plots of thermal efficiency against kinematic viscosity values of biodiesel and some of its blends are as depicted in Figures 1–2.

Figure 1 is a plot of the thermal efficiency values against the kinematic viscosity values of some biodiesels and biodiesel blends. The thermal efficiency values can be seen to be indirectly proportional to the kinematic viscosity values, although this cannot be said to be applicable in some instance given an indication that other fuel properties will have an impact on the engines thermal efficiency.

Biodiesels despite having similar properties to petroleum diesel posses some characteristics such as oxygen content, fatty acid composition, and moisture content which differs from that of petroleum diesel and thus can impact the performance characteristics of an engine fuelled with it [27–29].

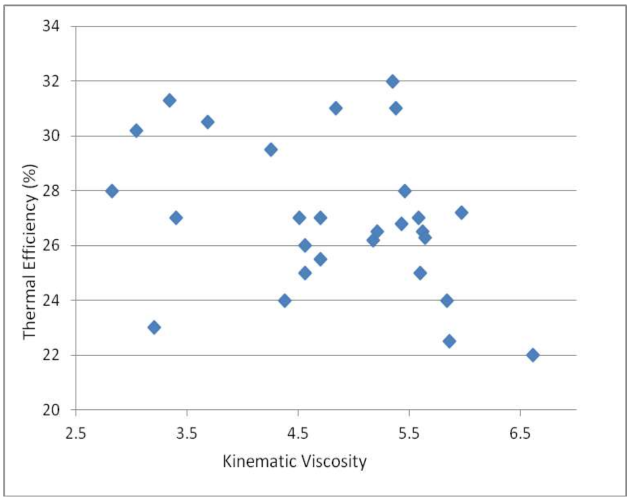

Figure 1 – Thermal efficiency kinematic viscosity plots of biodiesels and its blends

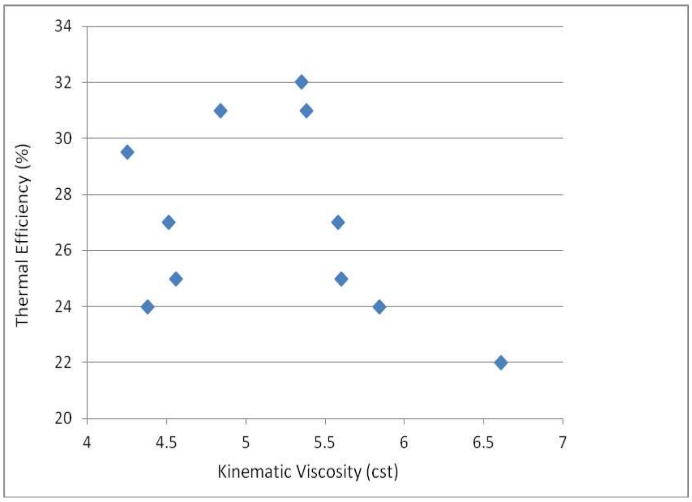

Figure 2 – Thermal efficiency kinematic viscosity values at 40 °C plots of biodiesels

Table 1 – Summary of thermal efficiency values

Kinematic viscosity, cSt	Thermal efficiency, %	Biodiesel source	Reference	Kinematic viscosity, cSt	Thermal efficiency, %	Biodiesel source	Reference
5.35	32.0	Karanja	[16]	6.61	22.0	Jatropha	[17]
3.04	30.2	Karanja	[17]	4.84	31.0	Jatropha	[20]
5.17	26.2	Pongamia	[10]	3.34	31.3	Soybean	[3]
5.43	26.8	Pongamia	[10]	3.68	30.5	Soybean	[3]
5.62	26.5	Pongamia	[10]	4.25	29.5	Soybean	[3]
4.56	26.0	Pongamia	[18]	5.58	27.0	Manhua	[21]
5.46	28.0	Pongamia	[18]	4.56	25.0	Palm oil	[22]
5.38	31.0	Canola	[2]	2.82	28.0	Palm oil	[22]
5.60	25.0	Honge	[8]	3.40	27.0	Palm oil	[22]
4.38	24.0	Jatropha	[7]	4.70	27.0	Palm oil	[23]
5.84	24.0	Jatropha	[8]	4.70	25.5	Corn oil	[24]
5.21	26.5	Jatropha	[10]	5.86	22.5	Corn oil	[24]
5.64	26.3	Jatropha	[10]	3.20	23.0	Neem	[25]
5.97	27.2	Jatropha	[10]	4.51	27.0	Neem	[26]

To mitigate the impact of some of the differences which exist between biodiesels and biodiesel-petroleum diesel blends on its performance when used as a fuel in engines, the impact of kinematic viscosity on an engine thermal efficiency is viewed from the aspect of only pure biodiesels, also the obtained kinematic viscosity values utilized in arriving at the plot in Figure 1 were not all determined at a uniform temperature, and as it has been stated in different literature that fluid viscosity is dependent on temperature [30–32], the plot of thermal efficiency against fuel kinematic viscosity values all measured at 40°C was done and is as shown below in Figure 2.

The thermal efficiency values are seen to be a function of the fuels kinematic viscosity values except for some of the few cases where despite the relatively low values of the fuels kinematic viscosity, the thermal efficiency value was lower (4.38 cSt – 24.0 %, 4.56 cSt – 25.0 %, and 4.51 cSt – 27.0 %).

As stated earlier, literature has established that the thermal efficiency of an engine is a function of its calorific value [2–32], and as shown in Figure 2, the thermal efficiency is also a function of the fuels kinematic viscosity, except for the stated observed exceptions, it is hence imperative to examine if the reasons for the exception can be attributed to the calorific value property of the fuel. This table shows biodiesels with kinematic viscosity values of lesser than 5 cSt and the corresponding calorific and thermal efficiency values is presented in Table 2.

Table 2 – Pure biodiesel properties

Kinematic viscosity, cSt	Calorific value, kJ/kg	Thermal efficiency, %
4.25	36.2	29.5
4.51	37.1	27.0
4.56	40.6	25.0
4.84	37.2	31.0

The Biodiesel with a kinematic viscosity value of 4.56 cSt despite having a higher value of calorific value than the others listed in Table 2 gave a lower value of thermal efficiency, given an indication that the observed few exceptional cases in the thermal efficiency against kinematic viscosity value plot in Figure 2 could have been due to other factors not directly related to the properties of the fuels.

3 Conclusions

Compression ignition engines have wide application in the transportation, agricultural, construction and industrial sectors which are critical for the economic sustainability of any nation. These engines are powered with petroleum diesel which is however, been threatened by the reality of crude oil going into extinction in some couple of years if new reserves are not discovered, and also the need to reduce global warming; a consequence of the effect of its combustion products.

In this paper, research works of literature on the study of biodiesel and biodiesel-petroleum diesel blends have been reviewed, and a correlation has been shown to exist between the fuels kinematic viscosity value and the thermal efficiency of an engine operated on it.

4 Acknowledgements

The support of our colleagues at the Department of Mechanical Engineering, Adeleke University is appreciated for their understanding during the period of carrying out this research work.

References

1. Tat, M. E., & van Gerpen, J. H. (1999). The Kinematics Viscosity of Biodiesel and its Blends with Diesel Fuel. *JAOCS*, Vol. 76 (12), pp. 1511–1513.
2. Anbarasu, A., & Karthikeyan, A. (2014). Performance and Emission Characteristics of Direct Injection Diesel Engine Running On Canola Oil / Diesel Fuel Blend. *American Journal of Engineering Research*, Vol. 3(8), pp. 202–207.
3. Al-Dawody, M. F., & Bhatti, S. (2014). Effect of Variable Compression Ratio on the Combustion, Performance and Emission Parameters of a Diesel Engine Fuelled with Diesel and Soybean Biodiesel Blending. *World Applied Sciences Journal*, pp. 1852–1858.
4. Xue J., Grift, T. E., & Hansena, A. C. (2011). Effects of Biodiesel on Engine Performance and Emissions. *Reneable and Sustainable EnergyReviews*, Vol. 15, pp. 1098–1116.
5. Altin, R., Cetinkaya, S., & Yucesu, H. S. (2001). Potential of using Vegetable Oil Fuels as Fuel for Diesel Engines. *Energy Coversion Manage*, Vol. 42, pp. 529–538.
6. Li, R., Wang, Z., Ni, P., Zhao, Y., Li, M., & Li, L. (2014). Effects of Cetane Number Improvers on the Performance of Diesel Engine Fuelled with Methanol / Biodiesel Blend. *Fuel*, Vol. 128, pp. 180–187.
7. Dwivedi, G., Jain, S. & Sharma, M. P. (2011). Impact of Biodiesel and Its Blends with Diesel and Methanol on Engine Performance" *International Journal of Energy Science*, Vol. 1(2), pp. 105–109.
8. Basavarajappa, Y., Banapurmath, N., & Sangameshwar, A. (2014). Performance, Combustion and Emission Characteristics of a Dual Fuel Engine Operated with Compressed Natural Gas (CNG) and Honge and Jatropha Biodiesels. *Universal Journal of Petroleum Sciences*, Vol. 2, pp. 46–73.
9. Mamilla, V. R., Mallikarjun, M., & Rao, G. N. (2013). Effect of Combustion Chamber Design on a DI Diesel Engine Fuelled with Jatropha Methyl Esters Blends with Diesel. *International Conference On Design and Manufacturing, IConDM 2013, Elsevier Ltd.*, pp. 479–490.
10. Anandan, M., Sampath, S., & Sudharsan, N. M. (2014). Study of Combustion and Performance Characteristics on a Single Cylinder DI Diesel Engine with Jatropha and Pongamia Methyl Ester Blends. *Global Journal of Researches in Engineering: A Mechanical and Mechanics Engineering*, Vol. 14(7), pp. 26–40.
11. Naveen, K., Parameshwaran, T. P., & Azhagiri, P. (2014). Experimental Investigation of Variable Compression Ratio Diesel Engine using Ziziphus Jujuba Oil. *2014 International Conference on Innovations in Engineering and Technology, ICIET'14, International Journal of Innovative Research in Science, Engineering and Technology*, pp. 1134–1139.
12. Selvam, D., Panner, J., & Vadivel, K. (2012). Performance and Emission Analysis of DI Diesel Engine Fuelled with Methyl Esters of Beef Tallow and Diesel Blends. *Proceedia Engineering*, Vol. 38, pp. 342–358.
13. Nandi, S. (2013). Performance of C.I. Engine by Using Biodiesel-Mahua Oil. *American Journal of Engineering Research*, Vol. 2(10), pp. 22–47.
14. Nazal, I. T., & Al-Kayiem, H. H. (2012). Experimental Characterization of Diesel Engine Performance Fuelled By Various Sunflower Oil-Diesel Mixtures. *Journal of Applied Sciences*, Vol. 12(24), pp. 2604–2609.
15. Gaurav, P., Ambarish, D., & Bijan, K. M. (2014). An Experimental and Numerical Investigation of the Performance, Combustion and Emission Characteristics of a Diesel Engine Fueled with Jatropha. *Energy Procedia*, Vol. 54, pp. 455–467.
16. Bhabani, P. P., Chandrakanta, N., & Basanta, K. N. (2013). Investigation on utilization of biogas and Karanja oil biodiesel in dual fuel mode in a single cylinder DI diesel engine. *International Journal of Energy and Environment*, Vol. 4(2), pp. 279–290.

17. Sivaramakrishnan, K. (2017). Investigation on Performance and Emission Characteristics of a Variable Compression Multi Fuel Engine Fuelled with Karanja Biodiesel – Diesel Blend. *Egypt. J. Petrol*, pp. 1–10.
18. Haribabu, N., Rao, B. V. A., Adinarayana, S., Sekhar, Y. M. C., & Rambabu, K. (2010). Performance and Emission Studies on Di-Diesel Engine Fuelled with Pongamia Methyl Ester Injection and Methanol Carburetion. *Journal of Engineering Science and Technology*, Vol. 5(1), pp. 30–40.
19. Jaichander, S., & Annamalai, K. (2012). Performance and Exhaust Emission Analysis on Pongamia Biodiesel with Different Open Combustion Chambers in a DI Diesel Engine. *Journal of Scientific and Industrial Research*, Vol. 71, pp. 487–491.
20. Nasim, M. N., Yarasu, R. B., & Sarda, R. H. (2013). Experimental Investigation on Compression Ignition Engine Powered by Preheated Neat Jatropha Oil. *Journal of Petroleum Technology and Alternative Fuels*, Vol. 4(7), pp. 119–124.
21. Savariraj, S., Ganapathy, T., & Saravanan, C. (2011). Experimental Investigation of Performance and Emission Characteristics of Mahua Biodiesel in Diesel Engine. *Renewable Energy*, pp. 1–6.
22. Gad, M. S., El-Araby, R., Abed, K. A., El-Ibiari, N. N., El Morsi, A. K. & El-Diwani, G. I. (2017). Performance and Emission Characteristics of C.I. Engine Fuelled with Palm Oil/Palm Oil Methyl Ester Blended with Diesel Fuel. *Egypt. J. Petrol*, pp. 1–5.
23. Patil, S. (2013). Thermodynamic Modelling for Performance Analysis of Compression Ignition Engine Fuelled with Biodiesel and its Blends with Diesel. *International Journal of Recent Technology and Engineering*, Vol. 1(6), pp. 134–138.
24. Jehad, Y., Nina, S., & Hamdan, M. (2009). Performance of CI Engines using Biodiesel as Fuel. *GCREEDER International Conference*, pp. 1–13.
25. Dharmadhikari, H. M., Kumar, P. R., & Rao, S. S. (2012). Performance and Emission of C.I. Engine using Blends of Biodiesel and Diesel at Different Injection Pressures. *International Journal of Applied Research in Mechanical Engineering*, Vol. 2(2), pp. 1–6.
26. Tutak, W., Jamrozik, A., & Pyrc, M. (2016). Experimental Investigation on Combustion, Performance and Emission Characteristics of Compression Ignition Engine Powered by B100/Ethanol Blend. *Energy and Fuels*, pp. 1–10.
27. Nair, J. N., Kaviti, A. K. & Daram, A. K. (2017). Analysis of Performance and Emission on Compression Ignition Engine Fuelled with Blends of Neem Biodiesel." *Egyptian Journal of Petroleum*, Vol. 26(4), pp. 927–931.
28. Ramos, J. N., Fernandez, C. M., Casas, A., Rodriguez, L., & Perez, A. (2009). Influence of Fatty Acid Composition of Raw Materials on Biodiesel Properties. *Bioresources Technology*, Vol. 100(1), pp. 261–268.
29. Yasin, M. H. M., Mamat, R., Ali, O. M., Yusop, A. F., Hamidi, M. A., Ismail, M. Y., & Rasul, M. (2016). Study of Diesel-Biodiesel Fuel Properties and Wavelet Analysis on Cyclic Variations in A Diesel Engine. *Energy Procedia*, Vol. 110, pp. 498–503.
30. Ra, Y., Reitz, R. D., Mcfarlane, J., & Daw, S. C. (2008). Effects of Fuel Physical Properties on Diesel Engine Combustion Using Diesel and Bio-Diesel Fuels. *SAE International*, pp. 1–16.
31. Dwivedi, S. D., Akshay, A., Shrivastav, S., & Padwa, G. (2015). Study of dependency of Temperature on Kinematic Viscosity for Blended Oils." *International Journal of Engineering Research and Technology*, Vol. 4(10), pp. 486–492.
32. Boda, M. A., Bhasagi, P. N., Sawade, A. S., & Andodgi, R. A. (2015). Analysis of Kinematic Viscosity for Liquids by Varying Temperature. *Internal Journal of Innovative Research in Science, Engineering and Technology*, Vol. 4(4), pp. 1951–1954.

Продуктивність двигунів із запалюванням стисненням від властивостей біопалива

Товоджу О. А.[1], Жекаїнфа С.О.[1, 2]

[1] Університет Аделеке, Еде-Осогбо роуд, м. Еде, штат Осун, Нігерія;
[2] Технологічний університет А. Акінтола, Огбомосо роуд, м. Огбомосо, Нігерія

Анотація. Двигуни із запалюванням стисненням мають широке застосування у транспортній, сільськогосподарській, будівельній і промисловій галузях, що є надважливими для економічної стійкості будь-якої країни. Ці двигуни працюють на нафтовому дизельному паливі. При цьому видобуток сирої нафти через кілька років перебуватиме під загрозою, якщо не будуть виявлені нові запаси. Також при цьому необхідно враховувати загрози глобального потепління як наслідок суттєвого збільшення викидів продуктів згорання. Біодизель є поновлюваним паливом зі схожими властивостями з нафтовим дизелем. Він може використовуватися самостійно або в сумішах. Тепловий коефіцієнт корисної дії двигуна є надважливим показником ефективності, а науковці робліть усе необхідне для забезпечення зростання цього показника. Кінематична в'язкість є однією із властивостей палива, що сприяє тепловій ефективності двигуна. Таким чином, ця робота спрямована на огляд попередніх досліджень у розробленні біодизеля та його сумішей для двигунів. У результаті знайдено зв'язок між кінематичною в'язкістю і тепловою ефективністю. Також встановлено кореляцію між кінематичною в'язкістю палива і тепловою ефективністю двигуна.

Ключові слова: біодизель, кінематична в'язкість, калорійність, властивості біодизеля, теплова ефективність.

DSMIE 2019

2nd International Conference on
Design, Simulation, Manufacturing:
The Innovation Exchange
June 11-14, 2019 | Lutsk, Ukraine

http://dsmie.sumdu.edu.ua

DSMIE-2019

English language

Keynote Speakers

Keynote & Technical Sessions

Industrial companies

Industry Tour

Universities

Become a Sponsor

Become a Sponsor of DSMIE-2019 and expose your organization, company, product or service to hundreds of people interested in Engineering.

About

DSMIE-2019 focuses on a broad range of research challenges in the fields of **Manufacturing Engineering**, **Mechanical Engineering** and **Chemical Engineering**, addressing current and future trends in design approaches, simulation techniques, computer-aided systems, software development, ICT tools and Industry 4.0 strategy implementation for engineering tasks solving.

DSMIE-2019

Organizer & Partners

Sumy State University

ЛНТУ

TECHNICKÁ UNIVERZITA V KOŠICIACH

Kielce University of Technology

UNIVERSITY OF WEST BOHEMIA

InnovativeFET

Промышленность в Фокусе

UNICHECK

Contacts

Sumy State University, 2 Rymskogo-Korsakova St., Sumy, 40007, Ukraine
E-mail: dsmie@teset.sumdu.edu.ua
Tel.: +38-066-488-03-19

Together we can do more for science, technology, engineering and education
© DSMIE Team

JOURNAL OF ENGINEERING SCIENCES
ЖУРНАЛ ІНЖЕНЕРНИХ НАУК
ЖУРНАЛ ИНЖЕНЕРНЫХ НАУК
Web site: http://jes.sumdu.edu.ua
DOI: 10.21272/jes.2019.6(1).h1 Volume 6, Issue 1 (2019)

UDC 504.054:631.46

Remediation of Soil Contaminated with Heavy Metals

Plyatsuk L. D.[1], Chernysh Y. Y.[1*], Ablieieva I. Y.[1], Yakhnenko O. M.[1],
Bataltsev E. V.[1], Balintova M.[2], Hurets L. L.[1]

[1] Sumy State University, 2 Rymskogo-Korsakova St., 40007 Sumy, Ukraine;
[2] Technical University of Kosice, 1 Letna St., 04001 Kosice, Slovakia

Article info:

Paper received:	October 13, 2018
The final version of the paper received:	February 9, 2019
Paper accepted online:	February 14, 2019

[*]Corresponding Author's Address:
e.chernish@ssu.edu.ua

Abstract. The paper is focused on the research of the applied aspects of soil remediation, in particular the process of heavy metals (HM) binding and intensifying the cultivation of a soil microbiome using various organic-mineral compositions: biogenic composite, which is the product of anaerobic transformation of sewage sludge and phosphogypsum; organic-mineral compost, based on a mixture of phosphogypsum, superphosphate and cattle humus; and a combination of a mixture of sodium humate and superphosphate. The integration of theoretical and experimental principles in the synergy analysis of the interrelations in the system "object – subject of research" in the study of the dynamics of changes in the forms of HM finding in the soil was carried out. The percentage content of the mobile forms of HM released by the extractant from their gross content before and after the treatment of the soil with organic-mineral compositions was determined with the spectrophotometric method using. The comparison of the soil processing efficiency was determined. Correlation relations of the dynamics in the biomass oxidative ability values for the soil biome and the rate of the substrate oxidation was proved over time treatment with different doses of the biocomposite with using of mathematical statistics methods.

Keywords: heavy metals, soil remediation, organic-mineral compositions, phosphogypsum, soil biome, oxidative ability of the biomass.

1 Introduction

The growing anthropogenic impact on the ecosystem causes changes in the natural soil-forming process. The dangerous factors of anthropogenic origin are the processes of intensification of heavy metals (HM) migration in the edaphotop, which cause devegetation and dehumidification, destructive changes in the agrophysical, physicochemical and biological properties of the soil, until its toxicity. The soil receives HM by various ways: with the gas-dust emissions from industrial enterprises and vehicles, liquid and solid household waste, with sewage from agricultural enterprises, pesticides, with impurities of organic and mineral fertilizers in particular, etc. They are accumulated in the soil to concentrations that are hazardous for living objects.

HM fall from the atmosphere into the soil principally in the form of oxides, which gradually dissolve, passing into hydroxides, carbonates or in the form of exchanged cations [1].

It should be noted that heat power takes the first place by the impact value and gross inflow of HM into the atmosphere due to combustion of organic fuel in boiler units (on thermal power stations, boiler houses and in the industrial furnaces). The combustion of coal and fuel oil, which are still dominated it the fuel structure of most countries, is the main source of HM in the atmosphere. The coal contains almost all known heavy metals. One ton of carbon soot can contain maximum 10 kg of Sr, V, Zn and Ge [2].

It is known that the mobility of HM in the system "soil – plant" is largely determined by the physical and chemical properties of soils, by the content of organic matter and the activity of microorganisms that actively participate in the transformation of substances in soils.

The processes of the migration of HM occur or intensify under the impact of the plants root extract that makes the soil aggregates wet, affects the physical and chemical exchange (absorption) capacity of the soil, and binds cations of two- and polyvalent metals with carboxyl and hydroxyl groups of polysaccharides, amino acids and carboxylic acids into complex compounds, and it also concentrates cations, which cause the gradual toxication of soil ecosystems.

So, the current task for today is the regulating of the buffer properties of soils by improving existing and developing new ways to reduce the mobility of HM in the ecosystem that come from various anthropogenic sources.

2 Literature Review

Rehabilitation of soils contaminated with heavy metals is usually based on the use of such meliorants as lime, gypsum, as well as phosphates and organic matter of different genesis.

The use of lime is more effective on soils with acid reaction, on high-buffer soils. An increasing pH to 7.5 and more causes to the formation of compounds of hexavalent chromium, which are very mobile, toxic and not sorbtive. Besides, lime and phosphorus-containing compounds reduce the arrival of toxic metals into the plant, complicate absorption of metabolites (Cu, Zn, Mn), creating their shortage and reducing crop's productivity [3, 4].

The use of natural sorbents is advantageous because they are affordable, cheap and environmentally friendly. At the same time, not all is clear about their role as an inactivators of HM in the soil [5].

The introduction of organic fertilizers is a method that reduces the mobility of lead in the soil and reduces its entry into plants, but it is unclear how long this immobilization effect will be shown, because organic fertilizers are eventually mineralized, which also affects the mobility of lead in the soil [6].

The importance of liming as a method of soil melioration is well known and well-studied for turf-podzolic soils. However, liming cannot be considered only as a way of eliminating the soil acidity, because acidic soils have a complex of adverse properties. Physical and physical-chemical properties of soils are improved during the liming, the density decreases significantly, the filtration and aeration increases, the mechanical resistance is reduced, the cation exchange capacity increases, the composition of the soil absorption complex changes.

Liming affects the use of nutrients from soil and fertilizers by plants. It influence is significant on soil microflora. Besides, the ability of the roots to absorb a number of HM, in particular lead, decreases as a result of increasing Ca. Liming also contributes to the formation of complexes of organic substances of soil with HM, which reduces the mobility of Hg, Cd, Zn, Cu, Ni, Cr [7–9].

A recent analysis [10] showed that many types of materials such as lime, metal oxides, phosphate compounds, organic matter, calcium carbonate, red mud, bone meal, and fly ash may be used to the media for soil amendments.

The results obtained by [11] suggest phosphate compounds enhance the immobilization of metal(loid)s such as Cd, Pb, and Zn in soils through various processes. Rock phosphate reduced Pb, Cd, and Zn by 99.9–24.0%, DAP reduced Cd and Zn by more than 77 % and 91 % for Cd [12]. The P application is considered an attractive technology for managing metal(loid)-contaminated soils, however the large-scale use of P compounds can contaminate surface and groundwater, future research should aim to develop the remediation method with the minimum impact of P on quality of water sources.

According to [13] strongest reductions occurred after cyclonic ashes (CA) + steel shots (SS) and compost (C) + + cyclonic ashes (CA) + steel shots (SS) treatments (99–97 % for Cd and Zn), while Pb and Cu leaching increased after C and C + CA treatment (3.3–17.0 %, respectively). Noteworthy, if too many OM is added into soil, nutrition can be released at the short time, an outflow of them into the groundwater and subsequently make water polluted. In addition, the incorporation of OM in soil can be time consuming.

Xie Y. et al. [14] analyzed the effectiveness of six amendments (composed with bentonite, phosphate, humic acid, biochar, sepiolite powder, biological matrix, silicon fertilizer on the for remediating cadmium and copper co-contaminated soil and reducing the metal concentration in Rhizoma Chuanxiong. The disadvantage of the method is that the maximum possible efficiency of the extraction of heavy metals such as Cd, Cu, Pd and Zn with the use of compositions with different compositions is revealed, which does not allow to unify the application of the method.

There is a method [15] for the remediation of the soil technogenically contaminated with heavy metals, it includes a one-time treatment of soil with a combination of a mixture of sodium humate with superphosphate, lime or organic matter in accordance with the soil. Sodium humate, superphosphate and lime are used for soil containing Cd, Cr. Sodium humate, superphosphate and manure are used for soil containing Zn.

The disadvantages of this method are the lack of a unified approach to the treatment of soils with a different combination of heavy metals, that limits its use. Besides, the influence of the pH of the soil environment, which affects the mobility of heavy metals and the efficiency of their binding in the low soluble compounds, was not taken into account.

There is a method [16] for purifying chernozem soils contaminated with heavy metals, which includes the use of an inducing agent. Organic-mineral compost is used as such a substance, it is prepared by mixing phosphogypsum, simple superphosphate and cattle's humus. Compost is introduced into the soil once for 4–5 years at a dose of 100–110 tons/hectare with an organic content in it up to 20 % and pH of 6.0–6.5. This contributes to lowering the alkalinity of chernozem soils to pH 7.2–7.8, then it is laid by a cultivator to a depth of 20–25 cm.

The main disadvantage of this method is the lack of technological conditions that ensure the detoxification of organic and mineral waste during their composting. So, harmful impurities may be in sewage sludge and phosphogypsum. It is heavy metals, which are in exchange form during composting and may subsequently be available to plants when such compost is introduced to soil.

A well-known method [17] describes the technical solution "Washing of contaminated soils", aimed at the purification and recovery of soils and sediments contaminated with HM, using a detergent solution with chelating agents.

The chelating agent forms water-soluble complexes with metals and in this way facilitates removal of the metal from soils and sediments into the washing solution. This method involves the separation of the solid phase of the soil and sediment, and the rinsing solution used in the filter press chamber and the rinsing of the solid phase to remove all residual mobilized contaminants at the same time. The recycle of chelating agents and process water in a closed process circuit is provided by applying a pH gradient and using advanced oxidation processes for treatment of process water.

The disadvantages of this method include the complexity of the implementation process, the need for mechanical removal of soil contaminated with heavy metals in order to further treatment it in a known way, the high energy consumption of the treatment process, the use of expensive chelating agents and the generation of secondary waste requiring disposal or destruction.

There is a method [18] for purifying clay soils and sludge, which includes removing radionuclides and heavy metals by treating slimes and soils with a chemical reagent. An aqueous solution of epy di- or triammonium salt of ethylenediaminetetraacetic acid (EDTA) with a concentration of 0.01–0.05 mol/dm^3 is used as a reagent.

But this method can be used on soils containing HM, capable of forming stable complex compounds with EDTA, and with high content of clay components (14–20 %). Similarly, chelate-assisted remediation of HM can also cause off-site movement of HM [19]. During EDTA-assisted solubilization of HM, plants can absorb only a limited fraction of mobilized metal and the remaining amount of HM are generally leached down [20]. Therefore, it is highly necessary that application of chelating agents is limited to their lowest level for ecological and economic benefits.

Improvement of compositions and the creation of new organo-mineral complexes for regulating the soil buffer properties that allow the regulation of mobility of HM are actual. It may help to eliminate or at least reduce the harmful effects of excessive amount of HM on the biotic constituent of ecosystems and edafopops.

The paper is focused on the research of the applied aspects of soil remediation, in particular the process of heavy metals (HM) binding and intensifying the cultivation of a soil microbiome, using various organic-mineral compositions.

To achieve the aim, the following tasks were set:

– research of the binding process of heavy metals in the soil under the various organic-mineral compositions action;

– comparison of different approaches to the determination of the metabolic activity of microorganisms in soil microzones under the stimulating effect of the biogenic composite as a product of anaerobic treatment of sewage sludge and phosphogypsum.

3 Research Methodology

3.1 The theoretical foundations of the work

For the formation of a general research concept the synergism of the object and subject of research should be considered. The object of the research can be represented as the impact of heavy metals on the soil ecosystem. At the same time such an impact can lead to the passage of the ecosystem through the bifurcation point when the boundary condition is reached (for example, the maximum bioaccumulation values of the pollutant in the natural components) even with minor fluctuations of the system parameters. This brings the ecosystem to a new development level, in our case – to degradation and increasing instability. A general scheme for combining scientific-theoretical and experimental researches (Figure 1) was formed in the context of developing an integrated methodological approach to the process of studying biotechnological techniques for soil remediation. In particular, the main direction is the formation of the biochemical basis of the research organization to find out how organic-mineral compositions effect on the process of binding heavy metals and the microbial biome oxidative ability of the soil.

The subject of research can be characterized as a process aimed at reducing the negative impact by introducing organic-mineral compositions for binding heavy metals, which through ecosystem autocatalysis can increase its degree of stability and intensify the development process of the soil biome and the humification process directly associated with the rate of productive substrate oxidation.

3.2 Conditions of the microfield experiment

Research of quantitative and qualitative changes in the fractional composition of the soil complex of gray forest soil was carried out with increasing doses of organic-mineral complexes.

The experiment carried out in blocks of organic glass with perforated bottom with a surface area 0.2 m^2. Blocks were filled with gray forest soil from a territory with a high level of anthropogenic impact, containing lead at levels of 17.6–21.2 mg/kg and cadmium – 0.55–1.00 mg/kg (gross shape). The indoor temperature was maintained at the level of 22–25 °C.

Ammonia-acetate buffer solution with a pH 4.8 was used to prepare the extract from air-dry soil samples. This extractant is accepted by the agrochemical service for the extraction of microelements available to plants and serves to assess the soils nutrition with these elements. The obtained solutions were analyzed on a spectrophotometer "C115-M1" (OJSC "SELMI", Ukraine) with an electrothermal atomizer.

Statistical processing of the results was carried out in MS EXEL. The percentage content of the HM mobile forms released by the extracting from their gross content before and after the treatment of the soil by organic-mineral compositions was determined.

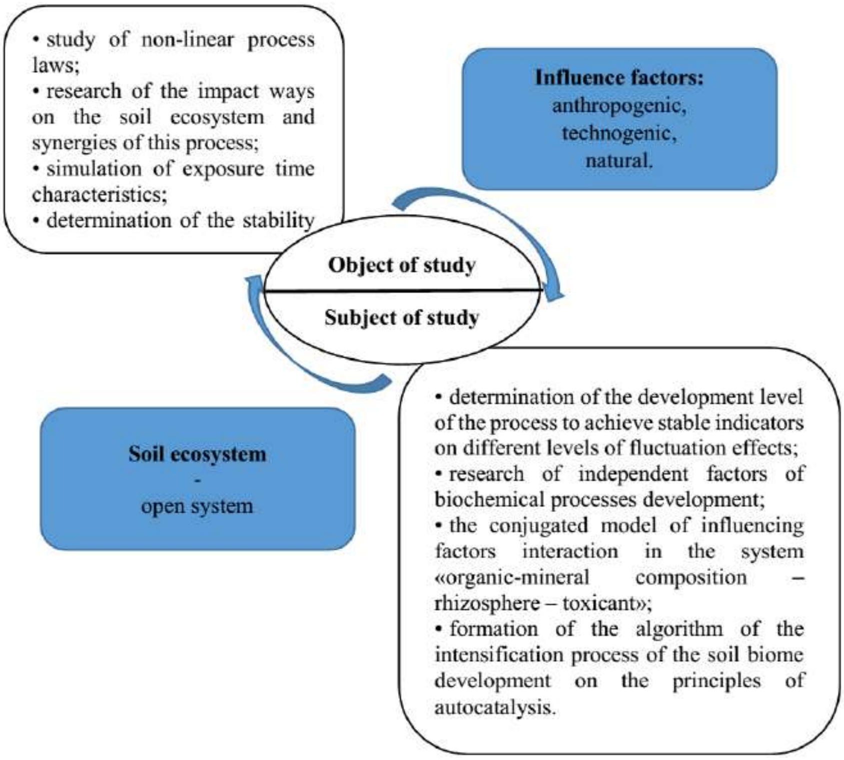

Figure 1 – Block diagram of the integration of theoretical and experimental research in the framework of interrelations in the system «object-subject» of the research

Then the degree of decrease in the heavy metals mobility in the soil was determined by adding various organic-mineral composites according to the formula:

$$D_{HM} = \frac{b_0 - b_1}{b_0} \cdot 100\ \%, \qquad (1)$$

where D_{HM} – degree of decrease of heavy metals mobility in the soil, %; b_0 – initial percentage content of moving forms of HM, %; b_1 – percentage of moving HM forms after processing, %.

The effect of different doses of the biocomposite on the soil biome can be estimated by the change in the kinetic parameters of the development of rhizosphere microorganisms, in particular, by the accumulation of microbial biomass.

The method for the determination of microbial carbon in the soil is based on the respiratory response of microorganisms to the introduction of glucose (10 g of soil was mixed with glucose at a proportion of 10 mgC/g) [21]. The biocomposite, after anaerobic treatment, has a high level of mineralization of sewage sludge with a biotransformed phosphogypsum as mineral base. Therefore, it was decided to apply this method. It should be noted that this method is not recommended for use in soils enriched with fresh decomposed organic matter (straw, manure, etc.).

According to the X-ray diffractometric analysis [22], the mineral spectrum of the biocomposite revealed the following compounds: quartz, gypsum, potassium hydrogen phosphate hydrate, ammonium sulfate, calcium carbonate, calcium aluminum sulfate and complex sulfide fraction.

The optimal biocomposite concentrations are determined experimentally in the range 2.5–7.5 kg/m^2.

In this case, microbial biomass can be recalculated according to the formula [21]:

$$C_{micro} = 30.0 \cdot 10^{-3}\ \text{cm}^3\ CO_2\text{–}C\ /\ g^{-1} \cdot h^{-1}. \qquad (2)$$

The determination of organic carbon is carried out using the Tyurin method, which is based on the decomposition of organic matter with potassium bichromate in an acidic medium, according to existing methods [23].

The initial period of incubation is characterized by increased CO_2 emissions due to the redistribution of nutrients in the soils microzones with mixing, separated from the period of determination (from 0 to 5 hours). So, the calculation of average values was chosen in a 25-hour interval with a relatively constant rate of CO_2.

4 Results and Discussion

4.1 Research of the influence of various organic-mineral compositions on moving forms of heavy metals

Figure 2 shows the characteristic of the influence of various organic-mineral compositions on the reduction degree of HM mobile forms in the soil (gray forest soils) with an exposure duration is 2 months.

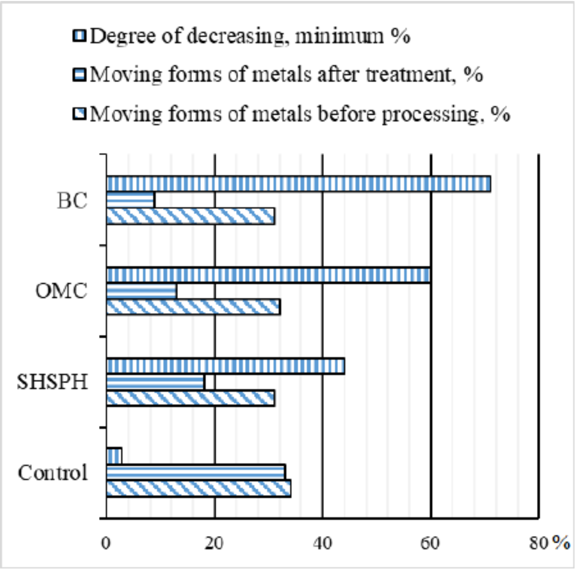

Figure 2 – Comparative characteristics of the influence of various organic-mineral complexes on the binding process of heavy metals moving forms (Pb, Cd): BC is biogenic composite, product of anaerobic processing of the sludge sediments and phosphogypsum; OMC is organic-mineral compost based on a mixture of phosphogypsum (10 % by weight), superphosphate (1 % by weight) and cattle humus; SHSPH is a combination of a mixture of sodium humate and superphosphate (1:1)

When organic-mineral compost (OMC) is introduced on the basis of the mixture of phosphogypsum, superphosphate and manure, a decrease in the volume of HM mobile forms by 12 % of the metals total content was determined under the degree of reduction of HM mobile forms was achieved 60 %, which is 1.3 times higher than this indicator compared with tillage using a combination of a mixture of sodium humate with superphosphate (SHSPH). There was determined that a more rational content of OMC composition. But exactly the combination HM with humic acids is considered a very effective way of their immobilization when the mineral component of the soil is involved. However, the artificial introduction of humates into the soil in a certain composition does not always determine the high efficiency of the binding of HM into the forms that are not available for migration, which indicates the need for additional research and rationalization of relations in the composition of sodium humate and superphosphate mixture according to biochemical and physical-chemical soil conditions. Industrial humates show a stimulating effect on plant growth, but depending on the production technology and materials they demonstrates a certain level of toxic effects in relatively high doses, which should also be taken into account, because the chemical structure and properties of natural and industrial humates are different. That affects their ecological functions in the soil complex.

There is a higher degree of decrease in HM mobility (at least 70 %) compared with other organomineral complexes under introducing biogenic composite, which is the product of anaerobic sludge and phosphogypsum processing. It should be noted that the main characteristics of the biogenic composite were studied in previous works [22, 24] with the reasoning of certain theoretical positions of biochemical influence of biogenic composite on the soil complex.

Thus, it is important to determine the correlation of the changes dynamics in kinetic quantities that characterize the effect of different doses of biogenic composite on the soil biome and the rate of the substrate oxidation over time using mathematical statistics methods.

4.2 Investigation of the comparison different approach for biomass oxidative capacity in the soil microzones

Soil respiration in an ecosystem is often used in complex studies of the level of environmental pollution by HM. Analysis of changes in the intensity of soil respiration, measured in situ, in several pollution gradients formed by large point sources of pollutant emission is used as a rapid method to assess the state of the ecosystem. Evaluate soil respiration by the rate of productive oxidation of the substrate by soil microorganisms, according to the release of carbon dioxide.

By approximating the experimental values, one can determine the rate of carbon dioxide ($C - CO_2$) emission in the soil ecosystem by the equation [25]:

$$v = v_0^{pr} \cdot \exp\left(\mu_m \cdot \tau\right) + v_0^0, \tag{3}$$

where v_0^{pr} is the initial rate of productive oxidation of the substrate, mg/(cm^3·h); v_0^0 – initial velocity of the idle oxidation of the substrate to carbon CO_2, mg/(cm^3·h); μ_m – maximum specific growth rate of microorganisms, h^{-1}; τ – time, h.

Equation (2) can provide an opportunity to assess the effect of a biocomposite on the metabolic activity of microorganisms in the rhizosphere zone, which play an important role in soil recovery under the biochemical binding of toxic substances, in particular heavy metals.

In the previous work [24] mathematically determined the biomass oxidative ability (BOA) of the soil biome, which determines the protective mechanisms of the soil complex in a consistent transformation with a biocomposite under the process of the interaction in the system "biotic component – biogenic product – toxicant". Thus, with the initial condition $\tau = 0$ we have got the equation:

$$\frac{k_f}{1 + \frac{k_f}{k_d} + \frac{k_f}{k_a \cdot S_{org} \cdot Y_{bio}}} \cdot \tau = BOA, \frac{g}{cm^3} h \tag{4}$$

where S_{org} – total organic substrate, including the organic component of the biocomposite, g/cm^3; Y_{bio} – economic coefficient of biomass output for an additional substrate – biocomposite; k_f – the constant of biochemical binding or fixation of metals in the organic-mineral structure; k_d is dissociation constant; k_a – aggregation constant (Table 1).

The obtained mathematical mapping of BOA of the soil biome can be compared with the magnitude of the substrate oxidation rate by the soil microbial biomass with the release of CO_2 according to the equation (2) and experimental data (Table 2).

Table 1 – Values of the parameters that determine the biomass oxidative ability (BOA)

Indicator	Unit of measurement	Value
kf	–	0.078
k_d	–	0.013
k_a	–	0.344
Y_{bio} with a dose of biocomposite:	–	–
2.5	–	1.23
5.0	–	2.45
7.5	–	2.56
S_{org}	g/cm^3	7.50–14.80

The growth rate of microorganisms from equation (2) in its essence can characterize the rate of biomass development, which is taken into account in dependence (3) with used economic biomass yield coefficient under an additional substrate, the biocomposite. This feature can be used to assess the process of stimulating the development of the necessary ecological-trophic groups of microorganisms. Accordingly, it is important to trace the presence of a correlation relationship between the rate of substrate oxidation by the soil microbial biomass with the release of CO_2 according to equation (2) and the dynamics of changes in the forms of HM compounds of the soil biome (equation (3)) depending on the biocomposite dose applied to the soil. It should be noted, that both of these indicators can characterize soil respiration and their comparison will allow us to assess the reliability of the mathematical dependence that was obtained in [24].

Table 2 – Experimental data

Sampling zone	Dose of biocomposite, kg/m^2	Maximum specific growth rate of micro-organisms μ_m, h^{-1}	Microbial biomass, µgC/g
The soil of the rhizosphere	2.5	0.254 ± 0.002 0.234 ± 0.002 0.246 ± 0.005	192 ± 3 188 ± 5 183 ± 2
The soil of the rhizosphere	5.0	0.311 ± 0.002 0.303 ± 0.004 0.317 ± 0.003	253 ± 3 274 ± 2 269 ± 4
The soil of the rhizosphere	7.5	0.312 ± 0.002 0.310 ± 0.004 0.314 ± 0.002	263 ± 5 255 ± 3 277 ± 3

BOA directly takes into account the processes of HM transformation, which can be effectively used for the environmental assessment of the edaphotops conditions during the implementation of remediation measures as a separate indicator of the effectors effect.

Figure 2 shows the comparative dynamics of changes in the values of the biomass oxidative ability (BOA) of the soil biome and the rate of the substrate oxidation (v) over time when various doses of the biocomposite with the appropriate determination coefficients are applied.

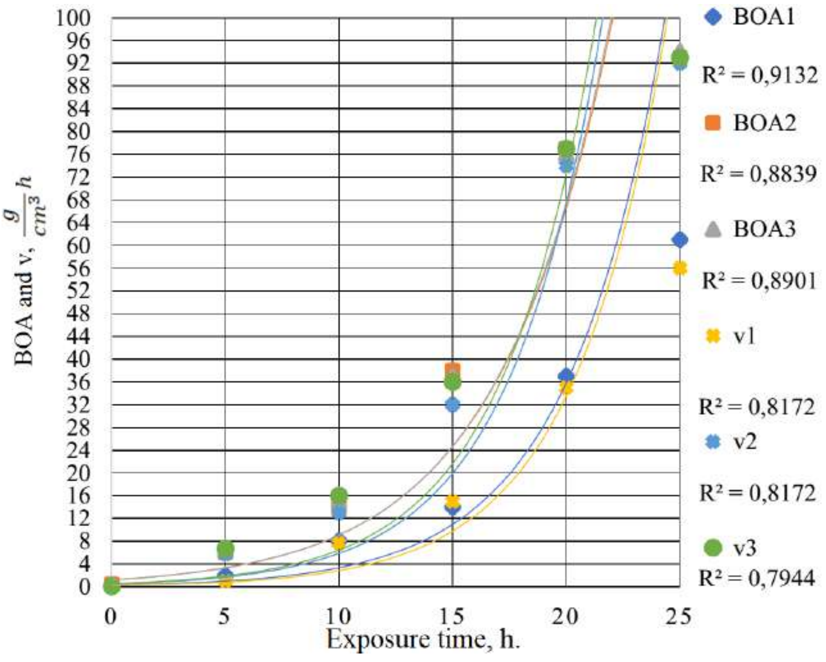

Figure 3 – Comparison of changes in the biomass oxidative ability (BOA) of the soil biome and the rate of the substrate oxidation with the release of carbon dioxide (v) over time when different doses of biocomposite are applied: BOA1 and $v1$ – with a dose of biocomposite 2.5 kg/cm^2; BOA2 and $v2$ – with a dose of biocomposite 5.0 kg/cm^2; BOA3 and $v3$ – with a dose of biocomposite 7.5 kg/cm^2

Thus, the obtained mathematical expression of the BOA (3) agrees well with the experimental data and their standard mathematical processing. At the same time, it allows to describe the soil respiration and the effect of biocomposite on this process as a result of the leveling of the heavy metals toxic action on the microbial biome (described by the values of the constants $k_ф$, k_d, k_a) and stimulation of the development of soil microorganisms of the rhizosphere zone (Y_{bio}) knowing only the total content of organic matter in the soil.

5 Conclusions

The maximum degree of reduction in the heavy metals mobility (not less than 70 %) was achieved in the case of the biogenic composite use based on the research of the influence on the HM moving forms of such organic-mineral compositions as a biogenic composite – a product of anaerobic conversion of sludge sediments and phosphogypsum, organic-mineral compost based on a mixture of phosphogypsum (10 % by weight), superphosphate (1 % by weight) and manure, and a combination of a mixture of sodium humate with superphosphate (1:1).

The experimental data was obtained regarding the velocity magnitude of the substrate oxidation by the soil microbial biomass with the release of CO_2, by the values of which the growth rate of microorganisms was determined. Correlation relations of the dynamics in BOA values for the soil biome and the rate of the substrate oxidation was proved over time treatment with different doses of the biocomposite with using mathematical statistics methods.

The development of methodical principles for the rapid assessment of the ecological characteristics of the soils of natural and human-made landscapes will be developed in further research under rationalizing the biocomposite dosage on different types of soils.

References

1. Panchenko, T., Pradivlyana, A., & Ursul, O. (2018). Estimation of the influence of thermal energy objects on the environment. *Materialy XLVII Naukovo-Tekhnichnoyi Konferentsiyi Pidrozdiliv VNTU,* Vinnytsya, https://conferences.vntu.edu.ua/index.php/all-fksa/all-fksa-2018/paper/view/4574.
2. Shevchenko, O. (2013). The heavy metals content in the atmospheric air of Kyiv and sources of their receipt. *Chasopys kartohrafiyi : zbirnyk naukovykh prats*’, Vol. 6, pp. 207–216.
3. Bolshakov, V., & Borisochkina, T. (2002). Reclamation methods of soil contaminated with heavy metals. *Pratsi Hruntovoho Instytutu named after V. V. Dokuchayev*, No. 56, pp. 122–127.
4. Sharkova, S. (2010). The use of reclamation techniques for growing spring wheat under the technogenesis conditions. *Plodorodiye*, No. 3, pp. 51–52.
5. Mineyev, V., Kochetavkin, A., & Nguyen, V. (1989). Using natural zeolites to prevent heavy metals contamination of soil and plants. *Agrokhimiya*, No. 8, pp. 85–95.
6. Sharkova, S., & Nadezhkina, Ye. (2008). The ways to improve the quality of grain in the conditions of anthropogenic pollution. *Vestnik Rossiyskoy Akademii Sel’skokhozyaystvennykh Nauk*, No. 4, pp. 82–84.
7. Ilin, V., Baydina, N., & Konarbayeva, G. (2000). The content of heavy metals in soils and plants of Novosibirsk. *Agrokhimiya*, No. 1, pp. 66–73.
8. Barvinskyy, A. (2012). Soil physico-chemical factors of increasing land productivity in Polissya agrolandscapes. *Zemleustriy, Kadastr i Monitorynh Zemel*, No. 3–4, pp. 66–75.
9. Efremova, S. Y. (2012). Detoxication Receptions Chemically polluted soils. *Izv. Penz. Gos. Pedagog. Univ. named after V. G. Belinskiy*, No. 29, pp. 379–382.
10. Derakhshan, Z., Myung, N., Jung C., & Kim, K.-H. (2017). Remediation of soils contaminated with heavy metals with an emphasis on immobilization technology. *Environmental Geochemistry and Health*, doi: 10.1007/s10653-017-9964-z.
11. Chen, Y. H., & Li, F. A. (2010). Kinetic study on removal of copper (II) using goethite and hematite nano-photocatalysts. *Journal of Colloid and Interface Science*, Vol. 347(2), pp. 277–281.
12. Basta, N., & McGowen, S. (2004). Evaluation of chemical immobilization treatments for reducing heavy metal transport in a smelter-contaminated soil. *Environmental Pollution*, Vol. 127(1), pp. 73–82.
13. Ruttens, A., Colpaert, J., Mench, M., Boisson, J., Carleer, R., & Vangronsveld, J. (2006). Phytostabilization of a metal contaminated sandy soil. Part II. Influence of compost and/or inorganic metal immobilizing soil amendments on metal leaching. *Environmental Pollution*, Vol. 144(2), pp. 533–539.
14. Xie, Y., Xiao, K, Sun, Y, Gao, Y, Yang, H, & Xu, H. (2018). Effects of amendments on heavy metal immobilization and uptake by Rhizoma chuanxiong on copper and cadmium contaminated soil. *R. Soc. Open Ssci.*, Vol. 5, 181138, doi: 10.1098/rsos.181138.
15. Patent of UA for utility model No. 85002. *Method of remediation technogenically contaminated with heavy metals of soil*. Published on 11.11.2013. Retrieved from http://uapatents.com/7-85002-sposib-remediaci-tekhnogenno-zabrudnenogo-vazhkimi-metalami-runtu.html.
16. Patent of RF for utility model No. 2492944. *Method of cleaning black soil contaminated with heavy metals*. Published on 20.09.2013. Retrieved from http://www.freepatent.ru/patents/2492944.
17. Patent of USA for utility model No. 9108233. *Washing of contaminated soils*. Published on 18.08.2015.

18. Patent of UA for utility model No. 82303. *A method for cleaning clay-based soils and slurries*. Published on 25.03.2008.
19. Shahid, M., Xiong, T., Masood, N., Leveque, T., Quenea, K., Austruy, A., Foucault, Y., & Dumat, C. (2014). Influence of plant species and phosphorus amendments on metal speciation and bioavailability in a smelter impacted soil: a case study of food-chain contamination. *J. Soil. Sediment*, Vol. 14, pp. 655–665.
20. Saifullah, Shahid, M., Zia-Ur-Rehman, M., Sabir, M., & Ahmad, H.R., (2015). Phytoremediation of Pb-contaminated soils using synthetic chelates. *Soil Remediation and Plants*. Elsevier Inc.
21. Edelgard, Kaiser, Torsten, Müller, Rainer, Georg, Joergensen, & Heinemeyer, O. (1992). Evaluation of methods to estimate the soil microbial biomass and the relationship with soil texture and organic matter. *Soil Biology and Biochemistry*. Vol. 24(7), 675–683, doi: 10.1016/0038-0717(92)90046-Z.
22. Chernysh, Y. Y., & Plyatsuk, L. D. (2018). Binding of heavy metals in the soil complex at the introduction biocomposite based on sewage sludge and phosphogypsum. *Young Scientist,* No. 1(53), pp. 446–450.
23. Derzhspozhyvstandart Ukrayiny (2016). *The quality of the soil. Determination of humus group composition by Tyurin method in modification of Konov and Belchikova : DSTU 7855:2015*. Kyiv, Ukraine.
24. Chernysh, Ye., & Plyatsuk, L. (2017). Modeling of the process of stimulation the protective functions of the soil complex using a biogenic composite based on technogen waste. *Ecological science*, No. 1–2 (16–17), pp. 129–140.
25. Panikov, N. S. (1992). *Growth kinetics of microorganisms: general patterns and environmental applications*. Science, Moscow.

Remediation of Soil Contaminated with Heavy Metals

Пляцук Л. Д.[1], Черниш Є. Ю.[1], Аблєєва І. Ю.[1], Яхненко О. М.[1],
Батальцев Є. В.[1], Балінтова М.[2], Гурець Л. Л.[1]

[1] Сумський державний університет, вул. Римського-Корсакова, 2, 40007, м. Суми, Україна;
[2] Технічний університет м. Кошице, вул. Летна, 1, 40001, м. Кошице, Словаччина

Анотація. Стаття присвячена дослідженню прикладних аспектів рекультивації ґрунтів, зокрема процесу зв'язування важких металів та інтенсифікації вирощування ґрунтового мікробіома з використанням різних органічно-мінеральних композицій.: біогенний композит, який є продуктом анаеробного перетворення осадів стічних вод і фосфогіпсу; органічно-мінеральний компост на основі суміші фосфогіпсу, суперфосфату і гумусу великої рогатої худоби; та комбінацію суміші гумату натрію і суперфосфату. Була проведена інтеграція теоретичних і експериментальних принципів в синергетичний аналіз взаємозв'язків у системі «об'єкт – предмет дослідження» при вивченні динаміки змін форм знаходження важких металів у ґрунті. Відсотковий вміст мобільних форм важких металів, що виділяються екстрагентом від їх питового вмісту до і після обробки ґрунту органічно-мінеральними композиціями визначені з використанням спектрофотометричним методом. Здійснено порівняння ефективності обробки ґрунту. Використання методів математичної статистики дозволило довести кореляційний зв'язок між динамікою значень окислювальної здатності біомаси для біома грунту і швидкостю окислення субстрату для різного вмісту біокомпозиту.

Ключові слова: важкі метали, рекультивація грунта, органічно-мінеральні композиції, фосфогіпс, біом ґрунту, окислювальна здатність біомаси.

JOURNAL OF ENGINEERING SCIENCES
ЖУРНАЛ ІНЖЕНЕРНИХ НАУК
ЖУРНАЛ ИНЖЕНЕРНЫХ НАУК
Web site: http://jes.sumdu.edu.ua
Volume 6, Issue 1 (2019)

Copyright Agreement

We, the Authors of the Manuscript publishing in the Journal of Engineering Sciences, in the case of acceptance for publication, transfer to Founders and Editorial Board the underlined rights:

– publishing this article in English and distribution of the printed version;
– English translation of the article and distribution the hard copy of the translation;
– distribution of the electronic version of the article through any electronic means (by hosted on the official website of the Journal, in electronic databases, repositories, etc.).

We reserve the rights without the consent with the Editorial Board or Founders:

– to use the article materials partially or in whole for educational purposes;
– to use the article materials partially or in whole to write own dissertations;
– to use the article materials for thesis preparing, conference materials, as well as for presentations;
– to post electronic copies (including the final electronic version downloaded from the official website of the Jounal):
– on the personal web-sources of all the co-authors (websites, web-pages, blogs, etc.);
– on the web-sources of authors working organizations (including electronic institutional repository);
– on the International Scientometric Databases (CrossRef, DOAJ, Index Copernicus Indexing, etc.);
– on non-commercial Open Access sources (e.g. arXiv.org).

In all cases, the presence of citations to the article or hyper-link to the electronic copy of on the official web-site of the journal is obligatory.

By this agreement, we also certify that the submitted manuscript:

– does not violate the copyrights of other persons or organizations;
– has not been published previously in other publishing houses and submitted for publication in other Journals.

JOURNAL OF ENGINEERING SCIENCES
ЖУРНАЛ ІНЖЕНЕРНИХ НАУК
ЖУРНАЛ ИНЖЕНЕРНЫХ НАУК
Web site: http://jes.sumdu.edu.ua
Volume 6, Issue 1 (2019)

Dear Authors of the Journal of Engineering Sciences!

The Editorial Board of the Journal of Engineering Sciences pays special attention to the structure of the articles according to the **List of Scientific Professional Editions of Ukraine** (Category "B", Minutes No. 1208 of 07.11.2018, Appendix No. 8). Only original articles by the authorship of up to 5 authors are accepted for the publication according the **Template** with the following elements:

– general statement of the problem and its relation with the important scientific or practical problems;
– analysis of the recent investigations and publications in the same research field;
– statement of the significance of the general problem that were not solved before;
– statement of the purpose of the research article;
– description of the initial data of the research with the justification of the achieved scientific results;
– conclusions and ways for further development of the research.

All the articles are reviewed by the independent double-blind procedure.

All the authors should sent via e-mail jes@sumdu.edu.ua the electronic version of the following materials:

– article **in English** according to the **Template**;
– information about authors and their affiliation with the related address.

ATTENTION!

If one of the mentioned components is not sent or there are many stylistic, orthographic and grammatical errors, the article will not be taken into consideration by the Editorial Board and will not be reviewed.

Minimum size of the materials:

1. Scientific – theoretical articles (up to 25 000 symbols, about 14 pages) that deal with the theoretical research and descriptions of physical laws concerning the investigated phenomena; theoretical generalizations and fundamental principles proved by the experimental research data.
2. Scientific-practical articles (up to 10 000 symbols, about 6 pages) that deal with scientific experiments and real experience. They include the statement of the proposed methods for the experimental research or means for the observation of the studied phenomena. An essential part of these articles is the description of the achieved results and their explanation acquired in the process of immediate interaction with the object of investigations, its significance and practical implementations.
3. Scientific-methodological articles (up to 15 000 symbols, about 8 pages) that deal with the review of processes, methods, instruments for solving scientific and applied problems; the statement of the new methodology, results of which allow creating more precise methodology on the basis of up-to-date methodology for the implementation of discovered laws.

The Ministry of Education and Science of Ukraine

Міністерство освіти і науки України

Министерство образования и науки Украины

JOURNAL OF ENGINEERING SCIENCES

ЖУРНАЛ ІНЖЕНЕРНИХ НАУК

ЖУРНАЛ ИНЖЕНЕРНЫХ НАУК

Scientific Journal

Науковий журнал

Научный журнал

Відповідальний за випуск	Responsible for release:
Д. В. Криворучко	D. V. Kryvoruchko
Комп'ютерне складання та верстання:	**Computer design and typesetting**
І. В. Павленко	I. V. Pavlenko
Коректори:	**Correctors:**
Н. З. Клочко, С. М. Симоненко	N. Z. Klochko, S. M. Symonenko

Підписано до друку 01.06.2019. Формат 60x84/8.
Папір офс. Друк офс.
Ум. друк. арк. 15,82. Обл.-вид. арк. 21,51.
Наклад 100 пр. Замовлення №
Сумський державний університет, вул. Римського-Корсакова, 2, 40007, м. Суми, Україна
Свідоцтво про внесення суб'єкта видавничої справи до Державного реєстру
ДК № 3062 від 17.12.2007.

Надруковано у друкарні СумДУ,
вул. Римського-Корсакова, 2, 40007, м. Суми, Україна

Editorial Board: 2 Rymskogo-Korsakova St., 40007 Sumy, Ukraine
Contact Phones: +38 (0542) 331024; +38 (099) 3845740
E-mail: jes@sumdu.edu.ua
Web-site: http://jes.sumdu.edu.ua

State registration certificate of the print mass-media No. 20499-10299 ПР.
